SYNTHESIS AND STUDY OF NOVEL HYBRID MOLECULES

A THESIS SUBMITTED IN PARTIAL FULFILLMENT OF THE REQUIREMENTS FOR THE DEGREE OF DOCTOR OF PHILOSOPHY

LALDINGLUAIA KHIANGTE

MZU REGISTRATION NO. : 1807294

PH.D REGISTRATION NO. : MZU/Ph.D./1252 of 16.08.2018

DEPARTMENT OF INDUSTRIAL CHEMISTRY

SCHOOL OF PHYSICAL SCIENCES

DECEMBER, 2022

SYNTHESIS AND STUDY OF NOVEL HYBRID MOLECULES

BY

LALDINGLUAIA KHIANGTE

Department of Industrial Chemistry

Under the supervision of

Dr. VED PRAKASH SINGH

Submitted

In partial fulfillment of the requirement of the Degree of Doctor of Philosophy in Industrial Chemistry of Mizoram University, Aizawl.

SYNTHESIS AND STUDY OF NOVEL HYBRID MOLECULES

BY

LALDINGLUAIA KHIANGTE

Department of Industrial Chemistry

Under the supervision of

Dr. VED PRAKASH SINGH

Submitted

In partial fulfillment of the requirement of the Degree of Doctor of Philosophy in Industrial Chemistry of Mizoram University, Aizawl.

MIZORAM UNIVERSITY
(A central University under the Act of Parliament)
Department of Industrial Chemistry
School of Physical Sciences

Dr. Ved Prakash Singh
Associate Professor

CERTIFICATE

This is to certify that the thesis entitled **"*Synthesis and study of novel hybrid molecules*"** submitted by **Laldingluaia Khiangte** to Mizoram University, Tanhril, Aizawl, for the award of the degree of ***Doctor of Philosophy*** in Industrial Chemistry is a *bona fide* record of the original investigations carried out by him under my supervision. He has been duly registered and the thesis presented is worthy of being considered for the award of the Ph.D. degree. This work has not been submitted for any degree in any other university.

Dated: (Dr. VED PRAKASH SINGH)
Supervisor

Declaration of the Candidate

Mizoram University

December, 2022

I, Laldingluaia Khiangte, hereby declare that the subject matter of this thesis is the record of work done by me, that the contents of this thesis did not form basis of the award of any previous degree to me or to do the best of my knowledge to anybody else, and that the thesis has not been submitted by me for any research degree in any other University/ Institute.

This is being submitted to the Mizoram University for the degree of Doctor of Philosophy in Industrial Chemistry.

(LALDINGLUAIA KHIANGTE)

Candidate

(Dr. VED PRAKASH SINGH)

Head

(Dr. VED PRAKASH SINGH)

Supervisor

ACKNOWLEDGEMENT

Firstly, I thank to God the Almighty for His blessing with health, strength, and knowledge to complete my work. Without His grace and mercy, I am nothing.

Then, I thank my supervisor, ***Dr. Ved Prakash Singh***, *Associate Professor, Department of Industrial Chemistry, Mizoram University*, for his immense dedication, support and motivation during my Ph.D research work. His scientific knowledge had a great impact on the ease of my research work. I appreciate his empathy, encouragement, and patience with me during my entire research program.

As I started my research in the department of chemistry, I extend my gratitude to all the teaching faculty, *Prof. Muthukumuran R., Head, Department of Chemistry, MZU, Prof. Diwakar Tiwari, Dean, School of Physical Sciences, all the faculties of Chemistry Department and Industrial Chemistry,* and laboratory staff, *Mr. Brojendro Singh Shagolsem, Sr. Laboratory Technician, and Mr. John Vanlalhruaia, Technical Assistant, Chemistry Department. MZU*, for their endless help and support throughout my academic career.

I appreciate the good cooperation I have experienced from my fellow research scholar of the Department of Chemistry and Industrial Chemistry. I would like to give credit to my fellow labmates *Dr. Jayanta Dowarah, Dr. Lalhruaizela, Brilliant N. Marak, Biki Hazarika, Lalropuia, Saurabh Chetia, and Lalremruati* for their limitless support in my research work. They were my devoted friends and never failed to comfort me during my times of difficulties. Their good deeds would be remembered during my entire life.

I also express my deepest gratitude to an expert crystallographer *Dr. Ramesh Kataria, Department of Chemistry, Panjab University, Chandigarh,* and *Prof. Necmi Dege, Department of Physics, Ondokuz Mayıs University, Samsun, Turkey,* for their collaboration in refining the crystal structure of my compounds.

I also thank Banaras Hindu University, Varanasi, CSIR-North East Institute of Science and Technology (CSIR-NEIST) and Central Drug Research Institute (CDRI), Lucknow, and Indian Institute of Chemical Technology (IICT), Hyderabad for collecting NMR and Mass spectra.

I also thank the Government of Mizoram for giving me permission to continue research for my Ph.D., and my colleagues in Govt. Serchhip College for their valuable advice and full support during my research work.

I express my heartfelt thanks to my wife, Lalnunpuii for her courage, strength, and hard work she went through for the accomplishment of my research work.

(LALDINGLUAIA KHIANGTE)

CONTENTS

CHAPTER 1

INTRODUCTION

CHAPTER 2

SYNTHESIS AND STUDY OF 2-PYRIDONE-BASED HYBRID MOLECULES

CHAPTER 3

SYNTHESIS AND STUDY OF PYRANOPYRAZOLE AND SPIROOXINDOLE DERIVATIVES

CHAPTER 4

BIOLOGICAL STUDY OF FLEXIBLE PYRIDINE-BASED HYBRID MOLECULES

LISTS OF TABLES

LISTS OF FIGURES

ABBREVIATIONS

2D	Two-Dimensional
3D	Three-Dimensional
5-LOX	Arachidonate 5-lipoxygenase
^{13}C NMR	Carbon-13 nuclear magnetic resonance
^{1}H NMR	Proton nuclear magnetic resonance
Ach	Acetylcholine protein
ADME	Absorption, Distribution, Metabolism, and Excretion
AIDS	Acquired Immune Deficiency Syndrome
AKR1C3	Aldo-keto reductase family 1 member 3
ALK	Anaplastic lymphoma kinase
$CDCl_3$	Deuterated chloroform
Chk1	Checkpoint kinase 1
CIF	Crystallographic Information File
COX-2	Cyclooxygenase 2
D…A	Donor…Acceptor
D–H	Donor – Hydrogen
D–H...A	Donor–Hydrogen…Acceptor
DDQ	2,3-Dichloro-5,6-dicyano-1,4-benzoquinone
DHPM	Dihydropyrimidinone
DMF	Dimethylformamide
DMSO	Dimethyl sulfoxide
DNA	Deoxyribonucleic acid
FDA	Food and Drug Administration
Eg5	Kinesin spindle protein
EGFR	Epidermal growth factor receptor
ER	Enrichment ratio
EtOAc	Ethyl acetate

FTNMR	Fourier Transform Nuclear Magnetic Resonance
GABA	γ-Aminobutyric acid
H…A	Hydrogen…Acceptor
HEPES	4-(2-hydroxyethyl)-1-piperazineethanesulfonic acid
HIV	Human Immunodeficiency Virus
IUPAC	International Union of Pure and Applied Chemistry
MHz	Megahertz
MS	Mass spectrometry
NMR	Nuclear Magnetic Resonance
NSAIDs	Non-Steroidal Anti-Inflammatory Drugs
ORTEP	Oak Ridge Thermal Ellipsoid Plot
PDB	Protein Data Bank
PET	Photoinduced Electron Transfer
RB	Round bottom flask
RCSB	Research Collaboratory for Structural Bioinformatics
RMSD	Root-mean-square deviation
RNA	Ribonucleic acid
RT	Room temperature
SAR	Structure-Activity Relationship
SC-XRD	Single Crystal X-ray Diffraction
TAR RNA	Transactivation responsive RNA
TLC	Thin-layer chromatography
TME	Tumor microenvironment
TMS	Tetramethylsilane
UV	Ultraviolet
vdW	van der Waals

MIZORAM UNIVERSITY
(A central University under the Act of Parliament)
Department of Industrial Chemistry
School of Physical Sciences

Dr. Ved Prakash Singh
Associate Professor

CERTIFICATE

This is to certify that the thesis entitled **"*Synthesis and study of novel hybrid molecules*"** submitted by **Laldingluaia Khiangte** to Mizoram University, Tanhril, Aizawl, for the award of the degree of ***Doctor of Philosophy*** in Industrial Chemistry is a *bona fide* record of the original investigations carried out by him under my supervision. He has been duly registered and the thesis presented is worthy of being considered for the award of the Ph.D. degree. This work has not been submitted for any degree in any other university.

Dated: (Dr. VED PRAKASH SINGH)
Supervisor

Declaration of the Candidate

Mizoram University

December, 2022

I, Laldingluaia Khiangte, hereby declare that the subject matter of this thesis is the record of work done by me, that the contents of this thesis did not form basis of the award of any previous degree to me or to do the best of my knowledge to anybody else, and that the thesis has not been submitted by me for any research degree in any other University/ Institute.

This is being submitted to the Mizoram University for the degree of Doctor of Philosophy in Industrial Chemistry.

(LALDINGLUAIA KHIANGTE)

Candidate

(Dr. VED PRAKASH SINGH)

Head

(Dr. VED PRAKASH SINGH)

Supervisor

ACKNOWLEDGEMENT

Firstly, I thank to God the Almighty for His blessing with health, strength, and knowledge to complete my work. Without His grace and mercy, I am nothing.

Then, I thank my supervisor, ***Dr. Ved Prakash Singh***, *Associate Professor, Department of Industrial Chemistry, Mizoram University*, for his immense dedication, support and motivation during my Ph.D research work. His scientific knowledge had a great impact on the ease of my research work. I appreciate his empathy, encouragement, and patience with me during my entire research program.

As I started my research in the department of chemistry, I extend my gratitude to all the teaching faculty, *Prof. Muthukumuran R., Head, Department of Chemistry, MZU, Prof. Diwakar Tiwari, Dean, School of Physical Sciences, all the faculties of Chemistry Department and Industrial Chemistry,* and laboratory staff, *Mr. Brojendro Singh Shagolsem, Sr. Laboratory Technician, and Mr. John Vanlalhruaia, Technical Assistant, Chemistry Department. MZU*, for their endless help and support throughout my academic career.

I appreciate the good cooperation I have experienced from my fellow research scholar of the Department of Chemistry and Industrial Chemistry. I would like to give credit to my fellow labmates *Dr. Jayanta Dowarah, Dr. Lalhruaizela, Brilliant N. Marak, Biki Hazarika, Lalropuia, Saurabh Chetia, and Lalremruati* for their limitless support in my research work. They were my devoted friends and never failed to comfort me during my times of difficulties. Their good deeds would be remembered during my entire life.

I also express my deepest gratitude to an expert crystallographer *Dr. Ramesh Kataria, Department of Chemistry, Panjab University, Chandigarh,* and *Prof. Necmi Dege, Department of Physics, Ondokuz Mayıs University, Samsun, Turkey,* for their collaboration in refining the crystal structure of my compounds.

I also thank Banaras Hindu University, Varanasi, CSIR-North East Institute of Science and Technology (CSIR-NEIST) and Central Drug Research Institute (CDRI), Lucknow, and Indian Institute of Chemical Technology (IICT), Hyderabad for collecting NMR and Mass spectra.

I also thank the Government of Mizoram for giving me permission to continue research for my Ph.D., and my colleagues in Govt. Serchhip College for their valuable advice and full support during my research work.

I express my heartfelt thanks to my wife, Lalnunpuii for her courage, strength, and hard work she went through for the accomplishment of my research work.

(LALDINGLUAIA KHIANGTE)

CONTENTS

CHAPTER 1

INTRODUCTION

CHAPTER 2

SYNTHESIS AND STUDY OF 2-PYRIDONE-BASED HYBRID MOLECULES

CHAPTER 3

SYNTHESIS AND STUDY OF PYRANOPYRAZOLE AND SPIROOXINDOLE DERIVATIVES

CHAPTER 4

BIOLOGICAL STUDY OF FLEXIBLE PYRIDINE-BASED HYBRID MOLECULES

LISTS OF TABLES

LISTS OF FIGURES

ABBREVIATIONS

2D	Two-Dimensional
3D	Three-Dimensional
5-LOX	Arachidonate 5-lipoxygenase
^{13}C NMR	Carbon-13 nuclear magnetic resonance
^{1}H NMR	Proton nuclear magnetic resonance
Ach	Acetylcholine protein
ADME	Absorption, Distribution, Metabolism, and Excretion
AIDS	Acquired Immune Deficiency Syndrome
AKR1C3	Aldo-keto reductase family 1 member 3
ALK	Anaplastic lymphoma kinase
$CDCl_3$	Deuterated chloroform
Chk1	Checkpoint kinase 1
CIF	Crystallographic Information File
COX-2	Cyclooxygenase 2
D…A	Donor…Acceptor
D–H	Donor – Hydrogen
D–H...A	Donor–Hydrogen…Acceptor
DDQ	2,3-Dichloro-5,6-dicyano-1,4-benzoquinone
DHPM	Dihydropyrimidinone
DMF	Dimethylformamide
DMSO	Dimethyl sulfoxide
DNA	Deoxyribonucleic acid
FDA	Food and Drug Administration
Eg5	Kinesin spindle protein
EGFR	Epidermal growth factor receptor
ER	Enrichment ratio
EtOAc	Ethyl acetate

FTNMR	Fourier Transform Nuclear Magnetic Resonance
GABA	γ-Aminobutyric acid
H…A	Hydrogen…Acceptor
HEPES	4-(2-hydroxyethyl)-1-piperazineethanesulfonic acid
HIV	Human Immunodeficiency Virus
IUPAC	International Union of Pure and Applied Chemistry
MHz	Megahertz
MS	Mass spectrometry
NMR	Nuclear Magnetic Resonance
NSAIDs	Non-Steroidal Anti-Inflammatory Drugs
ORTEP	Oak Ridge Thermal Ellipsoid Plot
PDB	Protein Data Bank
PET	Photoinduced Electron Transfer
RB	Round bottom flask
RCSB	Research Collaboratory for Structural Bioinformatics
RMSD	Root-mean-square deviation
RNA	Ribonucleic acid
RT	Room temperature
SAR	Structure-Activity Relationship
SC-XRD	Single Crystal X-ray Diffraction
TAR RNA	Transactivation responsive RNA
TLC	Thin-layer chromatography
TME	Tumor microenvironment
TMS	Tetramethylsilane
UV	Ultraviolet
vdW	van der Waals

CHAPTER 1

1. INTRODUCTION

1.1 Background

The chemistry of heterocyclic compounds has considerable attention from chemists due to their widespread applications. More than half of the compounds produced in nature have structures incorporated with heterocyclic rings. Many alkaloids derived from heterocyclic molecules are used as drugs. The influence of these heterocycles in day-to-day life has been convincingly established. Moreover, pharmaceutical and agrochemical industries have significant developments to quench the quest of organic chemists to develop applied heterocyclic compounds for the benefit of humanity. It is well known that most antibiotics are the most effective drugs. However, most drugs are generally synthesized products, which are heterocyclic compounds.

A quick search of the FDA databases demonstrates the structural importance of nitrogen-containing heterocycles in drug design and pharmaceutical engineering. A nitrogen heterocycle is found in over 75% of all small-molecule medicines. Vitaku et al. published a comprehensive compendium of nitrogen heterocycles with structural diversity, substitution patterns, and their frequency in heterocycles in FDA-approved medications (Vitaku et al., 2014). Nitrogen atoms can establish hydrogen bonds with biological targets very easily. So, N-heterocyclic skeletons have many therapeutic applications and are used as the building blocks of several drugs (Zhang & Studer, 2015).

The study is based on the design of drugs by combining two or more distinct active pharmacophores from different target molecules to obtain hybrid structures with a broad range of biological activities with high efficiency and low toxicity. This strategy is applied to develop multi-target drugs (Kuang et al., 2018). The methodical arrangement of pharmacophores from selective ligands is the most selective method for preparing hybrid ligands. A cleavable or non-cleavable linker may link the pharmacophores, which are overlapped by improving structural similarities

(overlapping pharmacophores) (Morphy et al., 2004). Over the last few years, combining different chemotherapy mechanisms of action has been a popular treatment method. Consequently, the hybrid structure containing drugs could be helpful for treating cancer due to their multiple targets (Mayur et al., 2009; Sashidhara et al., 2010).

Many drug development strategies aim to influence multiple targets in a parallel mode for better success. Among them, multiple target methods are one of the most fundamental combinatorial therapies used to treat many diseases, such as cancer, atherosclerosis, depression, and AIDS (Korcsmáros et al., 2007). Recently developed 'multi-target lead discovery' using combination therapies is a hopeful tool to identify some novel drugs (Borisy et al., 2003; Dancey & Chen, 2006; Millan, 2006). Some effective drugs, such as antidepressants, anti-neurodegenerative agents, non-steroidal anti-inflammatory drugs (NSAIDs), salicylate, metformin, and multi-target kinase inhibitors, affect many objectives instantaneously (Huang, 2002; Korcsmáros et al., 2007; Morphy et al., 2004).

1.2 Hybrid molecules

A hybrid molecule is a synthetic compound that combines two or more molecules by a chemical bond. Combining natural or synthetic active compounds forms a new compound with collaborative activity and reduces side effects or toxicity. Molecular hybridization links the constituents directly through some linker or merges the active structural parts into a single molecule (Mohsin & Ahmad, 2018). One of the approaches of clinicians to treat unresponsive patients has reinvigorated researchers worldwide toward designing ligands consisting of multiple pharmacophores. These kinds of designed single molecules regulate multiple targets owing to problems related to combination therapy.

Molecular hybridization aims at the rational design of the ligands or prototypes through the fusion of the molecular structure of two or more known bioactive derivatives, leading to the design of the new molecular hybrid structure. It maintains the pre-selected features of the innovative prototype. This is a new drug design and development concept to form a new drug with improved efficacy and affinity

concerning the target compounds. In this method, two drugs are covalently connected and presented as a single molecule (Nepali et al., 2014). The two known drug pharmacophores are incorporated into one molecule to possess dual drug action. One of the hybrid parts may be incorporated to balance the known side effects or to intensify its impact through action (Hulsman et al., 2007). Associated entities should be affixed to their precise targets and provide a more significant therapeutic effect by intensifying or applying multifactorial biological activity. Such a sole hybrid agent can moderate multiple targets involved in proliferation and capably destroy the target cells. Moreover, it keeps a more detailed pharmacokinetic profile, decreasing drug-drug interactions and simplifying drug development (Claudio Viegas-Junior et al., 2007).

Multi-targeted agents are usually planned as per the multi-pharmacophore approach. The techniques used to generate multiple ligands from the selective ligands result in the combination of pharmacophores. The pharmacophores are linked together by a cleavable or non-cleavable linker or overlap by taking advantage of structural similarities (Szumilak et al., 2021). The multi-pharmacophore model may be divided into four distinct types based on the degree of pharmacophore overlapping: conjugated pharmacophore with the cleavable or non-cleavable linker, fused and merged pharmacophore **(Figure 1.1)** (Fu et al., 2017; Morphy et al., 2004).

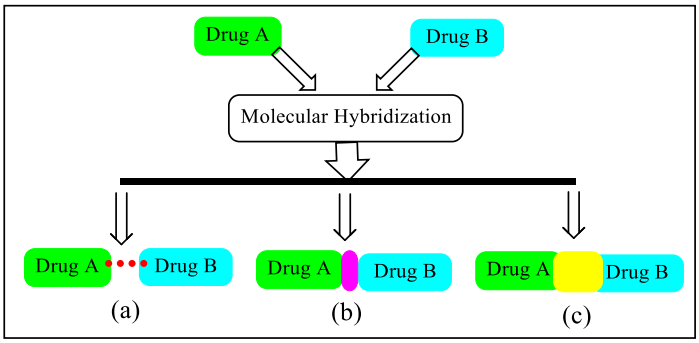

Figure 1.1: Different molecular hybridization strategies: (a) Conjugate hybrid (Cleavable/non-cleavable linker), (b) Fused hybrid (Linker is reduced/removed), (c) Merged hybrid (linker is absent, two drugs merged by taking advantage of common pharmacophore).

The main advantage of developing hybrid molecules is that they can target multiple pathological processes involved in complex diseases by combining the structural elements of selective biological active moieties into a single molecule that

can simultaneously span numerous types of targets. The advantages of hybrid compounds include reduced toxicity and the demonstration of synergistic benefits in the therapeutic effectiveness of the separate moieties. Hybrid molecules have evolved better biological potential, which should lead to significant advancements in treating inflammation and the wide range of disorders it causes.

The synthesis of hybrid molecules as a range of pharmacological agents has steadily increased over the past two decades. The naturally occurring coumarin has attracted the attention of researchers for exploiting its broad biological properties. Therefore, warfarin, acenocoumarol, armillarisin A, hymecromone, and carbochromen have been approved for therapeutic use **(Figure 1.2)**. Several recent reports have shown that backbone coumarin combined with nitrogen-containing heterocyclic substances like azetidine, thiazolidine, thiazole, etc. These can significantly increase the antibacterial effect of hybrid molecules. Zhou et al. (Shi & Zhou 2011) reported coumarin and triazole hybrids and, checked against A. *fumigatus*, showed significantly improved antifungal activities compared with fluconazole. There is still scope to discover the treasure trove of simple and natural antifungal moieties. Such compounds can be hybridized to obtain new molecules with better efficacy and pharmacological behavior.

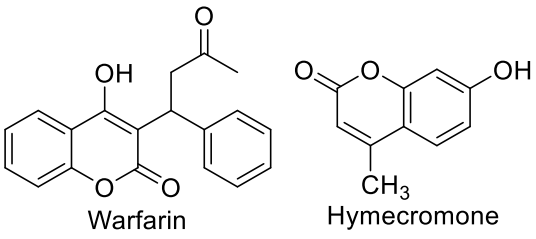

Figure 1.2: Coumarin hybrid molecules

1.3 Molecular recognition

The key features of life, such as information processing, replication, and metabolism, are essentially mediated by specialized interactions between biological molecules such as protein, DNA, etc. Molecular recognition refers to the contact between two molecules via various forms of bonding. It is the foundation for biological processes such as enzyme catalysis, cellular signaling, transcription, translation, DNA

replication, and transport (Baron & McCammon, 2013). These interactions are primarily between proteins and between proteins and DNA. Understanding how two molecules identify one other is thus one of biochemistry's essential concerns. Molecular recognition is also important in applied biochemistry since it decides whether a molecule has clinically beneficial qualities. The area of enzymology provided the initial understanding of this idea.

Emil Fisher, a Dutch Chemist, postulated in 1894 that the enzyme and substrate fit together “like lock and key." He stated unequivocally that molecular recognition is based on the complementarities of interacting surfaces. According to a contemporary theory of molecular recognition, the interacting molecules are flexible and can change shape throughout the recognition process. Many protein-ligand interactions have been observed experimentally. The complementarities between two molecules at the molecular level are determined by various variables such as the shape of the two molecules, hydrogen bonding, electrostatic interaction, hydrophobic contact, ion-ion interaction, and *van der* Waals force,, among others (Chothia & Janin, 1975; Connolly, 1986; Jones & Thornton, 1996). The molecular recognition process might be either static or dynamic. Static recognition happens when a single visitor and a single host binding site interact. The binding of the first guest at the first binding site causes a conformation change that impacts the affiliation of the second guest at the second binding site in dynamic recognition.

Molecular recognition is determined by the information involved in the binding and choice of the substrate. Various factors incline these processes, and it makes their study difficult. It requires a quantitative understanding of these factors. Some key functional group interactions, such as hydrogen bonding, are well understood. Hydrogen bonds are single-point interactions with well-defined geometry, and the electrostatic forces resolve their magnitude among the donor hydrogen atom and the acceptor atom.

1.4 Non-covalent Interactions at protein-ligand interfaces

Non-covalent interactions play a central role in supramolecular chemistry, pharmaceutical design, molecular biology, crystal engineering, etc. Intensive research efforts have been devoted to elucidating and quantifying non-covalent interactions like hydrogen bonding, cation-π, π-π stacking, electrostatics, hydrophobicity, and van der Waals (vdW) interactions (Meyer et al., 2003). Recently halogen bonding, the non-covalent interaction between halogen atoms and neutral Lewis bases or anions, has attracted interest among chemists and structural biologists (Metrangolo et al., 2005). Organic halides exhibit an anisotropic charge distribution, with one negatively charged equatorial ring and a positively charged region, known as the σ-hole, along the extension of the C-X bonds (Politzer et al., 2010).

Intermolecular non-covalent interactions have been the subject of intense interest from experimental as well as theoretical points of view. It is because of their fundamental role in forming the three-dimensional structure of many biologically important molecules. These molecules control the specific recognition and association between various interacting partners. Much effort has been made to understand how these interactions interfere with fluid behavior, molecular assembly, ligand binding, protein folding, and enzyme catalysis (Leckband & Israelachvili, 2001).

In recent decades, non-covalent chemistry has become of great importance to medicinal chemists searching for the unique "glue" that keeps holding drugs and their receptors together (Bissantz et al., 2010). Several research papers have been published to explore the structure, geometry, energy, and thermodynamics of the specific and non-specific interactions involved in receptor-ligand recognition and binding. They consider their function and biological significance in rational drug design (Williams et al., 2004).

Various chemical forces, some are strong, and some are weak; some specific, some not specific; some direct, some indirect; some controlled by enthalpy, some controlled by entropy. However, the characteristics and nature of these forces are quite different. They work together to coordinate a delicate and complex non-covalent network for precise control of the reversible binding event of a cognate substrate and

non-cognate ligand to their biological receptor. It leads to space-time-specific modulation of binding and dissociation between the receptor and the ligand (Zhou et al., 2012).

Structure-based drug design aims to identify and optimize this network architecture. This process requires knowledge of the structure and strength of these interactions that can be obtained from crystallographic data and theoretical characterization (Bissantz et al., 2010). Structural and thermodynamic knowledge of several non-covalent interactions of medical interest involving protein-ligand interactions has been accumulated abundantly and can be utilized in drug design.

1.5 Hydrogen bonds

Hydrogen bonds are the most important non-covalent interactions in biological recognition processes. Ligand binding with receptors arises three effects from hydrogen bonding (Kubinyi, 2001): (i) Orientation of ligands, (ii) Recognition of substrates, agonists, antagonists, and inhibitors (iii) the ligand affinity. Hydrogen bonding also affects membrane transport and drug delivery in biological systems **(Figure 1.3)** (Lin & Lu, 1997).

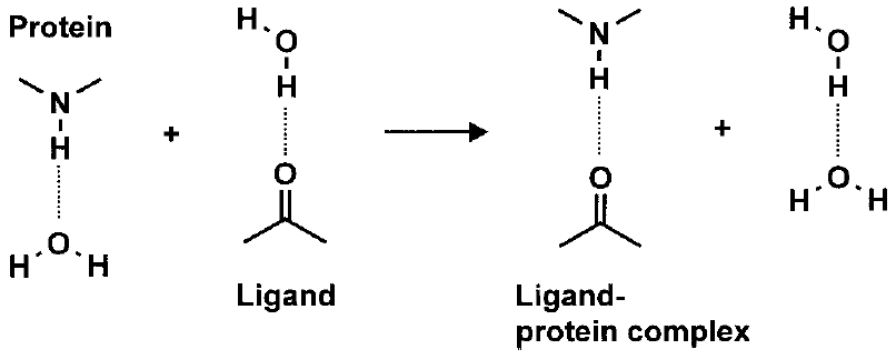

Figure 1.3: Solvation and desolvation in the formation of a ligand-protein complex

Hydrogen bonding is a widespread phenomenon in the binding of ligands to their cognate or non-cognate protein receptors. A recent test of 2320 small ligand-protein complex structures found that hydrogen bonding occurred in 67% of these complexes and that 66% formed with the –NH protein group. Crystallographic examination revealed various types of hydrogen bonds present in the protein-ligand

complexes. Apart from the classical O – H … O, N - H … O, and O - H …. N bonds, there are also several non-conventional hydrogen bonds, such as C_α –H … O and O–H…π bonding, involves the binding of a small molecule to a protein. Recently it has been found that hydrogen bonding involving a sulfur or halogen atom is a potential contributor to the binding (Kim et al., 2000). Based on this, Weiss *et al.* proposed a new concept of hydrogen bonds that involves not only the N-H and O-H donor groups. It can be a C-H donor and other acceptor groups, like S and π-systems (Weiss et al., 2001). The acceptor capabilities of hydrogen bond by halogen atom has been studied and is important in the ion channel of the metabolic system (Hille, 1992), and halide salts waste remediation (Brammer et al., 2001). The International Union of Pure and Applied Chemistry (IUPAC) proposed an updated definition of hydrogen bonding in 2011 to address the different forms of interactions that contain protons (Desiraju, 2011).

The ligands prefer to use their more robust hydrogen-bonding capacity to interact with the protein residue, leaving weaker interactions for water binding. Hydrogen bonds involving special functional groups: (i) The amide N – H and C = O moieties are found deep within the bonding site and are often involved in hydrogen bonds with the corresponding counter-group of ligands (Cotesta & Stahl, 2006). (ii) Different chemical fragments of the drug-like ligands have been observed to exhibit distinct tendencies to form hydrogen bonds. They form hydrogen bonds with side chains of Asp, Glu, Arg, and His in the active sites of the protein (Chan et al., 2010) Similar conclusion was made by Imai et al. with a large number of ligands in interaction with the 14 side chains of polar and aromatic amino acids (Imai et al., 2007).

1.6 Anion…π interaction

Anion…π interactions are commonly referred to as the preferred non-covalent contact between an electron-deficient (π-acidic) aromatic system and an anion. Elegant studies show that anion…π interactions are generally dominated by the contribution of electrostatic and anion-induced polarization, but dispersion contributes as well. The electrostatic composition is correlated with the magnitude of the quadrupole electric moment Q_{ZZ} of the aromatic ring. However, the binding energies of the anion…π

interaction are not only electrostatic but trends can be predicted using only electrostatic terms. As a result, the binding energy decreases as the ionic radius of the anion increases. In aromatics systems with large positive Q_{ZZ} values, such as hexafluorobenzene, the electrostatic charge dominates the anion…π interaction, but as the Q_{ZZ} decreases, the polarization energy becomes more important (Salonen et al., 2011).

An anion can make non-covalent interaction with the π system in four different ways **(Figure 1.4)**: a) hydrogen bonding, b) anion…π interactions, c) strongly covalent σ interactions, and d) weakly covalent σ interactions.

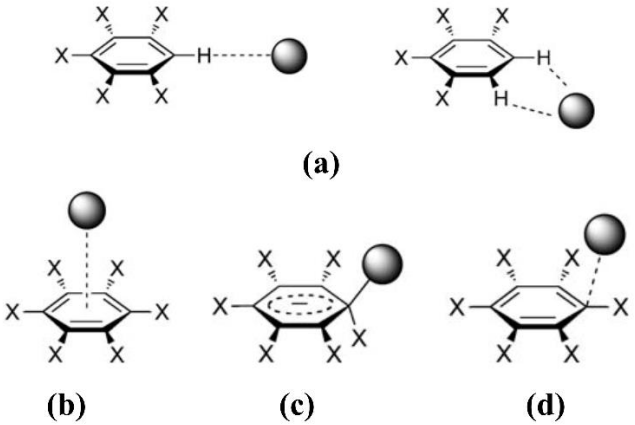

Figure 1.4: Type of aromatic interactions: a) C…H hydrogen bonding; b) non-covalent anion–π interaction; c) strongly covalent σ interaction; d) weakly covalent σ interaction.

1.7 Cation…π interaction

The cation…π interaction is a short-range non-covalent interaction between cations and adjacent π systems **(Figure 1.5)**. It results from the intense attraction between positively charged entities and the π electron cloud of aromatic groups. This cation…π interaction is very relevant to the physicochemical properties of the membrane protein's dual hydrophobic/hydrophilic environment (Infield et al., 2021).

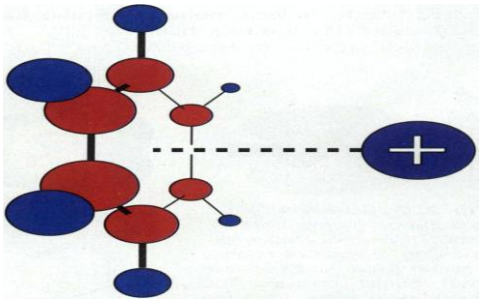

Figure 1.5: The cation-π interaction, showing a generic positive charge interacting with benzene (hydrogens are blue, carbons red).

Cation…π interactions are abundant in nature. Dougherty and his colleagues have made fundamental contributions to understanding how nature exploits this interaction to bind biologically relevant molecules (Petti et al., 1988; Shepodd et al., 1986). Investigations of multiple synthetic receptor and model systems for onium ion recognition have shown the strength of the cation…π interactions. It is proportional to the number of aromatic rings and the contribution of free enthalpy ΔG per aromatic ring (Meyer et al., 2003). In biological systems, acceptor cations can be found in the primary side chains of proteins, along with various ligands, toxins, other small molecules, or even ions that can interact closely with proteins (**Figure 1.6)**.

Similarly, the π-electron partner in the cation…π interaction can be provided by an aromatic side chain (Phe, Tyr, or Trp) or by an aromatic group of the interacting ligand (Infield et al., 2021). The histidine side chain can act as a cation or an aromatic group, so special attention is needed (Liao et al., 2013). In the guanidinium moiety of arginine, a dispersed π-system can interact with the side chain through perpendicular (T-shaped) or parallel (stacking) geometries (**Figure 1.7)**.

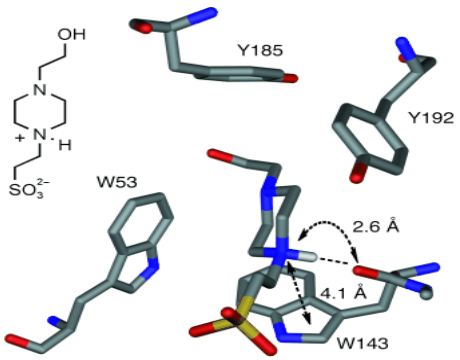

Figure 1.6: Cation…π interaction of HEPES molecule and Trp143 in the ACh binding site of Ach-binding protein (PDB code:1I9B)

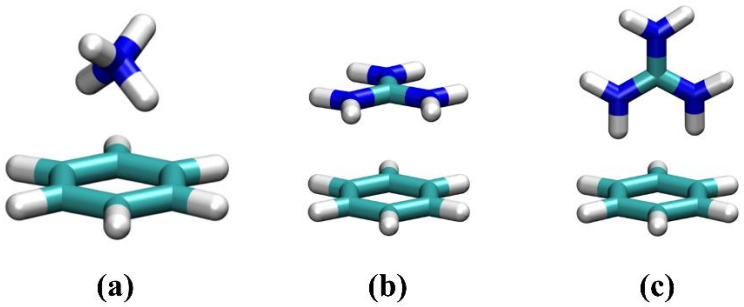

Figure 1.7: Idealized geometry for cation-π interactions. (a) the interaction of NH_4^+ and benzene, (b) stacked and (c) t-shaped interaction of guanidinium with benzene

Many small molecules are transported across the cell membrane by large integral membrane proteins, commonly known as transporters. The cation-π interaction is utilized in substrate recognition by many transporters. For example, cation-π interactions play an important role in the activity of neurotransmitter transporters that facilitate the reuptake of 5HT, dopamine, GABA, glycine, and norepinephrine, thus terminating synaptic transmission (Zacharias, 2002).

1.8 π-π stalking interaction

The π–π stacking interaction is an attractive and nondestructive type of non-covalent interaction. It has been extensively explored for applications in modern chemistry, molecular biology, and supramolecular chemistry. Their biological applications attracted considerable attention due to unique benefits such as reliable binding power, nondestructive fabrication process, and simple operation. Significant achievements in these interactions have been made in nucleo-base stacking, biosensors, controlled drug release, protein folding, molecular recognition, self-assembles, model-driven synthesis, etc. (Chen et al., 2018).

Among the various non-covalent interactions between molecules, the π-π interaction dominates in aromatic systems. The π-π interaction is one of the most controversial supramolecular interactions (Desiraju & Gavezzotti, 1989; Martinez & Iverson, 2012; Sherrill, 2013). With the advancement of single-crystal X-ray diffraction and the beginning of crystal engineering, π-π interactions in many supra-molecular systems have been pursued to understand them and their applications. In previous decades, the main focus was on understanding the nature of these interactions

and building a solid architecture using these interactions. However, in the last two decades, researchers have mainly focused on potential applications related to this interaction (Thakuria et al., 2019).

Based on geometrical structure, the π-π interactions between the two aromatic systems may be extensively classified into three categories: parallel displaced, co-facial parallel stacked, and edge-to-face T-shaped **Figure 1.8** (Wheeler, 2011). The small molecules of unsubstituted compounds prefer edge-to-face, T-shaped arrangements, whereas substituted and large polycyclic aromatic systems prefer parallel displaced geometry. Whereas co-facial parallel stacked geometry is somewhat hardly observed.

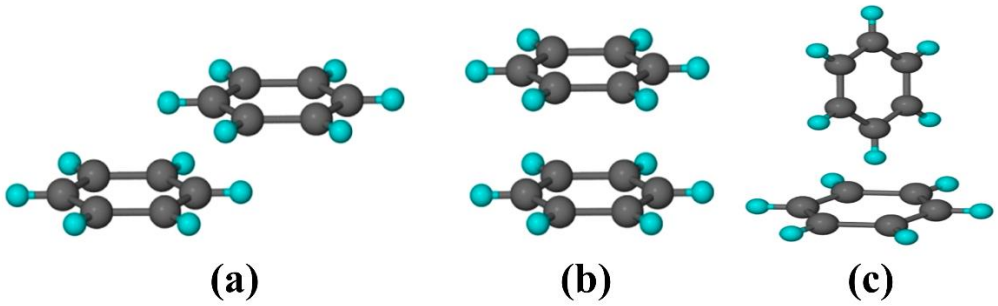

Figure 1.8: (a) parallel displaced, (b) co-facial parallel stacked, and (c) Edge-to-face T-shaped geometries of π-π interactions between aromatic systems.

After the vast potential of the π-π interaction is realized, it has applications from materials science to molecular biology. The π-π interaction is vital in proteins' thermal stability and folding. Burley and Petsko studied 34 proteins and showed that 60% of aromatic side chains were involved in π-π interactions. Among these interactions, the dominant conformation of π-π interactions was the T-shape conformation. McGaughey et al. studied larger proteins and demonstrated that π-π interactions prevail through parallel displaced geometries (McGaughey et al., 1998). Iverson and colleagues exploited π-π stacking in folding oligomers into a pleated structure (Scott Lokey & Iverson, 1995). The π-π stacking interaction is essential in forming efficient charge transport channels for small molecule and polymer semiconductor materials (Mas-Torrent & Rovira, 2011).

1.9 Halogen bonding (X.B.)

In the last few decades, halogen bonding (x-bond) has become one of the most thoroughly investigated non-covalent interactions (Legon, 2010; Politzer et al., 2010). This is because this interaction is accountable for several physical and chemical properties revealed by numerous molecular species. Generally, it is accepted that the anisotropy of charge distribution is responsible for the halogen bond formation (Legon, 2010; Metrangolo et al., 2005; Politzer et al., 2010).

A halogen bond, R – X ….Y – Z, occurs when there is proof of an attractive interaction between bonded halogen and atoms in the nucleophilic region. Halogen atom X belongs to a molecule's electrophilic region or a molecular portion of R – X (where R can be another atom, including X or a group of atoms). It is a nucleophile region of a molecule or a fragment of molecule Y – Z (Corradi et al., 2000; Desiraju et al., 2013). The electrostatic potential of a covalently bonded halogen atom is anisotropic, having a positive region at the tip of X (Cl, Br, I). This positive region was later called σ-hole (Clark et al., 2007), conforming to the maximum electrostatic potential charted on a surface. Halogen bonds are an electrostatically driven non-covalent interaction between the positive σ-hole and the adjacent nucleophilic sites containing molecules **(Figure 1.9)** (Costa, 2017).

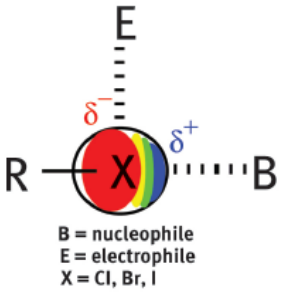

Figure 1.9: Schematic Representation of halogen bond R-X…B showing the anisotropic charge distribution on X atom. The possible orthogonal side-on interaction with an electrophile is also demonstrated (Costa, 2017).

The intermolecular halogen bond has a broad application in molecular self-assembly, supramolecular chemistry, crystal engineering, and drug design (Han et al., 2017). The halogen bonds appear to play a role in recognition of thyroid hormones. It

was evident by the study of I…O contacts of tetraiodothyronine. Its transport protein transthyretin **Figure 1.10 (a) & (b)** (Auffinger et al., 2004; Mondal et al., 2020).

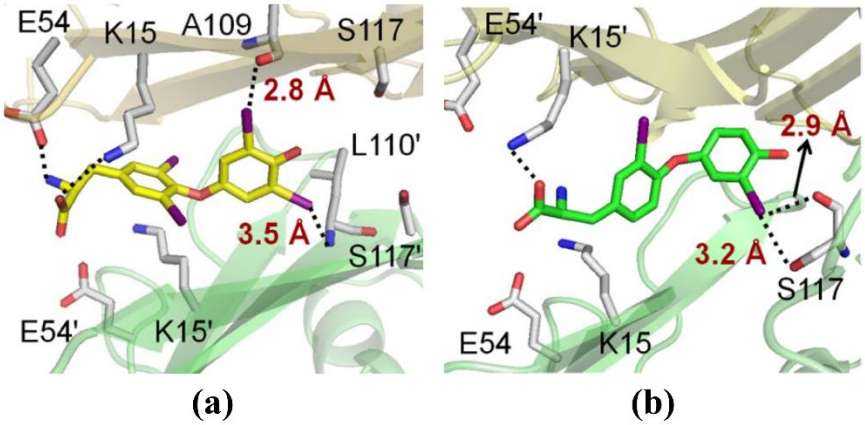

Figure 1.10: (a) Thyroxine (T4), (b) Triiodothyronine (T3), (c) X-ray crystal structure of human transthyretin (TTR) bound to T4, showing the hydrogen and halogen-bonding interactions of T4 (PDB code: 2ROX), (d) X-ray crystal structure of human transthyretin (TTR) bound to T3, indicating the interactions responsible for molecular recognition (PDB code: 1THA)

1.10 Bioisosteres

A bioisostere is a powerful concept for medicinal chemistry. It allows for improved oral absorption, membrane permeability, absorption, distribution, metabolism, and excretion (ADME) of drugs while maintaining their biological properties. Bioisostere is derived from "isostere," whose physical and chemical properties, like steric size, hydrophobicity, and electronegativity, are similar (Hamada & Kiso, 2012). Using bioisosteres and the structural changes to the lead compound allows for altering the compound's shape, size, electronic distribution, polarity, dipole, polarizability, lipophilicity, and pKa while retaining the potent bioactivity (Dick & Cocklin, 2020). Therefore, the bioisosteric approach should be used to rationalize a lead compound into a more attractive therapeutic agent with better potency, excellent selectivity, fewer side effects, decreased toxicity, improved pharmacokinetics, increased stability, simplified synthesis with the bonus of generating novel intellectual property.

Bioisostere has been classified into two, classical and non-classical bioisostere (Patani & LaVoie, 1996). Classical bioisostere signifies the results of an early

appreciation of the perception and incorporates structurally simple atoms or groups. Substituting hydrogen for fluorine is one of the frequently employed isosteric replacements. The size of hydrogen and fluorine are very similar; their van der Waal radii are 1.2 Å and 1.35 Å, respectively, making them easily replaceable atoms. Then, their electronic effects are the basis for their pharmacological difference. Fluorine has been substituted for hydrogen, and naphthyl-fused diazepine **(Figure 1.11)** enhanced affinity and efficacy. The more excellent receptor binding affinity of the fluorine atom is due to the inductive effect, which facilitates a more vital interaction with the receptor (Zhang et al., 1994).

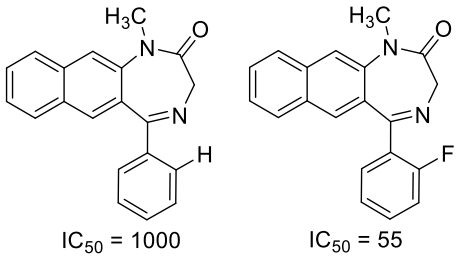

Figure 1.11: Naphthyl-fused diazepines *in vitro* potency to displace [^{3}H] flunitrazepam from benzodiazepine receptor.

Non-classical bioisosteres are structurally dissimilar, usually containing a different number of atoms, and show different steric and electronic properties (Mondal et al., 2020). These isosteres can uphold the same biological activity by representing the electronic properties or other physicochemical properties of the molecule or functional group, which is critical for retaining biological activity. Olaparib is an FDA-approved drug for the treatment of ovarian cancer. They use the diazaspiro core (**Figure 1.12)** as piperazine bioisostere shows reduced DNA damage and cytotoxicity with better aqueous solubility and oral absorption (Reilly et al., 2018).

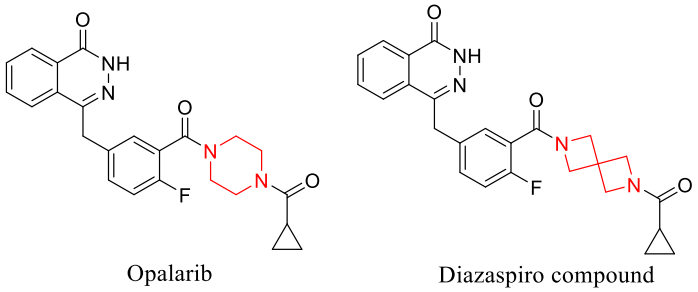

Figure 1.12: Non-classical bioisostere of Opalarib

Lee and colleagues discovered a novel peptidomimetic in an RNA-targeted SAR study. This study replaced the guanidine group with a squaryldiamine as a potent bioisostere (**Figure 1.13)**. A new squaric acid diamide analog showed a quadruple decrease in binding affinity (from K_D. of 1.8 µM to 7.7 µM). This is the first time bioisosteres have successfully mimicked the guanidine group (Lee et al., 2005).

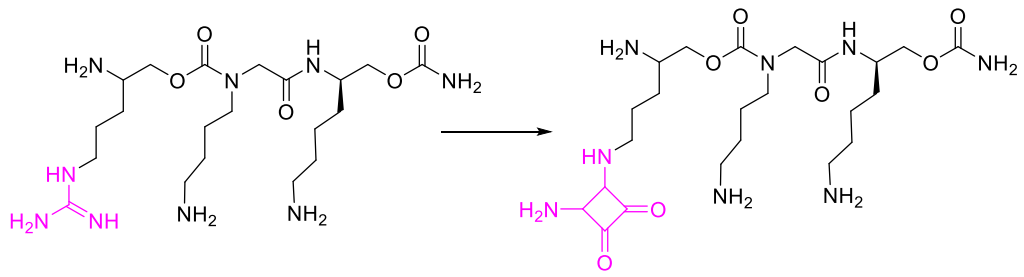

Figure 1.13: Squaryldiamide bioisostere for guanidine moiety as novel HIV-1 Tat-TAR RNA inhibitor

1.11 Supramolecular chemistry

Supramolecular chemistry is a branch of chemistry dealing with the association of two or more chemical species through intermolecular forces, such as electrostatic interactions, hydrogen bonding, van der Waals forces, etc. (Lehn, 1985, 1988). It is one of the fastest-growing inter-disciplines, covering many topics, from chemistry to other branches of science. These are employed in catalysis, drug delivery, biomedical therapy, electrochemical sensors, and self-healing materials (Lu et al., 2019).

Supramolecular chemistry is also defined as "chemistry beyond the molecule. "It emphasizes the study of molecular recognition and high-ordered assembly formed by non-covalent interactions. Since supramolecular systems are composed of building blocks linked by non-covalent interactions, they can exhibit stimulus-responsive behavior. Furthermore, it is very difficult to prepare attractive chemical architectures, such as catenanes, rotaxanes, and knots, from covalent chemistry. Supramolecular chemistry can be readily utilized for synthesis through template-based synthesis. In recent decades, supramolecular chemistry has been extensively explored in many fields, including molecular sensors, molecular machines, nano-reaction, gas absorption, chemical catalysis, and drug delivery. Supramolecular chemistry is a hybrid or multidisciplinary branch of organic chemistry, polymer chemistry,

coordination chemistry, physical chemistry, materials science, biological science, and more (Huang & Anslyn, 2015) **(Figure 1.14)**.

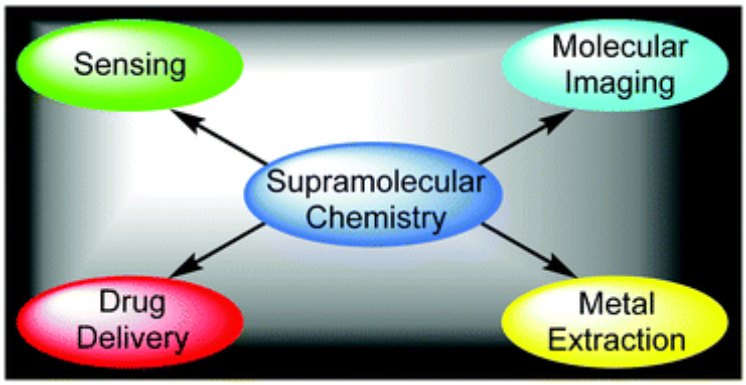

Figure 1.14: Application of Supramolecular chemistry

A.P. de Silva and its working group combined the concept of host-guest chemistry and fluorescence, directing supramolecular chemistry to the realm of optical sensing. They accomplished this in optical sensing by attaching a crown ether to a fluorophore system capable of photoinduced electron transfer (PET) property (de Silva et al., 1996; de Silva & Sandanayake, 1989; Uchiyama et al., 2016). It was fine-tuned to give distinct sodium, potassium, and calcium responses. It is presently used to measure blood ion concentrations in real-time (Kolesnichenko & Anslyn, 2017).

1.12 Method to study non-covalent interactions

The nature of the non-covalent forces makes them important in biological function because they have a specificity that does not give as much stiffness as the covalent forces. We have used X-ray crystallography and Hirschfeld surface analysis to study the non-covalent interactions in the crystals. Molecular docking simulation is also done to study the ligand-protein interaction of the synthesis molecules.

1.12.1 X-Ray Crystallography

X-ray crystallography diffraction is a scientific method used to determine the arrangement of the atoms in the 3D of a crystalline solid. This technique uses the inter-atomic distances of crystalline solids as the diffraction gradient for X-ray light, whose wavelength is 1 Å (10^{-8} cm). Angles and intensities of the diffracted beams observed, a crystallographer can create a three-dimensional picture of the electron density in the

crystal. This electron density can be used to determine the average positions of the atoms in the crystal, their chemical bonds, their disorder, and much more. Single-crystal X-ray diffraction (SCRD) is a nondestructive analytical technique that provides detailed information about the internal lattice of crystalline substances, including unit cell size, bond length, bond angle, and details of site order of positions. The single crystal refining process is directly related to the data generated from the X-ray analysis. After interpretation and refining, the data crystal structure can be developed.

X-ray crystallography has provided insight into chemical bonds and non-covalent interactions. Scientists routinely use X-ray crystallography to study drug interactions with protein targets (Scapin, 2006). But still, inner membrane proteins are challenging to crystallize because they require some mediums to dissolve them in isolation and interfere with crystallization. These membrane proteins include many proteins of considerable physiological importance, such as ion channels and receptors (Lundstrom, 2006).

1.12.2 Hirshfeld surface analysis

The Hirshfeld surface originates from an attempt to determine the space occupied by a molecule in a crystal to partition the electron density of the crystal into molecular fragments (Spackman & Byrom, 1997). Hirshfeld surfaces are named after F.L Hirshfeld, whose "stockholder partitioning" scheme for identifying atoms in a molecule has suggested an extension of the definition of a molecule in a crystal. Recently it has been utilized to define an atom fragment in a molecule. So, the atomic charges and other properties can be obtained by numerical integration.

The contours of $w_A(\mathbf{r})$ surrounding a benzene molecule in a crystal are illustrated in **Figure 1.15 (a)**. The contours are close together and surround the molecule near the van der Waals surface. The weight function is extremely flat on the molecule itself, with $w_A(\mathbf{r}) > 0.9$, decreasing rapidly to values below 0.1. This behavior supported to test for isometric faces of $w_A(\mathbf{r})$, and it turned out that the isosurface defined by $w_A(\mathbf{r}) = 0.5$ is quite special. This isosurface of the Hirshfeld surface encloses the molecule. It also defines the volume of space where the electron density of the promolecule exceeds the electron density of all neighboring molecules. It ensures

maximum proximity of neighboring molecular volumes, but the volumes never overlap due to the nature of the weight function. The Hirshfeld surface of benzene is given in **Figure 1.15 (b)**, has the exact dimensions and orientation as the 0.5 contours in **Figure 1.15 (a)**, and is surrounded by the 12 nearest neighbor molecules in the crystal (Spackman & Jayatilaka, 2009).

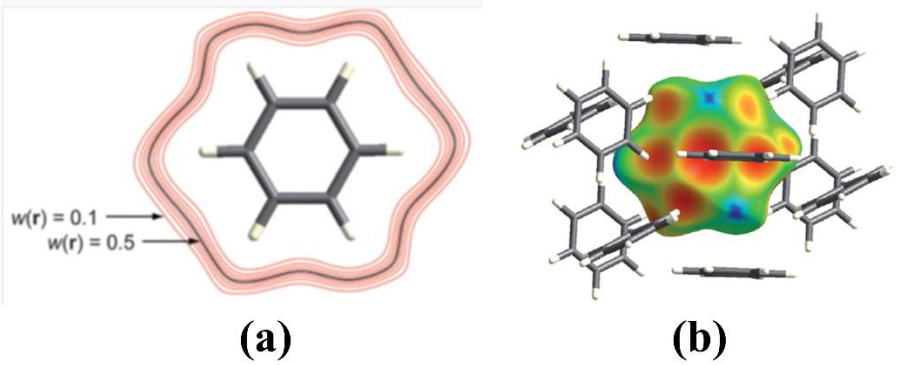

Figure 1.15: (a) Contours of a benzene molecule in the crystal (b) Hirshfeld surface for benzene mapped with d_e plotted at the same size and orientation as in (a)

Curvature is an innate feature of any surface and plays an important role in many areas of biology, chemistry, and condensed matter physics. The shape index has the advantage that a change in the sign of a complementary pair's shapes differs. A shape index map on the Hirshfeld surface was used to identify complementary hollows with red colour and protrusions with blue colour. These two are observed due to surface interactions of two molecular entities with each other. Curvedness is a function of the root-mean-square curvature of the surface. Curvedness maps of analysis typically show large (relatively flat) green areas separated by dark blue edges (large positive curvature).

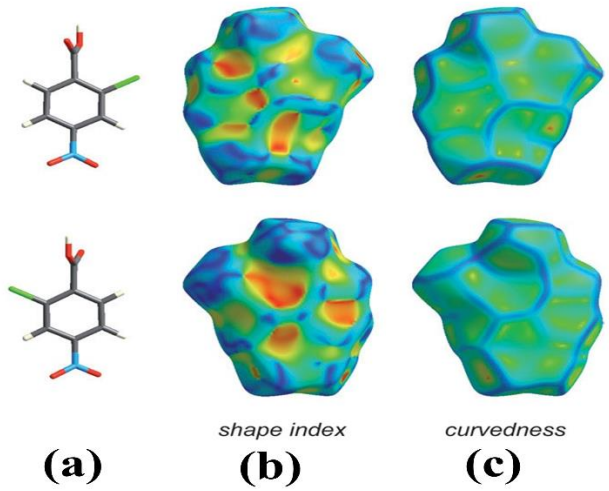

Figure 1.16: Front and back view of Hirshfeld surface of 2-cloro-4-nitrobenzoic acid showing shape index and curvedness

Figure 1.16 and **Figure 1.17** illustrate the application of shape index and curvedness to perceive the packing modes, especially planar stacking arrangements, or even the approaches of adjoining molecules' contact with one another. For example, the shape index surface in **Figure 1.16** suggests that two sides of a molecule are concerned with many contacts with neighboring molecules. This is because the curvedness plots display no flat surface patches above both aspects of the benzene ring. So, these figures do not prove planar stacking among molecules.

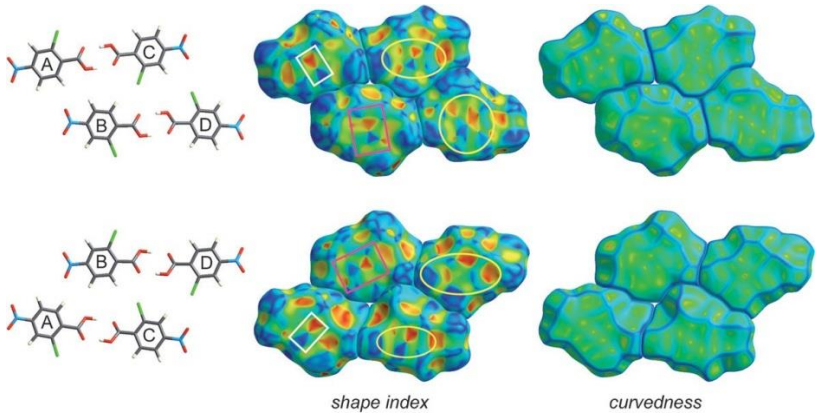

Figure 1.17: Front and back view of Hirshfeld surfaces for a cluster of 4 molecules of 2-chloro-4-nitrobenzoic acid showing shape index and curvedness.

The nature of interaction in **Figure 1.17** is entirely different. Here the curvedness surfaces display broad, tremendously flat features of planar stacking of

molecules. Also, exclusive functions may be diagnosed at the shape index plots, which may be used to examine the approaches of the various molecules in their packing. The yellow ellipses define self-complementary areas: there is some other same molecule above each, associated via an inversion center. Triangular patterns on the shape index surface are diagnosed for close C…C inter-planar contacts (McKinnon et al., 2004). The presence or absence of this packing pattern in the crystal structure can be easily identified by fingerprint mapping, especially in combination with a breakdown of the fingerprint plot.

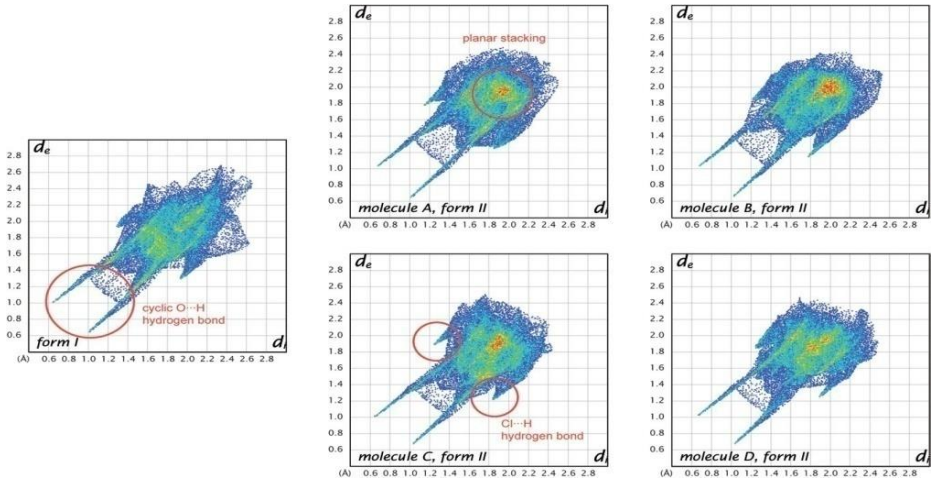

Figure 1.18: Comparison between fingerprint plot for single-molecule (form I) and four molecules (form II) of 2-chloro-4-nitrobenzoic acid. Key intermolecular contacts are circled in red.

The distances from the Hirshfeld surface to the nearest nucleus inside the surface (or internal, $\boldsymbol{d_i}$) and outside the surface (or external, $\boldsymbol{d_e}$) were the first distance functions explored for mapping the Hirshfeld surface. In the recent study, the combination of $\boldsymbol{d_i}$ and $\boldsymbol{d_e}$ in the form of 2D fingerprint plots provides more informative usage of these quantities **(Figure 1.18)**. The $\boldsymbol{d_{norm}}$ property is a symmetric function of the surface distances between the nuclei inside and outside the Hirshfeld surface ($\boldsymbol{d_i}$ and $\boldsymbol{d_e}$, respectively). The red region represents the shorter and the blue region longer inter-contacts on the $\boldsymbol{d_{norm}}$, while the white colour represents the contacts around *van der* Waals radii. A two-dimensional fingerprint plot gives relevant information about the intermolecular contacts in the crystal. Hirshfeld surface analysis has become a useful technique to explain the nature of crystal intermolecular interactions (McKinnon et al., 2004). Hirshfeld surface analysis is widely used to study polymorphism

(Lemmerer et al., 2012; Munshi et al., 2008), co-crystallization, the inclusion of small molecules in cavities of macromolecules, and search for correlations between the strength of the interaction and the melting point (Tojiboev et al., 2020).

The Hirshfeld surface and 2D fingerprint plots were calculated using a CIF format file in Crystal Explorer 17.5 (Wolff et al., 2012). The two distances on the Hirshfeld isosurface are defined as $\boldsymbol{d_i}$, distance to the nearest nucleus internal to the surface, and $\boldsymbol{d_e}$, distance from the point to the nearest nucleus external to the surface. The $\boldsymbol{d_{norm}}$ that is normalized contact distance can be given depending on $\boldsymbol{d_i}$ and $\boldsymbol{d_e}$ as

$$d_{norm} = \frac{\left(d_i - r_i^{vdw}\right)}{r_i^{vdw}} + \frac{\left(d_e - r_e^{vdw}\right)}{r_e^{vdw}} \qquad \ldots\ldots \text{(Eq. 1)}$$

where r_i^{vdw} and r_e^{vdw} are the van der Waals radii of the atoms.

The enrichment ratio (Jelsch et al., 2014) is derived from the percentage contribution of interacting atoms to the Hirshfeld surface to determine favorable and disfavor interactions. For calculating the enrichment ratio, the following formulae are employed.

$$S_A = C_{AA} + \frac{1}{2}\sum_{B \neq A} C_{AB} \qquad \ldots\ldots\ldots \text{(Eq. 2)}$$

Where S_A is the proportion of atom A on the molecular surface and C_{AB} is the proportion of Hirshfeld surface contacts involving the A and B interactions.

The ratio of random contacts R_{AB} between the two contact atoms A and B is then calculated using probability products (Eq. 3), assuming all types of A···B contacts are equally distributed.

$$R_{AA} = S_A S_A \text{ and } R_{AB} = 2S_A S_B \qquad \ldots\ldots \text{(Eq. 3)}$$

The enrichment ratio E_{AB} of the interacting atoms A and B is then given as

$$E_{AB} = \frac{C_{AB}}{R_{AB}} \qquad \ldots\ldots\ldots \text{(Eq. 4)}$$

1.12.3 Molecular Docking

Molecular docking has emerged in the last four decades, driven by the need for structural molecular biology and structure-based drug discovery. This has been greatly facilitated by the increasing ease of access to small protein and molecular databases (Berman et al., 2002; Hendlich, 1998; Hu et al., 2005; Irwin & Shoichet, 2005). Automated molecular docking software aims to understand and predict molecular recognition by knowing binding modes and predicting binding affinity. Molecular docking is typically executed between a small molecule or ligand and a target macromolecule or receptor. This is commonly referred to as protein-ligand docking. But now, there is an increasing demand for protein-protein docking.

Molecular docking has many applications in drug discovery, including structure-activity studies, lead optimization, searching potential leads by virtual screening, and providing binding hypotheses to support predictive aid for mutagenesis studies. It supports x-ray crystallography in substrate fitting and inhibitors electron density, chemical mechanism studies, and combinatorial libraries pattern.

Virtual screening of (in)active ligands has great utility in finding hits and leads through library enrichment for screening (Pozzan, 2006). A well-used strategy to minimize and enrich the ligand library for molecular screening, recent reports show that shape-based, ligand centric is better and often superior to protein-centric docking (Hawkins et al., 2007). However, in the final step in virtual screening, molecular docking helps to provide three-dimensional (3D) structural hypotheses about ligand-target interactions.

Docking involves finding the ligand's most favorable binding mode(s) to the target of interest. The binding mode of the ligand for the receptor can be determined by its state variables. It includes their position (x-, y-, and z-translations), alignment, and conformation. Each state variable describes a degree of freedom and its bounds. Rigid body docking is faster than flexible ligand docking since the search space size is much smaller. However, if the ligand's conformation is incorrect, the probability of finding a complementary fit will be lower (Morris & Lim-Wilby, 2008).

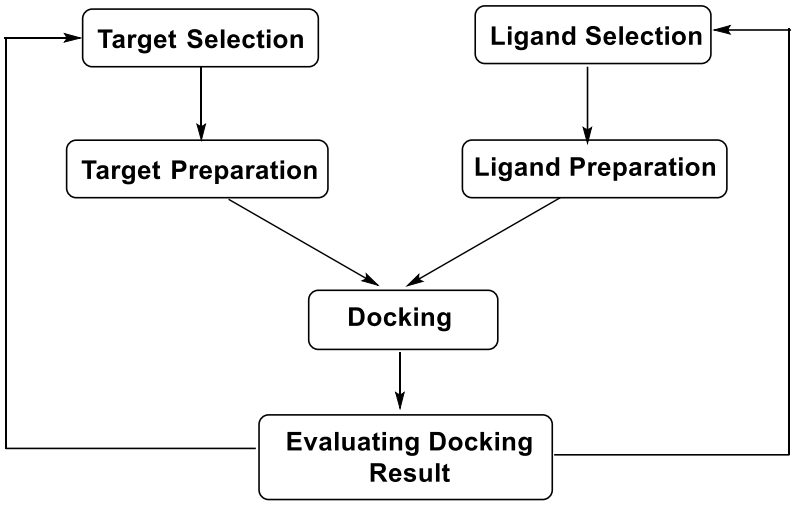

Figure 1.19: A typical docking workflow.

Molecular docking is the most widely used technique **(Figure 1.19)**. However, the main application is structure-based virtual screening for identifying novel compound activity against a specific target protein. This has produced some success stories; it is one of the techniques often integrated into a different *in-silico* and experimental workflow. Several research groups focused on evaluating the performance of various docking programs or improving scoring function when experimental tests were performed (Meng et al., 2011). Such efforts can provide useful guidance for selecting a methodology for a particular target system.

1.13 Scope of the study

The proposed work is to synthesize new organic hybrid molecules to study molecular recognition properties (intramolecular and intermolecular) within the molecule and with biological systems. Supramolecular architectures of the synthesized molecules will be studied to understand inter and intra-molecular non-covalent interactions. Molecular docking will be performed to study the ligand-protein interaction towards their respective biological target protein.

1.14 Objectives of the present work

The objectives of the present research are:

(i) The primary objective of the present study is to develop a simple and convenient method to synthesize hybrid molecules.

(ii) Molecular recognition properties of the synthesized compounds to understand the inter and intra-molecular non-covalent interactions within the supramolecular framework.

(iii) In silico analysis of the synthesized compounds to understand the binding of drug with target receptors.

CHAPTER 2

2. SYNTHESIS AND STUDY OF 2-PYRIDONE-BASED HYBRID MOLECULES

2.1. Introduction

Heterocycles occupy an important place within the biologically active libraries and pharma industries. They are involved in most biological systems like amino acids, carbohydrates, proteins, enzymes, etc. Therefore, researchers are always keen to design and discover new pharmacologically active heterocyclic molecules having the potential to overcome health problems. Nitrogenous heterocycles are prevalent cores in FDA-approved drugs and bioactive natural compounds. It represents a vital framework for agrochemical and drug development (Kerru et al., 2020).

Furthermore, the electron-rich nitrogen heterocycle may easily accept or donate a proton, as well as generate a variety of various weak interactions. Some of these intermolecular forces, such as hydrogen bond formation, hydrophobic effects, dipole-dipole interactions, van der Waals forces, and pi-stacking interactions of nitrogen compounds, have grown in relevance in the field of medicinal chemistry and allows them to bind to a wide range of enzymes and receptors in biological targets due to enhanced solubility. The structural features of their derivatives are advantageous because they exhibit a wide range of biological activities.

The dihydropyridone motifs are familiar structures of many natural product chemical compounds and biologically active compounds (Simal et al., 2012). Dihydropyrimidinones (DHPMs) are structural analogues of monastrol (**Figure 2.1**), a biomolecule with several biological activities. Other DHPM analogues have been synthesized, and their pharmacological properties have been reported. Monastrol is the protagonist of the DHPM class. Many studies have been done with monastrol that revealed its inhibitory effect on human kinesin Eg5. This inhibition results from mitotic arrest and apoptosis (Kapoor et al., 2000). Later on, some more studies have done and showed other probable targets, including centrin (Duan et al., 2015), calcium channel modulating activity (Rovnyak et al., 1992), and topoisomerase 1 (Zhu et al., 2011).

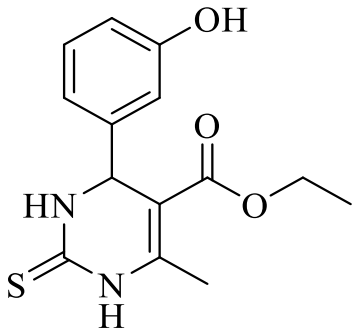

Figure 2.1: Monastrol

Pyridone is a heterocycle that contains an amide group in a 6-membered aromatic ring. There are two forms of pyridones based on the location of the nitrogen atom relative to the carbonyl fragment: 2-pyridones and 4-pyridones. Isomerization between the hydroxy pyridine and the equivalent pyridone can occur if nitrogen of the amide group is unsubstituted. The amide form generally predominates in the solid and solution phases despite the electronic nature of the substituent in the pyridone ring. As a result, the pyridone form is favored over 2-hydroxyl pyridine under physiological conditions (Forlani et al., 2002). Pyridones are found as essential fragments in various natural compounds, having antibacterial, anti-inflammatory, antitumor, neurotrophic and insecticidal properties (Ding et al., 2014; Jessen & Gademann, 2010; Li et al., 2018; Xu et al., 2014). Pirfenidone (Taniguchi et al., 2010) and Ciclopirox (Shen & Huang, 2016) are the two pyridone-based small molecule marketed drugs (**Figure 2.2**) used for the treatment of idiopathic pulmonary fibrosis, a lung disease, and as an antifungal agent. Due to its remarkable structural features and related pharmacological consequences, pyridone has been employed as a preferred scaffold in drug design & development.

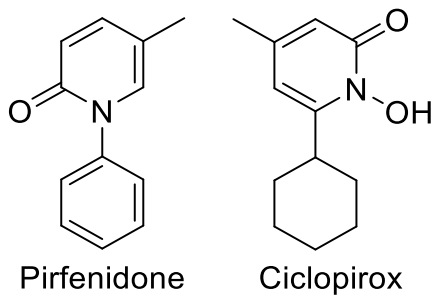

Figure 2.2: 2-pyridone-based marketed drugs

2.2. Present work

This chapter presents the simple and convenient method for synthesizing hybrid molecules of pyrans, dihydropyridones, and pyridones derivatives and studies their crystal structures. The synthesized compounds subsume a hybrid of two biologically active structural features to show a broader range of activity **(Figure 2.3)**. All the products were collected and recrystallized in a suitable solvent. Compounds that form a suitable crystal were studied by single crystal XRD and Hirshfeld surface analysis to evaluate the non-covalent interactions to stabilize the crystal structure.

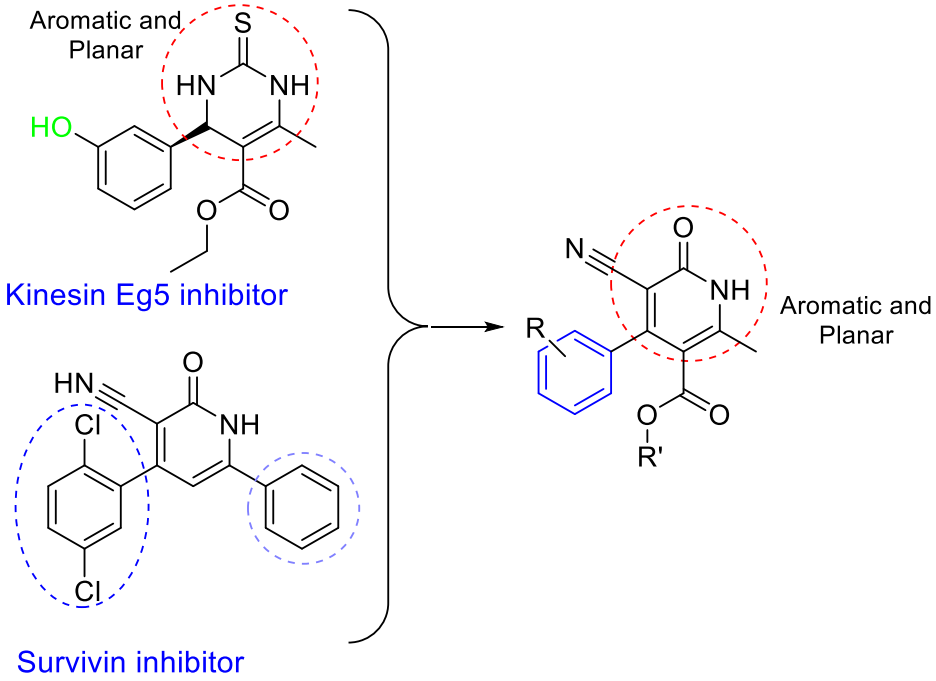

Figure 2.3: Pyridone-based hybrid molecules: a compound of interest

2.3. Synthesis of 2-pyridone-based hybrid derivatives

The derivatives of 4H-pyrans **(1.1A-1.1I)** were synthesis using multicomponent condensation reactions and then further subjected to a catalytic ring rearrangement of the pyrans to form 3,4-dihydro-2-pyridones **(1.2A-1.2I)**. Then, these dihydropyridones again on oxidation to form 2-pyridone derivatives **(1.3A-1.3I)** shown in **Scheme 1**.

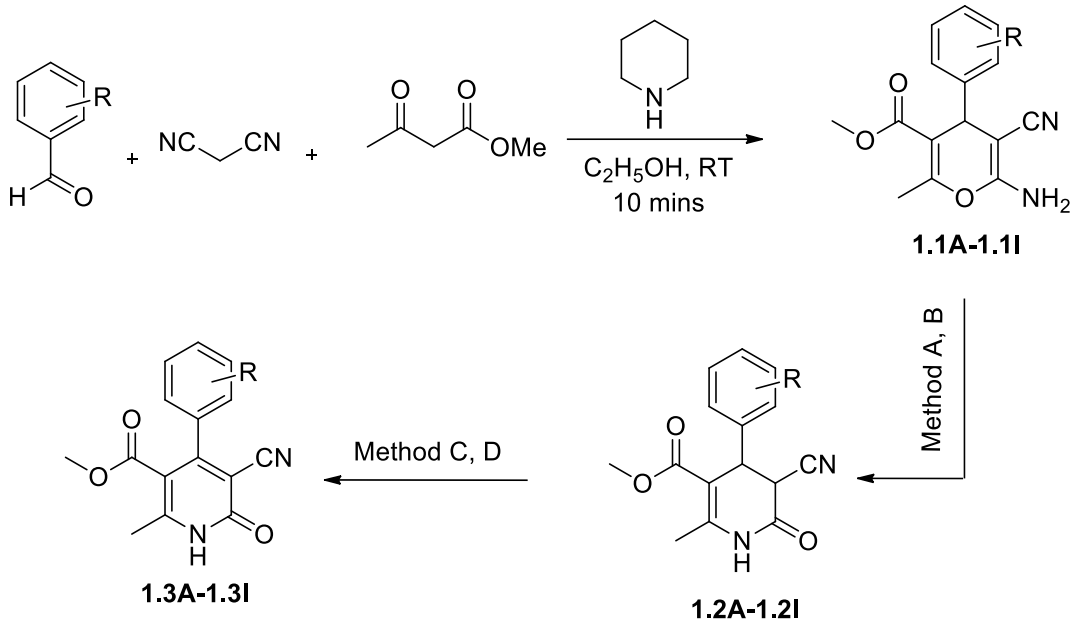

R = 4-Cl, 3-Cl, 2-Br-4-Cl, 2-Cl, 2-CH_3, 4-OCH_3, 2-OCH_3, 2-Br-5-F, -4CH_3

Entry = A, B, C, D, E, F, G, H, I

Method A: I_2, Reflux; Method B: Formic acid, Reflux; Method C: DDQ, Microwave; Method D: DDQ, Thermal

Scheme 1

2.4. Experimental

^{1}H NMR (600 MHz) and ^{13}C NMR (150 MHz) spectra were recorded on Bruker AVANCE NEO 600 MHz FTNMR spectrometer. TMS was used as an internal reference, and chemical shift values are expressed in ppm units (δ). All the compounds' melting points were recorded using the electrically heated instrument and were uncorrected. Thin-layer chromatography (TLC) on pre-coated aluminum sheets from Merck was used to monitor all reactions, and chromatograms were seen under UV light. Flash column chromatography with size 230-400 mesh silica gel was used to purify the product.

2.4.1. General procedure for the synthesis of 4H-pyrans (1.1A-1.1I)

In a 100 mL round bottom flask, ethanol (40 mL) was poured, followed by the addition of aldehyde (10 mmol) and malononitrile (10 mmol). The mixture added methyl acetoacetate (10 mmol) and piperidine (0.3 mL, three mmol). The mixture was stirred at room temperature for 10 minutes. 4H-pyran derivatives **(1.1A-1.1I)** were

purified by filtering the precipitate in a sintered glass funnel and washed with ice-cold methanol.

2.4.1.1. Methyl 6-amino-4-(4-chlorophenyl)-5-cyano-2-methyl-4H-pyran-3-carboxylate (1.1A): White solid, yield: 89%, m.p.243°C, **^{1}H NMR (600 MHz, $CDCl_3$):** δ ppm 2.35 (3H, s, CH_3), 3.58 (3H, s, CH_3), 4.41 (1H, s, CH), 4.56 (2H, s, NH_2), 7.12 (2H, d, Ar-H, *J*=6 Hz), 7.25 (2H, d, Ar-H, J=6 Hz); **^{13}C NMR (150 MHz, $CDCl_3$):** δ ppm 17.7, 38.8, 52.3, 58.1, 109.1, 119.1, 128.7, 130.4, 131.1, 142.2, 155.0, 159.2, 167.2. **MS (m/z):** 306.06 (M+1).

2.4.1.2. Methyl 6-amino-4-(3-chlorophenyl)-5-cyano-2-methyl-4H-pyran-3-carboxylate (1.1B): White solid, yield: 83%, m.p.176°C, **^{1}H NMR (600 MHz, $CDCl_3$):** δ ppm 2.34 (3H, s, CH_3), 3.56 (3H, s, CH_3), 4.40 (1H, s, CH), 4.54 (2H, s, NH_2), 7.10 (1H, d, Ar-H, *J*=6 Hz), 7.31 (1H, t, Ar-H, *J*=6 Hz), 7.40 (1H, d, Ar-H, *J*=6 Hz), 7.65 (1H, s, Ar-H); **^{13}C NMR (150 MHz, $CDCl_3$):** δ ppm 17.7, 38.8, 52.3, 58.1, 109.1, 119.1, 125.8, 128.8, 130.0, 134.2, 143.6, 155.0, 159.2, 167.2. **MS (m/z):** 305.06 (M+1).

2.4.1.3. Methyl 6-amino-4-(2-Bromo-4-chlorophenyl)-5-cyano-2-methyl-4H-pyran-3-carboxylate (1.1C): White solid, yield: 78%, m.p.227°C, **^{1}H NMR (600 MHz, $CDCl_3$):** δ ppm 2.36 (3H, s, CH_3), 3.59 (3H, s, CH_3), 4.42 (1H, s, CH), 4.55 (2H, s, NH_2), 7.25-7.30 (2H, m, Ar-H), 7.71 (1H, s, Ar-H); **^{13}C NMR (150 MHz, $CDCl_3$):** δ ppm 17.7, 35.0, 52.3, 58.1, 109.1, 119.1, 125.4, 127.7, 130.2, 132.0, 132.6, 139.1, 155.0, 159.2, 167.2. **MS (m/z):** 382.98 (M+1).

2.4.1.4. Methyl 6-amino-4-(2-chlorophenyl)-5-cyano-2-methyl-4H-pyran-3-carboxylate (1.1D): White solid, yield: 88%, m.p.164°C, **^{1}H NMR (600 MHz, $CDCl_3$):** δ ppm 2.38 (3H, s, CH_3), 3.55 (3H, s, CH_3), 4.53 (2H, s, NH_2), 5.02 (1H, s, CH), 7.10-7.25 (3H, m, Ar-H), 7.32 (1H, d, Ar-H, *J* = 6 Hz); **^{13}C NMR (150 MHz, $CDCl_3$):** δ ppm 17.7, 33.7, 52.3, 58.1, 109.1, 119.1, 126.4, 126.7, 127.1, 128.7, 131.4, 143.7, 155.0, 159.2, 167.2. **MS (m/z):** 305.06 (M+1).

2.4.1.5. Methyl 6-amino-5-cyano-2-methyl-4-(o-tolyl)-4H-pyran-3-carboxylate (1.1E): White solid, yield: 75%, m.p. 184°C, **^{1}H NMR (600 MHz, $CDCl_3$):** δ ppm

2.39 (3H, s, CH_3), 2.48 (3H, s, CH_3), 3.55 (3H, s, CH_3), 4.42 (2H, s, NH_2), 4.77 (1H, s, CH), 7.01-7.18 (4H, m, Ar-H); **^{13}C NMR (150 MHz, $CDCl_3$):** δ ppm 17.7, 19.6, 36.3, 52.3, 58.1, 109.1, 119.1, 122.6, 124.6, 125.6, 130.3, 135.6, 136.8, 155.0, 159.2, 167.2. **MS (m/z):** 285.12 (M+1).

2.4.1.6. Methyl 6-amino-5-cyano-4-(4-methoxyphenyl)-2-methyl-4H-pyran-3-carboxylate (1.1F): Pale yellow solid, yield: 78%, m.p. 219°C, **^{1}H NMR (600 MHz, $CDCl_3$):** δ ppm 2.34 (3H, s, CH_3), 3.52 (3H, s, CH_3), 3.86 (3H, s, CH_3), 4.43 (1H, s, CH), 4.52 (2H, s, NH_2), 6.89 (2H, d, Ar-H, *J*=6 Hz), 7.13 (2H, d, Ar-H, *J*=6 Hz); **^{13}C NMR (150 MHz, $CDCl_3$):** δ ppm 17.7, 38.8, 52.3, 55.8, 58.1, 109.1, 114.2, 119.1, 130.0, 136.4, 155.0, 157.6, 159.2, 167.2. **MS (m/z):** 301.11 (M+1).

2.4.1.7. Methyl 6-amino-5-cyano-4-(2-methoxyphenyl)-2-methyl-4H-pyran-3-carboxylate (1.1G): White solid, yield: 76%, m.p. 172°C, **^{1}H NMR (600 MHz, $CDCl_3$):** δ ppm 2.37 (3H, s, CH_3), 3.54 (3H, s, CH_3), 3.76 (3H, s, CH_3), 4.46 (1H, s, CH), 4.57 (2H, s, NH_2), 6.85-7.02 (3H, m, Ar-H), 7.41 (1H, d, Ar-H, *J*=6 Hz); **^{13}C NMR (150 MHz, $CDCl_3$):** δ ppm 17.1, 32.9, 52.3, 56.1, 58.1, 109.1, 112.2, 119.1, 120.9, 121.0, 126.7, 130.0, 155.0, 158.6, 159.2, 167.2. **MS (m/z):** 301.11 (M+1).

2.4.1.8 Methyl 6-amino-4-(2-bromo-5-fluorophenyl)-5-cyano-2-methyl-4H-pyran-3-carboxylate (1.1H): White solid, yield: 79%, m.p. 195°C, **^{1}H NMR (600 MHz, $CDCl_3$):** δ ppm 2.38 (3H, s, CH_3), 3.65 (3H, s, CH_3), 4.32 (1H, s, CH), 5.23 (2H, s, NH_2), 6.85-7.02 (2H, m, Ar-H), 7.51 (1H, d, Ar-H, *J*=6 Hz); **^{13}C NMR (150 MHz, $CDCl_3$):** δ ppm 17.1, 35.9, 52.3, 58.1, 109.1, 114.2, 118.3, 119.1, 119.8, 133.0, 142.6, 155.0, 159.6, 161.8, 167.2. **MS (m/z):** 368.00 (M+1).

2.4.1.9 Methyl 6-amino-5-cyano-2-methyl-4-(p-tolyl)-4H-pyran-3-carboxylate (1.1I): White solid, yield: 82%, m.p. 183°C, **^{1}H NMR (600 MHz, $CDCl_3$):** δ ppm 2.06 (3H, s, CH_3), 2.35 (3H, s, CH_3), 3.64 (3H, s, CH_3), 4.36 (1H, s, CH), 4.72 (2H, s, NH_2), 6.85 (2H, t, Ar-H, *J*=6 Hz), 7.18 (2H, t, Ar-H, *J*=6 Hz); **^{13}C NMR (150 MHz, $CDCl_3$):** δ ppm 17.7, 21.3, 38.9, 58.1, 109.1, 128.7, 135.4, 141.2, 155.6, 159.2, 167.2. **MS (m/z):** 285.12 (M+1).

2.4.2. General procedure for the synthesis of 3,4-dihydro-2-pyridones (1.2A-1.2I)

Method A: Each of the synthesized 4H-pyrans **(1.1A-1.1I)** (6.7 mmol) was dissolved in ethanol (50 mL) in 150 mL RB at 80°C. Iodine (10 mol%) was added and refluxed for 3-4 hours at 85°C. Reaction progress was monitored by TLC (EtOAc/hexane 3:7). After completion of the reaction, the mixture was concentrated under reduced pressure and then treated with a ten mol% solution of sodium thiosulphate to remove unreacted iodine. The compound was extracted with ethyl acetate (twice), followed by a standard workup. Compound 3,4-dihydro-2-pyridones **(1.2A-1.2I)** were purified over a silica gel column using Hexane: EtOAc (70:30) solvent.

Method B: The 4H-pyrans **(1.1A-1.1I)** (10 mmol) and excess formic acid (20 mL) were heated at 115°C for 3-4 hours under reflux. Following the completion of the reaction, the formic acid was reduced using a rotary evaporator, and the residue produced was recrystallized in ethanol to obtain pure products **(1.2A-1.2I)**.

2.4.2.1. Methyl 4-(4-chlorophenyl)-5-cyano-2-methyl-6-oxo-1,4,5,6-tetrahydropyridine-3-carboxylate (1.2A): White solid, yield: 76%, m.p.268°C, **^{1}H NMR (600 MHz, $CDCl_3$):** δ ppm 2.45 (3H, s, CH_3), 3.66 (3H, s, CH_3), 4.42 (1H, d, CH, *J*=1.3 Hz), 4.58 (1H, d, CH, *J*=1.3 Hz), 7.12-7.45 (4H, m, Ar-H), 10.97 (1H, s, NH); **^{13}C NMR (150 MHz, $CDCl_3$):** δ ppm 18.1, 27.9, 38.8, 52.3, 106.1, 116.8, 128.7, 129.1, 131.5, 138.7, 147.4, 167.2, 171.8. **MS (m/z):** 305.06 (M+1).

2.4.2.2. Methyl 4-(3-chlorophenyl)-5-cyano-2-methyl-6-oxo-1,4,5,6-tetrahydropyridine-3-carboxylate (1.2B): White solid, yield: 72%, m.p.200°C, **^{1}H NMR (600 MHz, $CDCl_3$):** δ ppm 2.50 (3H, s, CH_3), 3.62 (3H, s, CH_3), 4.40 (1H, d, CH, *J*=1.3 Hz), 4.43 (1H, d, CH, *J*=1.3 Hz), 7.20-7.39 (3H, m, Ar-H), 7.71 (1H, s, Ar-H), 11.04 (1H, s, NH); **^{13}C NMR (150 MHz, $CDCl_3$):** δ ppm 18.1, 27.4, 38.8, 52.3, 106.1, 116.8, 125.8, 126.0, 127.5, 130.0, 134.2, 142.0, 147.4, 167.2, 171.8. **MS (m/z):** 305.06 (M+1).

2.4.2.3. Methyl 4-(2-Bromo-4-chlorophenyl)-5-cyano-2-methyl-6-oxo-1,4,5,6-tetrahydropyridine-3-carboxylate (1.2C): White solid, yield: 78%, m.p.227°C, **^{1}H**

NMR (600 MHz, $CDCl_3$): δ ppm 2.54 (3H, s, CH_3), 3.68 (3H, s, CH_3), 3.98 (1H, d, CH, *J*=1.3 Hz), 4.12 (1H, d, CH, *J*=1.3 Hz), 7.25-7.30 (2H, m, Ar-H), 7.75 (1H, s, Ar-H), 11.01 (1H, s, NH); **^{13}C NMR (150 MHz, $CDCl_3$):** δ ppm 18.1, 24.1, 38.1, 52.3, 106.1, 116.8, 124.1, 127.7, 130.2, 131.3, 132.2, 141.6, 147.4, 167.2, 171.8. **MS (m/z):** 383.97 (M+1).

2.4.2.4. Methyl 4-(2-chlorophenyl)-5-cyano-2-methyl-6-oxo-1,4,5,6-tetrahydropyridine-3-carboxylate (1.2D): White solid, yield: 75%, m.p.204°C, **^{1}H NMR (600 MHz, $CDCl_3$):** δ ppm 2.46 (3H, s, CH_3), 3.65 (3H, s, CH_3), 3.83 (1H, d, CH, *J*=1.3 Hz), 3.92 (1H, d, CH, *J*=1.3 Hz), 7.18-7.41 (3H, m, Ar-H), 7.72 (1H, d, Ar-H, J=7.5 Hz), 10.96 (1H, s, NH); **^{13}C NMR (150 MHz, $CDCl_3$):** δ ppm 18.1, 22.8, 38.3, 52.3, 106.1, 116.8, 126.7, 127.3, 128.7, 129.1, 133.0, 138.2, 147.4, 167.2, 171.8. **MS (m/z):** 305.06 (M+1).

2.4.2.5. Methyl 5-cyano-2-methyl-6-oxo-4-(o-tolyl)-1,4,5,6-tetrahydropyridine-3-carboxylate (1.2E): Pale yellow solid, yield: 71%, m.p.214°C, **^{1}H NMR (600 MHz, $CDCl_3$):** δ ppm 2.51 (3H, s, CH_3), 2.55 (3H, s, CH_3), 3.63 (3H, s, CH_3), 4.79 (1H, d, CH, *J* = 1.3 Hz), 4.86 (1H, d, CH, *J* = 1.1 Hz), 6.92-7.16 (4H, m, Ar-H), 11.02 (1H, s, NH); **^{13}C NMR (150 MHz, $CDCl_3$):** δ ppm 18.1, 19.5, 25.4, 25.4, 39.1, 52.3, 106.1, 116.8, 124.6, 125.6, 125.8, 130.3, 137.4, 139.0, 147.4, 167.2, 171.8. **MS (m/z):** 285.12 (M+1).

2.4.2.6. Methyl 5-cyano-4-(4-methoxyphenyl)-2-methyl-6-oxo-1,4,5,6-tetrahydropyridine-3-carboxylate (1.2F): Pale yellow solid, yield: 81%, m.p.246°C, **^{1}H NMR (600 MHz, $CDCl_3$):** δ ppm 2.36 (3H, s, CH_3), 3.67 (3H, s, CH_3), 3.81 (1H, d, CH, *J*=1.3 Hz), 3.86 (3H, s, CH_3), 3.94 (1H, d, CH, *J*=1.3 Hz), 6.86 (2H, d, Ar-H, *J*=7.5 Hz), 7.23 (2H, d, Ar-H, *J*=7.5 Hz), 10.97 (1H, s, NH); **^{13}C NMR (150 MHz, $CDCl_3$):** δ ppm 18.1, 27.9, 38.8, 52.3, 55.8, 106.1, 114.2, 116.8, 128.7, 132.9, 147.4, 157.8, 167.2, 171.8. **MS (m/z):** 301.11 (M+1).

2.4.2.7. Methyl 5-cyano-4-(2-methoxyphenyl)-2-methyl-6-oxo-1,4,5,6-tetrahydropyridine-3-carboxylate (1.2G): White solid, yield: 71%, m.p.207°C, **^{1}H NMR (600 MHz, $CDCl_3$):** δ ppm 2.42 (3H, s, CH_3), 3.64 (3H, s, CH_3), 3.78 (3H, s, CH_3), 3.86 (1H, d, CH, *J*=1.3 Hz), 3.97 (1H, d, CH, *J*=1.3 Hz), 6.87-7.05 (3H, m, Ar-

H), 7.51 (1H, d, Ar-H, *J*=7.5 Hz), 10.99 (1H, s, NH); **^{13}C NMR (150 MHz, $CDCl_3$):** δ ppm 18.1, 22.0, 39.1, 52.3, 56.1, 106.1, 112.2, 116.8, 120.9, 126.2, 126.9, 128.7, 147.4, 155.8, 167.2, 171.8. **MS (m/z):** 301.11 (M+1).

2.4.2.8. Methyl 4-(2-bromo-5-fluorophenyl)-5-cyano-2-methyl-6-oxo-1,4,5,6-tetrahydropyridine-3-carboxylate (1.2H): White solid, yield: 78%, m.p.220°C, **^{1}H NMR (600 MHz, $CDCl_3$):** δ ppm 2.22 (3H, s, CH_3), 3.64 (3H, s, CH_3), 3.80 (1H, d, CH, *J*=1.3 Hz), 3.87 (1H, d, CH, *J*=1.3 Hz), 7.15 (1H, s, Ar-H), 7.27-7.56 (2H, m, Ar-H), 10.89 (1H, s, NH); **^{13}C NMR (150 MHz, $CDCl_3$):** δ ppm 18.1, 24.1, 38.2, 52.3, 106.1, 114.9, 116.8, 118.5, 133.2, 145.6, 147.4, 161.8, 167.2, 171.8. **MS (m/z):** 368.00 (M+1).

2.4.2.9. Methyl 5-cyano-2-methyl-6-oxo-4-(p-tolyl)-1,4,5,6-tetrahydropyridine-3-carboxylate (1.2I): White solid, yield: 84%, m.p.217°C, **^{1}H NMR (600 MHz, $CDCl_3$):** δ ppm 2.12 (3H, s, CH_3), 2.34 (3H, s, CH_3), 3.78 (3H, s, CH_3), 3.82 (1H, d, CH, *J*=1.3 Hz), 3.87 (1H, d, CH, *J*=1.3 Hz), 6.91-7.24 (4H, m, Ar-H), 10.95 (1H, s, NH); **^{13}C NMR (150 MHz, $CDCl_3$):** δ ppm 18.1, 21.0, 29.1, 38.9, 52.3, 106.1, 116.8, 127.8, 128.9, 135.6, 137.5, 147.4, 167.2, 171.8. **MS (m/z):** 285.12 (M+1).

2.4.3. General procedure for the synthesis of 2-pyridones (1.3A-1.3I)

Method C (microwave-assisted reaction): DDQ (3.52 mmol) was added to each solution of 3,4-dihydro-2-pyridone **(1.2A-1.2I)** (3.52 mmol) in methanol (15 ml) and microwaved for 2 minutes. TLC (EtOAc/hexane 5:5) was used to monitor the reaction progress of synthesis. After completion of the reaction, methanol (10 ml) was added to the reaction vessel, allowing the formation of pure crystals of 2-pyridone **(1.3A-1.3I)** (which was further collected). The residual liquids containing 2-pyridone **(1.3A-1.3I)** were collected and purified by column chromatography Hexane: EtOAc (50:50) over silica gel.

Method D (thermal assisted reaction): DDQ (3.52 mmol) was added to a solution of 3,4-dihydro-2-pyridone **(1.2A-1.2I)** (3.52 mmol) in methanol (15 ml) and heated on a heating mantle at 100°C for 8-10 minutes. TLC (EtOAc/hexane 5:5) was used to monitor the reaction. After completion of the reaction, ethanol (10 ml) was

added to the reaction vessel, allowing the formation of pure crystals of 2-pyridone **(1.3A-1.3I)** (which was further collected). The residual liquids containing 2-pyridone **(1.3A-1.3I)** were collected and purified by column chromatography Hexane: EtOAc (50:50) over silica gel.

2.4.3.1. Methyl 4-(4-chlorophenyl)-5-cyano-2-methyl-6-oxo-1,6-dihydropyridine-3-carboxylate (1.3A): White solid, yield: 84%, m.p.285°C, **^{1}H NMR (600 MHz, $CDCl_3$):** δ ppm 2.39 (3H, s, CH_3), 3.35 (3H, s, CH_3), 7.16 (2H, d, Ar-H, *J*=7.5 Hz), 7.35 (2H, d, Ar-H, *J*=7.5 Hz), 13.50 (1H, s, NH); **^{13}C NMR (150 MHz, $CDCl_3$):** δ ppm 19.6, 52.4, 110.8, 115.3, 115.8, 128.7, 130.0, 130.6, 133.5, 149.9, 161.5, 165.0, 169.4. **MS (m/z):** 303.06 (M+1).

2.4.3.2. Methyl 4-(3-chlorophenyl)-5-cyano-2-methyl-6-oxo-1,6-dihydropyridine-3-carboxylate (1.3B): White solid, yield: 72%, m.p.221°C, **^{1}H NMR (600 MHz, $CDCl_3$):** δ ppm 2.62 (3H, s, CH_3), 3.50 (3H, s, CH_3), 7.12 (1H, d, Ar-H, *J*=7.5 Hz), 7.26-7.39 (3H, m, Ar-H), 13.49 (1H, s, NH); **^{13}C NMR (150 MHz, $CDCl_3$):** δ ppm 19.6, 52.4, 110.8, 115.3, 115.8, 126.4, 127.0, 128.0, 130.0, 133.9, 134.2, 149.9, 161.5, 165.0, 169.4. **MS (m/z):**303.06 (M+1).

2.4.3.3. Methyl 4-(2-Bromo-4-chlorophenyl)-5-cyano-2-methyl-6-oxo-1,6-dihydropyridine-3-carboxylate (1.3C): White solid, yield: 72%, m.p.275°C, **^{1}H NMR (600 MHz, $CDCl_3$):** δ ppm 2.71 (3H, s, CH_3), 3.55 (3H, s, CH_3), 7.15 (1H, d, Ar-H, *J*=7.5 Hz), 7.41 (1H, d, Ar-H, 7.5 Hz), 7.65 (1H, s, Ar-H), 13.55 (1H, s, NH); **^{13}C NMR (150 MHz, $CDCl_3$):** δ ppm 19.6, 52.4, 110.8, 115.3, 115.8, 120.2, 127.7, 130.0, 130.2, 134.2, 136.3, 149.9, 161.5, 165.0, 169.4. **MS (m/z):** 382.97 (M+1).

2.4.3.4. Methyl 4-(2-chlorophenyl)-5-cyano-2-methyl-6-oxo-1,6-dihydropyridine-3-carboxylate (1.3D): White solid, yield: 89%, m.p.246°C, **^{1}H NMR (600 MHz, $CDCl_3$):** δ ppm 2.54 (3H, s, CH_3), 3.39 (3H, s, CH_3), 7.22 (1H, t, Ar-H, *J*=7.5 Hz), 7.30-7.54 (3H, m, Ar-H), 13.53 (1H, s, NH); **^{13}C NMR (150 MHz, $CDCl_3$):** δ ppm 19.6, 52.4, 110.8, 115.3, 115.8, 126.7, 127.8, 129.3, 129.9, 131.1, 135.3, 149.9, 161.5, 165.0, 169.4. **MS (m/z):** 303.06 (M+1).

2.4.3.5. Methyl 5-cyano-2-methyl-6-oxo-4-(o-tolyl)-1,6-dihydropyridine-3-carboxylate (1.3E): White solid, yield: 76%, m.p.238°C, **^{1}H NMR (600 MHz, $CDCl_3$):** δ ppm 2.25 (3H, s, CH_3), 2.64 (3H, s, CH_3), 3.41 (3H, s, CH_3), 6.92-7.48 (4H, m, Ar-H), 13.66 (1H, s, NH); **^{13}C NMR (150 MHz, $CDCl_3$):** δ ppm 19.6, 52.4, 110.8, 115.3, 115.8, 125.6, 126.3, 127.8, 131.3, 134.6, 136.1, 149.9, 161.5, 165.0, 169.4. **MS (m/z):** 283.10 (M+1).

2.3.4.6. Methyl 5-cyano-4-(4-methoxyphenyl)-2-methyl-6-oxo-1,6-dihydropyridine-3-carboxylate (1.3F): White solid, yield: 79%, m.p.272°C, **^{1}H NMR (600 MHz, $CDCl_3$):** δ ppm 2.42 (3H, s, CH_3), 3.68 (3H, s, CH_3), 3.78 (3H, s, CH_3), 6.89 (2H, d, Ar-H, *J*=7.5 Hz), 7.56 (2H, d, Ar-H, *J*=7.5 Hz), 8.40 (1H, s, NH); **^{13}C NMR (150 MHz, $CDCl_3$):** δ ppm 19.6, 52.4, 55.8, 110.8, 114.2, 115.3, 115.8, 124.8, 130.1, 149.9, 159.8, 161.5, 165.0, 169.4. **MS (m/z):** 299.10 (M+1).

2.4.3.7. Methyl 5-cyano-4-(2-methoxyphenyl)-2-methyl-6-oxo-1,6-dihydropyridine-3-carboxylate (1.3G): White solid, yield: 79%, m.p.230 °C, **^{1}H NMR (600 MHz, $CDCl_3$):** δ ppm 2.63 (3H, s, CH_3), 3.46 (3H, s, CH_3), 3.82 (3H, s, CH_3), 7.01-7.35 (4H, m, Ar-H), 13.55 (1H, s, NH); **^{13}C NMR (150 MHz, $CDCl_3$):** δ ppm 19.6, 52.4, 56.2, 110.9, 111.4, 115.3, 115.8, 119.9, 120.9, 128.9, 129.7, 149.9, 157.6, 161.5, 165.0, 169.4. **MS (m/z):** 299.10 (M+1).

2.4.3.8. Methyl 4-(2-bromo-5-fluorophenyl)-5-cyano-2-methyl-6-oxo-1,6-dihydropyridine-3-carboxylate (1.3H): White solid, yield: 79%, m.p.198 °C, **^{1}H NMR (600 MHz, $CDCl_3$):** δ ppm 2.73 (3H, s, CH_3), 3.54 (3H, s, CH_3), 6.98 (1H, dd, Ar-H, *J*=8.1 Hz, 3.0 Hz), 7.06-7.10 (1H, m, Ar-H), 7.65 (1H, dd, Ar-H, *J*=8.9 Hz, 5.0 Hz), 13.59 (1H, s, NH); **^{13}C NMR (150 MHz, $CDCl_3$):** δ ppm 19.6, 52.4, 110.8, 113.4, 114.4, 115.3, 115.9, 116.9, 133.9, 139.8, 149.9, 161.5, 161.8, 165.0, 169.4. **MS (m/z):** 366.98 (M+1).

2.4.3.9. Methyl 5-cyano-2-methyl-6-oxo-4-(p-tolyl)-1,6-dihydropyridine-3-carboxylate (1.3I): White solid, yield: 79%, m.p.214 °C, **^{1}H NMR (600 MHz, $CDCl_3$):** δ ppm 2.34 (3H, s, CH_3), 2.73 (3H, s, CH_3), 3.56 (3H, s, CH_3), 7.10-7.35 (4H, m, Ar-H), 13.43 (1H, s, NH); **^{13}C NMR (150 MHz, $CDCl_3$):** δ ppm 19.6, 21.3, 52.4,

110.9, 115.3, 115.8, 128.9, 129.5, 234.5, 137.6, 149.9, 161.5, 165.0, 169.4. **MS (m/z):** 283.12 (M+1).

2.5. Results and discussions

In **scheme 1**, a series of 4H-pyran derivatives **(1.1A-1.1I)** were synthesized using multicomponent condensation reactions. These pyrans compounds are converted to 3,4-dihydropyridone derivatives **(1.2A-1.2I)** using a catalyst through methods **A** and **B** with a high product yield. Then, 3,4-dihydropyridone derivatives were oxidized to the 2-pyridone derivatives **(1.3A-1.3I)** by methods **C** and **D** with a good product outcome. All the 2-pyridone compounds **(1.3A-1.3I)** gave a suitable crystal for analysis. The crystals were studied using single-crystal X-ray diffraction (SC-XRD) and Hirshfeld surface analysis.

2.5.1. X-ray crystallographic studies and Hirshfeld surface analysis of compounds 1.3A to 1.3I

2.5.1.1. Crystal analysis of compound 1.3A

The compound **1.3A** crystallizes two symmetry-independent molecules in the asymmetric unit, Z' = 2 **(Figure 2.4)**. It was crystallized in methanol at room temperature with slow solvent evaporation. The compound crystallizes in an orthorhombic crystal system. The space group of the system is *Pna2₁*, with eight molecules per unit cell. Molecules **A1** and **A2** are dimerized through the N-H…O interactions of the 2-pyridone ring with graph set $R_2^2(8)$ in length 1.909 Å, and angle through H atom 174.38° and 175.47° **(Figure 2.6 (b))**.

Structurally molecules are the same, but there is a difference in the spatial orientation of the atoms between the two molecules. It can be visualized from the overlay of the two structures. They have a root-mean-square deviation (RMSD) value of 1.447 Å **(Figure 2.5)**. There are slight differences at the crystal packing level of the two molecules, **A1** and **A2**. It can be visualized in a two-dimensional (2D) hydrogen network of molecules **A1** and **A2**.

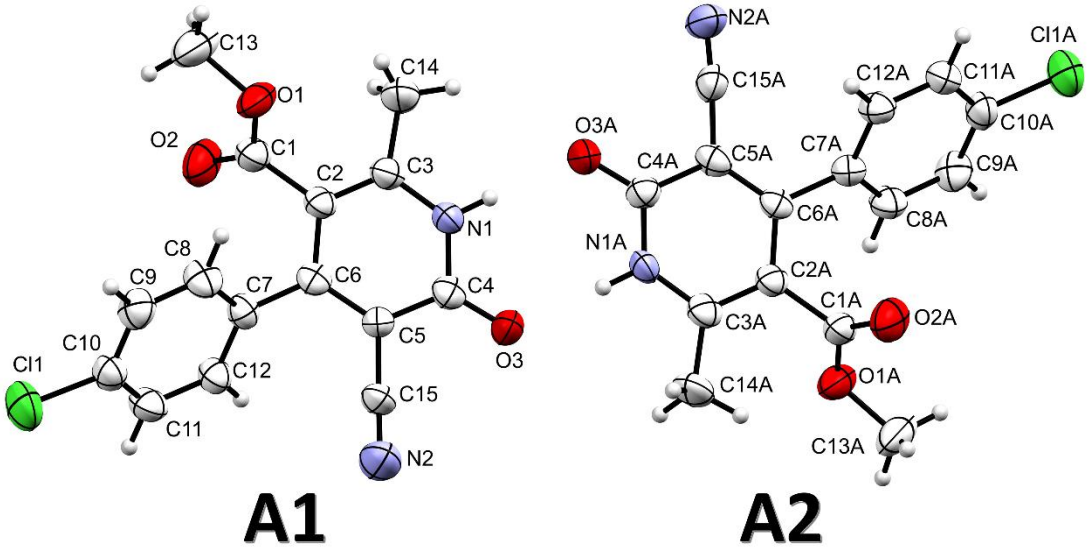

Figure 2.4: ORTEP of compound **1.3A**

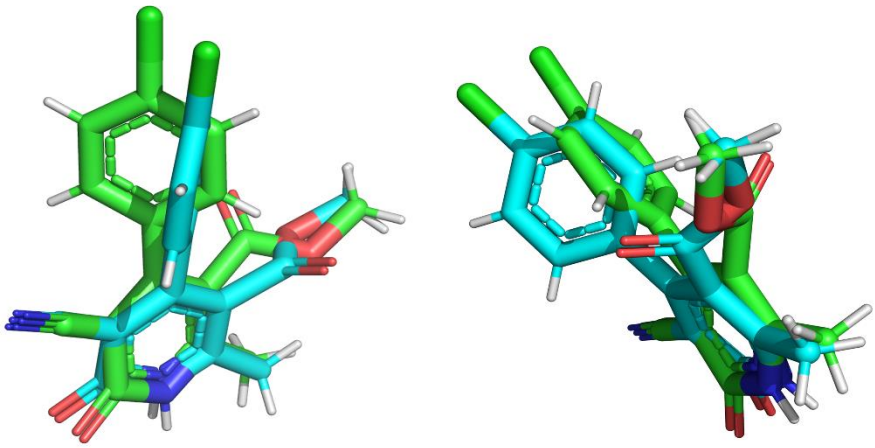

Figure 2.5: Overlay diagram of molecules **A1**(green) and **A2**(blue)

The pyridone ring of molecules **A1** and **A2** are planar, and these planes have a dihedral angle of 1.58°. The torsional angles C7-C6-C5-C4 in **A1** and C7A-C6A-C5A-C4A in **A2** are -176.43° and 177.42°, respectively. The dihedral angle between the planes of the pyridone ring and the **A1** and **A2** benzene ring is 52.78° and 52.63°, respectively. The compound crystallized in cell length **a** = 15.6529(6) Å, **b** = 8.9949(3) Å and **c** = 20.1865(8) Å, and cell angles are α = 90°, β = 90° and γ = 90°. The crystal information of compound **1.3A** is summarized in **Table 2.1.**

Table 2.1: Crystal data of compounds **1.3A** and **1.3B**

Compound	**1.3A**	**1.3B**
Identification code	2222467	2222465
Empirical formula	$C_{15}H_{11}ClN_2O_3$	$C_{15}H_{11}ClN_2O_3$
Formula weight	302.71	302.71
Temperature (K)	293(2)	293(2)
Crystal system	orthorhombic	orthorhombic
Space group	$Pna2_1$	Pbca
a/Å	15.6529(6)	6.8511(2
b/Å	8.9949(3)	15.2057(5)
c/Å	20.1865(8)	26.8498(10)
α/°	90	90
β/°	90	90
γ/°	90	90
Volume ($Å^3$)	2842.18(18)	2797.10(17)
Z	8	8
ρ ($calcg/cm^3$)	1.415	1.438
μ (mm^{-1})	0.28	0.284
F(000)	1248	1248
Crystal size (mm^3)	0.2 × 0.18 × 0.16	0.2 × 0.17 × 0.15
Radiation	Mo Kα (λ = 0.71073)	MoKα (λ = 0.71073)
2Θ range for data collection (°)	6.588 to 52.744	6.676 to 54.884
Index ranges	$-18 \le h \le 19$, $-11 \le k \le 10$, $-17 \le l \le 25$	$-8 \le h \le 7$, $-14 \le k \le 19$, $-34 \le l \le 23$
Reflections collected	14373	13996
Independent reflections	4635 [Rint = 0.0380, Rsigma = 0.0419]	3001 [Rint = 0.0416, Rsigma = 0.0373]
Data/restraints/parameters	4635/1/383	3001/0/192
Goodness-of-fit on F^2	1.031	1.078
Final R indexes [I>=2σ (I)]	R1 = 0.0451, wR2 = 0.1005	R1 = 0.0969, R2 = 0.3042
Final R indexes [all data]	R1 = 0.0626, wR2 = 0.1128	R1 = 0.1194, wR2 = 0.3236
Largest diff. peak/hole/e $Å^{-3}$	0.22/-0.31	1.60/-0.85

Supramolecular framework of compound 1.3A: Compound **1.3A** has a strong hydrogen bond between the symmetry-independent molecules **A1** and **A2** and a strong halogen-nitrogen interaction between different molecules. The molecule has suitable hydrogen bond acceptors of N and O, but the classical hydrogen bond is not

present beyond the dimer molecule. However, the non-classical hydrogen bond interaction forms weak C-H donors with N and O accepters. Nevertheless, C-H…O, N-H…O, and C-H…π interactions play a crucial role in forming an extensive supramolecular framework. The two symmetry-independent molecules (**A1** and **A2**) exhibited different supramolecular arrangements. Strong hydrogen bond interactions associate the two symmetry-independent molecules of N1-H1…O3A, C14-H14D…O3A, N1-H1…C4A from molecule **A1** and their back donation of N1A-H1A…O3, N1A-H1A…C4 from molecule **A2** with a distance of 1.909 Å, 2.673 Å, 2.80 Å, and 1.909 Å, 2.811 Å respectively **(Figure 2.6 (b))**. The crystal hydrogen bond and other interactions of compound **1.3A** is summarized in **Table 2.2.**

Table 2.2: Hydrogen bonds and other interactions in **1.3A**

Donor-H...Acceptor	D – H, Å	H...A, Å	D...A, Å	D - H...A,°
N1-H1…O3A	0.860	1.909	2.767	174.38
N1A-H1A…O3	0.860	1.909	2.767	175.47
C9A-H9A…O3A	0.930	2.543	3.364	147.37
C14-H14D…O3A	0.960	2.673	3.488	142.98
N1-H1…C4A	0.860	2.800	3.601	155.66
N1A-H1A…C4	0.860	2.811	3.611	155.51
C9-H9…O3	0.930	2.581	3.387	145.22
C12-H12…N2A	0.929	2.616	3.436	147.48
C12A-H12A…N2	0.929	2.498	3.290	143.28
C14-H14F...π(C7A-C12A)	0.961	2.764	9.689	161.67
C13-H13C...π(C2C6C5C4N1C3)	0.960	3.596	3.928	119.39
C13-H13B...π(C2C6C5C4N1C3)	0.960	3.367	3.928	103.20
Other contacts				
C15A-N2A…Cl1	1.133	3.170	3.531	99.09
C15-N2…Cl1A	1.143	3.344	3.859	108.29
O2A...π (C2C6C5C4N1C3)		3.292		
Intramolecular				
C12A-H12A…C15A	0.929	2.733	3.073	100.07
C14A-H14B…O1A	0.960	2.490	3.085	120.03
C13A-H13B…O2A	0.960	2.465	2.656	90.70
C12-H12…C15	0.929	2.739	3.019	98.42
C14-H14E…O1	0.959	2.565	3.086	114.27
C13-H13D…O2	0.961	2.578	2.675	85.26
C13-H13E…O2	0.960	2.717	2.675	77.32
C8-H8…C1	0.931	2.743	3.027	98.72

C8A-H8A…C1A	0.930	2.730	3.025	99.47
C1A-O2A...π(C7A-C12A)		3.796		
C1-O2...π(C7-C12)		3.810		

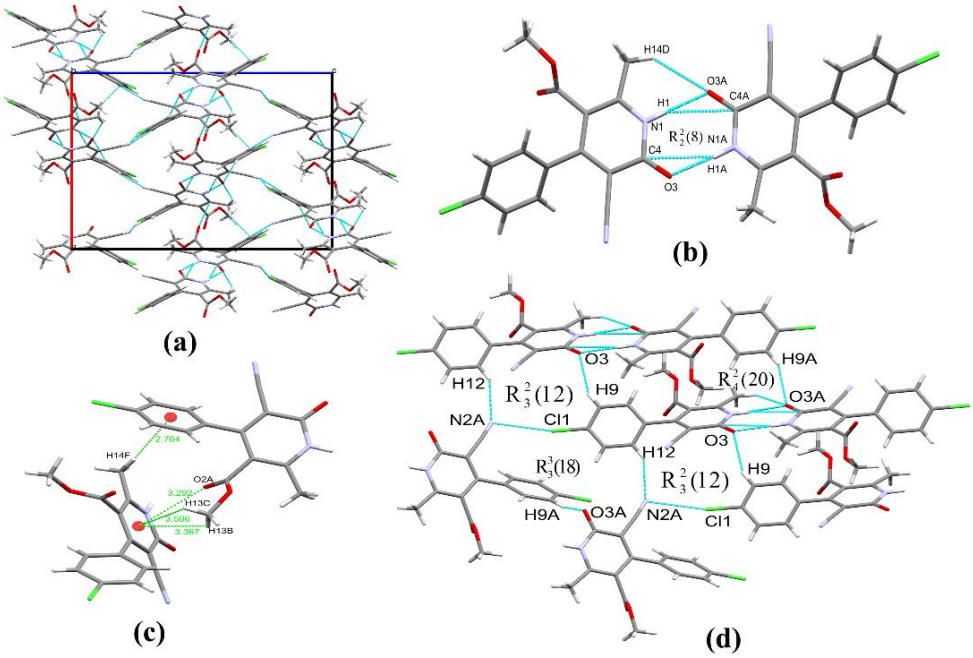

Figure 2.6: (a) packing of **1.3A** along the b-axis (b) interaction of two symmetry-independent molecules (c) C-H…π interactions of the molecules (d) graph sets representing an association of molecules in compound **1.3A**

The interaction of C9-H9…O3 from molecule **A2** and C9A-H9A…O3A from molecule **A1** non-classical hydrogen bond with a distance of respectively 2.581 Å and 2.543 Å, and bond angle of 145.22° and 147.37° respectively. N atom of the nitrile group bifurcated with the interaction of C12-H12…N2A from **A1** and C12A-H12A…N2 from molecule **A2** interact through a distance of 2.616 Å and 2.498 Å, respectively **(Figure 2.6 (d))**. The chlorine atom from molecules **A1** and **A2** formed a halogen bond to the N atom of the nitrile group with a distance of 3.17 Å and 3.344 Å, bond angles of 99.09° and 108.29°, respectively. For molecule **A2**, the C-H…π interaction with the benzene ring C14-H14F…Cg (C7A-C12A) with a distance of 2.764 Å. Similarly, in molecule **A1**, the C-H…π interactions with the pyridone ring are C13-H13C…Cg and C13-H13B…Cg with the distance of 3.596 Å and 3.367 Å, respectively. The lone pair…π interaction of the ester oxygen O2A…Cg (C2C6C5C4N1C3) also stabilized the supramolecular framework **(Figure 2.6 (c))**. The

graph sets $R_3^3(18)$ $R_3^2(12)$ and $R_4^2(20)$ formed from interlayer linkage reinforce the supramolecular structure **(Figure 2.6 (d))**.

Hirshfeld surface analysis of compound 1.3A: Hirshfeld surface analysis quantifies several intermolecular interactions in supramolecular systems. Hirshfeld's surface of the two symmetry-independent molecules, **A1** and **A2**, have a slight difference in their inter-atomic contacts as well as the relative percentage contribution of those contacts. The percentage contribution of the interactions from the 2D fingerprint plots for molecule **A1** are H…H(20.1%), C…H(21.4%), O…H(20.9%), N…H(13.0%), Cl…H(10.3%), C…O(4.60%), Cl…N(4.1%), Cl…C(2.8%) and O…N(1.3%), and molecule **A2** are H…H(21.0%), C…H(20.7%), O…H(20.8%), N…H(13.0%), Cl…H(10.0%), C…O(4.6%), Cl…N(4.1%), Cl…C(2.7%) and O…N(1.3%), respectively. The Hirshfeld surfaces of compound **1.3A** were mapped over d_{norm} in the range of -0.1919 – 1.4183 Å, and the small red spots indicate the short interactions involving non-classical hydrogen bonds of C-H…O interactions **(Figure 2.7 (a) & (b) and (d) & (e)).**

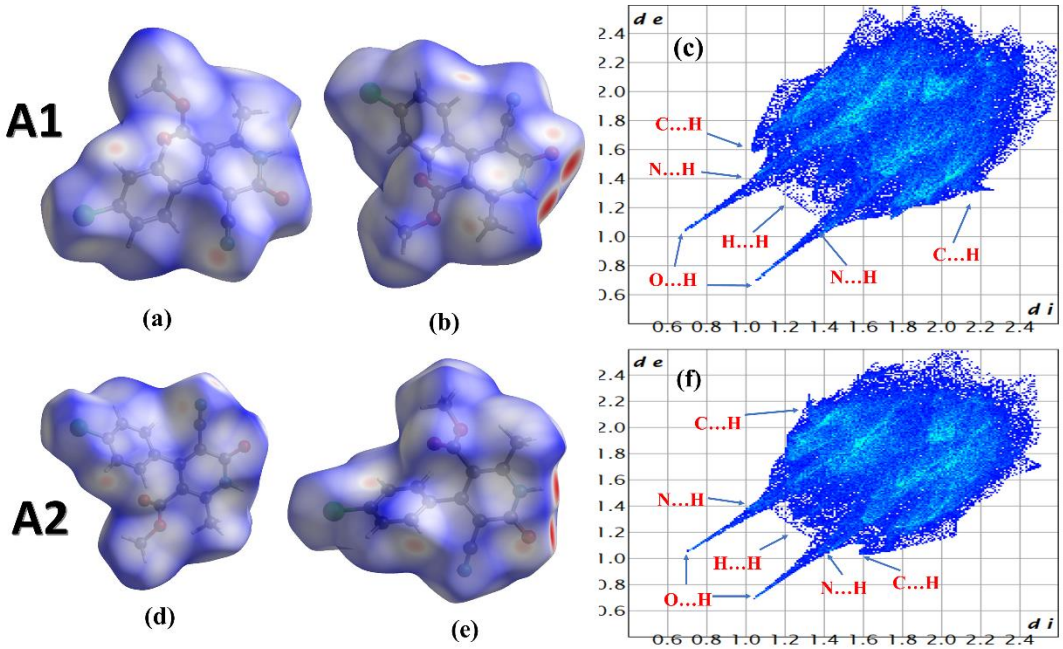

Figure 2.7: (a) & (b) Hirshfeld surface d_{norm} of molecule **A1** (c) 2D fingerprint plot of **A1** (d) & (e) Hirshfeld surface d_{norm} of molecule **A2** (f) 2D fingerprint plot of **A2**, in compound **1.3A**

The 2D fingerprint plot depicting the C…H/H…C, H…H, N…H/H…N, and O…H/H…O interactions are shown in **Figures 2.7 (c) and (f).** In this figure, all these interactions are in a pair of distinct spikes where the upper (di<de) and lower (di>de) spikes represent the donor and acceptor characters of the atoms, respectively. A pair of spikes at (di, de) ≈ (0.7, 1.05) represent the O…H/H…O interactions in molecule **A1** and (di, de) ≈ (0.7, 1.05) in molecule **A2**. The N…H/H…N spikes at (di, de) ≈ (1.35, 1.0) for molecule **A1** and (di, de) ≈ (1.45, 1.1) for molecule **A2**, where the lower spike is more in compound **A1**, which indicates that molecule **A1** has more acceptor property compared with molecule **A2** and vice versa. The C-H…π interactions evidence is also observed in the 2D fingerprint plot as the C-H…π interactions decompose into C…H contacts. C…H contacts appear as a characteristic wing in the 2D fingerprint plot.

In the shape index of compound **1.3A**, the blue and red regions represent donor and acceptor groups, respectively **(Figure 2.8 (a), (b), (e) & (f)).** As seen in the figure, no adjacent red and blue triangles confirm that a π-π stacking interaction is not present among the aromatic rings of the molecule. The curvedness mapping indicates the planarity of the complex. It also gave information about the π-π interactions between the aromatic rings and proved the absence of the π-π stacking interactions **(Figure 2.8 (c), (d), (g) &(h))**.

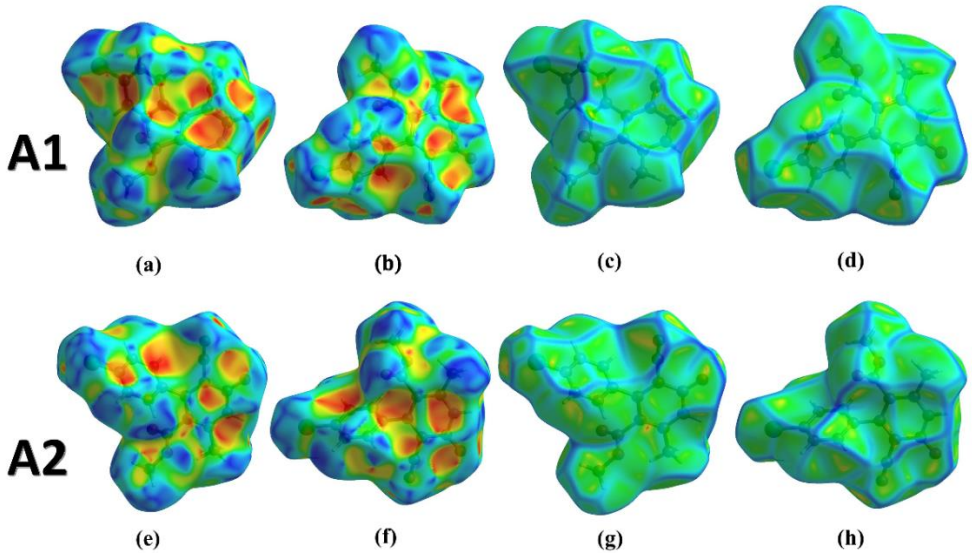

Figure 2.8: (a), (b), (e), (f) Shape index of molecule **A1 & A2**; (c), (d), (g), (h) Curvedness of molecule **A1 & A2**, in compound **1.3A**

The enrichment ratio (ER) of compound **1.3A** is calculated from the interatomic contacts between pairs of interacting atoms observed from the Hirshfeld surface analysis **(Table 2.3)**. For comparison of contacts, ER values pairs than unity tend to avoid intermolecular contacts. ER values are helpful for highlighting the favorable contacts in the supramolecular system. These contacts are the important driving force in three-dimensional arrangements of molecules in the supramolecular assembly. The H atoms in molecules **A1** and **A2** generate more than 52% of the total molecular surfaces, while Cl contributions are the least in molecule **A2**, only 9.4%. In molecule **A1**, the lowest contribution is N, with 9.4%.

Table 2.3: Enrichment ratios of compound **1.3A** (**A1** and **A2**)

Actual contacts (%)			**S_x**		**Random Contacts (%)**		**Enrichment Ratio (ER)**	
	A1	**A2**	**A1**	**A2**	**A1**	**A2**	**A1**	**A2**
H…H	20.10	21.00	52.90	53.25	27.98	28.36	0.72	0.74
C…C	0.20	0.20	14.60	14.20	2.13	2.02	0.09	0.10
N…N	0.20	0.20	9.40	9.40	0.88	0.88	0.23	0.23
O…O	0.00	0.00	13.65	13.75	1.86	1.89	0.00	0.00
Cl…Cl	0.60	0.60	9.45	9.40	0.89	0.88	0.67	0.68
C…H/H…C	21.40	20.70			15.45	15.12	1.39	1.37
O…H/H…O	20.90	20.80			14.44	14.64	1.45	1.42
N…HH…N	13.00	13.00			9.95	10.01	1.31	1.30
Cl…H/H…Cl	10.30	10.00			10.00	10.01	1.03	1.00
C…O/O…C	4.60	4.60			3.99	3.91	1.15	1.18
O…N/N…O	1.30	1.30			2.57	2.59	0.51	0.50
C…N/N…C	0.00	0.00			2.74	2.67	0.00	0.00
Cl…O/O…Cl	0.50	0.80			2.58	2.59	0.19	0.31
Cl…N/N…Cl	4.10	4.10			1.78	1.77	2.31	2.32
Cl…C/C…Cl	2.80	2.70			2.76	2.67	1.01	1.01

However, the ER value of O…H (E_{OH} = 1.45, 1.42) and N…H (E_{NH} = 1.31, 1.30) is greater than one in both **A1** and **A2** molecules. These values indicate that O…H and N…H interactions are favorable in these molecules and play an important role in the stability of the crystal molecule. ER value of C…H, E_{CH} = 1.39 & 1.37 in molecules **A1** and **A2** are favorable interactions. This corroborates the existence of C-H…π interactions in both molecules. The Cl…H interactions in both the molecules are slightly disfavored and only slightly enriched (E_{ClH} = 1.03 in **A1** and 1.00 in **A2**). Moreover, the N…Cl interactions in both molecules are highly favorable (E_{NCl} = 2.31 in **A1** and 2.32 in **A2**), reinforcing the supramolecular association in both molecules.

2.5.1.2. Crystal analysis of compound 1.3B

Compound **1.3B** crystallized in ethanol at room temperature by slow evaporation of the solvent **(Figure 2.9)**. The compound crystalized with cell lengths **a** = 6.8511(2) Å, **b** = 15.2057(5) Å, **c** = 26.8498(10) Å, and cell angles are $\boldsymbol{\alpha}$ = 90°, $\boldsymbol{\beta}$ = 90°, $\boldsymbol{\gamma}$ = 90°. The compound exhibits an orthorhombic crystal system, with space group Pbca containing eight molecules per unit cell **(Figure 2.10 (a))**. The dihedral angle between the 2-pyridone ring and benzene was 55.96°. Crystal data and structure refinement details of compound **1.3B** are summarized in **Table 2.1.**

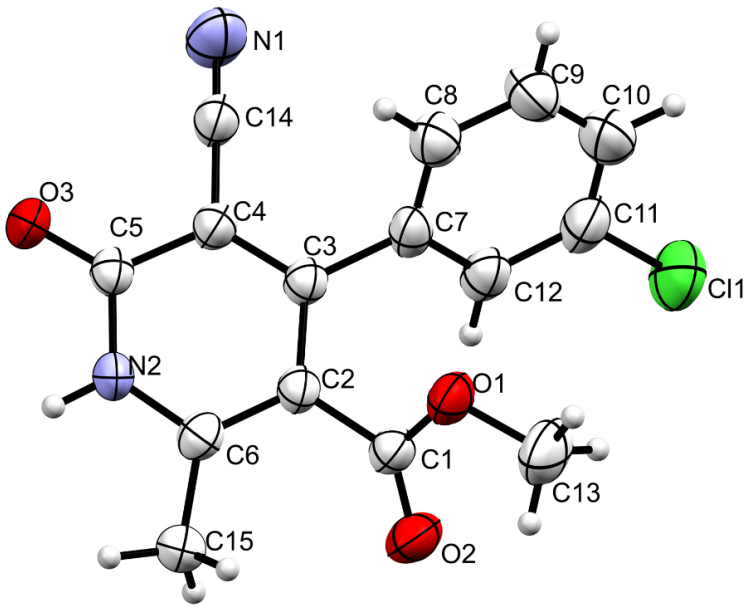

Figure 2.9: ORTEP of compound **1.3B**

Supramolecular framework of compound 1.3B: The molecular association of compound **1.3B** involves N-H…O hydrogen bonds to form an unsymmetrical dimer. The N2 donor of the molecule donates a proton to the acceptor O3 atom of the amide group of another molecule, which in turn donates back its proton from the N2 atom to amide O3. Thus, this donation and back donating of the proton generates a graph set notation, $R_2^2(8)$ as shown in **Figure 2.10 (b).** H2 forms a bifurcated hydrogen bond with the carbonyl carbon, which is a partially positive charge and forms a graph set $R_2^2(6)$, $R_1^2(3)$ to strengthen the dimerization of the molecules. The carbonyl carbon O3 acts as a bifurcated acceptor and forms N2-H2…O3 and C15-H15C…O3 interactions with bond distances of 1.914 Å and 2.548 Å, respectively, and bond angles on H are 171.43° and 170.13° respectively.

Table 2.4: Hydrogen bonds and other interactions in compound **1.3B**

Donor-H...Acceptor	D – H, Å	H...A, Å	D...A, Å	D - H...A,°
N2-H2…O3	0.860	1.914	2.767	171.43
C15-H15C…O3	0.960	2.548	3.497	170.13
C12-H12…N1	0.930	2.646	3.573	1750.30
C15-H15B...π(C7-C12)	0.960	2.858	3.444	120.34
C15-H15A...π(C7-C12)	0.960	3.272	3.444	92.17
Other contacts				
C1-O2…Cl1	1.196	3.120	4.025	132.42
C14-N1…C5	1.130	3.118	4.051	140.16
C1-O2….C14	1.196	3.132	3.888	121.15
Cl1…π(C2C3C4C5N2C6)		3.579		
N1…π(C2C3C4C5N2C6)		3.392		
Intramolecular				
C15-H15B…O2	0.960	2.652	2.987	101.01
C13-H13A…O2	0.960	2.420	2.628	91.60
C8-H8…C14	0.930	2.839	3.084	96.38
O1…π(C7-C12)		3.466		

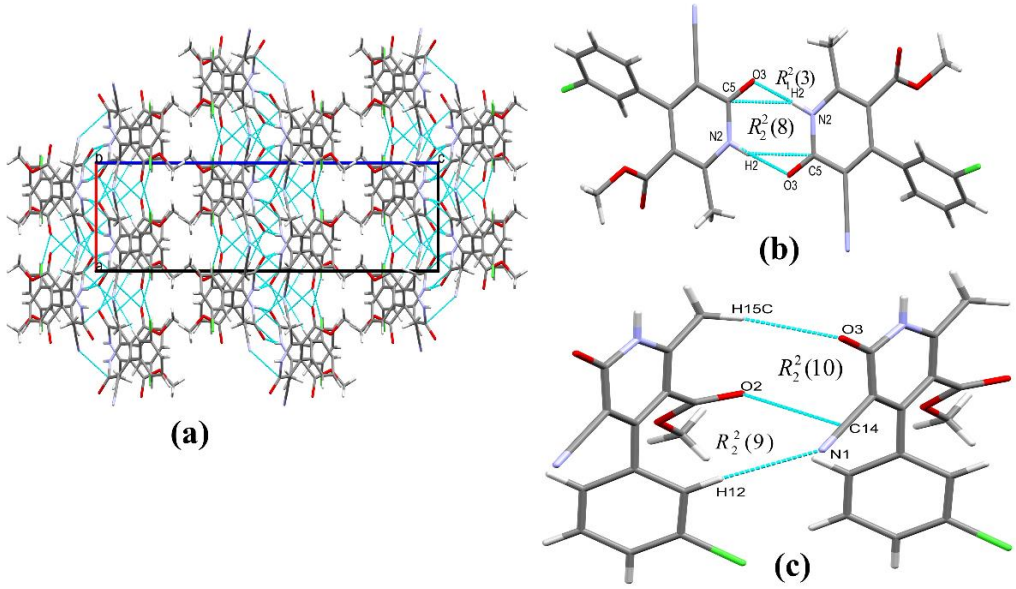

Figure 2.10: (a) Packing of compound **1.3B** along the b-axis (b) N-H…O interaction (c) C-H…O and C-H…N interactions of compound **1.3B**

The nitrile N1 bifurcated contacts with carbonyl carbon through ionic interaction and H12 of the aromatic ring with bond distances of 3.118 Å and 2.646 Å, respectively. However, carbonyl oxygen (O2) from the ester group bifurcated contacts with Cl1 and nitrile carbon C14 through a distance of 3.120 Å and 3.132 Å, respectively, and bond angles of 132.42° and 121.15°, respectively. The nitrile group forms a graph set $R_2^2(9)$ with the carbonyl oxygen and aromatic hydrogen of the other molecule to increase the stability of the molecular packing **(Figure 2.10 (c))**. In addition, there are other C-H…π interactions with distances of 2.858 Å and 3.272 Å, respectively, with C15-H15A…Cg and C15-H15B…Cg (Cg is centroid). Moreover, lone pair…π interactions of Cl1…Cg and N1…Cg with a distance of 3.579 Å and 3.392 Å help the molecule's supramolecular structure. Another interaction of the Chlorine atom with the aromatic ring of 2-pyridone and nitrogen of the nitrile group of the pyridone ring through a distance of 3.579 Å and 3.392 Å, respectively. It helps in the supramolecular association of the molecule **(Figure 2.11)**. The C15-H15C…O3 hydrogen bond and C1-O2…C14 ionic interaction generate a graph set to $R_2^2(10)$ reinforce the molecular association. The crystal hydrogen bond and other interactions of compound **1.3B** is summarized in **Table 2.4.**

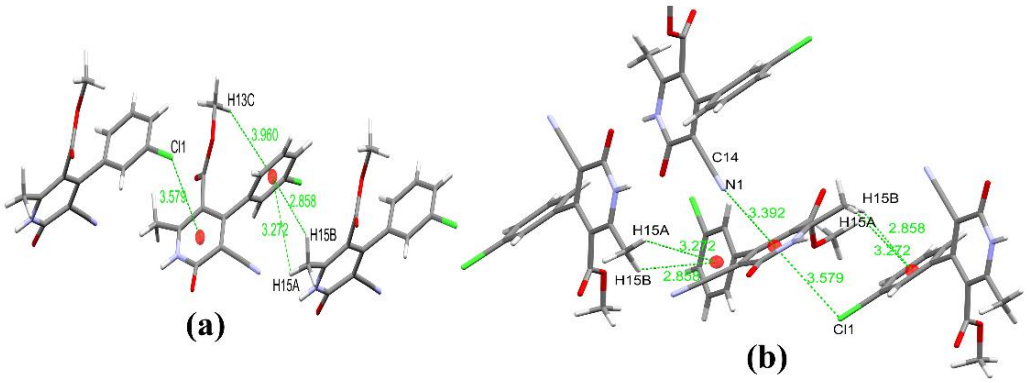

Figure 2.11: (a) & (b) various π-interactions stabilizing the crystal of compound **1.3B**

Hirshfeld surface analysis of compound 1.3B: Hirshfeld surfaces of compound **1.3B** mapped over a d_{norm} range of -0.6530 Å to 1.1424 Å. It is shown in **Figure 2.12 (a) & (b)**. The strong interaction between the carbonyl oxygen and amine N-H is visible as bright red areas on Hirshfeld surfaces. The light red spot is because of the other weak interactions due to more extended contacts on the Hirshfeld surface.

The 2D fingerprint plot of compound **1.3B** for the interaction O…H, C…H, Cl…H, N…H, and H…H are given in **Figure 2.12 (d)**. In the 2D fingerprint plots of compound **1.3B**, the presence of O…H intermolecular interactions appears as a pair of distinct spikes. The lower spike indicates in the 2D is an acceptor spike (di>de), while the upper spike corresponds to the donor spike (di<de). Other interactions like N…H, C…H, Cl…H, and H…H appear as distinct points in the 2D fingerprint plots. The relative contributions of different interactions to the Hirshfeld surface are H…H(29.4%), O…H(18.6%), C…H(12.3%), Cl…H(10.4%), N…H(10.0%), C…N(5.0%), C…O(3.8%), C…Cl(2.8%), O…Cl(2.7%) and C…C(1.3%). The C…N, and C…Cl contact indicates the presence of the lone pair … π interactions between the aromatic ring with nitrogen and chlorine atoms. However, the relative contributions of C…C contact is about 1.3% in compound **1.3B**, indicating no significant π…π interactions.

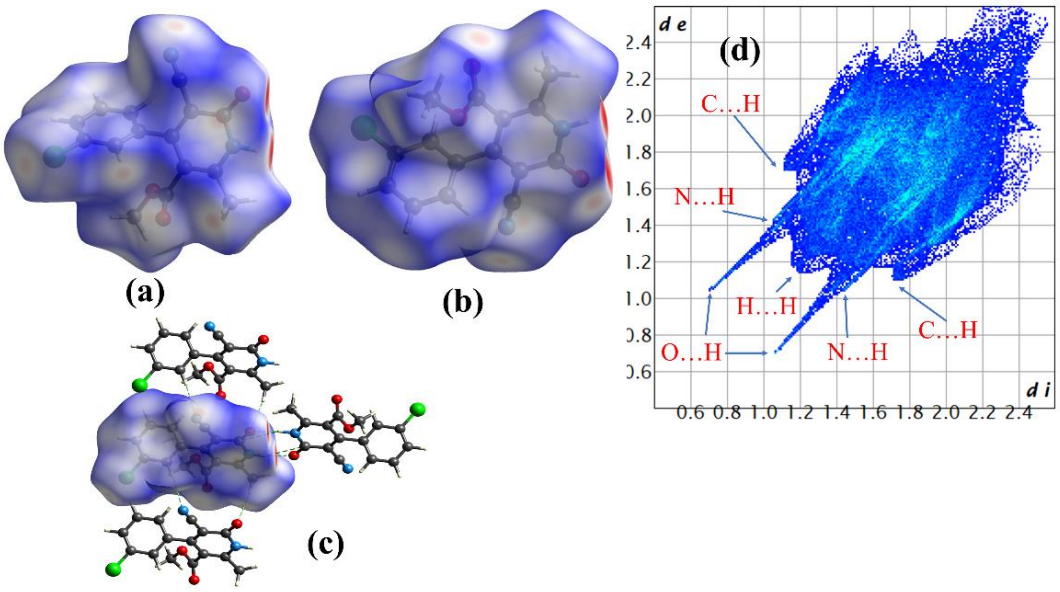

Figure 2.12: (a) and (b) d_{norm} both side view (c) H-bond interactions (d) 2D fingerprint plot showing H…H, O…H, N…H and C…H interactions, in compound **1.3B**

The shape index surface of compound **1.3B** does not have a complementary pair of red and blue triangles around the aromatic ring surface, indicating the absence of π…π stacking interaction. The yellowish-red concave region of the shape index indicates the acceptor region where C-H…π, N…π, and Cl…π interactions occur **(Figure 2.13 (a) and (b)).** The yellow and red-yellow colour spots in the curvedness of compound **1.3B** indicate the presence of weak interactions and strong hydrogen bonding, respectively, in the crystal **(Figure 2.13 (c) and (d)).** There was no green planar region at the curvedness of compound **1.3B.**

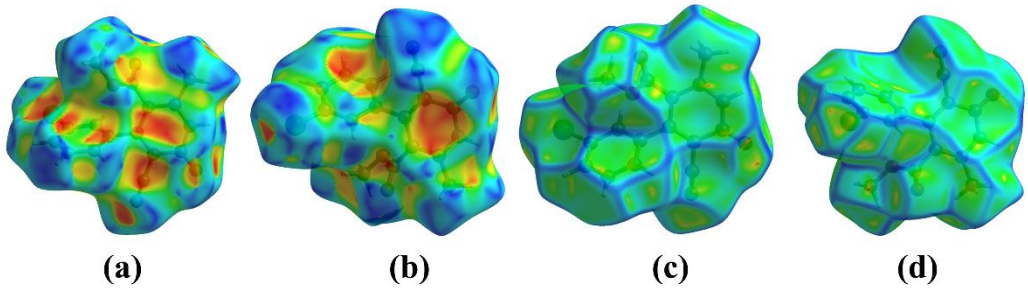

Figure 2.13: (a) and (b) shape index both side view, (c) and (d) Curvedness both side view, of compound **1.3B**

The enrichment ratio (ER) of compound **1.3B** is calculated similarly to the previous compound **(Table 2.5)**. This molecule is composed of two aromatic cycles,

and more than half (55.05%) of the molecular surface is generated by H atoms. From the enrichment ratio, O…H/H…O and Cl…H/H…Cl contacts are enriched, but other contacts with H are disfavoured. The contacts with C and N, O and Cl are also favored; C…N/N…C contact is enriched with E_{CN} = 2.03, confirming the interaction with nitrile N with the aromatic π system. The N…N contact E_{NN} = 1.39 indicates the interaction between the N of CN and pyridone is also feasible with a distance of 3.232 Å. Cl…O contact enrichment E_{OCl} = 1.24 also confirmed the chlorine and ester oxygen contact to form a halogen bond.

Table 2.5: Enrichment ratio (ER) of compound **1.3B**

Atoms	**H**	**C**	**N**	**O**	**Cl**
H	29.4	Actual contacts (%)			
C	12.3	1.3			
N	10	5	1.2		
O	18.6	3.8	0.9	0.2	
Cl	10.4	2.8	1.2	2.7	0
Surface (%)	55.05	13.25	9.30	12.75	8.55
H	30.3	Random contacts (%)			
C	14.6	1.8			
N	10.2	2.5	0.9		
O	14.0	3.4	2.4	1.6	
Cl	9.4	2.3	1.6	2.2	0.7
H	0.97	Enrichment ratio			
C	0.84	0.74			
N	0.98	2.03	1.39		
O	1.32	1.12	0.38	0.12	
Cl	1.10	1.24	0.75	1.24	0.00

2.5.1.3. Crystal analysis of compound 1.3C

The compound **1.3C** crystallized in ethanol by slow solvent evaporation at room temperature. The crystal compound was analyzed using single-crystal X-ray diffraction **(Figure 2.14)**. The compound is crystalized with unit cell lengths **a** = 9.9903(8) Å, **b** = 10.7627(8) Å, **c** = 15.1944(10) Å, and cell angles are $\boldsymbol{\alpha}$ = 90°, $\boldsymbol{\beta}$ = 104.365(8)°, $\boldsymbol{\gamma}$ = 90°. The compound exhibits a monoclinic crystal system, with space group $P2_1/c$, containing four molecules per unit cell **(Figure 2.15 (a))**.

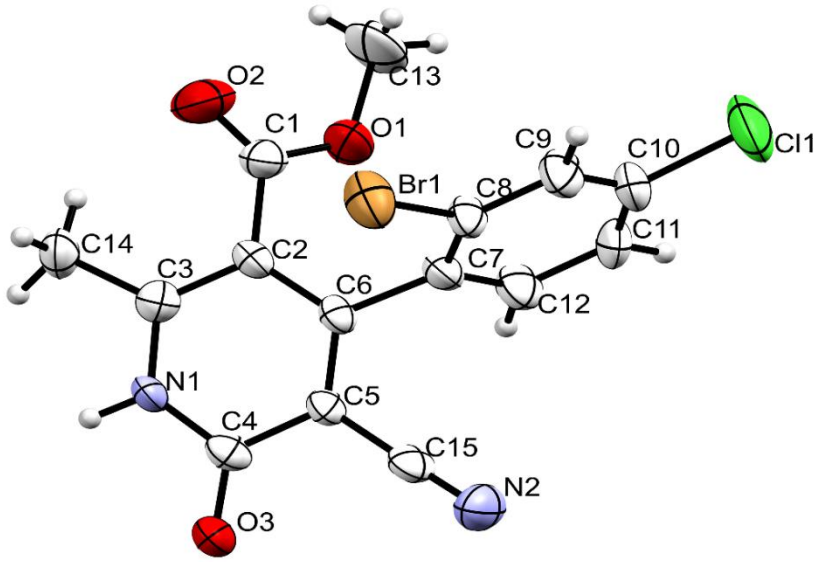

Figure 2.14: ORTEP of compound **1.3C**

The compound **1.3D** has two aromatic rings, and the dihedral angle between the benzene ring and the 2-pyridone rings is 73.41°. The crystallographic information is summarized in **Table 2.6.**

Table 2.6: Crystal data of compounds **1.3C** and **1.3D**

Compound	**1.3C**	**1.3D**
Identification code	2222469	2222468
Empirical formula	$C_{15}H_{10}BrClN_2O_3$	C15H11ClN2O3
Formula weight	381.61	302.71
Temperature (K)	293(2)	293(2)
Crystal system	monoclinic	monoclinic
Space group	$P2_1/c$	$P2_1/c$
a/Å	9.9903(8)	13.4881(5)
b/Å	10.7627(8)	7.2838(3)
c/Å	15.1944(10)	14.2923(5)
α/°	90	90
β/°	104.365(8)	96.934(3)
γ/°	90	90
Volume ($Å^3$)	1582.7(2)	1393.87(9)
Z	4	4
ρ ($calcg/cm^3$)	1.602	1.442
μ (mm^{-1})	2.778	0.285
F(000)	760	624
Crystal size (mm^3)	0.16 × 0.14 × 0.12	0.22 × 0.2 × 0.18
Radiation	MoKα (λ = 0.71073)	MoKα (λ = 0.71073)

2Θ range for data collection (°)	6.706 to 54.77	6.368 to 54.86
Index ranges	-12 ≤ h ≤ 9, -13 ≤ k ≤ 13, -19 ≤ l ≤ 18	-17 ≤ h ≤ 17, -9 ≤ k ≤ 9, -18 ≤ l ≤ 18
Reflections collected	12763	10846
Independent reflections	3366 [Rint = 0.0742, Rsigma = 0.1075]	2996 [Rint = 0.0312, Rsigma = 0.0337]
Data/restraints/parameters	3366/0/201	2996/0/192
Goodness-of-fit on F^2	1.042	1.074
Final R indexes [I>=2σ (I)]	R1 = 0.0610, wR2 = 0.1383	R1 = 0.0561, wR2 = 0.1588
Final R indexes [all data]	R1 = 0.1357, wR2 = 0.1616	R1 = 0.0788, wR2 = 0.1766
Largest diff. peak/hole/e $Å^{-3}$	0.98/-0.54	0.83/-0.29

Supramolecular framework of compound 1.3C: In the crystal, the molecule forms an asymmetric dimer via pairwise weak interactions N1H1…O3 with a bond distance of 2.0 Å and a bond angle of 160.54° to form a graph set of $R_2^2(8)$ ring motif **(Figure 2.15 (d)**). The methyl group of the ester functional group C13-H13B…N2 and C13-H13A…O3 interactions between the two molecules with a distance of 2.734 Å and 2.705 Å, respectively, formed a graph set of $R_2^2(8)$ the motif **(Figure 2.15 (b))** which extends along the a-axis to reinforce the supramolecular structure. The trifurcated interaction is observed between the carbonyl oxygen atom O3 of the pyridone ring with the hydrogen H1, ester methyl hydrogen H13A, and bromine Br1 of the neighboring molecules.

Table 2.7: Hydrogen bonds and other intermolecular interactions in compound **1.3C**

Donor-H...Acceptor	D – H, Å	H...A, Å	D...A, Å	D - H...A,°
N1-H1….O3	0.861	2.000	2.826	160.54
C13-H13A…O3	0.960	2.705	3.584	152.58
C13-H13B…N2	0.960	2.734	3.313	119.48
C9-H9...N2	0.930	2.598	3.508	166.18
Other contacts				
C8-Br1…O3	1.878	3.085	4.948	170.55
Cl1...π(C2C3C4C5C6N1)		3.405		
N2… π(C2C3C4C5C6N1)		3.695		
Intramolecular contact				

C13-H13A…O2	0.960	2.538	2.658	86.53
C14-H14B…O2	0.960	2.415	2.933	113.54
C14-H14B…C1	0.960	2.612	2.982	103.22
O1...π(C7-C12)		3.231		
C13-H13…π(C7-C12)	0.960	3.756		

The hydrogen H9 from the benzenoid ring interacts with the nitrogen N2 of the nitrile group of the pyridone ring to form an intermolecular hydrogen bond at a distance of 2.598 Å. It resulted in the formation of $R_2^2(16)$ a graph set **(Figure 2.15 (b))**, which increased the stability of the crystal. The halogen bond was formed between the bromine Br1 of the benzene ring and the carbonyl oxygen atom O3 of the pyridone ring linked layers at a distance of 3.085Å and a bond angle of 170.55°. Chlorine and nitrogen N2 atom also interact with the π system of the pyridone ring Cl1…Cg and N2…Cg (where Cg is centroid) at a distance of 3.405 Å and 3.695 Å, respectively **(Figure 2.15 (c))** to reinforce the supramolecular structure formation. However, the other graph set $R_2^4(22)$ involving four molecules assisted in the stability of the crystal packing of the crystal. The crystal hydrogen bond and other interactions of compound **1.3C** is summarized in **Table 2.7.**

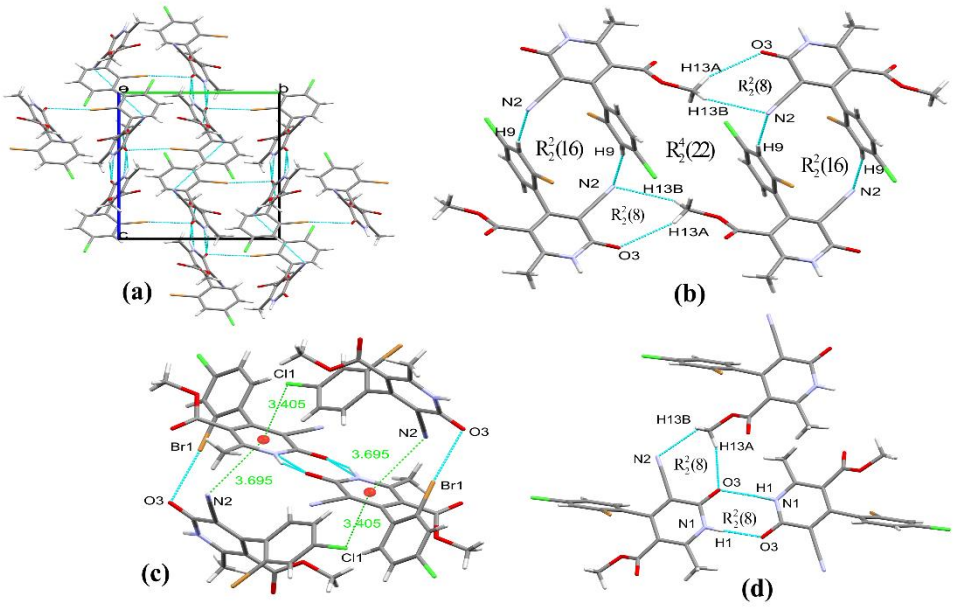

Figure 2.15: (a) Crystal packing along the a-axis, (b) and (d) C-H…O and N-H…O interactions showing graph sets, (c) lone pair…π and Br…O interactions, in compound **1.3C**

Hirshfeld Surface analysis of compound 1.3C: The Hirshfeld surfaces were mapped over d_{norm} in the ranges of -0.58 – 1.63Å for compound **1.3C** and are displayed in **Figure 2.16 (a) and (b).** The region of bright red spots on the surfaces is hydrogen bonding or short contacts with negative d-norm values, N-H…O, C-H…O, and N-H…N interactions. The region with white colour indicates the contacts around that of van der Waals radii with zero d-norm, and the more extended contacts with positive d-norm value are represented in blue colour.

The 2D fingerprint plot of compound **1.3C** for all interactions and the significant individual interactions are given in F**igure 2.16 (c).** The interaction among atoms are H…H(21.2%), O…H(18.9%), N…H(13.3%), Cl…H(12.3%), C…H(8.0%), Br…H(6.0%), C…Br(5.4%), C…Cl(4.4%), O….Br(2.4%) and other 8.1%. The contribution of H…H interaction was highest as a big spike was found in the 2D fingerprint plot in the region of $d_i + d_e \approx 2.4$Å. However, O…H/H…O contacts appears as pair of sharp spikes with di + de ≈ 1.9Å and have a percentage contribution of 18.9% to the total Hirshfeld surfaces. Interaction of N…H/H…N contributes 13.3% and di + de ≈ 2.4Å and is shown as pair of spikes in the fingerprint plot. Cl…H/H…Cl contacts account for 12.3% of the total interactions, and Br…H/H…Br contacts are 6.0% of the total contacts, and both interactions are shown as wings in the fingerprint plot, but both interactions do not have closed contacts.

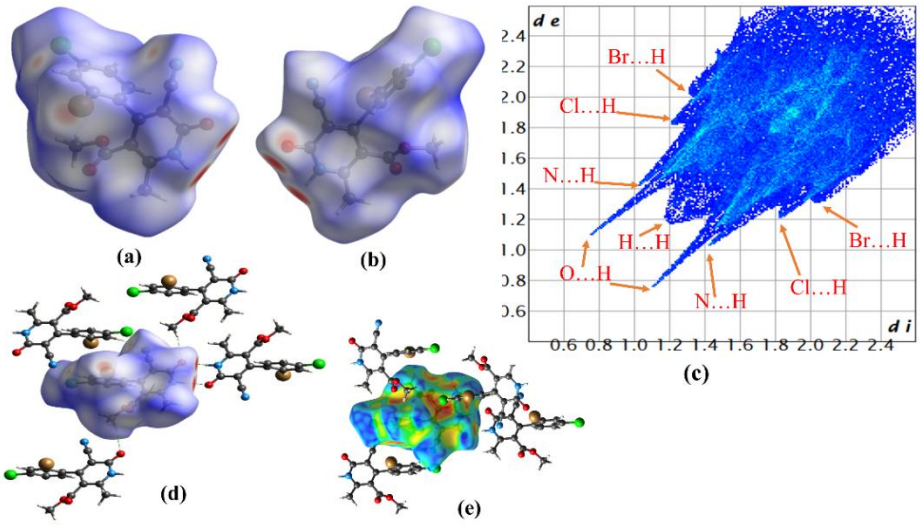

Figure 2.16: (a) and (b) d_{norm} both side view, (c) 2D fingerprint plot showing H…H, O…H, N…H, Cl…H and Br…H interactions, (d) and (e) Non-covalent interactions, in compound **1.3C**

The shape index was generated in the range of -1Å to 1Å for compound **1.3C**, which shows there is no complimentary pair of red and blue colours **(Figure 2.17 (a) & (b))**, which indicates the absence of π – π stacking interactions between the rings. The yellowish-red concave region around the surface of the aromatic ring represents the acceptor region where the halogen – π interactions occur. The curvedness of compound **1.3C (Figure 2.17 (c) & (d))** displays that the molecule does not have a flat surface in all directions, and there are no overlaying interactions.

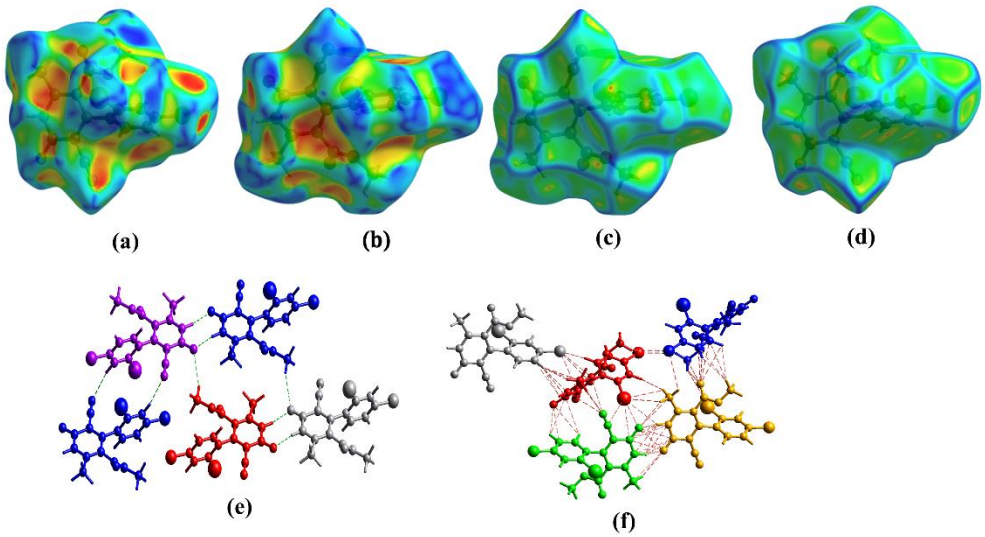

Figure 2.17: (a) and (b) shape index both side view, (c) and (d) curvedness both side view, (e) non-covalent H-bond, (f) closed contacts, in compound **1.3C**

Table 2.8: Enrichment ratio (ER) of compound **1.3C**

Atoms	**H**	**C**	**N**	**O**	**Cl**	**Br**
H	21.2	Actual contacts (%)				
C	8	0.7				
N	13.3	2	0.9			
O	18.9	0.8	0	0.1		
Cl	12.3	4.4	0.3	1.4	0	
Br	6	5.4	0.9	2.4	1.2	0
Surface (%)	50.45	11.00	9.15	11.85	9.80	7.95
H	25.5	Random contacts (%)				
C	11.1	1.2				
N	9.2	2.0	0.8			
O	12.0	2.6	2.2	1.4		
Cl	9.9	2.2	1.8	2.3	1.0	
Br	8.0	1.7	1.5	1.9	1.6	0.6

H	0.83	Enrichment ratio				
C	0.72	0.58				
N	1.44	0.99	1.07			
O	1.58	0.31	0.00	0.07		
Cl	1.24	2.04	0.17	0.60		
Br	0.75	3.09	0.62	1.27	0.77	

The enrichment ratio is useful in assessing the good contacts that are driving forces of the packing pattern of the supramolecular assembly. It is calculated from the interatomic contacts between pairs of interacting atoms X and Y. The compound **1.3C** is composed of two aromatic cycles, and about half of the molecular surface is generated by H atoms. The enrichment ratio is shown in **Table 2.8.** Here, we found that the interaction C…O/O…C, N…H/H…N, and Cl…H/H…Cl is enriched and favored, but C…H/H…C interaction is disfavored. The C…Cl/Cl…C and C…Br/Br…C interactions are enriched with the value of 2.04 and 3.09, respectively, which tells us about the presence of halogen…π interactions. O…Br/Br…O contacts are also enriched with E_{OBr}=1.27, confirming the bromine and oxygen interactions in the halogen bond.

2.5.1.4. Crystal analysis of compound 1.3D

The compound **1.3D** was crystallized in ethanol at room temperature by the slow evaporation method. The compound **1.3D** was analyzed using single-crystal XRD **(Figure 2.18).** The compound crystallized in cell length **a** = 13.4881(5) Å, **b** = 7.2838(3) Å and **c** = 14.2923(5) Å, and cell angles are $\boldsymbol{\alpha}$ = 90°, $\boldsymbol{\beta}$ = 96.934(3)°, $\boldsymbol{\gamma}$ = 90°. The compound exhibits a monoclinic crystal system, with space group $P2_1/c$ and four molecules per unit cell **(Figure 2.19 (a))**.

The compound **1.3D** has a 2-pyridone aromatic ring and benzenoid ring with a dihedral angle of 70.31°, and the torsion angle of C7-C6-C5-C4 is -173.74°. The crystallographic information of compound **1.3D** is summarized in **Table 2.6.**

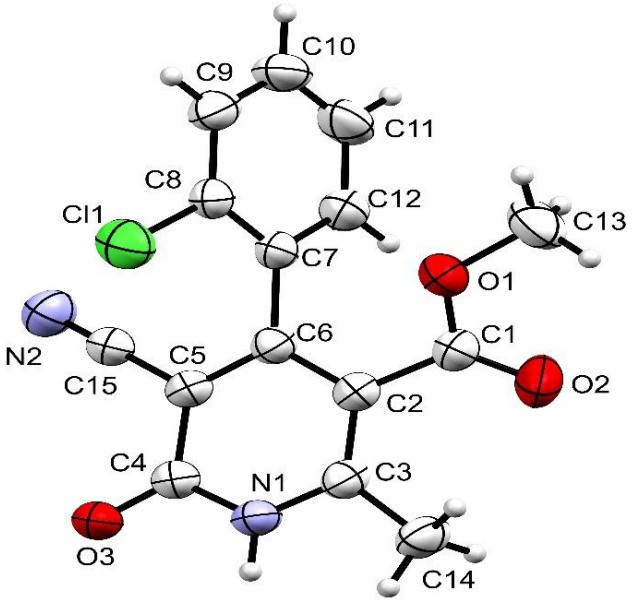

Figure 2.18: ORTEP of compound **1.3D**

Supramolecular framework of compound 1.3D: The compound **1.3D** molecule is associated with strong hydrogen bonding involving N-H…O of the pyridone ring to form a graph set of $R_2^2(8)$, and the bond length of 1.91 Å with a bond angle of 172.84° asymmetrical dimer **(Figure 2.19 (b))**. The H1 of the pyridone amine act as a bifurcated acceptor and forms a hydrogen bond with carbonyl O3 and the same carbonyl C4 of the 2-pyridone ring with the back donation. It forms graph sets $R_1^2(3)$ and $R_2^2(6)$ strengthens the dimerization of molecules. The carbonyl O3 bifurcated to accept the hydrogen bond from H1 of the pyridone ring and H12 from the benzene ring, N1-H1…3 and C12-H12…O3 with lengths 1.91 Å and 2.612 Å respectively, and bond angle through H atom are 172.84° and 158.04° respectively. The non-covalent interaction of compound **1.3D** was tabulated in **Table 2.9.**

Table 2.9: Hydrogen bonds and other interactions in compound **1.3D**

Donor-H...Acceptor	D – H, Å	H...A, Å	D...A, Å	D - H...A,°
N1-H1…O3	0.860	1.910	2.765	172.84
N1-H1…C4	0.860	2.802	3.601	155.21
C12-H12…O3	0.930	2.612	3.491	158.04
C11-H11…N2	0.930	2.721	3.596	157.14
C11-H11…C15	0.930	2.868	3.671	145.29
C14-H14C...π (N1C2-C6)		3.037		

C13-H13C…π (N1C2-C6)		3.538		
Other contacts				
Cl1…π (C7-C12)		4.053		
Intramolecular				
C13-H13A…O2	0.959	2.465	2.640	89.65
C14-H14B…O2	0.960	2.679	2.946	96.47
C1-O1… π(C7-C12)		3.323		
C13-H13C…π(C7-C12)		3.857		

The H11 of the benzene ring bifurcated to bond with the nitrile group with a graph set $R_1^2(3)$, the carbon atom in $C \equiv N$ bond has a partial positive charge, which interacts with H11 of the benzene ring through 2.868 Å apart, and the N2 atom at 2.721 Å apart with bond angle 157.14° and 145.29° respectively. These interactions form new intermolecular graph sets $R_2^2(8)$ and $R_2^2(9)$ increase the supramolecular structure formation **(Figure 2.19 (c))**. In addition, there were C-H…π interactions with a distance of 3.037 Å and 3.538 Å, respectively, with C14-C14C…Cg and C13-H13C…Cg (Cg = centroid). The chlorine atom form interacts with the aromatic ring through a lone pair …π interaction with a distance of 4.053 Å helps in the association of the molecules in the supramolecular framework **(Figure 2.19 (d))**.

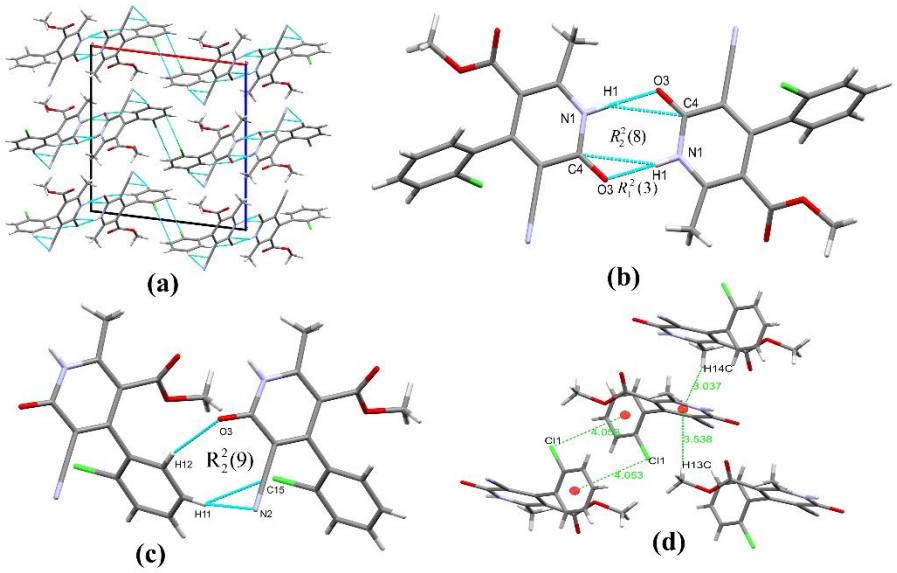

Figure 2.19: (a) packing diagram along b-axis (b) & (c) graph sets interactions (d) C-H… π and lone pair …π interactions, in compound **1.3D**

Hirshfeld surface analysis of compound 1.3D: The Hirshfeld surface of compound **1.3D** was mapped over d_{norm} in the range -0.6576 to 1.2340 Å and shown in **Figures 2.20 (a) and (b).** The strong interactions between the amine N-H and carbonyl carbon of the pyridone ring are visible as a bright red area in the Hirshfeld surface d-norm. The light red-white spot on the surface indicates the weak interaction with other molecules in the crystal. The 2D fingerprint plot of compound **1.3D** is depicted in **Figure 2.20 (c)**. As shown in the fingerprint plot of the compound **1.3D**, the relative contributions to the Hirshfeld surface by different interactions are H…H(21.8%), O…H(20.7%), C…H(18.2%), N…H(15.8%), Cl…H(14.1%), C…Cl(2.7%), C…N(2.3%) and N…O(1.7%). The O…H intermolecular interactions appear as a pair of spikes in the 2D fingerprint plot, and H…H interactions are found in the middle of the O…H spikes. The C…Cl interaction confirmed the lone pair … π interactions between the chlorine atom and the benzenoid ring. C…N interaction also indicates the weak interactions of nitrogen and aromatic π-system.

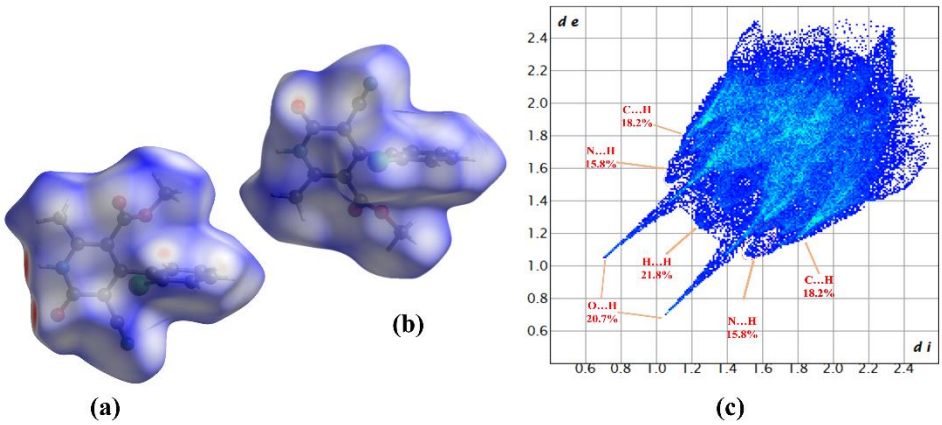

Figure 2.20: (a) & (b) Hirshfeld surface d_{norm} both side view (c) 2D fingerprint plots of compound **1.3D**

The shape index surface of compound **1.3D** does not have a complimentary pair of blue and red triangles around the aromatic ring surface **(Figure 2.21 (a) & (b))**, which indicates the absence of π-π stacking interactions in the crystals. It is also confirmed by 0.4% of the C…C interactions in the 2D fingerprint plot value. The concave region of the yellowish-red colour indicates the acceptor property of the interactions, and the donor regions are blue. In the Curvedness plot of the Hirshfeld surface, the yellow and reddish-yellow spots indicate weak and strong interactions, respectively **(Figure 2.21 (c) & (d)).** The absence of the flat green region in the

curvedness plot confirmed the π…π stacking interaction was not present in the intermolecular interaction.

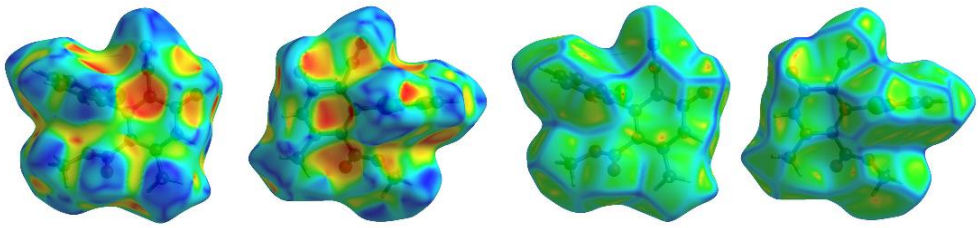

(a) (b) (c) (d)

Figure 2.21: (a) & (b) Shape Index both side view, (c) & (d) Curvedness both side view, of compound **1.3D**

The enrichment ratio (ER) calculated from the Hirshfeld surface analysis of interatomic contacts between a pair of interacting atoms of compound **1.3D** indicates whether the interactions are fruitful or not. The ER of compound **1.3D** is illustrated in **Table 2.10.** H atoms mainly cover the molecular surface with 56.2% of the total surface. From the enrichment ratio calculated, O…H/H…O, C…H/H…C, N…H/H…N, Cl…H/H…Cl and C…Cl/Cl…C contacts are favored with ER values 1.42, 1.31, 1.41, 1.48, and 1.29, respectively, but other contacts are not favored from this data. The contact C…N is very close to unity (E_{CN} = 0.93), and there is a weak interaction between these atoms. The ER also proved the supramolecular association of the crystal is confirmed by the strong interactions of O…H and N…H with E_{OH} = 1.42 and E_{NH} = 1.41, respectively; the Cl…H (E_{HCl} = 1.48) interaction also contributes to the additional stability of the association.

Table 2.10: Enrichment ratio (ER) of compound **1.3D**

Atoms	**H**	**C**	**N**	**O**	**Cl**
H	21.8	Actual contacts (%)			
C	18.2	0.4			
N	15.8	2.3	0		
O	20.7	0.7	1.7	1.4	
Cl	14.1	2.7	0.2	0	0
Surface %	56.20	12.35	10.00	12.95	8.50
H	31.6	Random contacts (%)			
C	13.9	1.5			
N	11.2	2.5	1.0		

O	14.6	3.2	2.6	1.7	
Cl	9.6	2.1	1.7	2.2	0.7
H	0.69	Enrichment ratio			
C	1.31	0.26			
N	1.41	0.93	0.00		
O	1.42	0.22	0.66	0.83	
Cl	1.48	1.29	0.12	0.00	0.00

2.5.1.5. Crystal analysis of compound 1.3E

The suitable crystal of compound **1.3E** formed in methanol at room temperature by the slow evaporation method was collected and subjected to SC-XRD data collection. The molecular structure is presented in ellipsoid style in **Figure 2.22.** The compound crystallized with cell lengths **a** = 13.5503(6) Å, **b** = 7.3621(3) Å, **c** = 14.2883(5) Å, i.e**., a ≠ b ≠ c** and cell angles $\alpha = 90°$, $\beta = 98.203(4)°$, $\gamma = 90°$, i.e., $\alpha = \gamma = 90°, \beta \neq 90°$ which indicate the crystal exhibiting a monoclinic crystal system, with space group $P2_1/c$. It contains four molecules per unit cell in the crystal packing **(Figure 2.23 (a))**. The pyridone ring is planar and exhibits a 72.96° dihedral angle with the benzene ring of the molecule. The crystal information of the compound is summarized in **Table 2.11.**

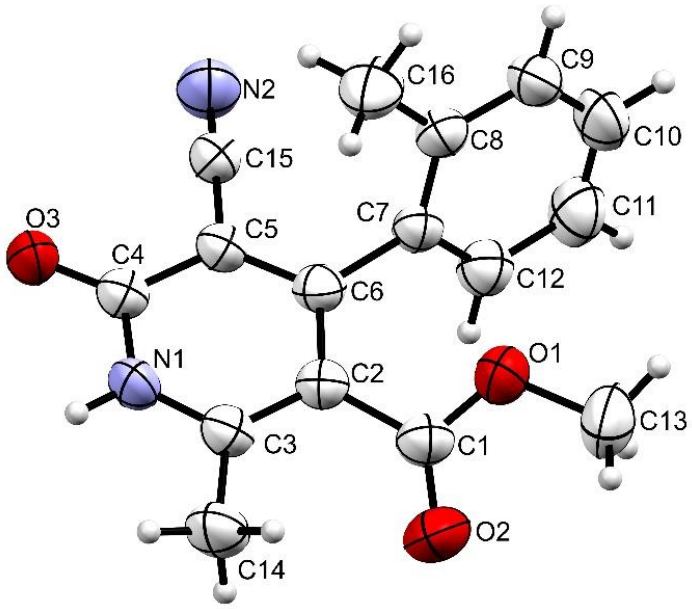

Figure 2.22: ORTEP of compound **1.3E**

Table 2.11: Crystal data compounds **1.3E**, **1.3F**, and **1.3G**

Compound	**1.3E**	**1.3F**	**1.3G**
Identification code	2222470	2222461	2222463
Empirical formula	C16H14N2O3	C16H14N2O4	C16H14N2O4
Formula weight	282.29	298.29	298.29
Temperature (K)	293(2)	293(2)	293(2)
Crystal system	monoclinic	monoclinic	triclinic
Space group	$P2_1/c$	I2/a	P-1
a/Å	13.5503(6)	16.5188(5)	8.9977(4)
b/Å	7.3621(3)	8.2318(2)	11.6901(4)
c/Å	14.2883(5)	22.6502(8)	16.0378(7)
α/°	90	90	70.114(4)
β/°	98.203(4)	108.935(3)	87.197(3)
γ/°	90	90	67.931(4)
Volume ($Å^3$)	1410.80(10)	2913.30(16)	1464.07(12)
Z	4	8	4
ρ (calcg/cm^3)	1.329	1.36	1.353
μ (mm^{-1})	0.093	0.099	0.099
F(000)	592	1248	624
Crystal size (mm^3)	0.15 × 0.13 × 0.09	0.18 × 0.16 × 0.14	0.25 × 0.23 × 0.21
Radiation	MoKα (λ = 0.71073)	MoKα (λ = 0.71073)	MoKα (λ = 0.71073)
2Θ range for data collection (°)	6.758 to 54.79	6.992 to 54.738	6.652 to 54.782
Index ranges	-15 ≤ h ≤ 17, -8 ≤ k ≤ 9, -17 ≤ l ≤ 17	-20 ≤ h ≤ 20, -10 ≤ k ≤ 10, -29 ≤ l ≤ 27	-11 ≤ h ≤ 11, -15 ≤ k ≤ 14, -20 ≤ l ≤ 17
Reflections collected	11048	15052	19008
Independent reflections	2990 [Rint = 0.0349, Rsigma = 0.0371]	3113 [Rint = 0.0310, Rsigma = 0.0256]	6219 [Rint = 0.0369, Rsigma = 0.0451]
Data/restraints/parameters	2990/0/193	3113/0/202	6219/0/403
Goodness-of-fit on F^2	1.073	1.07	1.055
Final R indexes [I>=2σ (I)]	R1 = 0.0502, wR2 = 0.1280	R1 = 0.0438, wR2 = 0.1211	R1 = 0.0658, wR2 = 0.1851
Final R indexes [all data]	R1 = 0.0785, wR2 = 0.1468	R1 = 0.0548, wR2 = 0.1297	R1 = 0.1058, wR2 = 0.2238
Largest diff. peak/hole/e $Å^{-3}$	0.17/-0.21	0.27/-0.20	0.47/-0.26

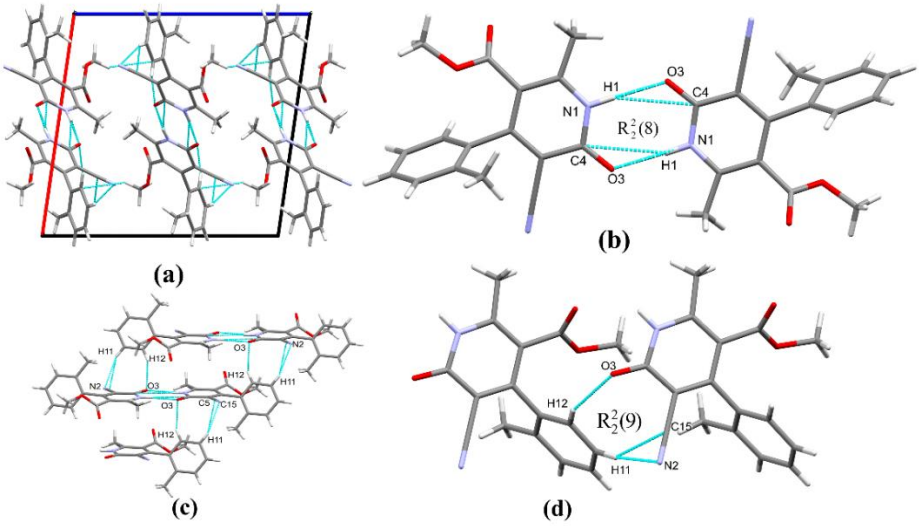

Figure 2.23: (a) packing diagram along b-axis, (b) H-bonding dimerized molecule showing graph set, (c) interlayer interactions, (d) C-H…O and C-H…N interactions showing graph set, in compound **1.3E**

Supramolecular framework of compound 1.3E: The molecular association of compound **1.3E** displays a strong non-covalent N-H…O bond, which strongly reinforces the dimerization of the molecule to form an asymmetric dimer. This interaction of N1-H1…O3 from the amide moiety of the pyridone ring with a back donation from another molecule forms a $R_2^2(8)$ graph set with a distance of 1.915 Å and bond angle of 172.84° through a hydrogen atom **(Figure 2.23 (b))**. Hydrogen H1 also interacts with C4 of the carbonyl carbon at a distance of 2.818 Å, strengthening the association of the molecules. The benzenoid hydrogen H11 bifurcated to interact with the nitrile group through carbon and nitrogen atom at a distance of 2.881 Å and 2.74 Å, respectively, and bond angles of 146.65° and 161.32°, respectively. The other benzenoid hydrogen H12 interacts with the carbonyl oxygen from the pyridone ring through C12-H12…O3 with a distance of 2.619 Å and bond angle of 152.38° help the association of molecules and interlink the layers of the molecule **(Figure 2.23 (c))**.

Thus, these C11-H11…N2 and C12-H12…O3 from the bifurcated oxygen O3 form a graph set notation $R_2^2(9)$ **(Figure 2.23 (d))**. Moreover, the hydrogen from the ester group forms C13-H13A…Cg (where Cg is centroid) and C13-H13C…Cg interaction with a benzenoid ring at a distance of 3.334 Å and 3.479 Å acts as an additional force in bringing the molecules to form a supramolecular network **(Figure**

2.24). Then, C14-H14C…Cg and lone pair…π interaction of O2…Cg with a distance of 3.091 Å and 3.827 Å, respectively, to strengthen the crystal packing of the molecule. The non-covalent interactions in compound **1.3E** are listed in **Table 2.12.**

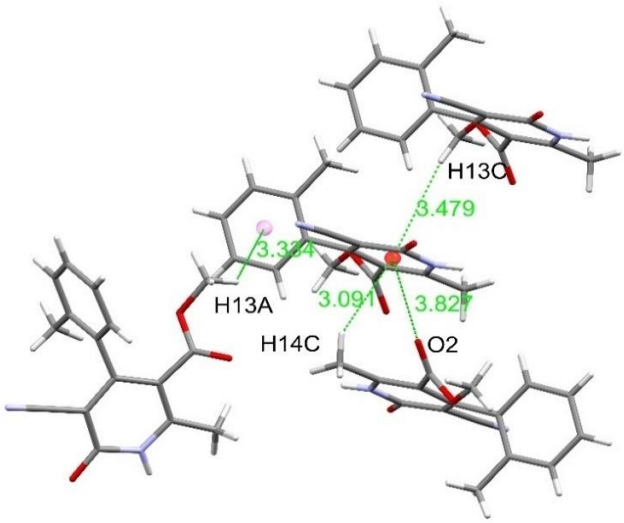

Figure 2.24: C-H…π interaction in compound **1.3E**

Table 2.12: Hydrogen bond and other interactions in compound **1.3E**

Donor-H...Acceptor	D – H, Å	H...A, Å	D...A, Å	D - H...A,°
N1-H1….O3	0.860	1.915	1.771	172.84
N1-H1….C4	0.860	2.818	3.617	155.38
C12-H12…O3	0.930	2.619	3.470	152.38
C11-H11…N2	0.930	2.740	3.633	161.32
C11-H11…C15	0.930	2.881	3.693	146.65
C13-H13A...π(C7-C12)	0.960	3.334	3.954	124.18
C13-H13C...π(N1C2-C6)		3.479		
C14-H14C…π(N1C2-C6)		3.091		
Other interaction				
O2…π(N1C2-C6)		3.827		
Intramolecular contact				
C14-H14…O2	0.960	2.700	2.952	95.59
C13-H13A…O2	0.960	2.583	2.636	82.53
C13-H13C…O2	0.960	2.620	2.636	80.44
C16-H16A…C15	0.960	2.846	3.411	118.58
O1...π(C7-C12)		3.321		
C16-H16C...π(N1C2-C6)	0.960	3.281	3.754	112.46
C14-H14…C1	0.960	2.731	2.977	95.24

Hirshfeld surface analysis of compound 1.3E: The intermolecular interaction involved in the crystal packing of compound **1.3E** is investigated in the same way as in previous molecules using crystal explorer. The Hirshfeld surface projected over the d_{norm} in the range -0.6531 Å to 1.2601 Å disseminates the characteristic packing of the compound **1.3E (Figure 2.25 (a) & (b))**. The bright red spots on the Hirshfeld surface are due to closed van der Waals (vdW) contacts such as N-H…O hydrogen bond interactions, which form an asymmetric dimer of the molecules. The weak non-classical hydrogen bond like C-H…O interactions appear in a smaller pale red-colored spot on the Hirshfeld surface.

The relative percentage contribution of the non-covalent interactions to the Hirshfeld surface is represented by the 2D fingerprint plot of the compound **(Figure 2.25(c)).** From this figure, O…H, N…H, and C…H shows a pair of spikes, where the upper and lower spikes indicate the donor and acceptor character of the atom, respectively. The percentage contribution of the intermolecular interactions from the 2D fingerprint plots are H…H(41.0%), O…H(20.1%), N…H(15.5%), C…H(17.7%), O…N(1.7%), O…O(1.2%), C…N(1.6%), O…C(0.8%) and C…C(0.4%). The O…H/H…O contacts with $d_i + d_e \approx 1.75$ Å contribute 20.1% to the total Hirshfeld surface. It indicates the crucial intermolecular weak interactions like N-H…O and C-H…O contributions in the crystal packing.

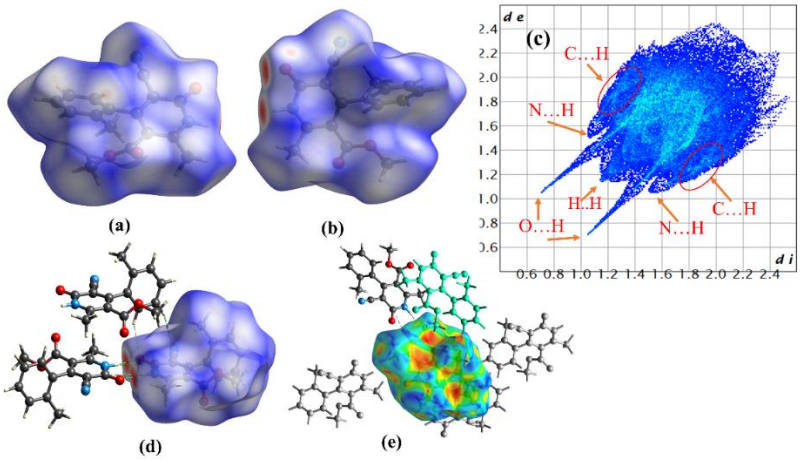

Figure 2.25: (a) and (b) Hirshfeld surface d_{norm} both side view, (c) 2D fingerprint plots showing H…H, O…H, C…H, and N…H interactions, (d) non-covalent hydrogen bond interactions, (e) C-H…π interactions, in compound **1.3E**

Furthermore, the N…H/H…N contact with $d_i + d_e \approx 2.6$ Å amounting to 15.5% indicates the presence of C-H…N interaction. C…H/H…C contact with $d_i + d_e \approx 2.75$ Å contribute relative contribution amounting to 17.7%, shows the presence of C-H…π interactions as it decomposed within the C…H contacts, and they occupy the same region in the 2D fingerprint plots region. There are no π-π stacking interactions in the molecule, which is confirmed by less contribution of C…C(0.4%) contacts.

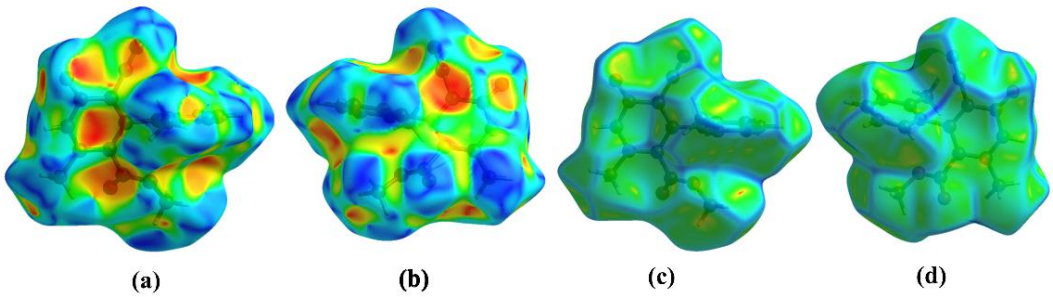

Figure 2.26: (a) and (b) Shape index both side view, (c) and (d) curvedness both side view, in compound **1.3E**

The shape index and curvedness plots of the Hirshfeld surface also reveal the various weak intermolecular interactions in compound **1.3E (Figure 2.26 (a) & (b)).** The shape index of the compound shows there is no complementary pair of red and blue colors, which proves there are no π-π interactions. The yellowish-red color concave region represents weak intermolecular interactions in the crystal packing. The curvedness plot **(Figure 2.26 (c) & (d))** illustrates there is no flat green region to confirm the absence of stacking interaction. The red-yellow and yellow spots on the curvedness plots indicate strong hydrogen bonds and weak interactions in the crystal.

The enrichment ratio (ER) is calculated from the Hirshfeld surface analysis of the interatomic contacts between pairs of interacting atoms X and Y. The ER value given in **Table 2.13** indicates that O…H, N…H, and C…H contacts are favored with $E_{OH} = 1.19$, $E_{NH} = 1.22$, and $E_{CH} = 1.25$, respectively. All these enrichment ratios agree with the interactions explained in the supramolecular framework and Hirshfeld surface analysis. The C…H contacts value indicates the presence of C-H…C and N-H…C interactions apart from C-H…π interactions.

Table 2.13: Enrichment ratio (ER) of compound **1.3E**

Atoms	**H**	**C**	**N**	**O**
H	41	Actual contacts (%)		
C	17.7	0.4		
N	15.5	1.6	0	
O	20.1	0.8	1.7	1.2
Surface (%)	67.65	10.45	9.40	12.50
H	45.8	Random contacts (%)		
C	14.1	1.1		
N	12.7	2.0	0.9	
O	16.9	2.6	2.4	1.6
H	0.90	Enrichment ratio		
C	1.25	0.37		
N	1.22	0.81	0.00	
O	1.19	0.31	0.72	0.77

2.5.1.6. Crystal analysis of compound 1.3F

Compound **1.3F** was crystallized in ethanol at room temperature by the slow evaporation method. The compound crystal is analyzed by single-crystal X-ray diffraction, and the perspective of compound **1.3F** ORTEP diagram is shown in **Figure 2.27**, and the crystallography details are given in **Table 2.11.** The compound crystallized with cell lengths **a** = 16.5188(5) Å, **b** = 8.2318(2) Å, **c** = 22.6502(8) Å, where **a** ≠ **b** ≠ **c**, and cell angles α = 90°, β = 108.935(3)°, γ = 90°, here **α = β =90°, γ ≠ 90°,** this indicates that the compound is exhibiting a monoclinic crystal system with I2/a space group. The unit cell of the crystals contains eight molecules **(Figure 2.28 (a))**. The crystal compound **1.3F** contains a planar 2-pyridone ring and benzenoid ring, and these two planar aromatic rings exhibited a dihedral angle of 51.67°.

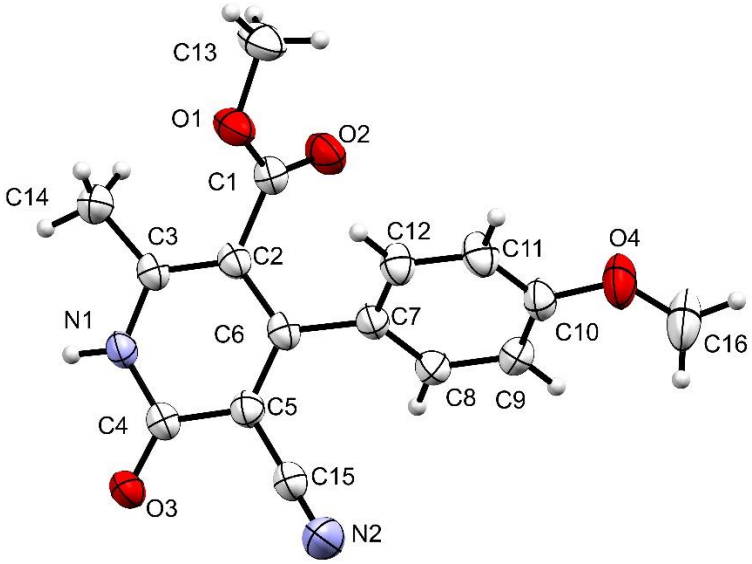

Figure 2.27: ORTEP of compound **1.3F**

Supramolecular framework analysis of compound 1.3F: The molecular packing of compound **1.3F** displayed a strong intermolecular N-H…O hydrogen bonding that assists the self-assembly of the 2-pyridone molecule in forming supramolecular architectures. It includes an asymmetric dimer containing the $R_2^2(8)$ graph set notation with a distance of 1.939 Å. The N2 donor of the molecule donates a proton to the oxygen O3 acceptor atom of the carbonyl group of another molecule, which in turn donates back its proton from the N2 atom to carbonyl O3. C-H contributes the additional reinforcement in the supramolecular assembly of compound **1.3F** through C-H…O and C-H…N, and C-H…π non-covalent interactions. The O3 of carbonyl acts as a bifurcated acceptor. It forms C-H…O and N-H…O interactions with bond distances of 2.688 Å and 1.939 Å, respectively, and their bond angles on the H atom are 143.66° and 177.64°, respectively, resulting in the formation of $R_2^1(6)$ graph set notation **(Figure 2.28 (b))**. The crystal hydrogen bond and other interactions of compound **1.3F** is summarized in **Table 2.14.**

Table 2.14: Hydrogen bond and other interactions in compound **1.3F**

Donor-H...Acceptor	D – H, Å	H...A, Å	D...A, Å	D - H...A,°
N1-H1….O3	0.860	1.939	2.799	177.64
N1-H1….C4	0.860	2.839	3.645	156.95

C14-H14…O3	0.960	2.688	3.507	143.66
C16-H16C…N2	0.960	2.683	3.499	143.21
C11-H11…C4	0.930	2.883	3.652	140.83
C13-H13C…O2	0.960	2.695	3.658	175.41
C13-H13B...π(N1C2-C6)	0.960	3.614	4.040	109.72
C13-H13C...π(N1C2-C6)	0.960	3.557	4.040	113.71
C14-H14A...π(C7-C12)	0.960	2.781	3.689	158.10
C11-H11…π(N1C2-C6)	0.930	3.456	4.349	161.77
C14-H14A…C10	0.960	2.732	3.562	145.14
Other contacts				
O2….C3		3.111		
Intramolecular contact				
C14-H14A…C1	0.960	2.809	2.973	90.31
C13-H13B…O2	0.960	2.660	2.687	81.23
C13-H13C…O2	0.960	2.658	2.687	81.33
C14-H14B…O1	0.960	2.715	3.058	101.69
C12-H12…C1	0.930	2.707	3.007	99.68
C8-H8…C15	0.930	2.752	3.039	98.92

However, carbonyl oxygen (O2) from the ester group interacts with the hydrogen from ester methyl C13-H13C…O2 with a distance of 2.695 Å and bond angle of 175.41° **(Figure 2.28 (d))**. The electron-withdrawing nature of the O3 oxygen atom enhances the ability of the C4 atom to act as a proton acceptor. It leads to a non-classical hydrogen bond between benzenoid H11 and the C4 atom, stabilizing the molecular packing. Another non-covalent interaction from methoxy hydrogen to the N2 at a distance of 2.683 Å links the interlayer of the supramolecular structure **(Figure 2.28 (c))**. Furthermore, the C-H…π interactions are observed as C13-H13B…Cg (Cg is centroid), C13-H13C…Cg, C14-H14A…Cg and C11-H11…Cg with a distance of 3.614 Å, 3.557 Å, 2.781 Å, and 3.456 Å, respectively, reinforce the supramolecular association of the molecules **(Figure 2.29 (a))**. The weak π…π stacking interactions are found by the pyridone ring interactions with a distance of 4.147 Å and the benzene ring with a distance of 4.808 Å, helping the stability of the molecular association **(Figure 2.29 (b))**.

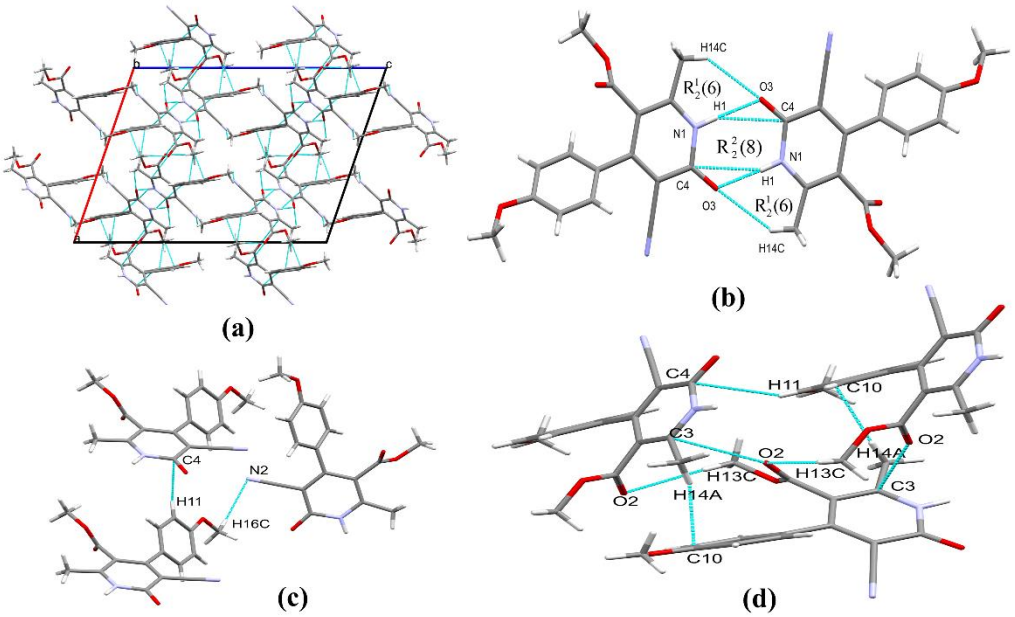

Figure 2.28: (a) crystal packing along the b-axis, (b) H-bonding to form dimer molecule, (c) and (d) C-H…O and other interactions in compound **1.3F**

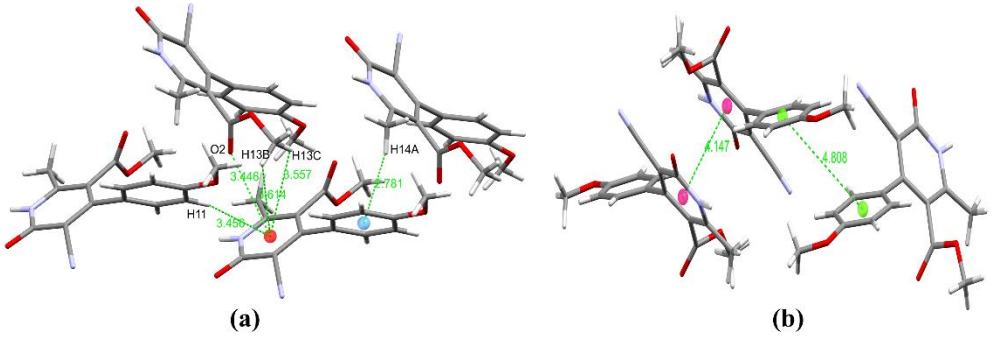

Figure 2.29: (a) C-H…π and lone pair …π interactions, (b) π … π interactions, in compound **1.3F**

Hirshfeld surface analysis of compound 1.3F: The intermolecular interaction involved in the crystal packing of compound **1.3F** is investigated in the same method as in previous crystals using Hirshfeld surface (HS) and fingerprint plots. The Hirshfeld surface mapped over the d_{norm} in the range -0.6348 to 1.3799 Å is displayed in **Figures 2.30 (a) and (b).** The region of bright red spots corresponds to short contacts, which are more dominant intermolecular N-H…O interactions. An area of lighter red spots indicates the weaker C-H…O interactions. The white and blue regions of the d-norm plot indicate the more extended interactions of the molecules. The 2D fingerprint plots of compound **1.3F (Figure 2.30 (c))** suggest that O…H, N…H, C…H, and H…H contacts appear as a pair of sharp spikes. In a 2D fingerprint plot, the upper

spike (di<de) and lower spike (di > de) shows the donor and acceptor nature of the atoms, respectively. The O---H/H---O contacts with di + de ≈ 1.75 Å have 23.7% of the total contacts. These O…H/H…O contacts play crucial intermolecular interactions like N-H…O and C-H…O interactions in the crystal packing. The N…H/H…N contact with di + de ≈ 2.6 amounting to 16.5% indicates C-H…N interactions in the molecular association. Moreover, the C…H/H…C contacts with di + de ≈ 2.6 Å contribute 19.7%, indicating the presence of C-H…π aromatic interactions. These are the composition of C…H contacts and appear as a pair of characteristic wings in the 2d fingerprint plot. H…H contacts contribute 31.6%, with di + de ≈ 2.4 Å constituting the highest contributions of the Hirshfeld surface. The interaction of the Hirshfeld surface with the other compound is represented in **Figure 2.30 (d)** and **(e)**.

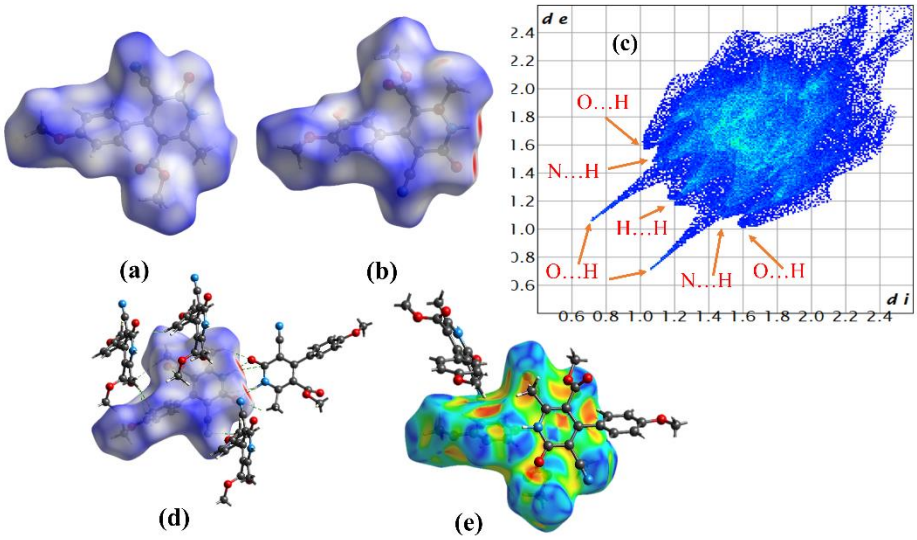

Figure 2.30: (a) and (b) Hirshfeld surface d_{norm} both side view, (c) 2D fingerprint plot showing H…H, O…H, N…H and C…H interactions, (d) non-covalent H-bonding, (e) π … π and C-H…π interactions, in compound **1.3F**

The Hirshfeld surface shape index **(Figure 2.31 (a) & (b))** is mapped over -1 Å to 1 Å for compound **1.3F**, showing a complimentary pair of red and blue triangles around the 2-pyridone aromatic ring surface, which indicates the weak π…π stacking interactions, and increase the stability of the supramolecule. The yellowish-red colored concave regions around the surface specify the acceptor region where weak C-H…π and O…π (lone pair…π) interactions are present in the supramolecular structure. The Curvedness plots of the Hirshfeld surface **(Figure 2.31 (c) & (d))** illustrate that there

is a small green flat region was found over the pyridone ring and confirmed the presence of the π…π stacking interactions.

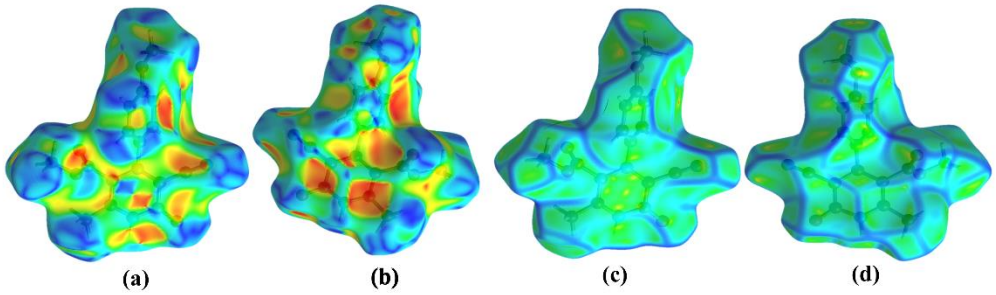

Figure 2.31: (a) and (b) Hirshfeld surface shape index both side view, (c) and (d) Curvedness both side view, in compound **1.3F**

The enrichment ratio (ER) is calculated from the Hirshfeld surface analysis of the interatomic contacts between pairs of interacting atoms. The ER values of compound **1.3F** given in **Table 2.15** indicate that the N…H/H…N, O…H/H…O, and C…H/H…O contacts are favored with ER values greater than unity. It is shown that H atoms generate more than 61% of the total molecular surface, while N atoms are the lowest, being only about 8.95%. The N…H and O…H interactions are favorable and significantly contribute to stabilizing the crystal system's self-assembly. Although the H…H contacts are the most abundant interactions in the system, the ER of H…H interaction (E_{HH} = 0.83) is impoverished and disfavored. The ER value of C…C contact is 0.98, which is lower than unity, but the presence of π…π stacking interaction was shown in the shape index plot. This stacking interaction is weak with a distance of more than 4 Å.

Table 2.15: Enrichment ratio (ER) of compound **1.3F**

Atoms	**H**	**C**	**N**	**O**
H	31.6	Actual contacts (%)		
C	19.7	1.8		
N	16.5	0	0	
O	23.7	3.8	1.4	1.3
Surface (%)	61.55	13.55	8.95	15.75
H	37.9	Random contacts (%)		
C	16.7	1.8		
N	11.0	2.4	0.8	
O	19.4	4.3	2.8	2.5

H	0.83	Enrichment ratio		
C	1.18	0.98		
N	1.50	0.00	0.00	
O	1.22	0.89	0.50	0.52

2.5.1.7. Crystal analysis of compound 1.3G

The compound **1.3G** crystallized in ethanol at room temperature by slow solvent evaporation. The crystal is collected and subjected to SCXRD analysis, and it crystallizes in two independent symmetries (**A** and **B**) in the asymmetric unit, Z' = 2 **(Figure 2.32).**

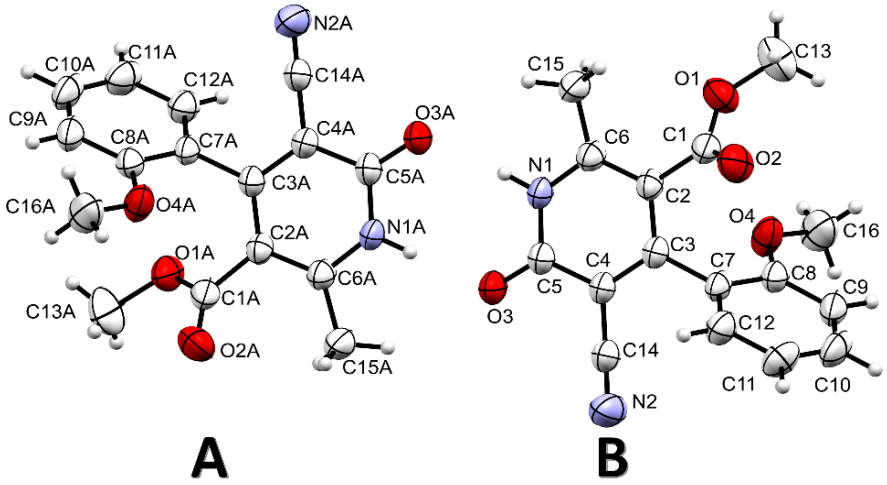

Figure 2.32: ORTEP of compound **1.3G**

The compound **1.3G** crystallizes in the triclinic crystal system of the $P\bar{1}$ space group. The crystal packing has four molecules per unit cell **(Figure 2.34 (a))**. Carbon skeletons of molecules **A** and **B** are structurally similar, but there is a difference in the spatial orientation of atoms in the 3D of the molecule. These differences can be visualized from the overlay diagram of the two structures. Molecules **A** and **B** have a root-mean-square deviation (RMSD) value of 2.051 Å **(Figure 2.33).** Besides this, there is a slight difference in the crystal packing of the system. **A** and **B** molecules in a two-dimensional (2D) hydrogen bond network differ in hydrogen bonding patterns.

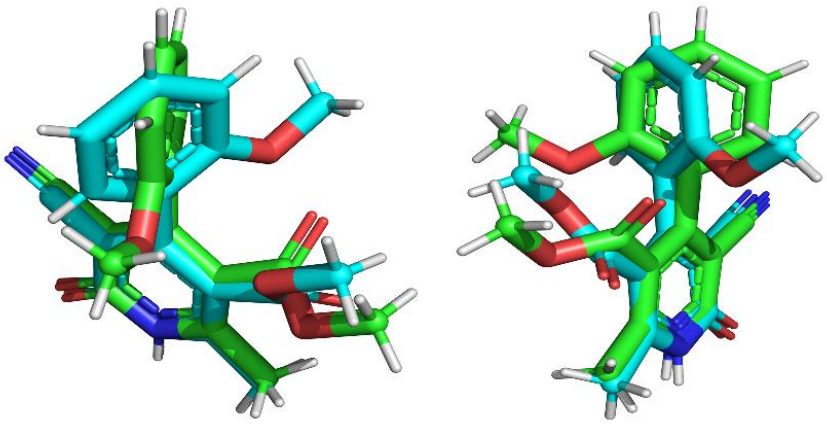

Figure 2.33: Overlay diagram of molecules **A**(green) and **B**(blue) of compound **1.3G**

The pyridone ring in molecules **A** and **B** are planar, and their planes have a dihedral angle of 5.24°; the dihedral angle of the planes of the benzene ring in molecules **A** and **B** is found to be 3.27°. The planes of the pyridone ring and benzene ring in molecules **A** and **B** are respectively 60.54° and 66.50°. The compound crystallized in cell length of **a** = 8.9977(4) Å, **b** = 11.6901(4) Å, **c** = 16.0378(7) Å, that is **a** ≠ **b** ≠ **c**, and cell angles are α = 70.114(4)°, β = 87.197(3)°, γ = 67.931(4)°. The crystallographic information of compound **1.3G** is summarized in **Table 2.11.**

Supramolecular framework of compound 1.3G: The compound **1.3G** experiences a strong hydrogen bond between the two symmetry-independent molecules **A** and **B**. These two symmetry-independent molecules have excellent hydrogen bond acceptors N and O, but the classical hydrogen bond is not found beyond the formation of the dimer. Non-classical hydrogen bond interactions with weak C-H donors are found in molecules **A** and **B**. C-H…O, N-H…O, and C-H…π weak interactions play a vital role in forming a widespread supramolecular framework. A robust non-covalent interaction N1-H1 associates the two symmetry-independent molecules N1-H1…O3A, N1A-H1A…O3, and N1A-H1A…C5 of the carbonyl carbon of amide part of pyridone ring with a distance of 1.997 Å, 1.917 Å and 2.837 Å respectively, which form a graph set notation of $R_2^2(8)$ and $R_1^2(3)$ respectively **(Figure 2.34 (b))**.

Table 2.16: Hydrogen bond and other interactions of compound **1.3G**

Donor-H...Acceptor	D – H, Å	H...A, Å	D...A, Å	D - H...A,°
N1-H1…O3A	0.860	1.997	2.854	173.81
N1A-H1A…O3	0.860	1.917	2.773	73.41
N1A-H1A…C5	0.860	2.837	3.460	155.98
C10-H10….N2	0.930	2.725	3.406	130.75
C16-H16B…N2	0.960	2.536	3.446	158.14
C16A-H16D…N2A	0.961	2.568	3.432	149.81
C13A-H13E…O2	0.960	2.572	3.370	140.74
C12A-H12A…O2	0.930	2.658	3.563	164.54
C15-H15A…O2A	0.960	2.608	3.292	128.42
C15A-H15E…C8	0.960	2.880	3.731	148.25
C15-H15A…π(N1AC2A-C6A)	0.960	3.657	4.573	160.54
C15-H15B...π(C7A-C12A)	0.960	3.079	3.911	145.80
C15A-H15E…π(C7-C12)	0.960	3.172	4.081	158.50
C11A-H11A...π(N1C2-C6)	0.960	3.363	3.886	117.90
C13A-H13D…π(C7-C12)	0.960	3.427	3.988	119.50
C15A-H15F...π(N1C2-C7)	0.960	3.633	4.553	161.44
Intramolecular contact				
C13-H13B…O2	0.960	2.375	2.616	93.57
C15-H15B…O1	0.960	2.582	2.945	102.59
C15A-H15E…O2A	0.960	2.624	2.892	96.32
C13A-H13F…O2A	0.960	2.295	2.637	100.02
C1-O2...π(C7-C12)	1.197	3.474	3.832	98.18
O1A...π(C7A-C12A)		3.375		

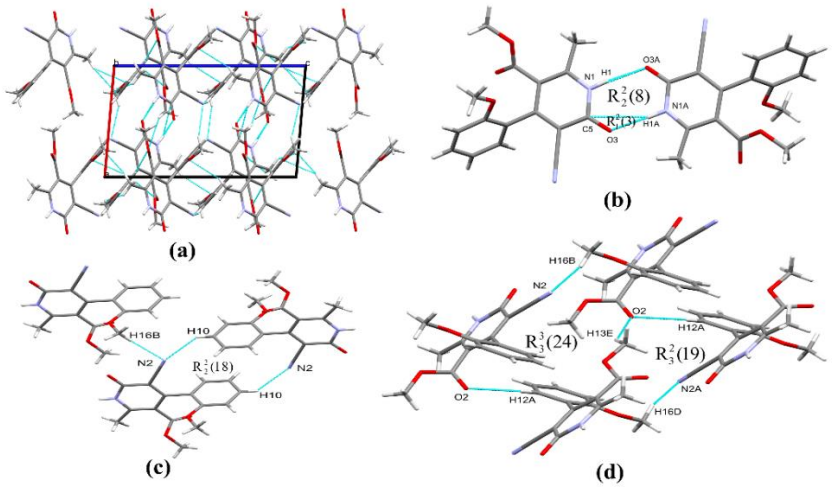

Figure 2.34: (a) Crystal packing, (b) N-H…O interactions between molecules **A** and **B**, (c) & (d) C-H…O and C-H…N interactions and graph set, in compound **1.3G**

Molecules **B** exhibit the interactions of C10-H10…N2 and C16-H16B…N2, having a distance of 2.725 Å and 2.536 Å, respectively, and bond angles of 130.75° and 158.14°, respectively. C15-H15A…O2A donor-acceptor interactions between molecules **B** to **A** helped in the association of the molecules with a distance of 2.608 Å. The interactions C16A-H16D…N2A in molecule **A** with a distance of 2.568 Å and angle through H atom 149.81° assemble the molecules. Further, the intermolecular interactions C13A-H13E…O2 and C12A-H12A…O2, from molecule **A** to **B** through the bifurcated acceptor O2 in molecule **B** with a distance of 2.572 Å and 2.658 Å, which interlink the molecules. For molecule **B**, the C-H…π interactions with the pyridone and benzene rings are C15-H15A…Cg and C15-H15B…Cg with a distance of 3.657 Å and 3.079 Å, respectively (where Cg is the centroid of the ring). Similarly, C-H…π interactions with benzene rings are C15A-H15E…Cg and C13A-H13D…Cg with a distance of 3.172 Å and 3.427 Å, respectively, found in molecule **A**. In contrast, those involving the pyridone ring in C-H…π interactions are C11A-H11A…Cg and C15A-H15F…Cg with a distance of 3.363 Å and 3.633 Å, respectively **(Figure 2.35)**. The intermolecular graph sets $R_2^2(18)$ stabilized the $R_3^3(24)$ crystal $R_3^2(19)$ through C-H…O and C-H…N interactions **(Figure 2.34 (c) & (d))**. It is important in the supramolecular framework of compound **1.3G**. The crystal hydrogen bond and other interactions of compound **1.3G** is summarized in **Table 2.16.**

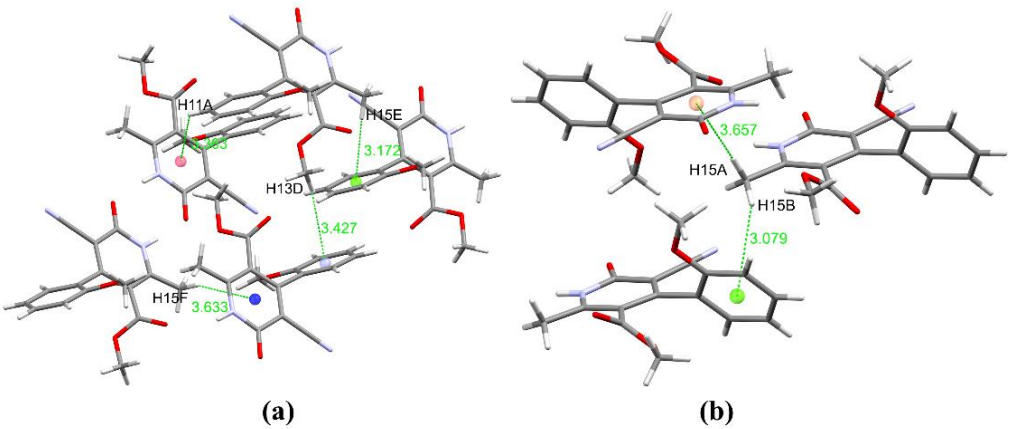

Figure 2.35: C-H…π interactions in compound **1.3G**

Hirshfeld surface analysis of compound 1.3G: Hirshfeld surface analysis validates intermolecular interactions in the crystal structure discussed in the

supramolecular framework. Hirshfeld's surface of both **A** & **B** of the two symmetry-independent molecules is somewhat distinct because the interatomic connections and relative percentage contribution of those contacts differ slightly between the two molecules.

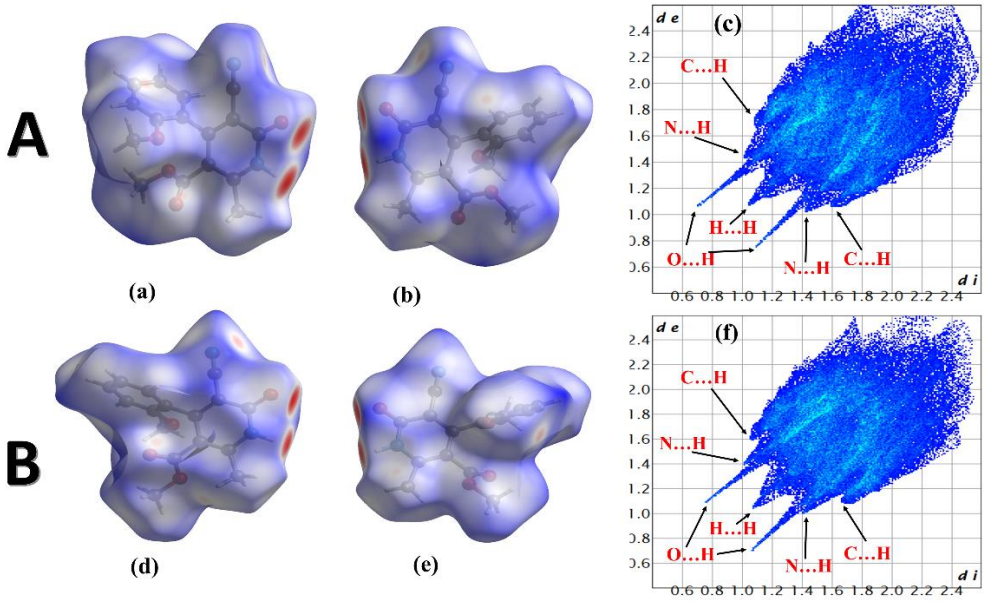

Figure 2.36: (a) & (b) Hirshfeld surface d_{norm} both side view of molecule **A** (c) 2D fingerprint of molecule **A** (d) & (e) Hirshfeld surface d_{norm} both side view of molecule **B** (f) 2D fingerprint of molecule **B**, of compound **1.3G**

The Hirshfeld surfaces of molecules **A** and **B** are mapped over d_{norm} in the range -0.6526 Å to 1.5817 Å and -0.6523 Å to 1.5724 Å, respectively, and presented in the figure **(Figure 2.36 (a), (b), (d) and (e))**. The bright red spots on the Hirshfeld surfaces correspond to the short interactions of N-H…O, while the lighter red spots indicate the C-H…O interactions. The 2D fingerprint plots of both the molecules **(Figure 2.36 (c) & (f))** illustrate the absence of a yellowish-red bin and lack of weak π…π stacking interactions. The O…H/H…O, N…H/H…N, and C…H/H…C contacts appear as a pair of spikes in a 2D fingerprint plot, where the upper and lower spikes represent the donor & acceptor nature of the atoms, respectively. O…H/H…O contacts with di + de ≈ 1.85 Å and di + de ≈ 1.75 Å of compound **A** have a percentage contribution of 28.2% and 26.9%, respectively, to the total Hirshfeld surface. These contacts imply a significant intermolecular interaction of the type N-H…O and C-H…O in the crystal structure. The fingerprint plots of C…H/H…C contacts appear as a pair of broad short

spikes with a percentage contribution of 22.8%, at di + de ≈ 2.7 Å for both compound **A** and **B**. 2D fingerprint plots also indicate the presence of C-H…π interactions, as they are fragmented into C…H/H…C contacts and present in a pair of characteristic wings.

The shape index plots and the curvedness plots of the 3D Hirshfeld surface revealed weak intermolecular interactions in molecules **A** and **B**. In the shape index surface, red and blue regions represent the acceptor and donor properties of the molecule, respectively **(Figure 2.37 (a), (b), (e) & (f)).** The yellowish-red color concave region indicates the presence of weak interactions, and the absence of adjacent red and blue triangles confirmed no π…π stacking in the crystal structure. On the curvedness surface, the red-yellow color spots show strong interactions in the crystal, which was found to be more in molecule **A** compared with molecule **B (Figure 2.37 (c), (d), (g) & (h)).**

The enrichment ratio (ER) helps examine the favorable contacts of the molecules. The ER value is calculated from the interatomic contacts between pairs of interacting atoms of the Hirshfeld surface analysis. The enrichment ratio values of compound **1.3G** are given in **Table 2.17**, indicating that H atoms generate more than 63% of the molecular surface in molecules **A** and **B**. Still, the contribution of N is the least, being only 8.75 – 9.2% in both molecules.

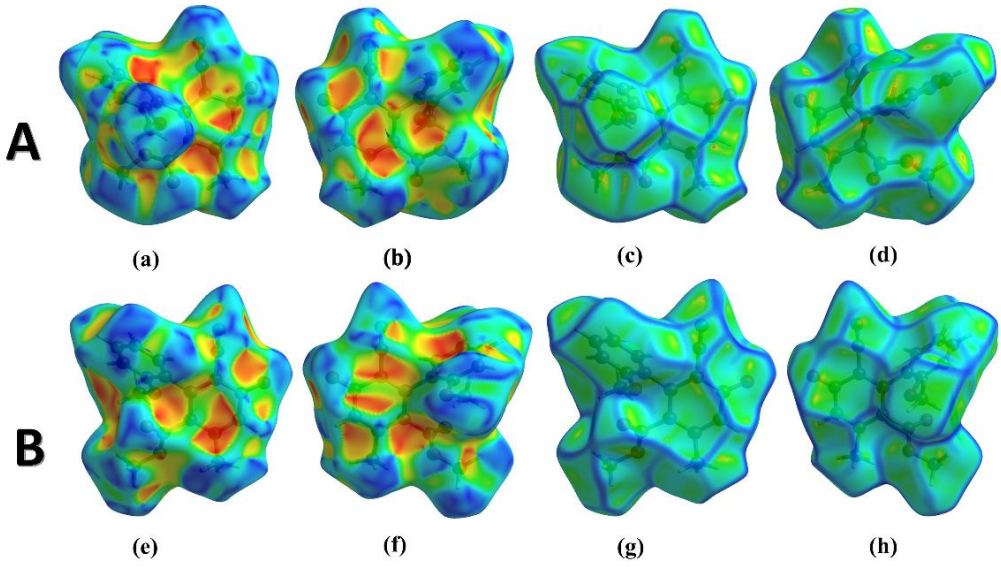

Figure 2.37: (a) (b) (e) and (f) Hirshfeld surface shape index, (c) (d) (g) and (h) Curvedness, both side view, of compound **1.3G**

Furthermore, the ER value of O…H (E_{OH} = 1.43, 1.46) and N…H (E_{NH} = 1.42, 1.42) is more significant than one in both **A** and **B** molecules. It shows that N…H and O…H interactions are favorable and important contributors to stabilizing supramolecular molecules. The C…H interaction is highly favored (E_{CH} = 1.50, 1.48) in molecules **A** and **B**. These values illustrate the presence of C-H…π interactions in both molecules, which helped in the association of the molecules to form a supramolecular framework. Although the H…H contacts are the most abundant interactions (more than 63%) in molecules **A** and **B**, the ER of the H…H interactions (E_{HH} = 0.75, 0.75) is impoverished and disfavored.

Table 2.17: Enrichment ratio (ER) of compound **1.3G**

Actual contacts %			**S_x**		**Random Contacts (%)**		**Enrichment Ratio (ER)**	
	A	**B**	**A**	**B**	**A**	**B**	A	B
H…H	30.4	31.3	63.80	64.60	40.70	41.73	0.75	0.75
C…C	0.4	0.4	11.95	11.90	1.43	1.42	0.28	0.28
N…N	0	0	8.75	9.20	0.77	0.85	0.00	0.00
O…O	0.4	0	15.50	14.30	2.40	2.04	0.17	0.00
C…H	22.8	22.8			15.25	15.37	1.50	1.48
O…H	28.2	26.9			19.78	18.48	1.43	1.46
N…H	15.8	16.9			11.17	11.89	1.42	1.42
C…O	0.3	0.2			3.70	3.40	0.08	0.06
O…N	1.7	1.5			2.71	2.63	0.63	0.57
C…N	0	0			2.09	0.00	0.00	0.00

2.5.1.8. Crystal analysis of compound 1.3H

The crystal of compound **1.3H** was prepared in the slow evaporation of ethanol at room temperature. The crystal suitable for SCXRD was analyzed and the compound crystallized in two symmetrically independent molecules in the symmetric unit Z'=0.25 **(Figure 2.38 (a))**.

Compound **1.3H** crystallized in the space group of $P2_1/n$ and monoclinic crystal system, there is only one molecule per unit cell **(Figure 2.39 (a))**. The two molecules of the symmetrically independent compound are superimposable. Still, their arrangement of the atoms in the space upon overlay shows the root-mean-square

deviation (RMSD) value of 2.932 Å **(Figure 2.38 (b))**. The two molecules are slightly tilted, while their molecular structure is similar.

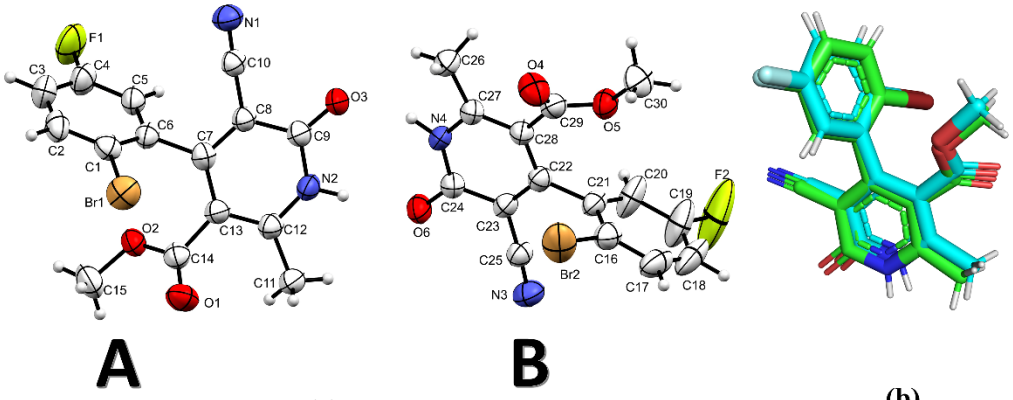

Figure 2.38: (a) ORTEP diagram, (b) Overlay diagram **A**(green) and **B**(cyan), of compound **1.3H**

The symmetrically independent molecules **A** and **B** are formed by the two-ring system. The pyridone ring planes of molecules **A** and **B** display a dihedral angle of 35.40°, but the dihedral angle of the two phenyl ring planes is closer at 7.38°. The dihedral angle of the two rings in the symmetry-independent molecule **A** is 63.35°, and the dihedral angle of molecule **B** is 77.94° in the crystal. These dihedral angles indicate the molecular shape of the two molecules is slightly different in their spatial orientation. The compound **1.3H** crystallized in cell length **a** = 8.5099(6) Å, **b** = 19.1449(16) Å, and **c** = 18.6472(12) Å, i.e., **a** ≠ **b** ≠ **c**, and the cell angles are **α** = 90°, **β** = 99.036(5)°, and **γ** = 90°, i.e., **α** = **γ** ≠ **β**. The crystal occupies a volume of 3000.3(4) $Å^3$; the crystal information was tabulated in **Table 2.18.**

Table 2.18: Crystal data of compounds **1.3H** and **1.3I**

Compound	**1.3H**	**1.3I**
Identification code	2219751	2219753
Empirical formula	C_{15} H_{10} Br_1 F_1 N_2 O_3	C_{16} H_{14} N_2 O_3
Formula weight	2921.28	282.29
Temperature (K)	293(2)	293(2)
Crystal system	monoclinic	orthorhombic
Space group	P 2_1/n	P n a 2_1
a/Å	8.5099(6)	15.8698(9)
b/Å	19.1449(16)	8.8389(5)
c/Å	18.6472(12)	20.5941(10)

α/°	90	90
β/°	99.036(5)	90
γ/°	90	90
Volume (Å^3)	3000.3(4)	2888.8(3)
Z	1	8
ρ (calcg/cm^3)	1.617	1.298
μ (mm^{-1})	2.764	0.091
F(000)	1456	1184
Crystal size (mm^3)		
Radiation	MoKα (λ = 0.71073)	MoKα (λ = 0.71073)
2Θ range for data collection (°)	3.068 to 58.7982	3.956 to 56.03
Index ranges	-9 ≤ h ≤ 11, -26 ≤ k ≤ 26, -25 ≤ l ≤ 25	-20 ≤ h ≤ 20, -11 ≤ k ≤ 11, -26 ≤ l ≤ 26
Reflections collected	25974	21224
Independent reflections	8192[Rint=0.0923, Rsigma=0.0951]	6867[Rint=0.0466, Rsigma=0.0648]
Data/restraints/parameters	8192/0/4009	6867/1/394
Goodness-of-fit on F^2	1.003	0.951
Final R indexes [I>=2σ (I)]	R1=0.0678, wR2=0.1430	R1=0.0579, wR2=0.1400
Final R indexes [all data]	R1=0.1795, wR2=0.1849	R1=0.0838, wR2=0.1550
Largest diff. peak/hole/e Å^{-3}	1.485/-1.80	0.48/-0.23

Supramolecular framework of compound 1.3H: The symmetrically independent molecules are held together by a strong hydrogen bond N4-H4…O3 and N2-H2…O6 through the carbonyl carbon atom of pyridone at 1.980 Å and 1.984 Å, respectively. Forming the graph set $R_2^2(8)$ at the asymmetric point **(Figure 2.39 (b))**. The interaction C11-H11B…N1 and C26-H26B…N3 of the cyano nitrogen in molecules **A** and **B**, respectively, formed graph sets of $R_4^4(20)$ and $R_4^4(24)$ with the other interactions assist in the molecular assembly. The carbonyl oxygen of the ester group from molecules **A** and **B** formed a hydrogen bond with phenyl hydrogen H18 and H2A, respectively, at 2.704 Å and 2.577 Å. We also observed the hydrogen bond interactions with the fluorine atom of molecule **A** with H11C of molecule **A** and H30B of molecule **B** at 2.616 Å and 2.588 Å, respectively. The other fluorine atom of molecule **B** exhibits a hydrogen bond with H15B of molecule **A** at 2.630 Å, which supports the molecular assembly of the compound. Moreover, the bromine atom of

molecule **B** also exhibits a hydrogen bond with 15B of molecule **A** at 2.978 Å. The hydrogen bond and other non-covalent interactions are shown in **Table 2.19.**

Table 2.19: Hydrogen bonds and other interactions in **1.3H**

Donor-H...Acceptor	D – H, Å	H...A, Å	D...A, Å	D - H...A,°
N4-H4…O3	0.891	1.980	2.827	158.22
N2-H2…O6	0.893	1.948	2.839	174.76
N2-H2…C24	0.893	2.818	3.635	152.78
C11-H11B…N1	0.960	2.589	3.532	167.53
C11-H11C…F1	0.961	2.616	3.335	131.85
C5-H5…N3	0.930	2.612	3.353	137.07
C15-H15A…F2	0.960	2.630	0.381	135.32
C18-H18…O1	0.930	2.704	3.298	122.48
C30-H30B….F1	0.960	2.588	3.257	126.90
C20-H20…N1	0.929	2.582	3.398	146.83
C2-H2A…O4	0.929	2.577	3.069	113.48
C15-H15B…Br2	0.956	2.978	3.573	121.50
C26-H26B…N3	0.960	2.636	3.564	162.55
C3-H3...π(N4C22-C24C27C28)	0.931	3.582	4.256	131.40
C11-H11B…π(N4C22-C24C27C28)	0.960	3.987	4.609	125.37
C30-H30A…π(C16-C21)	0.960	3.467	4.314	148.34
Other contact				
O3…N4		2.827		
N2…O6		2.835		
N1…C14		3.182		
C2…O4		3.069		
C29…N3		3.248		
N1…π(N4C22-C24C27C28)		3.311		
N3...π(N4C22-C24C27C28)		3.332		
Intramolecular				
C15-H15B…O1	0.959	2.563	2.657	84.98
C15-H15C...O1	0.960	2.670	2.657	78.81
C11-H11B…O1	0.960	2.656	2.922	96.32
C30-H30A…O4	0.960	2.713	2.647	75.79
C30-H30C…O4	0.960	2.513	2.647	87.24
C26-H26C…O4	0.960	2.676	2.920	95.00

Br1…C13		3.483		
Br1…C14		3.279		
Br2…C28		3.540		
Br2…C29		3.534		

Therefore, the hydrogen bond C20-H20…N1 in the crystal structure show an $R_4^4(26)$ graph set and $R_2^2(17)$ graph set with other interaction of C30-H30B…F1 to stabilized the structure **(Figure 2.39 (d))**. The interaction C11-H11B…N1 also exhibits the graph set $R_4^4(29)$. Moreover, C15-H15B…Br2 interaction in the compound exhibit the graph set $R_4^4(28)$, and with the other interaction of C2-H2A…O4 generates the graph set $R_2^2(16)$ to the molecular association in the crystal **(Figure 2.39 (c))**. The intermolecular interaction of C11-H11B…N1 and C26-H26B…N3 in the crystal compound exhibit the graph set involving four molecules $R_4^4(20)$ and $R_4^4(24)$ **(Figure 2.40 (b))**.

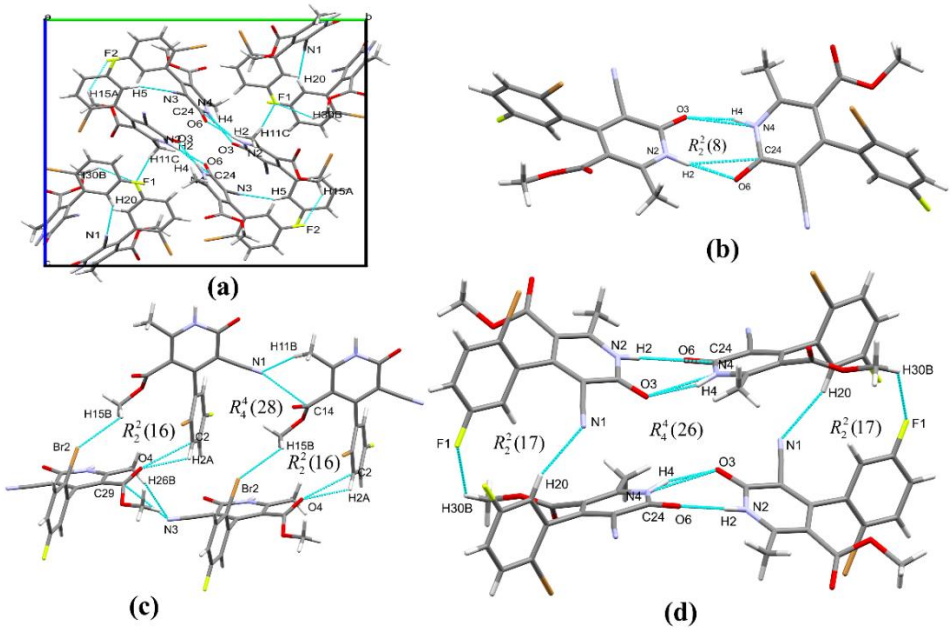

Figure 2.39: (a) packing of **1.3H** along the b-axis (b) interaction of two symmetry-independent molecules (c) & (d) graph sets representing an association of molecules in compound **1.3H**

Therefore, the C-H…π interaction of the compound **1.3H** was found in the pyridone ring of molecule **B** with C3-H3…Cg (where Cg is centroid) and C11-H11B…Cg of molecule **A** through a distance of 3.582Å and 3.987Å, respectively. Thus, C30-H30A…Cg from the same molecule **B** at 3.467Å results in the interaction

of molecule **B**, and then, C15-H15C…Cg from molecule **A** at 3.635 Å. Moreover, the lone pair-π interaction present between nitrogen N1 of molecule **A** and the pyridone ring of molecule **B**, and N3 of molecule **B** with the pyridone ring of molecule **A** at 3.311 Å and 3.332 Å, respectively **(Figure 2.40 (c))**.

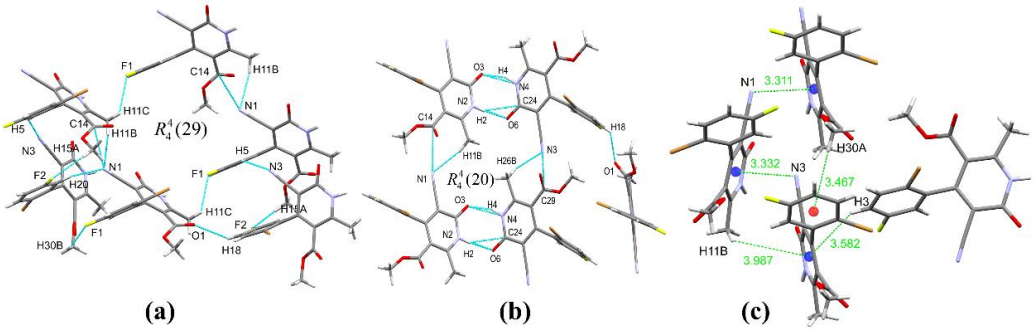

Figure 2.40: (a) and (b) non-covalent interactions illustrating graph set, (c) C-H…π and lone pair-π interaction, in compound **1.3H**

Hirshfeld surface analysis of compound 1.3H: The Hirshfeld surface analysis of compound **1.3H** was performed to know the outline of the crystal packing types and molecular interactions in the structure. The Hirshfeld surface was mapping over d_{norm} in the range of -0.6552 to 1.4068 Å in molecule **A** and the range of -0.5995 to 1.3454 Å in molecule **B (Figure 2.41 (a), (b), (d) & (e))**. The bright red spot at the dimerization point of the symmetrically independent molecules represents the strong hydrogen bond interaction. Another white dull red spot represents the weak interaction present in the compound.

The 2D fingerprint plot of the symmetry independent crystal **1.3H** display O…H/H…O, N…H/H…N, F…H/H…F, Br…H/H…Br, and H…H interaction of molecules **A** and **B** in **Figure 2.41 (c)** & **(f)**, respectively. The two different molecules exhibit a slightly different distribution of interaction. The percentage distribution of interaction in molecule **A** are O…H(22.2%), H…H(18.1%), C…H(13.7%), N…H(10.8%), Br…H(10.6%), F…H(9.2%), etc., and in molecule **B** are O…H(21.9%), H…H(16.4%), Br…H(14.4%), C…H(12.2%), N…H(11.3%), F…H(10.0%), C…N(2.9%), etc., respectively. A pair of spikes (d_i, d_e) ≈ (0.75, 1.1) in molecule **A** and (d_i, d_e) ≈ (0.75, 1.15) in molecule **B** denote the O…H/H…O interactions. The N…H/H…N interaction in molecule **A** spike is found below the main body but in molecule **B**, it is found above the O…H spike. The Br…H/H…Br

interactions are also clearly shown in the 2D fingerprint plot. In both plots, we are not having the wing-like structure, which indicates the absence of the π-π stacking interaction in the compound.

The compound **1.3H**-shaped index mapping displays the region of blue and yellow-red on the surface, which shows the donor and acceptor properties of the surface **(Figure 2.42 (a), (b), (e) & (f))**. The adjacent red and the blue triangle was not found on the surface and proved the absence of the π-π stacking interaction. Curvedness mapping of the compound showed that there was no green planarity present in the molecule. It also confirmed the π-π stacking interaction was absent in the symmetrically independent molecules **(Figure 2.42 (c), (d), (g) & (h))**.

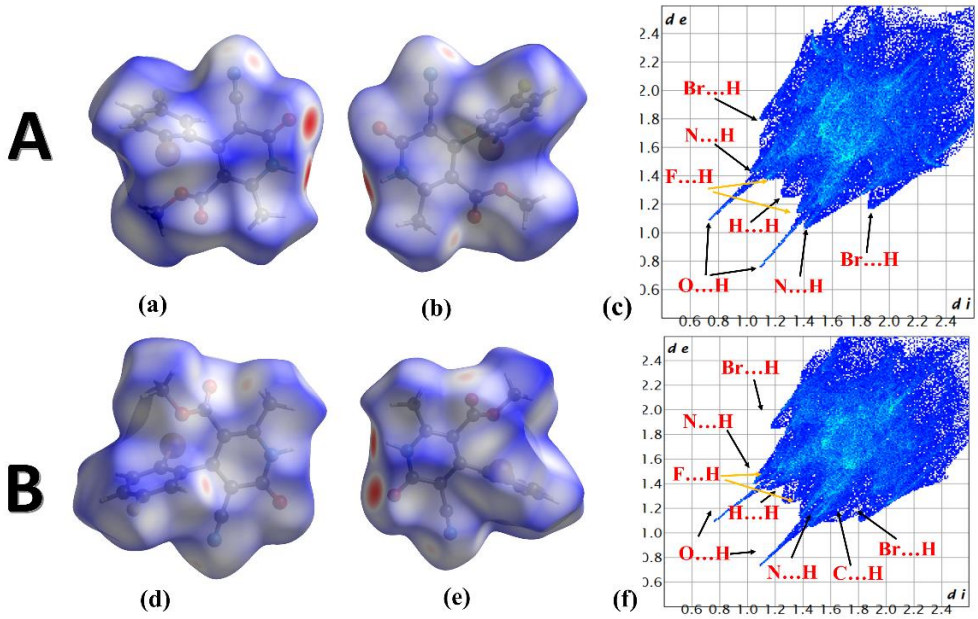

Figure 2.41: (a) & (b) Hirshfeld surface d_{norm} of molecule **A** (c) 2D fingerprint plot of **A** (d) & (e) Hirshfeld surface d_{norm} of molecule **B** (f) 2D fingerprint plot of **B**, of compound **1.3H**

Weak interactions present in the molecules of the compound from Hirshfeld surface calculation support the weak non-covalent interactions in the supramolecular framework. The C-H…O, N-H…O, and other interactions found in the molecule around a 3.4 Å radius are displayed in **Figure 2.43.**

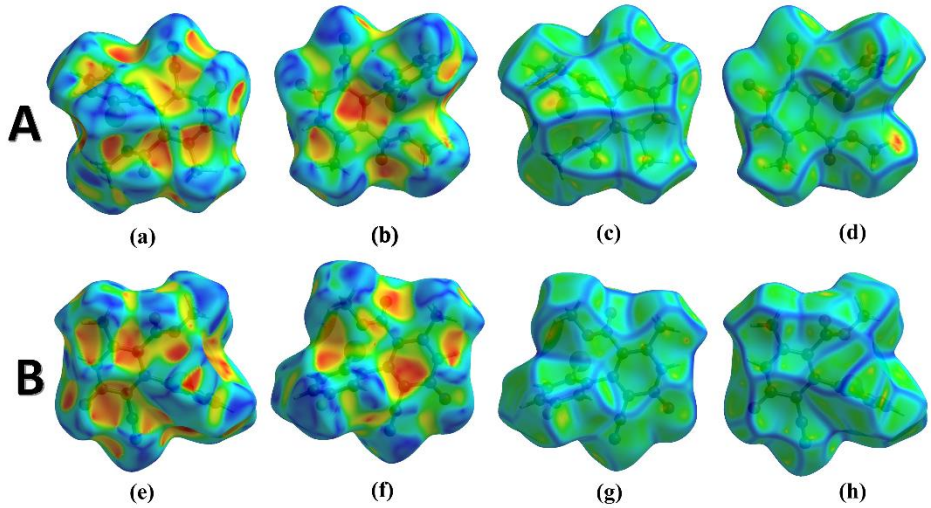

Figure 2.42: (a), (b), (e), (f) Shape index of molecule **A & B**; (c), (d), (g), (h) Curvedness of molecule **A & B,** of compound **1.3H**

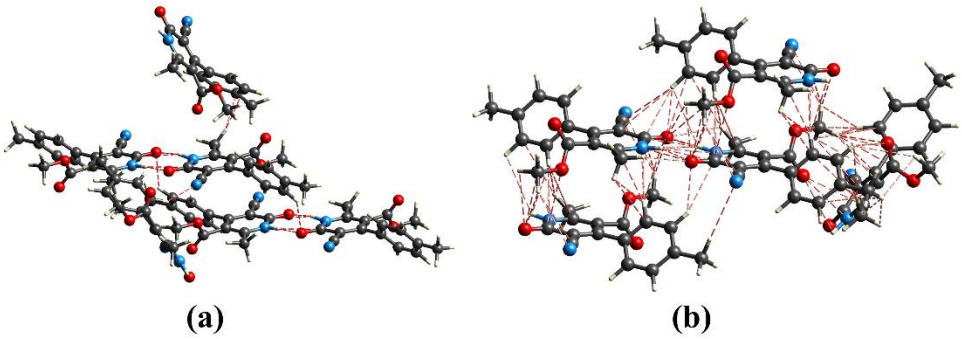

Figure 2.43: (a) & (b) weak non-covalent interaction of compound **1.3H**

The enrichment ratio of compound **1.3H** is calculated from the Hirshfeld surface interatomic contact of the interacting atoms, tabulated in **Table 2.20**. The enrichment ratio of C…C contact in both the molecules is more than unity, and it is enriched, which is estimated by the interaction between the pyridone carbon and other carbon atoms. The interaction between F…F and Br…Br also has more than unity in the ER, as they occupy the total surface of 7.15% to 9.80%. The molecule enrichment ratio of molecule **A** is slightly greater than that of molecule **B**, but both molecules show enriched interaction. The interaction of hydrogen atoms with all other atoms also exhibits an enrichment ratio more than unity, as they interact in the supramolecular framework. The ER of C…N interaction also supports the molecule's carbon–nitrogen interaction. The interaction C…F is also fruitful as it has an ER value of 1.13 in molecule **A**, but molecule **B** has only 0.89. The enrichment ratio of the compound

shows that the two symmetrically independent molecules are slightly different in their interaction with one another.

Table 2.20: Enrichment ratios of compound **1.3H** (**A** and **B**)

Actual contacts (%)			**S_x**		**Random Contacts (%)**		**Enrichment Ratio (ER)**	
	A	**B**	**A**	**B**	**A**	**B**	**A**	**B**
H…H	18.1	16.4	51.35	51.30	26.37	26.32	0.69	0.62
C…C	1.8	1.7	12.25	11.00	1.50	1.21	1.20	1.40
N…N	0.4	0.4	8.65	8.25	0.75	0.68	0.53	0.59
O…O	0	0	12.65	12.30	1.60	1.51	0.00	0.00
F…F	0.9	0.9	7.60	7.15	0.58	0.51	1.56	1.76
Br…Br	1.4	1.8	7.50	9.80	0.56	0.96	2.49	1.87
C…H	13.7	12.2			12.58	11.29	1.09	1.08
O…H	22.2	21.9			12.99	12.62	1.71	1.74
N…H	10.8	11.3			8.88	8.46	1.22	1.33
F…H	9.2	10			7.81	7.34	1.18	1.36
Br…H	10.6	14.4			7.70	10.05	1.38	1.43
C…O	0.6	0.6			3.10	2.71	0.19	0.22
O…N	1.5	1.2			2.19	2.03	0.69	0.59
O…F	0.9	0.8			1.92	1.76	0.47	0.45
O…Br	0.1	0.1			1.90	2.41	0.05	0.04
C…N	3	2.9			2.12	1.82	1.42	1.60
N…F	1.20	0.30			1.31	1.18	0.91	0.25
N…Br	0	0			1.30	1.62	0.00	0.00
F…Br	0	0			1.14	1.40	0.00	0.00
C…F	2.1	1.4			1.86	1.57	1.13	0.89
C…Br	1.5	1.5			1.84	2.16	0.82	0.70

2.5.1.9. Crystal analysis of compound 1.3I

Compound **1.3I** is crystallized in ethanol by slow evaporation at room temperature. The crystal collected was subjected to SCXRD analysis and crystallized in two symmetrically independent molecules (**A** and **B**) in the asymmetric unit **(Figure 2.44 (a))** $Z' = 2$.

Compound **1.3I** crystallized in the $Pna2_1$ space group with an orthorhombic crystal system, and there are eight molecules in a unit cell **(Figure 2.45 (a))**. The two molecules are virtually superimposable. While they have the same structural

arrangement, the superimposition of molecules **A** and **B** shows the root-mean-square deviation (RMSD) value of 2.601 Å **(Figure 2.44 (b))**. The molecular arrangement of atoms in space slightly deviates from one another. Besides this, they exhibited slightly different hydrogen bond networks in their crystal packing.

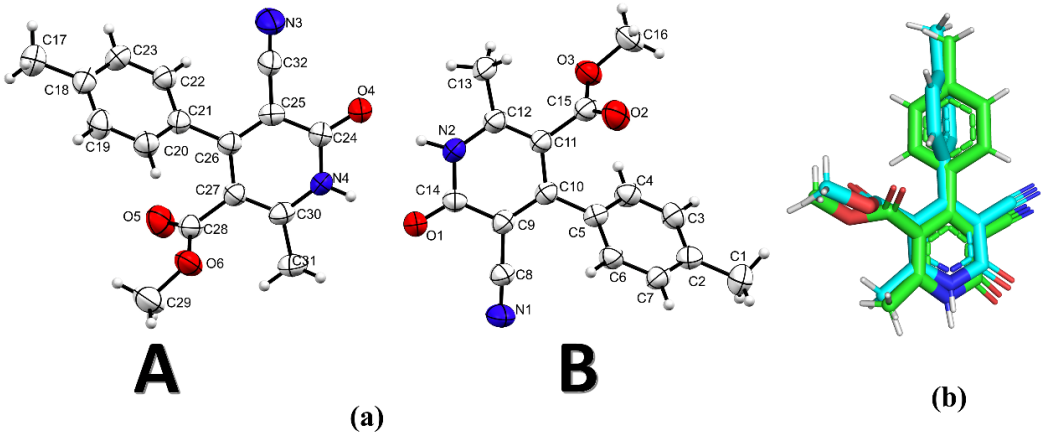

Figure 2.44: (a) ORTEP diagram, (b) overlay diagram **A**(green) **B**(cyan), of compound **1.3I**

The pyridone ring in both the molecules is planar, and their planes show that the dihedral angle of these two planes is 3.33°, and the dihedral angle between the toluene ring planes of the two molecules is 4.35°. The molecule contains two ring systems with different ring planes, which are found to have dihedral angles of 52.00° in molecule **A**, and 50.55° in molecule **B**. The compound **1.3I** crystallized in the cell length **a** = 15.8698(9) Å, **b** = 8.8389(5) Å, and **c** = 20.5941(10) Å, i.e., **a** ≠ **b** ≠ **c**, and the cell angles are **α** = 90°, **β** = 90°, and **γ** = 90°. The volume of the crystal is 2888.8(3) $Å^3$, and the crystallographic information of the compound **1.3I** is shown in **Table 2.18.**

Supramolecular framework of compound 1.3I: The two symmetrically independent molecules are held together by a strong hydrogen bonding between N4-H4…O1 and N2-H2…O4 through the carbonyl oxygen atom of the pyridone at 1.914 Å and 1.850 Å, respectively **(Figure 2.45 (b))**. It forms the $R_2^2(8)$ graph set. In addition, the lone pair interactions of the ring nitrogen atom (N2, N4) and carbonyl oxygen (O1, O4) stabilized the dimer structure. Carbonyl oxygen O1 and O4 act as bifurcated acceptors, and they interact with the phenyl ring hydrogen H3 and H19 at 2.600 Å and 2.663 Å, respectively **(Figure 2.45 (c))**, illustrates the graph set $R_4^2(20)$ involving four molecules to stabilize the supramolecular assembly of the compound. The interaction of nitrogen atoms N1 and N3 of the cyano group in both the molecules

B and **A** with phenyl hydrogen H22 and H6 at 2.695 Å and 2.580 Å can help in the association of the molecules and formed $R_4^4(22)$ **(Figure 2.45 (d))** and $R_5^5(27)$ **(Figure 2.46 (a))** graph sets with other interactions in the crystal.

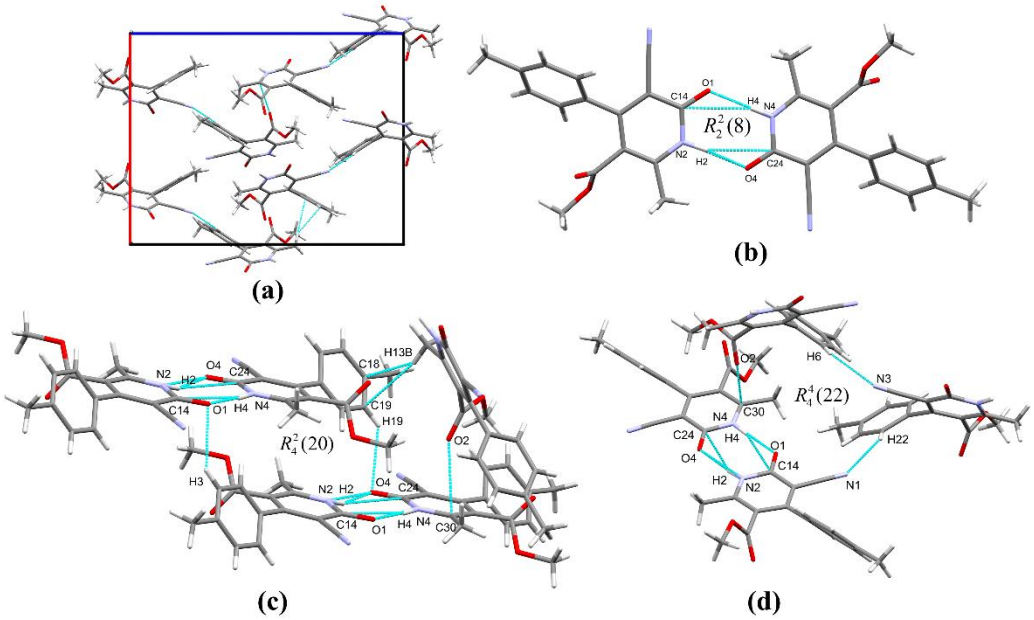

Figure 2.45: (a) Crystal packing, (b) N-H…O interactions between molecules **A** and **B** (c) & (d) C-H…O and C-H…N interactions and graph set in compound **1.3I**

Moreover, there were also C-H…π interactions in the crystal structure involving the pyridone and benzene aromatic rings. The pyridone aromatic ring of molecule **B** formed a hydrogen bond C29-H29C…Cg (where Cg is centroid) and C20-H20…Cg with molecule **A** at 3.415 Å and 3.456 Å, respectively, and thus the pyridone ring of molecule **A** formed a hydrogen bond with C16-H16…Cg of molecule **B** at 3.285 Å. Then, the phenyl ring of molecule **B** also exhibited the C-H…π interactions C31-H31A…Cg and C17-H17A…Cg with molecule **A**. The carbonyl oxygen atoms O5 and O2 of molecules **A** and **B** also interact with the pyridone ring of molecules **B** and **A** through a lone pair…π interaction at 3.347 Å and 3.299 Å, respectively **(Figure 2.46 (b))**. All these interactions indicate that the two symmetry-independent molecules demonstrate the different spatial arrangements in the space. The hydrogen bonding and other inter-molecular and intramolecular interactions are shown in **Table 2.21**.

Table 2.21: Hydrogen bond and other interactions of compound **1.3I**

Donor-H...Acceptor	D – H, Å	H...A, Å	D...A, Å	D - H...A,°
N4-H4…O1	0.860	1.914	2.773	176.27
N2-H2…O4	0.973	1.850	2.788	160.78
C22-H22…N1	0.930	2.695	3.478	142.37
C3-H3…O1	0.930	2.600	3.380	141.71
C6-H6…N3	0.930	2.580	3.355	141.23
C19-H19…O4	0.930	2.663	3.402	136.77
N4-H4…C24	0.860	2.729	3.632	158.92
N2-H2…C14	0.973	2.817	3.645	156.59
C31-H31A...π(C2-C7)	0.960	2.924	3.730	142.26
C29-H29C…π(N2C14C9-C12)	0.960	3.415	3.981	119.60
C20-H20…π(N2C14C9-C12)	0.930	3.456	4.307	153.16
C13-H13B…π(C18-C23)	0.960	3.000	3.793	140.88
C17-H17A…π(C2-C7)	0.961	3.143	3.764	123.79
C16-H16B...π(N4C30C24-C27)	0.960	3.285	3.934	126.67
Other contact				
O4…N2		2.788		
N4…O1		2.773		
O2...π(N4C30C24-C27)		3.299		
O5…π(N2C14C9-C12)		3.347		
Intramolecular contact				
C16-H16B…O2	0.960	2.442	2.669	92.93
C22-H22…C32	0.930	2.675	2.997	101.12
C29-H29C…O5	0.960	2.629	2.684	82.82
C29-H29B…O5	0.960	2.688	2.684	79.42

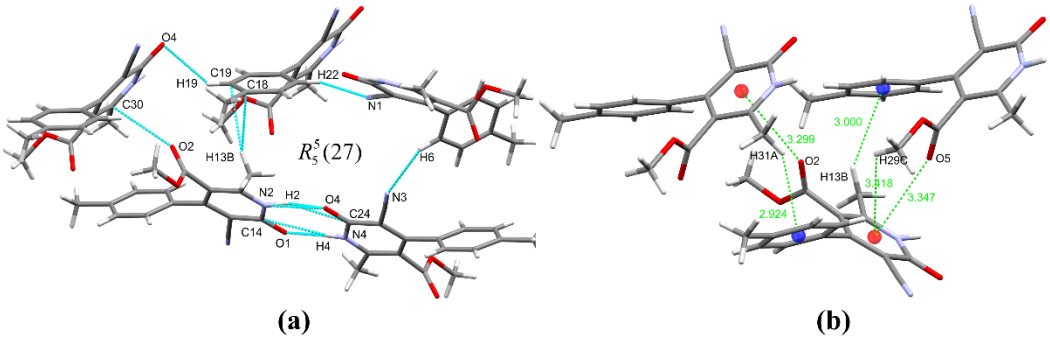

Figure 2.46: (a) Interactions showing graph set, (b) C-H…π interactions, in compound **1.3I**

Hirshfeld surface analysis of compound 1.3I: The Hirshfeld surface analysis of **1.3I** was carried out to recognize and get an outline of the packing types and inter-molecular interactions in their molecular structural features. The Hirshfeld surfaces have been mapped over d_{norm} in the range of -0.6550 to 1.2938 Å in molecule **A** and -0.6552 to 1.4068 Å in molecule **B (Figure 2.47 (a), (b), (d) & (e))**. The bright red spot at the surface of the dimerization point indicates the strong hydrogen bond interactions, and the other dull red colour represents the weak interaction of the molecule.

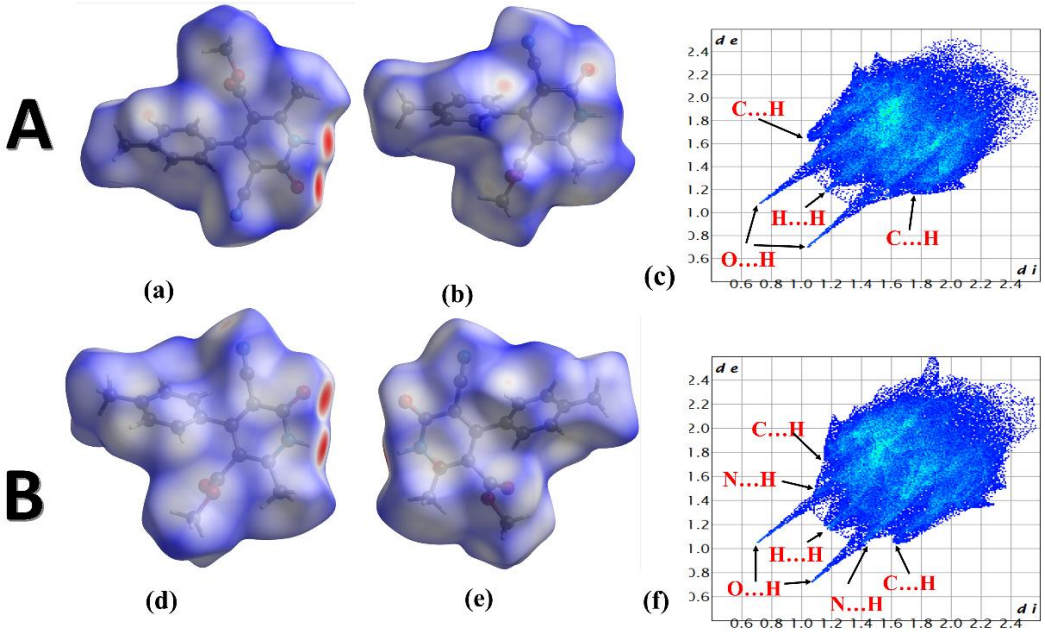

Figure 2.47: (a) & (b) Hirshfeld surface d_{norm} both side view of molecule **A** (c) 2D fingerprint of molecule **A** (d) & (e) Hirshfeld surface d_{norm} both side view of molecule **B** (f) 2D fingerprint of molecule **B**, of compound **1.3I**

The 2D fingerprint plot of compound **1.3I** depicting H…H, O…H, N…H, and C…H interaction are illustrated in **(Figure 2.47 (c) & (f))**. The two molecules of the symmetry-independent molecules **A** and **B** show slightly different interactions in the crystal compound. The percentage distribution of interactions involved in molecule **A** are H…H(35.4%), C…H(21.5%), O…H(20.3%), N…H(16.4%), C…O(4.8%), O…N(1.1%), and C…C(0.4%), and molecule **B** are H…H(34.5%), C…H(22.2%), O…H(20.8%), N…H(16.1%), C…O(4.7%), O…N(1.2%), and C…C(0.4%), respectively. A pair of spikes in (d_i, d_e) ≈ (0.7, 1.05) in molecule **A** and (d_i, d_e) ≈ (0.7, 1.05) in molecule **B** represents the O…H interactions. The N…H interactions are

shown inside the base of the O…H spikes, but C…H spikes in both the molecules display the different wing-like structures and spikes in the 2D fingerprint plot.

The shape index of compound **1.3I** represents the red-yellow and blue region, which indicates the acceptor and donor property of the surface, respectively **(Figure 2.48 (a), (b), (e) & (f))**. No adjacent red and blue triangles are present in the figure, and the π-π stacking interaction was absent in the molecules. Mapping of the curvedness of the surface of the molecules shows that there is no planarity in the compound, which indicates the information about the π-π interactions among the aromatic rings and confirms the absence of the π-π stacking interaction **(Figure 2.48 (c), (d), (g) & (h))**.

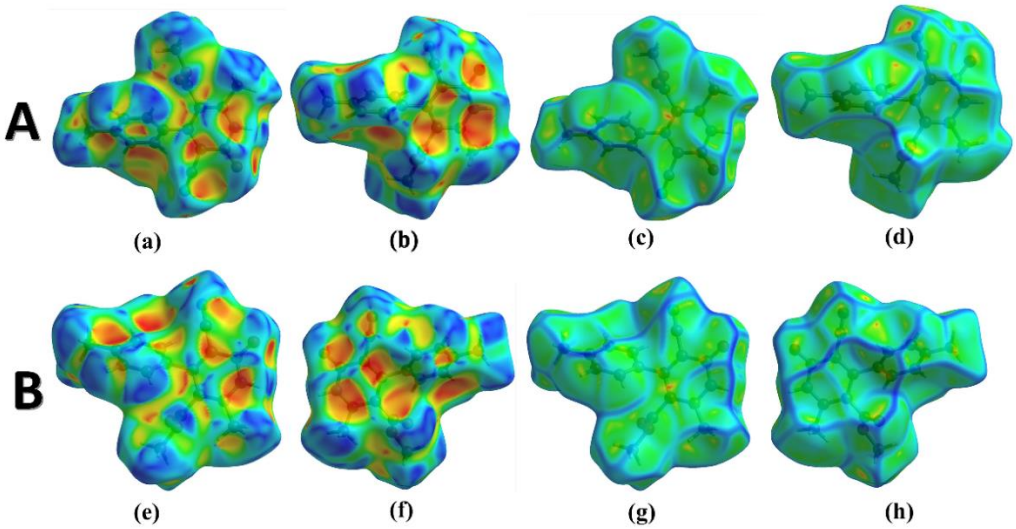

Figure 2.48: (a) (b) (e) and (f) Hirshfeld surface shape index, (c) (d) (g) and (h) Curvedness, both side view, of compound **1.3I**

The weak interactions in the molecules calculated from the Hirshfeld surface also support weak non-covalent interactions in the crystal packing. C-H…O, N-H…O, C-H…π and lone pair-π interactions around 3.4 Å radius are shown in **Figure 2.49**.

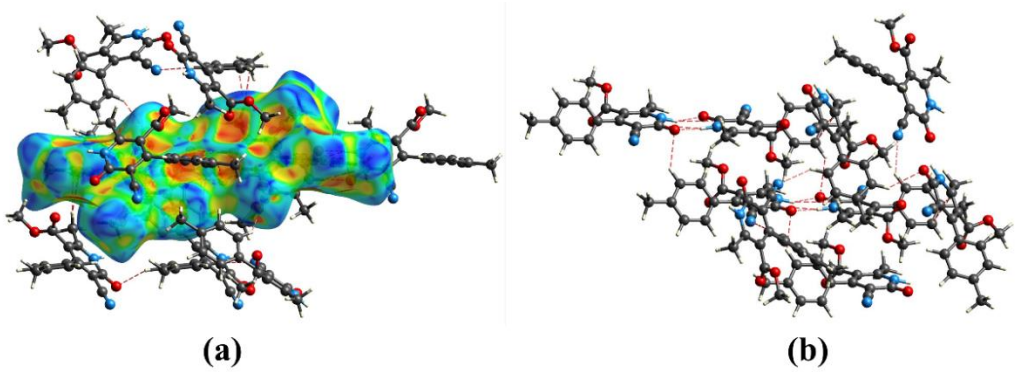

(a) (b)

Figure 2.49: Weak interactions in the radius of 3.4 Å of compound **1.3I**

The enrichment ratio of compound **1.3I** is calculated from the atomic contact of the pair of interacting atoms, tabulated in **Table 2.22**. The hydrogen atom in molecules **A** and **B** generate 64.50% and 64.05% of the total surface, respectively, but their propensity to make contacts calculated from the enrichment ratio is less than unity. C…H/H…C, O…H/H…O, and N…H/H…N contact enrichment ratio is enriched in molecule A of 1.23, 1.20, and 1.44, 1.25, 1.22, and 1.44 in molecule **B**. The C…O/O…C contact also has a 1.35 and 1.27 enrichment ratio, respectively, which proves the presence of the lone pair-π interaction between the carbonyl oxygen and the pyridone ring in the molecules **A** and **B**. The absence of the π-π stacking interaction is also confirmed in the enrichment ratio C…C contact (E_{CC} = 0.22, 0.21), which is less than unity.

Table 2.22: Enrichment ratio (ER) of compound **3.3I** (Molecule **A** and **B**)

Actual contacts (%)			**S_x**		**Random Contacts (%)**		**Enrichment Ratio (ER)**	
	A	**B**	**A**	**B**	**A**	**B**	**A**	**B**
H…H	30.4	31.3	63.80	64.60	40.70	41.73	0.75	0.75
C…C	0.4	0.4	11.95	11.90	1.43	1.42	0.28	0.28
N…N	0	0	8.75	9.20	0.77	0.85	0.00	0.00
O…O	0.4	0	15.50	14.30	2.40	2.04	0.17	0.00
C…H	22.8	22.8			15.25	15.37	1.50	1.48
O…H	28.2	26.9			19.78	18.48	1.43	1.46
N…H	15.8	16.9			11.17	11.89	1.42	1.42
C…O	0.3	0.2			3.70	3.40	0.08	0.06
O…N	1.7	1.5			2.71	2.63	0.63	0.57
C…N	0	0			2.09	0.00	0.00	0.00

2.6 Molecular docking studies of compounds 1.3A-1.3I

Kinesin spindle protein Eg5 was first identified as an mRNA-coded protein. It was precisely deadenylated and free from polysomes after egg fertilization of *Xenopus* (Le Guellec et al., 1991). The overexpression of Eg5 causes the instability of the genome in carcinogenesis and mouse model. Studies have shown that the activation of Eg5 expression has been stated in solid tumors like renal cell carcinoma (D. Sun et al., 2013), prostate cancer (Wissing et al., 2014), laryngeal squamous cell cancer (Lu et al., 2016), lung cancer (Saijo et al., 2006), pancreatic cancer (X. Sun et al., 2011), and breast cancer (Planas-Silva & Filatova, 2007). Survivin is a member of the apoptosis inhibitor of the proteins family (Ryan et al., 2009), and its expression in normal tissue is very low or undetectable (O'Connor et al., 2000). The overexpression of survivin correlates with the progression of tumors and resistance of the drug due to its key role in the formation of tumors and maintenance (Mita et al., 2008). Survivin is considered a supreme target for cancer treatment (Xiao & Li, 2015).

One of the most prominent Eg5 inhibitors, monastrol, has phenyl, methyl, and an ester group as ring substituents. A bioisostere with identical monastrol ring substituents and a standard drug milrinone heterocyclic ring scaffolds are the core structures in the 2-pyridone derivatives we synthesized in this chapter. A molecular docking study was done using AutoDockVina. The crystal structure of mitotic kinesin Eg5 and survivin enzymes were retrieved from the RSCB protein data bank (PDB id: 1X88 and 3UIH, respectively). The enzyme preparation was done using chimera by removing cofactors, co-crystallized ligands, and embedded water molecules. Then, using Autodock tool software, polar hydrogens and Kollman charges were added to the enzymes, and the file was saved in pdbqt format. Mercury software converts the titled compounds' CIF file to PDB format, and open babel converts the PDB file to PDBQT format. The grid parameters for the survivin enzyme were centered at x = -26.30, y = 1.84, z = -19.14; 31.74 Å x 25.0 Å x 23.65 Å. The Eg5 enzyme grid parameters are centered at x = 18.06, y = 24.56, z = 49.31, 18.46 Å x 21.52 Å x 21.82 Å. The crystal compounds were subjected to molecular docking with the target enzymes, and the exhaustiveness parameter for analyzing the binding affinity was set to 10 modes. The docking poses were analyzed and visualized using Discovery Studio

and PyMOL. The docking scores and amino acid residues involved in hydrogen bonding and other non-covalent interactions are tabulated in **Table 2.23.**

Table 2.23: Docking scores and residues involved in the interactions of **1.3A-1.3I**

Compounds	Docking score (kcal/mol)	Residues involved in H-bond	Residues involved in other interactions (π…anion, π…cation, π...σ, π...π, π…alkyl, and alkyl)
		EG5	
1.3A	-6.9	Glu118, Pro137	Glu116, Arg119, Ala133, Ala218
1.3B	-7.1	Pro137	Glu116, Arg119, Trp127, Ala133, Tyr211, Ala218
1.3C	-6.3		Glu116, Ile136, Leu214, Ala218, Phe239
1.3D	-6.3	Glu118, Pro137	Glu116, Arg119, Ala133, Trp211, Leu214, Ala218
1.3E	-6.3	Glu118, Pro137	Gly117, Arg119, Ala133, Tyr211, Leu214, Ala218
1.3F	-6.9	Pro137	Glu116, Arg119, Ala133, Ala218
1.3G	-5.6	Glu116	Pro137, Leu214, Ala218
1.3H	-6.0	Glu116, Glu118, Arg119	Glu116, Leu214, Ala218
1.3I	-7.2	Glu118, Pro137	Glu116, Arg119, Ala133, Ala218
		Survivin	
1.3A	-6.1	Lys90, Lys91	Glu40, Ala41, Ile74, His77, Phe86, Leu87, Val89
1.3B	-5.2	Phe87	Glu40, Leu87, Lys90
1.3C	-6.8	Lys90	Glu40, Ala41, Ile74, His77, Phe86, Leu87
1.3D	-6.6	Lys90, Lys91	Glu40, Ile74, Phe86, Leu87, Val89
1.3E	-6.6	Lys90, Lys91	Glu40, Ile74, Phe86, Leu87, Val89
1.3F	-6.0	-	Lys15, Glu40, Ile74, Phe86, Leu87, Lys90
1.3G	-5.1	Phe86, Lys90	Glu40, Ile74, Leu87
1.3H	-6.0	Lys90	Ile74, Phe86, Leu87
1.3I	-6.2	Lys90	Glu40, Ala41, Ile74, His77, Leu87, Phe86

The common tendency in the binding interactions of compounds **(1.3A-1.3I)** and the standard ligand monastrol is that the ester group protrudes outside the enzyme cavity of Eg5. These compounds **1.3I, 1.3B, 1.3A**, and **1.3F** exhibited higher binding affinities among the compounds with binding scores -7.2, -7.1, -6.9, and -6.9 kcal/mole, respectively. The docking analysis illustrates that all the compounds occupy the same position in the binding cavity of the Eg5 enzyme, which is shown in the overlay diagram **(Figure 2.50 (e))**. All the compounds showed carbon-hydrogen bonding interactions with residues Glu118, Pro137, and Glu116 except **1.3C (Figure 2.50)**. The π-anion interaction is shown in all compounds except **1.3E**, which formed amide π-stacked interaction. The other non-covalent interactions, π-alkyl, and alkyl, also stabilized the interaction at the binding cavity of Eg5. The alkyl interactions Ala133, Ala218, Pro137, Arg119, and Trp127 residues, and π-alkyl interactions of the residues Ala218, Ala133, Pro137, Tyr127, and Tyr211 are seen in enzyme Eg5 active site.

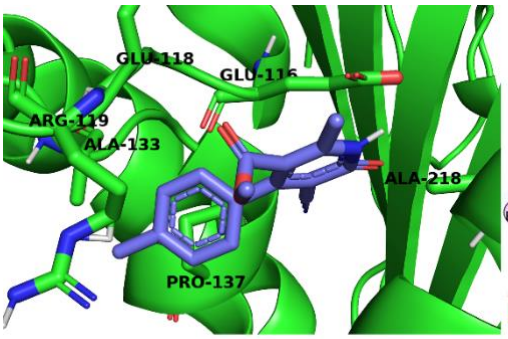

(a)

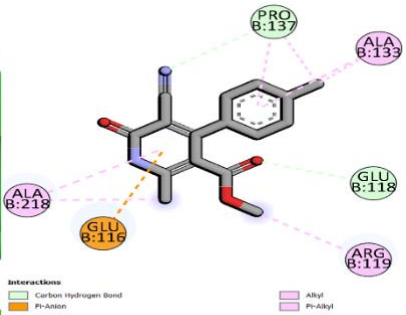

(b)

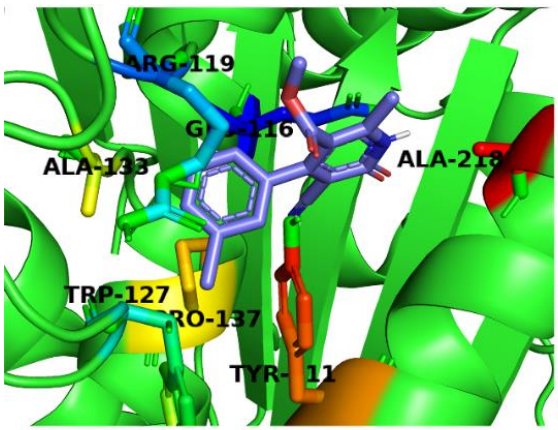

(c)

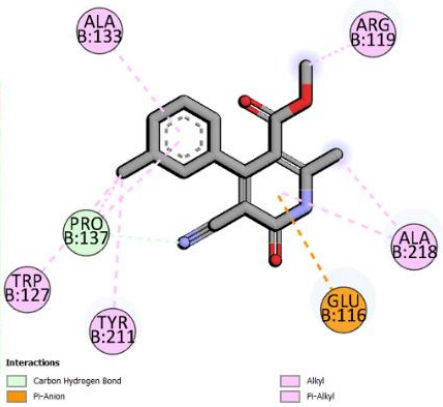

(d)

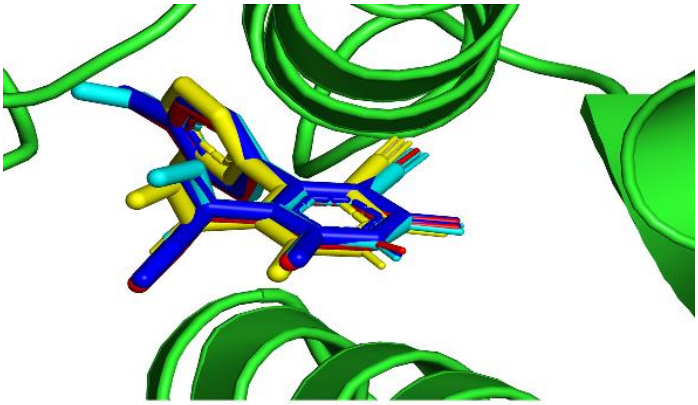

(e)

Figure 2.50: Binding of compounds in Eg5 protein (a) & (b) **1.3I,** (c) & (d) **1.3B**, (e) overlay diagram: **1.3I** (red), **1.3B** (yellow), **1.3A** (blue), **1.3F** (cyan)

The survivin enzyme has two distinct binding sites at the BIR domain and the dimerization interface. However, it has only been reported that the dimerization interface and the allosteric site nearby can accommodate the binding of small molecules. The docking analysis has shown that all the compounds **(1.3A-1.3I)** occupy an allosteric cavity near the dimerization interface of the receptor **(Figure 2.51 (a) & (b))**. Compounds **1.3C, 1.3D**, and **1.3E** exhibited higher binding affinities of -6.8, -6.6, and -6.6 kcal/mol, respectively **(Figure 2.51 (e))**. The hydrogen bond interactions are found with Lys90 in all the compounds except **1.3F** and **1.3B**. The compounds **1.3D, 1.3E,** and **1.3A** also formed weak carbon hydrogen interactions with Lys91 in the active site. Moreover, **1.3C, 1.3D,** and **1.3E** stabilized at the interface by the electrostatic π-anion interaction and hydrophobic π-alkyl and alkyl interactions. The π-anion interaction is found with residue Glu40, π-alkyl interactions with Lys90, Ile74, Leu87, Phe86, and His77 residues, and alkyl interactions with residue Ala41, Ile74, Leu87, and Val89.

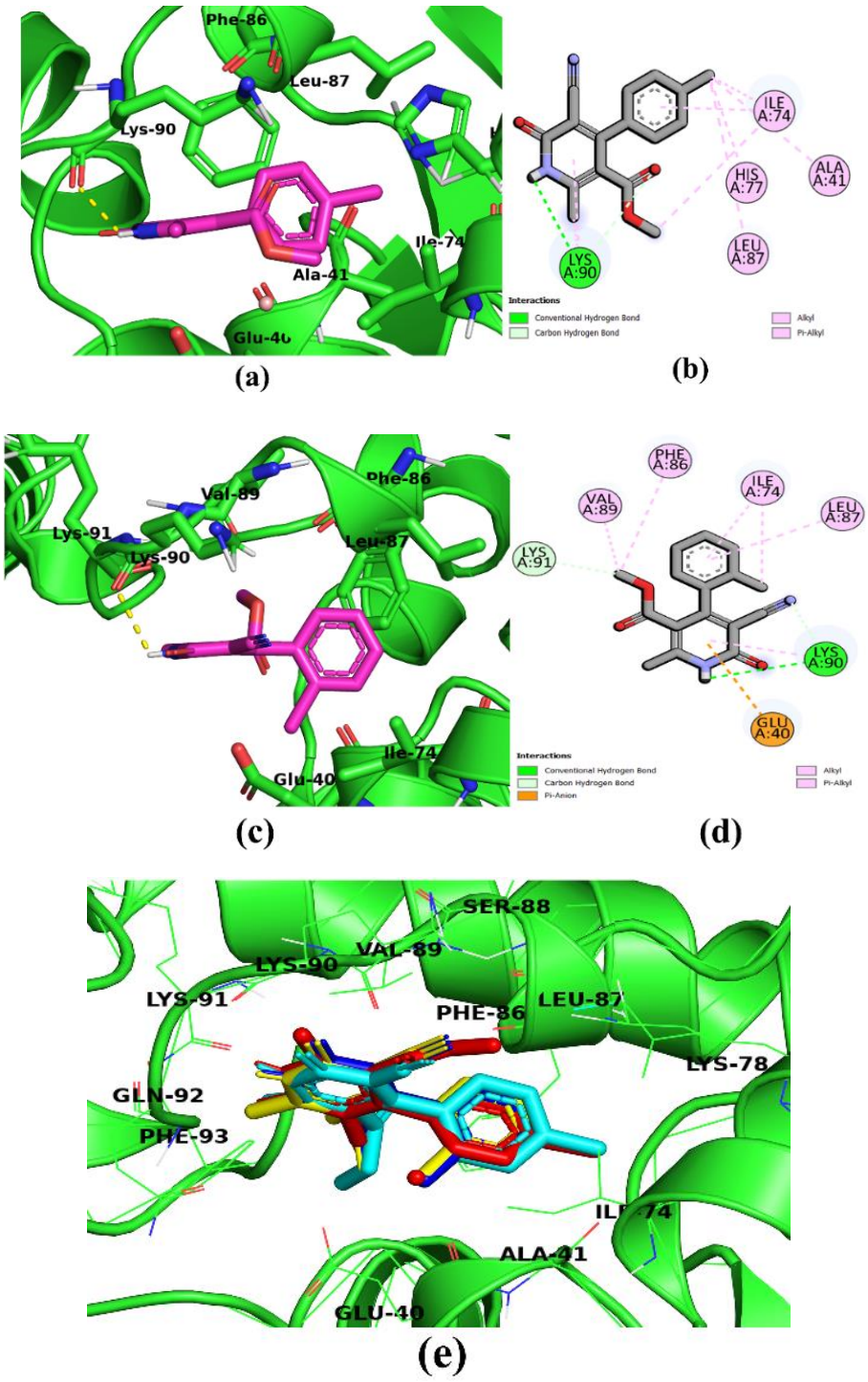

Figure 2.51: Compounds binding modes in the active site of survivin, (a) and (b) **1.3C**, (c) and (d) **1.3D,** (e) overlay diagram: **1.3C** (red), **1.3D** (blue), **1.3E** (yellow), **1.3I** (cyan)

2.7 Conclusion

A series of compounds is synthesized in this chapter, which are studied and analyzed. The compounds which form suitable crystals are subjected to single-crystal X-ray diffraction. The data from these crystals are analyzed to study the supramolecular framework and Hirshfeld surface analysis. It includes the enrichment ratio between the intermolecular contacts of the atoms in the molecules.

The substituent on the aromatic aldehyde plays an important role in synthesizing the pyridone-based hybrid compounds; the electron donating group present in the phenyl ring increases the yield of the product. Compared with the chloro derivatives, meta-derivatives yield is the highest among them. The crystal structure study shows that para chloro substitution **1.3A** does not form lone pair-π interaction with a chlorine atom, which is formed in ortho and meta chloro substitution **1.3B** and **1.3D** with pyridone ring and phenyl ring, respectively. In addition, **1.3A** crystals have lone pair-π interaction with O2A, and **1.3B** exhibit similar interactions with cyano nitrogen N1 to the pyridone ring. **1.3G** does not show the lone pair-π interactions among the ortho substitution. The para substitution also shows that **1.3A** and **1.3I** exhibit the lone pair-π interaction, but **1.3F** does not exhibit this interaction. Aromatic interactions play an important role in chemical and biological systems as they are ubiquitous. These aromatic interactions are very complex compared to simple weak interactions in hydrogen bonds; they are complicated because of the involvement of the larger functional groups, which provide a large surface area of intermolecular contacts. The intermolecular interactions such as C-H…O, C-H…N, C-H…C, C-H…π, and π…π interactions play an important role in stabilizing the stereochemistry of the synthesized compounds. These are useful for drug design, structure stabilization, crystal engineering, material science, etc.

The presence of C-H…π interaction in all the compounds is indicated by the wing-like structure in the 2D fingerprint plot, but the absence of a flat green region in the curvedness and shape index revealed the lack of π…π stacking interaction. The synthesized compounds' Hirshfeld surface analysis confirmed the supramolecular framework's intermolecular interactions. The interatomic contacts between the atoms of the molecule are also studied in the molecule's enrichment ratio (ER), which implies

the propensity of atoms inside the molecules. The intermolecular atomic contacts C…H, N…H, and O…H are mostly favorable contacts whose ER values are larger than unity. Those compounds having π…π stacking interactions are also supported by the ER values of C…C contacts more than unity or close to unity.

The molecular docking results show that the Eg5 protein binding score with **1.3I** is the highest, with the para substitution of methyl group followed by the meta chloro substitution **1.3B**. These results favour more towards electron donating groups but also favour electron-withdrawing groups at para positions. This result agrees with the non-covalent interactions found in the self-assembly of all compounds. Moreover, the docking score of survivin protein is highest in di-substitution, i.e., 2-bromo-4-chloro, followed by ortho substitution. It indicates that the pocket size of the receptor is better suited for bulky ligands. This study shows that compounds **1.3I** score the highest docking score with Eg5 protein at -7.2 kcal/mole with hydrogen bonding and π-anion and hydrophobic interaction. The compound **1.3C** exhibits the highest docking score of -6.8 kcal/mol, with the active survivin protein site hydrogen bonding with Lys90 residue.

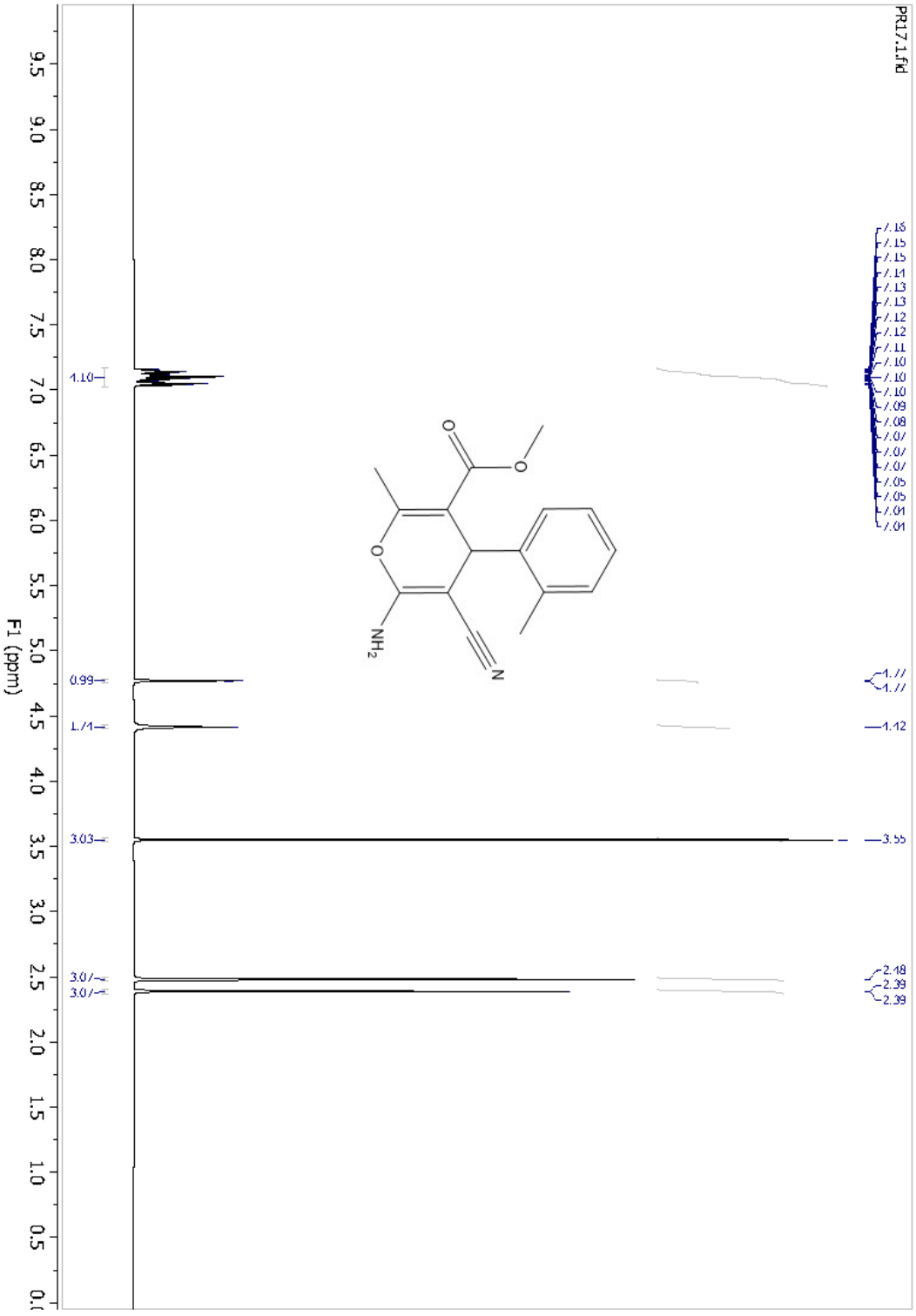

Figure 2.52: ^{1}H NMR spectra of compound **1.1E**

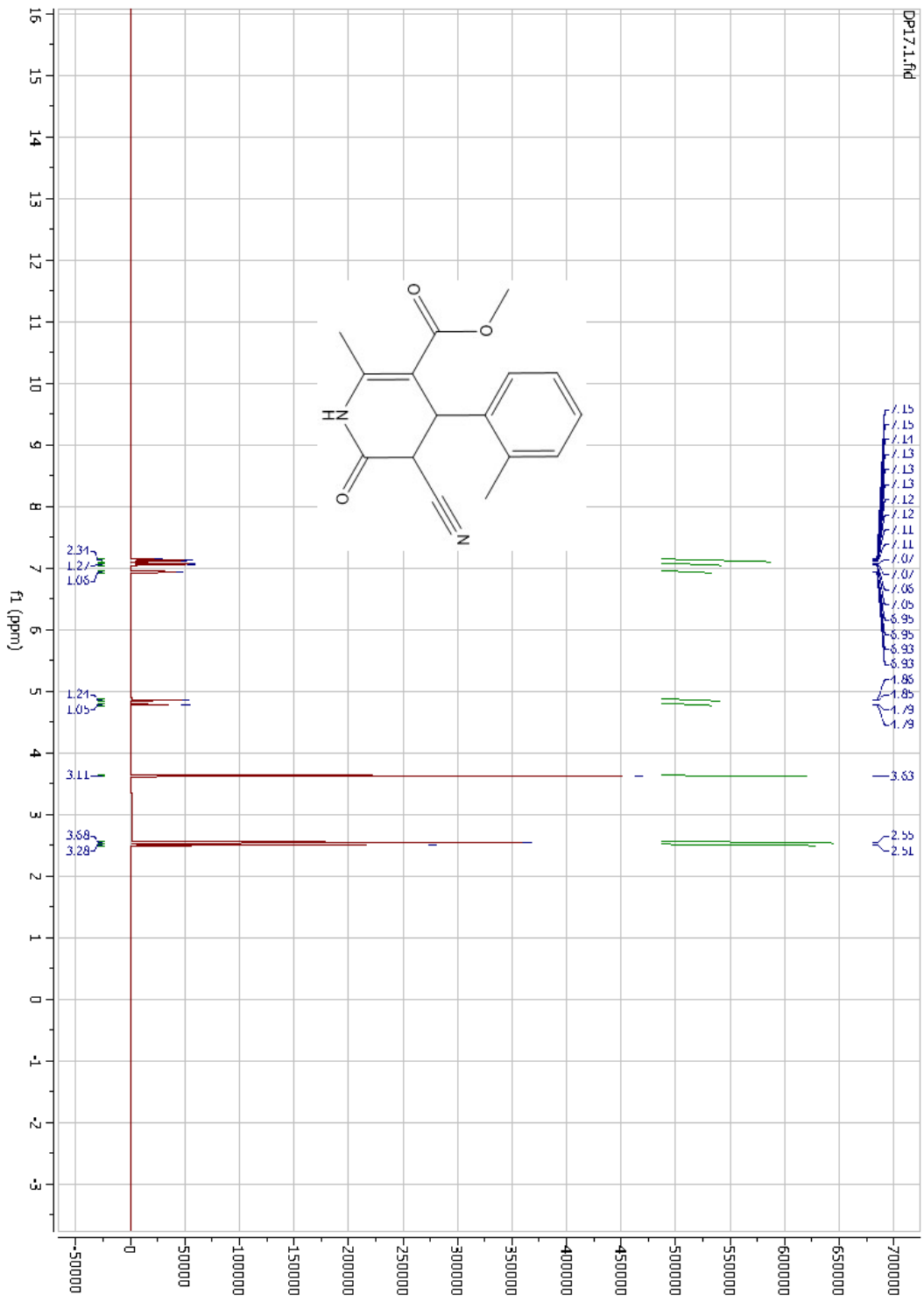

Figure 2.53: ^{1}H NMR spectra of compound **1.2E**

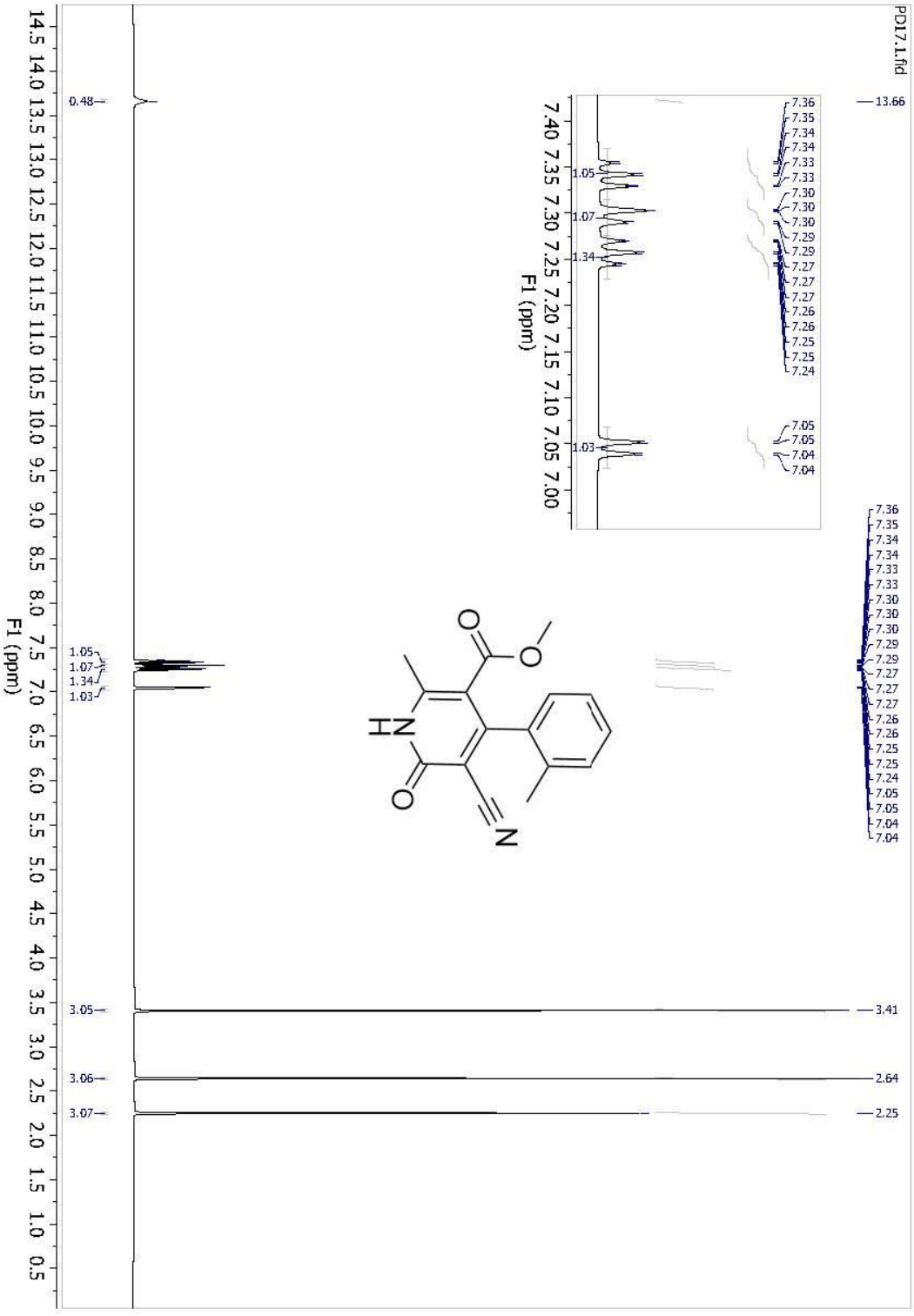

Figure 2.54: ^{1}H NMR spectra of compound **1.3E**

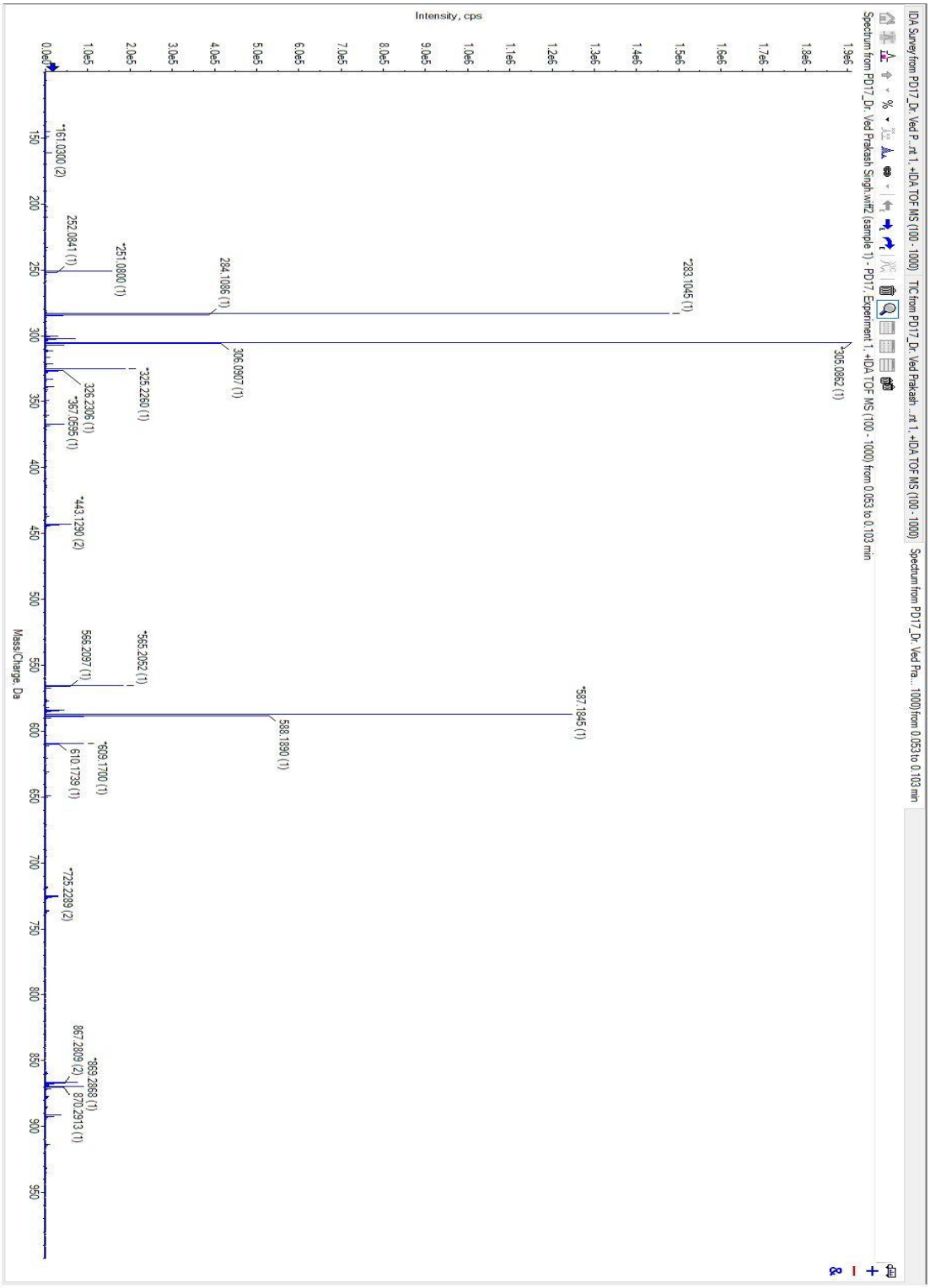

Figure 2.55: HRMS spectra of compound **1.3E**

CHAPTER 3

3. SYNTHESIS AND STUDY OF PYRANOPYRAZOLE AND SPIROOXINDOLE DERIVATIVES

3.1 Introduction

Nitrogen and oxygen functional heterocyclics play an important role in medicinal chemistry and have been extensively employed as drug development scaffolds. Multi-component reactions (MCRs) have become an effective tool for providing the molecular diversity required in combinatorial approaches for synthesizing bioactive molecules (Nandakumar et al., 2010). Because of their simple procedures, efficiency, convergence, and superficial implementation, multi-component reactions are one of the most effective strategies for synthesizing organic compounds (Dabiri et al., 2011).

4H-pyrans analogs display an important role in synthesizing medicinally important heterocyclic compounds. Due to their activity in the pharmacological and biological systems, the polyfunctionalized 4H-pyrans attracted researchers working in the area of drug discovery research. Pyrazoles or 1,2-diazoles are popular five-membered heterocyclic compounds in a wide range of synthetic and natural products. It shows chemical, biological, pharmacological, and agrochemical properties. The heterocyclic motif of fused pyran ring is also widely distributed among natural products.

Pyran is a heterocyclic compound with an oxygen atom in the ring, which shows a wide range of pharmacological applications. The pyran ring is the central unit of benzopyrans, chromones, flavonoids, coumarins, xanthones, and naphthoquinones, having various pharmacological properties. Pyran heterocycles are frequent among both "natural" and "man-made" heterocycles. Many natural compounds containing pyrans and benzopyrans have promising medicinal properties. They have raised substantial interest in the synthetic field regarding structure, reactivity, synthesis, and biological features (Kumar et al., 2017). Small heterocyclic molecules are widely recognized as the primary building blocks for biologically active compounds (Enders

et al., 2007; Tietze, 1996), whereas a growing variety of structural frameworks have been described as dominating structures (Kazemi et al., 2012). The bioactive metabolite β-lapachone (**Figure 3.1**) is an example of a pyran derivative with diverse biological activities (e.g., antibacterial, anti-cancer, and anti-inflammatory activities), making it significant for drug development. For example, Zanamivir (**Figure 3.1**) has been approved to prevent influenza A and B. Besides, zanamivir has emerged as the most sophisticated commercially available neuraminidase inhibitor. GlaxoSmithKline now markets this medication under the brand name "Relenza." Laninamivir octanoate is a laninamivir (**Figure 3.1**) prodrug that is structurally similar to zanamivir and is used orally (Kiso et al., 2010; Koyama et al., 2009). Condensed pyrans and benzopyrans are key structural units in many natural and synthetic compounds. They have a high activity profile due to their diverse biological activities, including anti-cancer properties (da Rocha et al., 2011; Dong et al., 2010). Because the pyran ring structural framework may readily open and rearrange to form other heterocyclic compounds. It is also a significant precursor for synthesizing other heterocyclic compounds (Lalhruaizela et al., 2021).

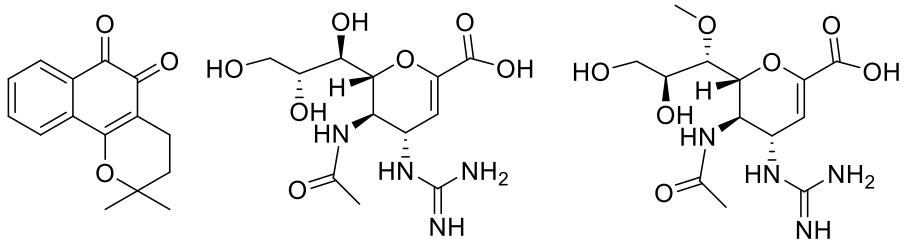

Figure 3.1: Pyran-based natural and synthetic drugs in clinical/pre-clinical trials

Pyranopyrazole derivatives have been known in the literature since the early nineteenth century (Junek & Aigner, 1973) and Otto (Otto, 1974). Much research has been done till now on synthesizing functionalized pyrano[2,3-c]pyrazole based on the applications in pharmaceutical chemistry. Pyranopyrazoles have occupied an important place in drug chemistry due to their pharmacological and biological (Mobinikhaledi et al., 2014) activities. It includes antibacterial activity comparable to cefazolin and ciprofloxacin (Mandha et al., 2012), antibacterial (Junek & Aigner, 1973), antifungal (Abdel-Rahman et al., 2004), antitumor (Bensaber et al., 2014),

analgesic and anti-inflammatory (Kaushik et al., 2012), anti-Alzheimer's disease (Yamamoto et al., 1988), antioxidant (Dandia et al., 2014), and also a potential Chk1 kinase inhibitor in humans (Foloppe et al., 2006). There are four possible isomers of pyranopyrazole, pyrano[2,3-c]pyrazole, pyrano[3,4-c]pyrazole, pyrano[3,2-c]pyrazole, and pyrano[4,3-c]pyrazole. Pyrano[2,3-c]pyrazoles (**Figure 3.2**) are the most common structures with pharmacological importance among heterocycles and have been most explored.

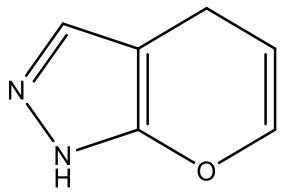

Figure 3.2: 1,4-dihydropyrano[2,3-c]pyrazole

The spirooxindole structure (Marti & Carreira, 2003) is found in a variety of bioactive natural compounds such as horsfiline, elacomine, alstonisine, coerulescine, welwitindolinone A, and spirotryprostatin A (Baran & Richter, 2005; Chang et al., 2005; Cui et al., 1996; Hilton et al., 2000). A natural alkaloid, spirotryprostatin A (Sannigrahi, 1999), derived from the *Aspergillus fumigutus* fermentation broth, has been found as a new inhibitor of microtubule assembly. Pteropodine and isopteropodine have been shown to alter muscarinic serotonin receptor function **(Figure 3.3)**. One of the most significant heterocyclic rings found in natural products and medicinal chemistry is the 3-substituted indole nucleus (Gribble, 2000). It is discovered as a scaffold in various bioactive compounds, particularly having anti-cancer, antitumor (Zhu et al., 2008), hypoglycemic, anti-inflammatory, antipyretic, and analgesic bio-activities (Nandakumar et al., 2010). The structural rigidity and complexity of the molecule are assigned due to the presence of the spiro center and then increasing its dependence upon proteins (Velazquez-Campoy et al., 2000).

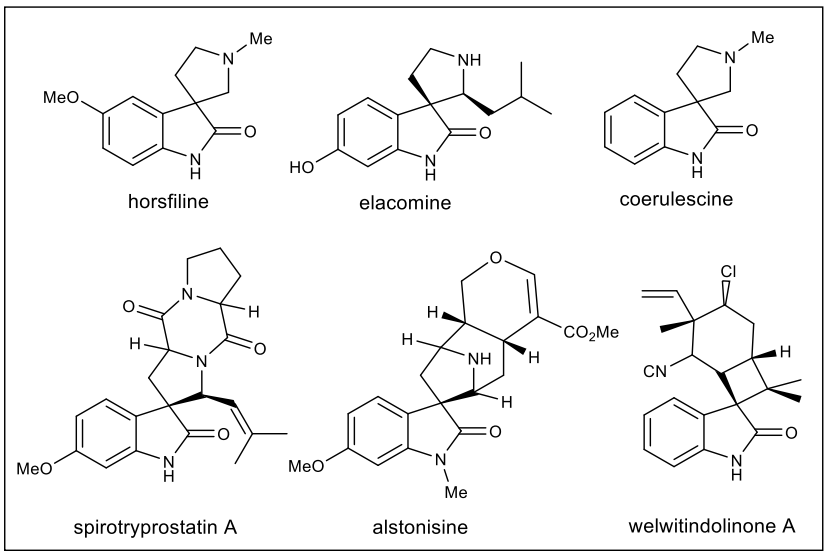

Figure 3.3: Structure representation of spirooxindole derivatives

3.2 Present work

This chapter studies a simple and convenient method for synthesizing pyranopyrazoles and spirooxindole derivatives and their crystal structures using single-crystal XRD. Their supramolecular framework and Hirshfeld surface analysis assess non-covalent interactions and enrichment ratios to stabilize the crystal structure. The synthesized compounds are a hybrid of two aromatic motifs **(Figure 3.4)** which show structural features of biological activity to a greater extent.

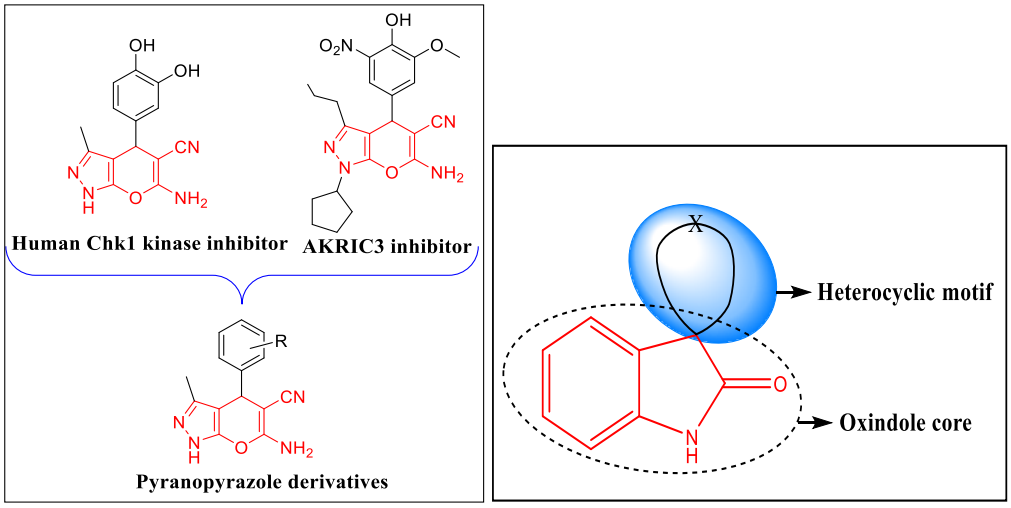

Figure 3.4: Pyranopyrazole and spirocyclic oxindoles derivatives: A compound of interest containing a hybrid of two structural motifs.

3.3. Synthesis of hybrid pyrans and pyranopyrazoles derivatives

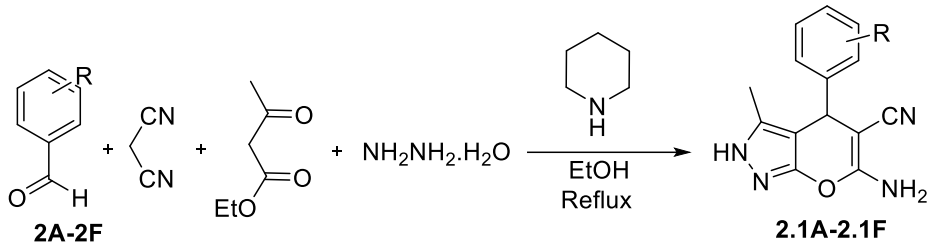

R= 3-NO_2, 3-OCH_3, 4-Cl, 3-Cl, 4-CH_3, 4-OCH_3

Entry= A, B, C, D, E, F

Scheme 2

The synthesis of a series of pyranopyrazole derivatives (2**.1A-2.1F**) is done through a multi-component reaction of 1,3-diketones, aldehydes, malononitrile, and hydrazine hydrate using piperidine as a base catalyst in ethanol as solvent shown in **scheme 2**. The synthesized compounds were recrystallized using an appropriate solvent, and those obtained decent crystals underwent single-crystal XRD analysis.

3.4. Experimental

^{1}H NMR (300 MHz) and ^{13}C NMR (75 MHz) spectra were recorded on a JEOL AL300 FTNMR spectrometer using TMS as an internal reference, and chemical shift values are expressed in δ, ppm units. The melting points of all the compounds were recorded on the electrically heated instrument and are uncorrected. All the reactions were monitored by thin-layer chromatography (TLC) on pre-coated aluminum sheets of Merck using an appropriate solvent system, and chromatograms were visualized under UV light.

3.4.1. General procedure for the synthesis of pyranopyrazoles (2.1A-2.1F)

In a 100 mL round bottom flask, ethanol (30 mL) was taken, aldehyde (10 mmol), malononitrile (10 mmol), ethyl acetoacetate (10 mmol), and hydrazine hydrate were added successively, followed by piperidine (0.3 mL, 3 mmol). The mixture was then heated under reflux at 80°C for 3 hours. After the reaction was completed

(monitored by TLC), it was cooled at room temperature, and then the solvent was reduced in a rotary evaporator. The residue was washed with cold ethyl alcohol to get the pure product of pyranopyrazole derivative compounds **(2.1A-2.1F)**.

3.4.1.1. 6-amino-3-methyl-4-(3-nitrophenyl)-2,4-dihydropyrano[2,3-c]pyrazole-5-carbonitrile (2.1A): White solid, yield: 87%, m.p. 214-215°C; **^{1}H NMR (300 MHz, DMSO):** δ ppm 1.79 (3H, s, CH_3); 4.87 (1H, s, CH); 7.03 (1H, s, Ar-H); 7.64 (2H, s, NH_2); 8.01 (2H, m, Ar-H); 8.14 (1H, m, Ar-H); 12.19 (1H, s, NH); **^{13}C NMR (75 MHz, DMSO):** δ ppm9.68, 35.55, 56.04, 96.59, 120.49, 121.77, 121.94, 130.19, 134.34, 135.88, 146.74, 147.80, 154.61, 161.07. **MS (m/z):** 298.09 (M+1).

3.4.1.2. 6-amino-4-(3-methoxyphenyl)-3-methyl-2,4-dihydropyrano[2,3-c]pyrazole-5-carbonitrile (2.1B): White solid, yield: 93%, m.p. 205-207°C; **^{1}H NMR (300 MHz, DMSO):** δ ppm 1.74 (3H, s, CH_3); 2.46 (3H, s, CH_3); 4.50 (1H, s, CH); 6.79 (2H, s, NH_2); 7.01 (2H, d, Ar-H); 7.09 (2H, d, Ar-H); 12.03 (1H, s, NH); **^{13}C NMR (75 MHz, DMSO):** δ ppm 9.8, 35.8, 55.6, 57.6, 97.9, 120.44, 121.75, 121.90,130.19, 135.4, 135.6, 145.2, 147.3, 154.60, 160.7.**MS (m/z):** 283.11 (M+1).

3.4.1.3. 6-amino-4-(4-chlorophenyl)-3-methyl-2,4-dihydropyrano[2,3-c]pyrazole-5-carbonitrile (2.1C): White solid, yield: 89%, m.p. 160-162°C; **^{1}H NMR (300 MHz, DMSO):** δ ppm 1.74 (3H, s, CH_3); 4.63 (1H, s, CH); 6.89 (2H, s, NH_2); 7.19 (2H, d, Ar-H, J = 8.4 Hz); 7.36 (2H, d, Ar-H, J = 8.4 Hz); 12.03 (1H, s, NH); **^{13}C NMR (75 MHz, DMSO):** δ ppm 9.9, 37.5, 58.1, 97.19, 120.65, 128.45, 129.36, 131.26, 135.69, 143.46, 154.72, 160.91. **MS (m/z):** 287.07 (M+1).

3.4.1.4. 6-Amino-4-(3-Chlorophenyl)-2,4-Dihydro-3-Methylpyrano[2,3-c]Pyrazole-5-Carbonitrile (2.1D): Light yellow solid, yield: 86%, m.p. 148-150°C; **^{1}H NMR (300 MHz, DMSO):** δ ppm 1.80 (3H, s, CH_3), 4.65 (1H, s, CH), 6.92 (2H, s, NH_2), 7.14 (2H, d, Ar-H, J = 8.4 Hz), 7.20 (1H, t, Ar-H, J = 8.4 Hz), 7.36 (1H, s, Ar-H), 12.1 (1H, s, NH); **^{13}C NMR (75 MHz, DMSO):** δ ppm 9.9, 37.5, 58.1, 97.19, 120.65, 128.45, 129.36, 131.26, 135.69, 143.46, 154.72, 160.91. **MS (m/z):** 287.068 (M+1).

3.4.1.5. 6-amino-3-methyl-4-(p-tolyl)-2,4-dihydropyrano[2,3-c]pyrazole-5-carbonitrile (2.1E); White solid, yield: 90%, m.p. 138-140°C; **^{1}H NMR (300 MHz, DMSO):** δ ppm 1.89 (3H,s, CH_3), 2.32 (3H, s, CH_3), 4.57 (1H, s, CH), 5.81 (2H, s, NH_2), 7.72-7.90 (4H, m, Ar-H), 12.04 (1H, s, NH); **^{13}C NMR (75 MHz, DMSO):** δ ppm 9.66, 35.80, 55.80, 96.48, 120.45, 123.83, 128.77, 128.51, 135.84, 146.30, 152.02, 154.58, 161.06. **MS (m/z):**267.12 (M+1).

3.4.1.6. 6-Amino-4-(4-Methoxyphenyl)-2,4-Dihydro-3-Methylpyrano[2,3-c]Pyrazole-5-Carbonitrile (2.1F); White solid, yield: 91%, m.p. 131-133°C; **^{1}H NMR (300 MHz, DMSO):** δ ppm 1.76 (3H, s, CH_3), 2.50 (3H, s, CH_3), 5.06 (1H, s, CH), 6.91 (2H, s, NH_2), 7.17–7-60 (4H, m, Ar-H), 12.08 (1H, s, NH); **^{13}C NMR (75 MHz, DMSO):** δ ppm 10.21, 35.93, 55.48, 58.15, 98.37, 114.25, 121.28, 128.96, 136.02, 136.96, 155.24, 158.45, 161.16. **MS(m/z):** 283.11 (M+1).

3.5. Results and discussions

In scheme **2**, a series of hetero-aromatic pyranopyrazole derivatives **(2.1A-2.1F)** were synthesis through a multicomponent reaction, and three compounds **(2.1B, 2.1C** and **2.1E)** gave a suitable crystal for the analysis. The crystal obtained in scheme **2** was studied by SC-XRD and Hirshfeld surface analysis.

3.5.1. X-Ray crystallographic studies and Hirshfeld surface analysis of compounds 2.1B, 2.1C and 2.1E

3.5.1.1. Crystal analysis of compound 2.1B

The compound **2.1B** was recrystallized in acetone at room temperature by slow evaporation of the solvent. The chiral asymmetric compound **2.1B** was analyzed using SC-XRD **(Figure 3.5)**. The compound crystallized with cell lengths **a** = 6.3778(2) Å, **b** = 10.2375(4) Å, **c** = 10.9960(3) Å, i.e., **a** ≠ **b** ≠ **c** and cell angles $\boldsymbol{\alpha}$ = 98.859(3)°, $\boldsymbol{\beta}$ = 98.678(2)°, $\boldsymbol{\gamma}$ = 99.345(3)°, i.e., $\boldsymbol{\alpha \neq \beta \neq \gamma \neq 90°}$. It indicates that the compound exhibits a triclinic crystal system, with space group P-1 that contains two molecules per unit cell **(Figure 3.6 (a))**.

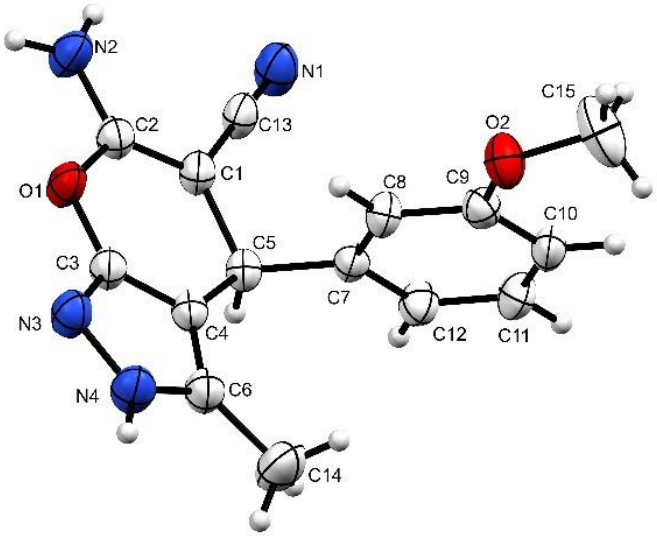

Figure 3.5: ORTEP diagram of compound **2.1B**

The chiral asymmetric compound **2.1B** crystal structure shows that the pyrazole and the anisole ring are planar and aromatic in nature. The fused heterocyclic pyranopyrazole ring atoms are almost planar. However, due to the sp^3 hybridization of the C5 atom, the planarity of the system is destroyed. The anisole ring twisted vertically to the plane of the pyranopyrazole ring. The dihedral angle between the two planes is 82.21°. The crystallographic information is summarized in **Table 3.1**.

Table 3.1: Crystal data on compounds **2.1B, 2.1C** and **2.1E**

Compound	**2.1B**	**2.1C**	**2.1E**
Identification code	2222474	2222476	2222473
Empirical formula	$C_{15}H_{14}N_4O_2$	$C_{14}H_{11}ClN_4O$	$C_{15}H_{14}N_4O$
Formula weight	282.30	286.72	266.30
Temperature(K)	293(2)	293(2)	293(2)
Crystal system	Triclinic	Orthorhombic	Triclinic
Space group	P-1	$P2_12_12_1$	P-1
a(Å)	6.3778(2)	5.1554(2)	6.3789(2)
b(Å)	10.2375(4)	8.3751(3)	9.8993(4)
c(Å)	10.9960(3)	32.4116(8)	10.6360(4)
α(°)	98.859(3)	90	78.507(4)
β(°)	98.678(2)	90	84.621(3)
γ(°)	99.345(3)	90	88.557(3)
Volume($Å^3$)	688.49(4)	1399.44(8)	655.25(4)
Z	2	4	2
ρ (g/cm^3)	1.362	1.361	1.350
μ(mm^{-1})	0.094	0.273	0.089
F(000)	296.0	592.0	280.0
Crystal size(mm^3)	0.32 × 0.3 × 0.24	0.28 × 0.26 × 0.24	0.24 × 0.22 × 0.2

Radiation	MoKα (λ = 0.71073)	MoKα (λ = 0.71073)	MoKα (λ = 0.71073)
2Θ range for data collection(°)	6.582 to 54.94	6.998 to 54.814	6.416 to 54.916
Index ranges	-7 ≤ h ≤ 8, -12 ≤ k ≤ 12, -14 ≤ l ≤ 14	-6 ≤ h ≤ 6, -10 ≤ k ≤ 10, -40 ≤ l ≤ 39	-8 ≤ h ≤ 7, -12 ≤ k ≤ 10, -12 ≤ l ≤ 13
Reflections collected	8848	12140	8421
Independent reflections	2914	2999	2775
Data/restraints/parameters	2914/0/200	2999/0/190	2775/0/188
Goodness-of-fit on F^2	1.045	1.057	1.097
Final R indexes [I>=2σ (I)]	R_1 = 0.0511, wR_2 = 0.1223	R_1 = 0.0417, wR_2 = 0.0945	R_1 = 0.0492, wR_2 = 0.1328
Final R indexes [all data]	R_1 = 0.0686, wR_2 = 0.1391	R_1 = 0.0560, wR_2 = 0.1029	R_1 = 0.0598, wR_2 = 0.1428
Largest diff.peak/hole/e $Å^{-3}$	0.20/-0.34	0.11/-0.21	0.22/-0.28

Supramolecular framework of compound 2.1B: The crystallographic arrangement of **2.1B** shows N-H…N interaction between the hydrogen H2A of the amino group and the nitrogen N1 of the cyano group between two molecules at a distance of 2.355 Å which results in the formation of unsymmetrical dimer exhibiting $R_2^2(12)$ graph set notation **(Figure 3.6 (b))**. The other hydrogen H2B from the amine group also forms an N-H…N bond with the pyranopyrazole nitrogen N3 at an interaction distance of 2.201 Å, which again results in the formation of another $R_2^2(12)$ graph set **(Figure 3.6 (b))**. The extensive network of these two N-H…N interactions along the plane of the pyranopyrazole ring manifests a polymeric chain giving a layer of sheets. The nitrogen N1 of the cyano group act as a trifurcated acceptor and accepts hydrogen H10 and H15C from the anisole moiety forming C-H…N interaction at a distance of 2.671 Å and 2.738 Å, respectively. It serves as an interconnecting tool between different layers of the packing.

The C-H…C interactions between the methoxy hydrogen H15A and the anisole ring carbon C12 at a distance of 2.712 Å and C-H…N interaction at 2.671 Å forms a graph sets of $R_2^2(14)$ and $R_2^2(18)$ **(Figure 3.6 (c))**. N-H stabilizes the crystal packing within the unit cell by N-H…O and N-H…C interactions. It forms between the trifurcated hydrogen H4 of the pyranopyrazole ring with the acceptor atoms O2, C9, and C15 of the anisole moiety at a distance of 2.059 Å, 2.825 Å, and 2.654 Å respectively. These non-covalent hydrogen bond found within the crystal packing also forms graph set notations of $R_2^2(16)$, $R_2^2(18)$, and $R_2^2(20)$. Beyond these interactions,

the molecular interconnection of compound **2.1B** also reveals C-H…π interaction between the hydrogen H14C from the alkyl substituent of the pyranopyrazole ring and the anisole p-orbital at a distance of 3.366 Å **(Figure 3.6 (e))**. In addition, π…π parallel displaced stacking at a distance of 4.163 Å is also found between the anisole rings **(Figure 3.6 (f))**. The non-covalent interactions are given in **Table 3.2**.

Table 3.2: Hydrogen bonds and other interactions in compound **2.1B**

Donor-H...Acceptor	**D – H, Å**	**H...A, Å**	**D...A, Å**	**D - H...A, º**
C11-H11…O2	0.930	2.711	3.527	146.84
C 15-H15C…N1	0.960	2.738	3.343	121.65
C10-H10…N1	0.930	2.671	3.601	179.72
C15-H15A…C12	0.960	2.712	3.663	171.20
N4-H4…O2	0.860	2.059	2.917	175.81
N4-H4…C9	0.860	2.825	3.586	148.34
N4-H4…C15	0.860	2.654	3.430	150.67
N2-H2A…N1	0.889	2.355	3.231	168.42
N2-H2B…N3	0.901	2.201	3.093	170.36
C14-H14C…π(C7-C12)	0.960	3.366	4.067	131.57
Other interaction				
π(C7-C12)…π(C7-C12)		4.163		
Intramolecular				
C8-H8…O1	0.930	3.846	4.414	122.39
C14-H14A…π((C7-C12)	0.960	3.463	3.983	116.39

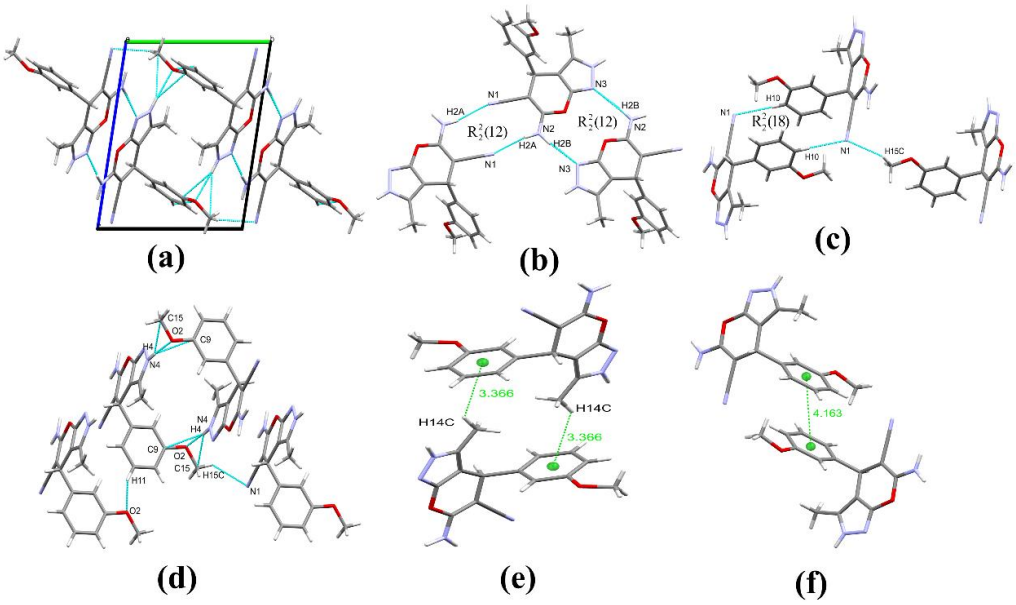

Figure 3.6: (a) Packing diagram of **2.1B**, (b), (c) and (d) Graph sets, (e) C-H…π interaction and (f) π…π interaction, in compound **2.1B**

Hirshfeld surface analysis of compound 2.1B: The Hirshfeld surface mapped over the d_{norm} in the range of -0.54 to 1.26 Å for compound **2.1B** is displayed in figure **(Figure 3.7 (a) and (b))**. The region of red spots corresponds to shorter contacts due to N-H…O, C-H…O, N-H…N. C-H…N, N-H…C and C-H…C contacts. The intensity of the red color and the size of the spots depends on interaction distance. The more dominant interaction is indicated by, the more intense the red color and the more prominent the size of the spots and vice versa.

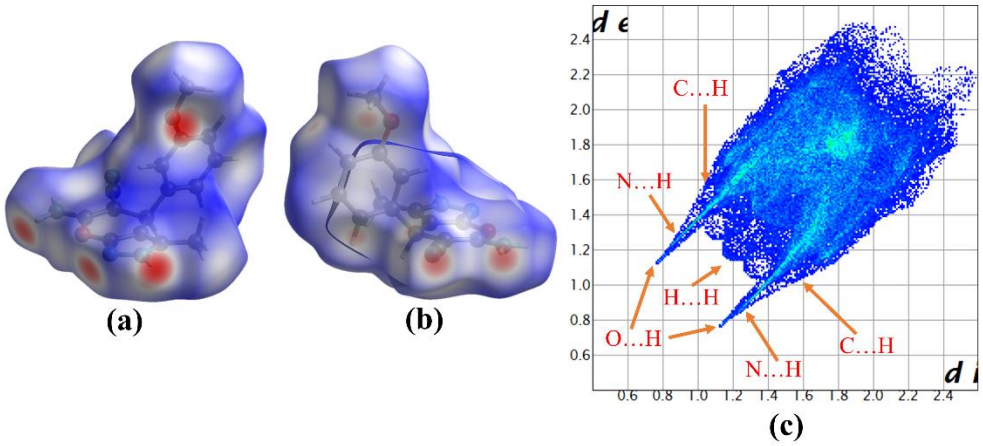

Figure 3.7: (a) and (b) d_{norm} both side view, (c) 2D fingerprint plot showing H…H, O…H, N…H and C…H interaction, of compound **2.1B**

The relative percentage contributions of non-covalent interaction to the Hirshfeld surface are summarized by the 2D fingerprint plot of compound **2.1B (Figure 3.7 (c))**. Those are H…H(42.3%), N…H(25.2%), C...H(13.9%), O…H(11.6%), C…C(2.7%),C…N(2.0%),C…O(0.9%), O…O(0.8%), N…N(0.3%) and N…O(0.2%). A pair of spokes-like patterns in the 2-D fingerprint plot in the region of di + de ≈ 1.9 Å corresponds to O…H interactions. N…H interaction also appears within the spike region in the $d_i + d_e \approx 2.1$ Å. The C-H...π and C…H contacts also appear as a pair of flipped wings-like patterns in $d_i + d_e \approx 2.5$ Å. The C…C contacts which account for 2.7%, indicate the presence of π-π stacking interaction.

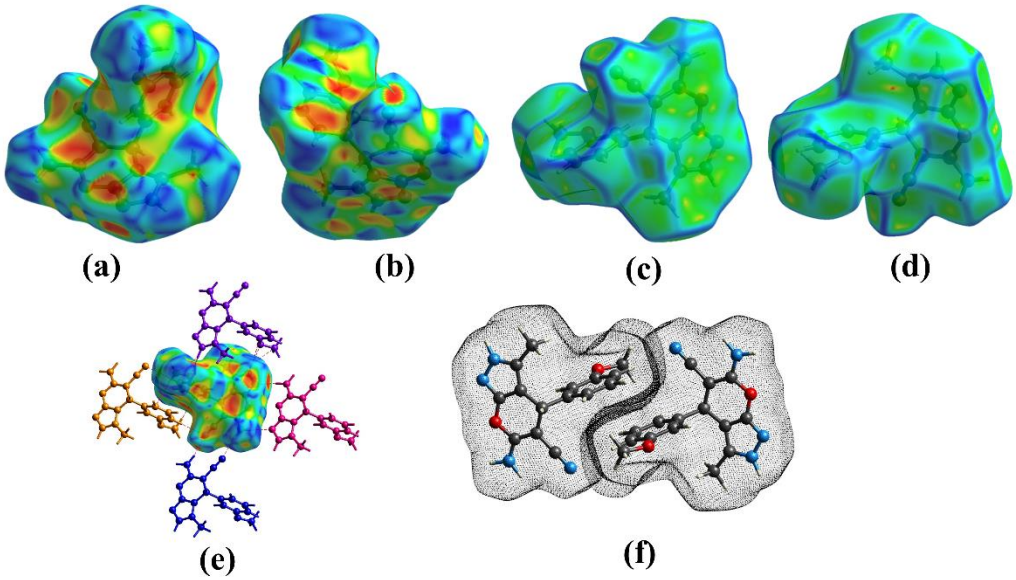

Figure 3.8: (a) and (b) Shape-index, (c) and (d) Curvedness, both side views of compound **2.1B**, (e) Non-covalent hydrogen bonding, (f) π…π interaction, in compound **2.1B**

In the shape index, red and blue indicate the acceptor and donor properties, respectively. The Hirshfeld surface mapped over the shape index in a range of -1 to 1 Å for compound **2.1B** shows yellowish-red colored concave regions and complementary blue and red triangles around the surface of the anisole ring. Which represents the presence of C-H...π and π…π stacking interactions **(Figure 3.8 (a) and (b))**. Similarly, the Hirshfeld surface was mapped over the curvedness in a range of -4 to 0.4 Å for compound **2.1B**, displaying a flat green region with a yellowish spot around the anisole ring surfaces, which reveals the presence of π…π stacking interaction **(Figure 3.8 (c) and (d))**.

The different types of non-covalent interactions found within the supramolecular framework of compound **2.1B** are also supported by the Hirshfeld calculation of weak interactions within the cluster of 3.8 Å radius from a single crystals fragment as shown in **Figure 3.8 (e)**. The π…π stacking interactions of compound **2.1B** overlap in **Figure 3.8 (f)**, supporting the supramolecular framework.

Table 3.3: Enrichment ratio (ER) of compound **2.1B**

Atoms	**H**	**C**	**N**	**O**
H	42.3	Actual contacts (%)		
C	13.9	2.7		
N	25.2	2	0.3	
O	11.6	0.9	0.2	0.8
Surface %	67.65	11.10	14.00	7.15
H	45.8	Random contacts (%)		
C	15.0	1.2		
N	18.9	3.1	2.0	
O	9.7	1.6	2.0	0.5
H	0.92	Enrichment ratio		
C	0.93	2.19		
N	1.33	0.64	0.15	
O	1.20	0.57	0.10	1.56

The surface contact data of compound **2.1B** resulting from the Hirshfeld surface analysis are used to derive the enrichment ratio that allows for analysis of the propensity of chemical species to interact in pairs in making crystal packing and are tabulated in **Table 3.3.** The enrichment ratio values of N…H, O…H, C…C, and O…O are greater than unity, indicating that these pairs have a larger tendency to form interconnection in the crystal structure. In contrast, the pairs with less than unity are not favorable contact and are disfavored. Interestingly, the H…H contacts occupy 67% of the total surface, but their ER value is only 0.92, and their interaction was not favorable. The higher ER value of C…C (E_{CC} = 2.19) supports the presence of the crystal structure's π…π stacking interaction.

3.5.1.2. Crystal analysis of compound 2.1C

The compound **2.1C** was recrystallized in acetone at room temperature by slow evaporation of the solvent. The chiral asymmetric compound **2.1C** was analyzed by SC-XRD (**Figure 3.9**). The compound crystallized with cell lengths **a** = 5.1554(2) Å, **b** = 8.3751(3) Å, **c** = 32.4116(8) Å, i.e., **a** ≠ **b** ≠ **c** and cell angles $\boldsymbol{\alpha}$ = 90°, $\boldsymbol{\beta}$ = 90°, $\boldsymbol{\gamma}$ = 90°, i.e., $\boldsymbol{\alpha = \beta = \gamma = 90°}$. It indicates that the compound exhibits an orthorhombic crystal system, with space group $P2_12_12_1$ that contains four molecules per unit cell **(Figure 3.10 (a))**.

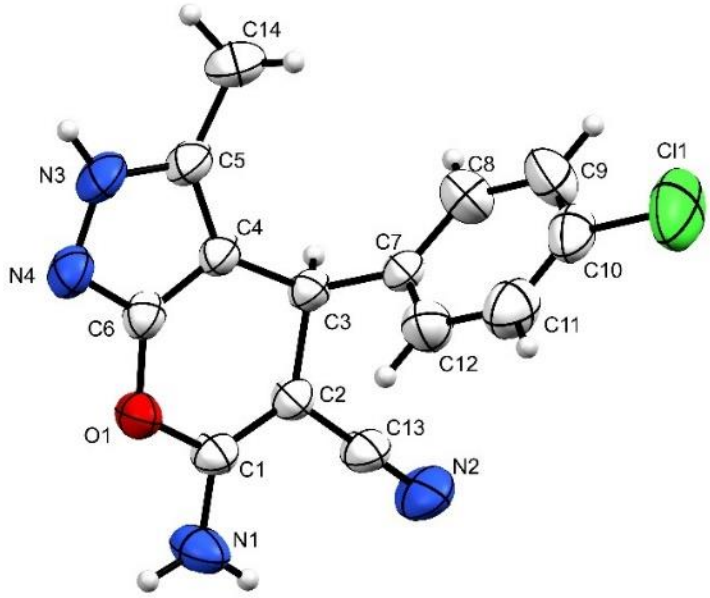

Figure 3.9: ORTEP diagram of compound **2.1C**

The chiral asymmetric compound **2.1C** crystal structure shows that the pyrazole and the anisole ring are planar and aromatic in nature. Due to the sp^3 hybridization of the C3 atom, the fused heterocyclic pyranopyrazole ring atoms do not lie in one plane. The chlorobenzene ring twisted vertically to the plane of the pyranopyrazole ring. The dihedral angle between the two planes is 81.06°. The crystallographic information is summarized in **Table 3.1**.

Supramolecular framework of compound 2.1C: The molecular arrangement of compound **2.1C** shows N-H…N interaction between the hydrogen H3 of the pyrazole ring moiety and the nitrogen N2 of the cyano group at a distance of 2.051 Å. It forms along the plane of the pyranopyrazole ring, forming a polymeric chain of the compound. C-H interconnects the polymeric chain from the different layers…C interaction between the hydrogen H3A of the pyran ring moiety and the carbon C6 atom from the pyranopyrazole ring at a distance of 2.895 Å. These N-H…N and C-H…C interactions together form $R_4^4(21)$ graph set notation **(Figure 3.10 (c))**.

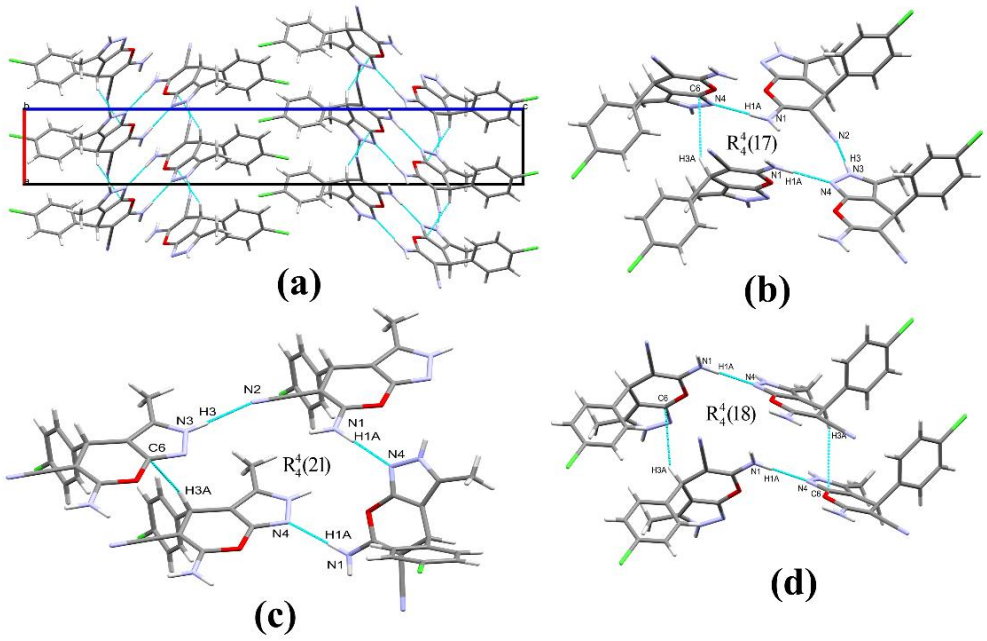

Figure 3.10: (a) Packing diagram of **2.1C**, (b), (c), and (d) Graph sets, in compound **2.1C**

The C-H…C interaction between the atoms H3A and C6 also furnished the hydrogen to interact with the pyrazole ring p-orbital at a distance of 2.891 Å. The same type of polymeric chain layer transversely runs across the other layer are interconnected by N-H...N interaction between the amino hydrogen H1A and the nitrogen N4 atom of the pyrazole moiety at a distance of 2.018 Å, and this interaction together with the interlayer C-H…C connectivity also forms a graph set notation of $R_4^4(21)$ and $R_4^4(18)$ **(Figure 3.10 (c) (d))**. The crystal packing within the unit cell is stabilized by N-H…N contacts with a 2.018 Å interaction distance. Beyond this, C-H…π interaction between the hydrogen H8, H11, and H14C and the chlorobenzene ring at a distance of 3.707 Å, 3.760 Å and 3.994 Å, respectively, assist the crystal packing **(Figure 3.11 (b))**.

Table 3.4: Hydrogen bonds and other interactions in compound **2.1C**

Donor-H...Acceptor	**D – H, Å**	**H...A, Å**	**D...A, Å**	**D - H...A, º**
N3-H3…N2	0.860	2.051	2.910	176.38
N1-H1A…N4	0.931	2.018	2.949	179.09
C3-H3A…C6	0.980	2.895	3.751	146.55
C8-H8…π(C7-C12)	0.930	3.707	4.209	116.83
C11-H11… π(C7-C12)	0.930	3.760	4.223	113.86

C14-H14C… π(C7-C12)	0.960	3.994	4.722	135.00
Other contacts				
Cl1…π(C7-C12)		4.598		
Intramolecular				
C12-H12…O1	0.930	3.627	4.230	125.00
C14-H14B…π(C7-C12)	0.960	3.700	4.312	124.12

The extensive crystal association of compound **2.1C** also shows lone pair…π interaction between the chlorine atom and the chlorobenzene ring at a distance of 4.598 Å and 5.517 Å, respectively **(Figure 3.11 (a))**. The weak non-covalent interactions are given in **Table 3.4**.

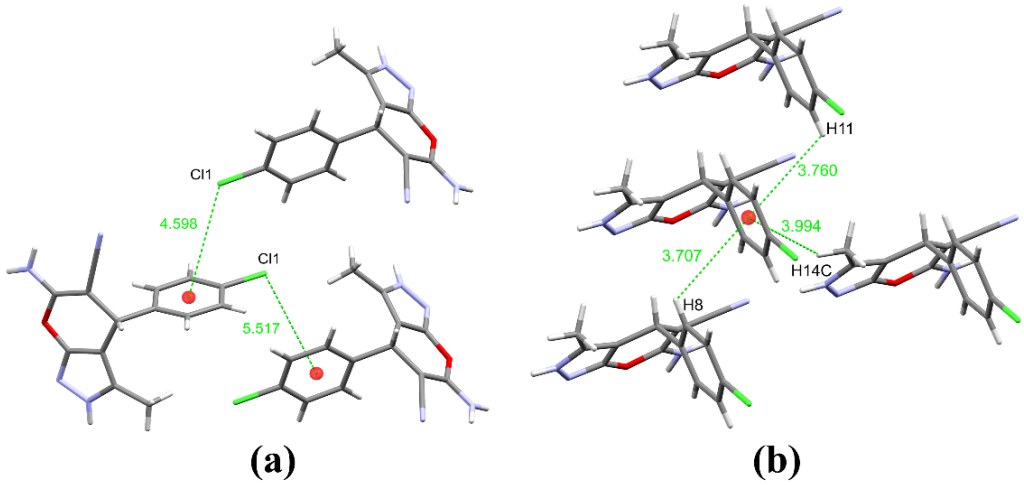

Table 3.11: (a) lone pair…π interactions, (b) C-H…π interaction, in compound **2.1C**

Hirshfeld surface analysis of compound 2.1C: The Hirshfeld surface mapped over the d_{norm} in the range of -0.54 to 1.26 Å for compound **2.1C** is displayed in **Figure 3.12 (a) and (b)**. The lighter white and blue regions of the Hirshfeld surface indicate weaker interactions due to more extended contacts. The region of bright red spots corresponds to shorter and dominant contacts due to N-H…N contacts.

The 2D fingerprint plot of compound **2.1C** shows the relative percentage contributions of non-covalent interaction to the Hirshfeld surface **(Figure 3.12 (c))**. Those interactions are N…H(25.7%), H…H(24.9%), C...H(18.9%), Cl…H(18.2%), O…H(5.0%), C…O(2.3%), N…N(1.6%), Cl…C(1.5%), C…N(1.1%) and N…O(0.8%). A pair of spokes-like patterns in the 2D fingerprint plot in the region of $d_i + d_e \approx 1.8$ Å corresponds to N…H interactions. The C-H...π and C…H contacts also

appear as a pair of flipped wings-like patterns in the region of $d_i + d_e \approx 2.8$ Å. The absence of C…C contact indicates the absence of π-π stacking interaction. The Cl…C contact, which contributes 1.5%, signifies the presence of lone pair…π interaction.

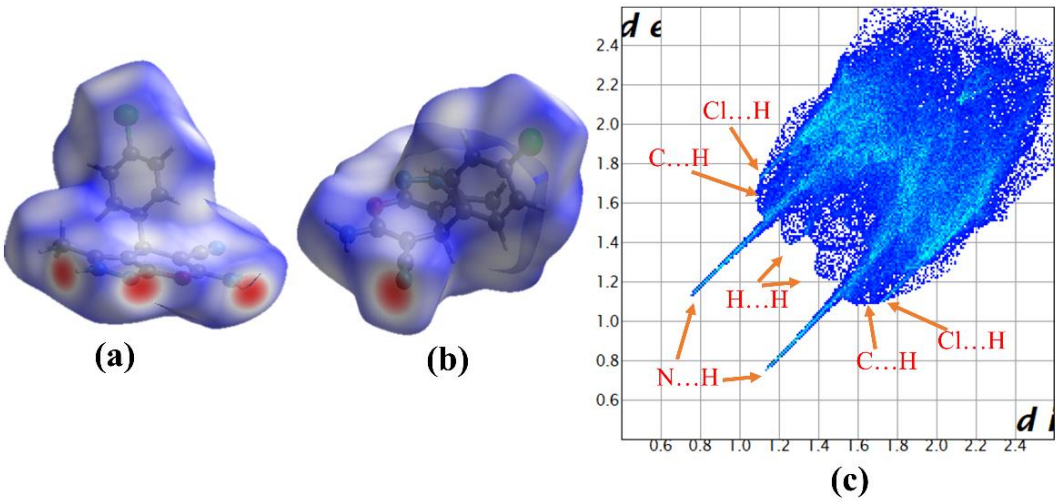

Figure 3.12: (a) and (b) d_{norm} both side view, (c) 2-D fingerprint plot illustrating H…H, N…H, C…H and Cl…H interaction, of compound **2.1C**

The Hirshfeld shape index mapped over the range of -1 to 1 Å for compound **2.1C** reveals yellowish-red colored concave regions around the surface of the chlorobenzene and the pyranopyrazole rings, which indicate the acceptor region where C-H...π interactions occur **(Figure 3.13 (a) and (b))**. Furthermore, the chlorobenzene ring exhibits another yellowish-red bin on the other side of the surface where lone pair…π interaction occurs. Similarly, the Hirshfeld surface mapped over the curvedness in a range of -4 to 0.4 Å for compound **2.1C** reveals the lack of a flat green region with a yellowish spot around the chlorobenzene surface, which indicates the absence of π…π stacking interaction **(Figure 3.13 (c) and (d)**.

The different types of interactions found within the supramolecular framework of compound **2.1C** are also supported by the Hirshfeld calculation of weak interactions within the cluster of 3.8Å radius from a single crystals fragment, as shown in **Figure 3.13 (e) & (f)**.

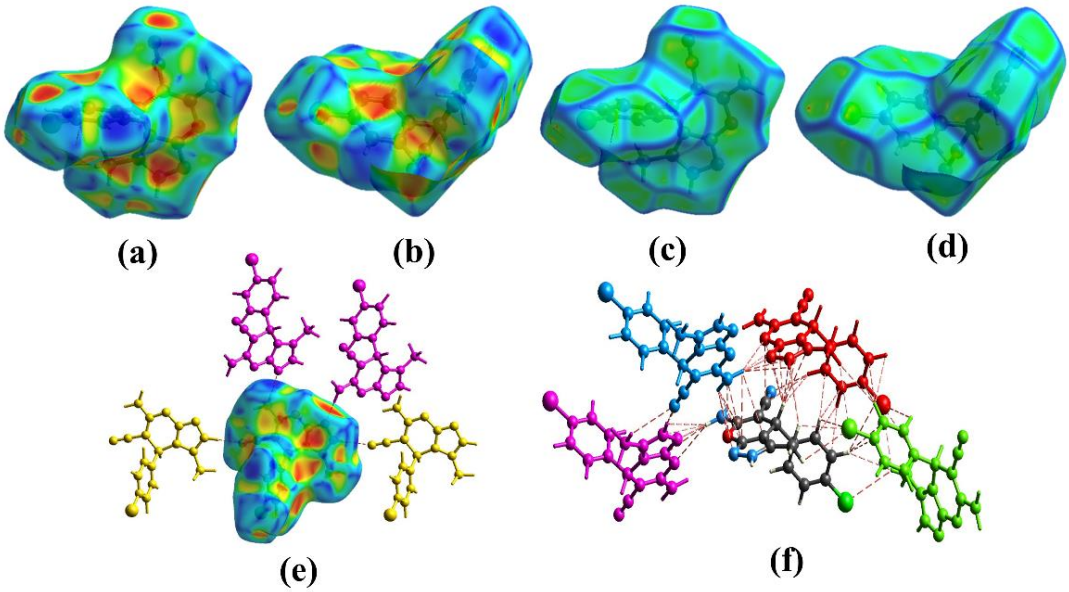

Figure 3.13: (a) and (b) Shape-index, (c) and (d) Curvedness, both side views of compound **1.2C**, (e) Non-covalent hydrogen bond, (f) short interactions within 3.8 Å, of compound **2.1C**

Table 3.5: Enrichment ratio (ER) of compound **2.1C**

Atoms	**H**	**C**	**N**	**O**	**Cl**
H	24.8	Actual contacts (%)			
C	18.9	0			
N	25.7	1.1	1.6		
O	5.0	2.3	0.8	0	
Cl	18.2	1.5	0	0	0
Surface %	58.70	11.90	15.40	4.05	9.85
H	34.5	Random contacts (%)			
C	14.0	1.4			
N	18.1	3.7	2.4		
O	4.8	1.0	1.2	0.2	
Cl	11.6	2.3	3.0	0.8	1.0
H	0.72	Enrichment ratio			
C	1.35	0.00			
N	1.42	0.30	0.67		
O	1.05	2.39	0.64	0.00	
Cl	1.57	0.64	0.00	0.00	0.00

The enrichment ratio (ER) was determined to confirm the nature and contribution of the bonds established in compound **2.1C** and is tabulated in **Table 3.5**. The enrichment ratio of C…H, N…H, O…H, and Cl…H are greater than unity, which indicates that these contacts are fruitful interactions with a larger propensity to form interconnection of the supramolecular structure of the crystal compound. The ER value of C…C is zero, indicating no π…π stacking interaction in the crystal structure. The hydrogen atom occupies 58.70% of the total surface, but the enrichment ratio of H…H contact is 0.72 and is not favored.

3.5.1.3. Crystal analysis of compound 2.1E

The compound **2.1E** was recrystallized in acetone at room temperature by slow evaporation of the solvent. The chiral asymmetric compound **2.1E** was analyzed by SC-XRD **(Figure 3.14)**. The compound crystallized with cell lengths **a** = 6.3789(2) Å, **b** = 9.8993(4) Å, **c** = 10.6360(4) Å, i.e., **a ≠ b ≠ c** and cell angles $\boldsymbol{\alpha}$ = 78.507(4)°, $\boldsymbol{\beta}$ = 84.621(3)°, $\boldsymbol{\gamma}$ = 88.557(3)°, i.e., $\boldsymbol{\alpha \neq \beta \neq \gamma \neq 90°}$. It indicates that the compound exhibits a triclinic crystal system, with space group P-1 that contains two molecules per unit cell **(Figure 3.15 (a))**.

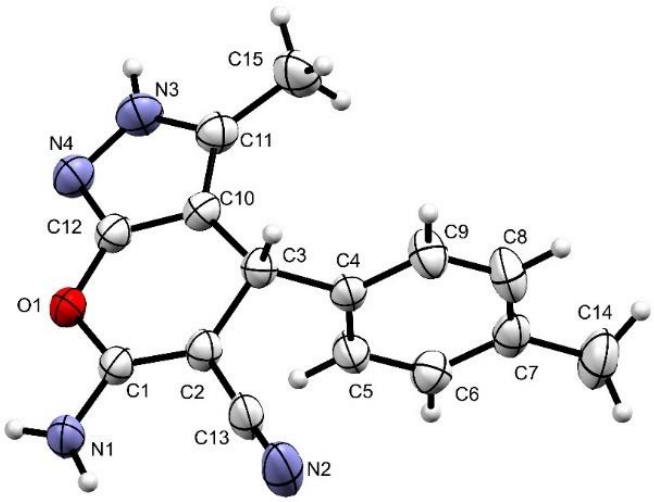

Figure 3.14: ORTEP diagram of compound **2.1E**

The chiral asymmetric compound **2.1E** crystal structure shows that the pyrazole and the benzenoid ring are planar and aromatic. The fused heterocyclic pyranopyrazole ring atoms almost lie in one plane. However, due to the sp^3 hybridization of the C3

atom, the pyran ring moiety of the fused ring is non-aromatic. The toluene ring twisted and flipped vertically to the plane of the pyranopyrazole ring. The dihedral angle between the two planes is 85.31°. The crystallographic information is summarized in **Table 3.1**.

Supramolecular framework of compound 2.1E: The molecular interaction of compound **2.1E** shows that hydrogen H1B of the amino interacts with the nitrogen N2 of the cyano group forming N-H…N interaction at a distance of 2.238 Å. It turns out to give an unsymmetrical dimer. The other hydrogen H1A from the amino group also forms N-H…N interaction with the nitrogen N4 from the pyrazole ring moiety having an interaction distance of 2.364 Å. These two sets of N-H…N interaction horizontally along the plane of the pyranopyrazole ring forms two different modes of $R_2^2(12)$ graph set notation **(Figure 3.15 (b))**. The aggregation of the compounds through extensive N-H…N connections results in forming a polymeric chain of sheets. Different layers of the sheet are interconnected by intermolecular C-H…C interactions between the hydrogen H14A from the alkyl group of the toluene and its carbon atom C9 at a distance of 2.807 Å. The nitrogen N2 of the cyano group acts as a bifurcated acceptor. It forms C-H…N interaction with the hydrogen H14B from the alkyl group of the toluene, having an interaction distance of 2.631 Å between a different layer of sheets. This result results in the formation of an $R_2^2(20)$ graph set **(Figure 3.15 (d))**.

Table 3.6: Hydrogen bonds and other interactions in compound **2.1E**

Donor-H...Acceptor	**D – H, Å**	**H...A, Å**	**D...A, Å**	**D - H...A, º**
N1-H1A…N4	0.820	2.364	3.174	169.81
N1-H1B….N2	0.909	2.238	3.142	172.74
N 3-H3…C7	0.860	2.537	3.377	165.85
N 3-H3…C6	0.860	2.797	3.594	154.93
N 3-H3…C14	0.860	2.841	3.622	151.98
C14-H14B…N2	0.960	2.631	3.357	153.51
C14-H14A…C9	0.960	2.807	3.691	132.65
C15-H15C…π(C4-C9)	0.960	3.577	4.192	124.16
N3-H3…π(C4-C9)	0.860	3.016	3.745	143.77
C8-H8…π(C4-C9)	0.930	3.915	4.129	96.94
C14-H14A…π(C4-C9)	0.960	3.369	4.059	130.56
Other contacts				
π(C4-C9)… π(C4-C9)		4.774		
Intramolecular				

C5-H5…O1	0.930	3.800	4.373	122.74
C15-H15A…π(C4-C9)	0.960	3.559	4.093	117.54

N-H stabilizes the crystal packing within the unit cell N-H…C interactions between the hydrogenH3 from the pyrazole ring moiety and the carbon atoms C6, C7, and C14 of the toluene group at a distance of 2.797 Å, 2.537 Å and 2.841 Å respectively **(Figure 3.15 (c))**. In addition, the interaction found within the crystal packing also facilitates C-H…π interaction between the hydrogen H3 and the toluene ring π-orbital and between the pyrazole ring π-orbital with the hydrogen H15A at a distance of 3.016 Å and 3.414 Å respectively. Similarly, the C-H…C and C-H…N interactions between molecules of different layers allow a very weak π…π stacking interactions at a distance of 4.774 Å between the toluene rings (**Figure 3.15 (f)**). Non-covalent hydrogen bonds and other interactions found in compound **2.1E** are given in **Table 3.6**.

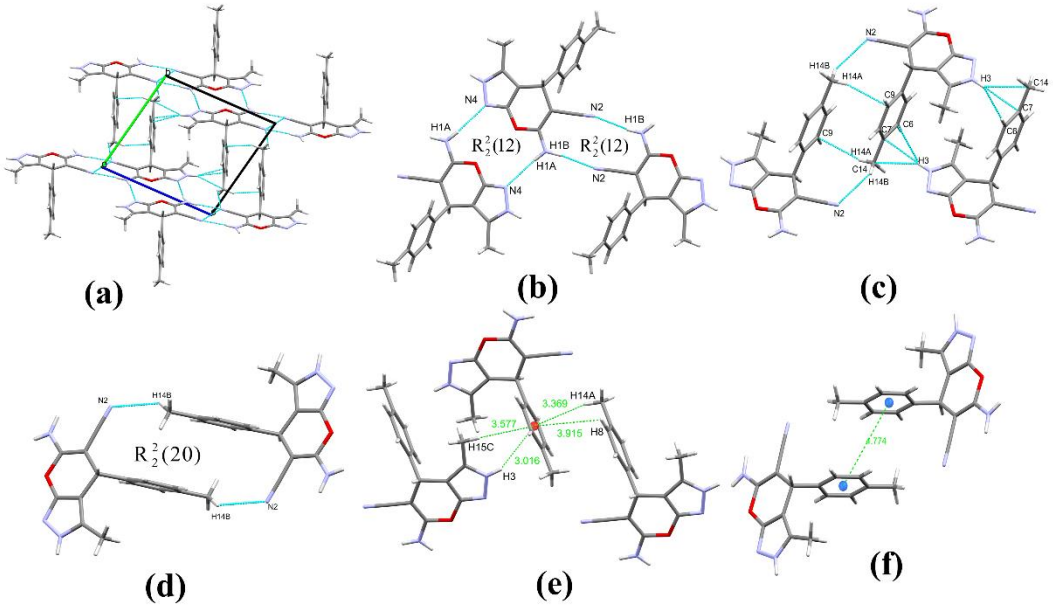

Figure 3.15: (a) Packing diagram of **2.1E**, (b), (c) and (d) Graph sets, (e) C-H…π interactions and (f) π…π interaction, in compound **2.1E**

Hirshfeld surface analysis of compound 2.1E: The Hirshfeld surface mapped over the d_{norm} in the range of -0.38 to 1.28 Å for compound **2.1E** is displayed in **Figure 3.16 (a) and (b)**. The region of bright red spots corresponds to shorter and more dominant contacts due to N-H…N and N-H…C interactions. The lighter red spots

indicate the less dominant interactions, which correspond to C-H…N and C-H…C contacts.

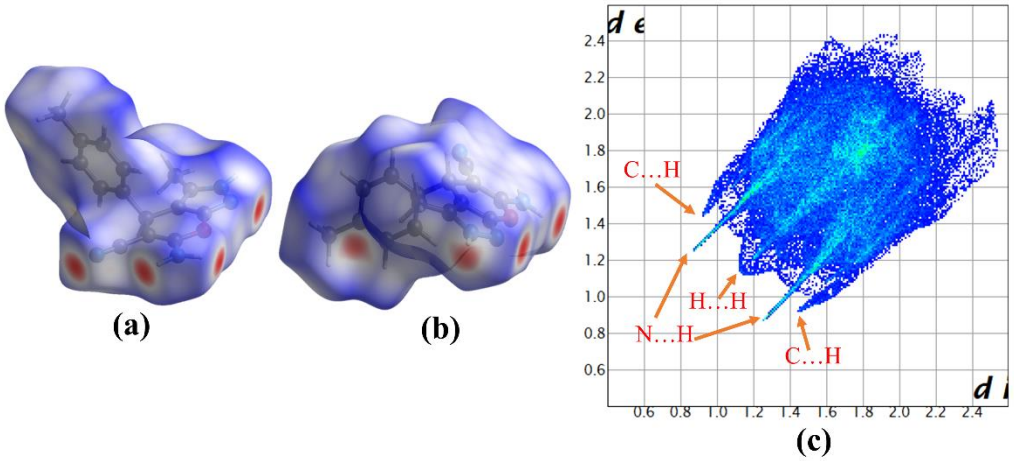

Figure 3.16: (a) and (b) d_{norm} both side view, (c) 2D fingerprint plot showing H…H, N…H and C…H interaction, of compound **2.1E**

The 2D fingerprint plot of compound **2.1E** gives the relative percentage contributions of non-covalent interaction to the Hirshfeld surface **(Figure 3.16 (c))**. Those interactions are H…H(44.4%), N…H(26.9%), C...H(16.9%), O…H(5.3%), C…N(2.3%), C…C(2.2%), C…O(0.7%), O…O(0.7%) and N…N(0.6%). A pair of spoke-like patterns in the 2-D fingerprint plot in the region of $d_i + d_e \approx 2.1$ Å corresponds to N…H interactions. The C-H...π and C…H contacts also appear as a pair of the shorter spike in the region of $d_i + d_e \approx 2.4$ Å. The C…C contacts which account for 2.2%, indicate the presence of π-π stacking interaction.

The Hirshfeld shape index in a range of -1 to 1 Å for compound **2.1E** shows a yellowish-red bin on the surface of the pyranopyrazole and the toluene rings, which represents the presence of C-H...π interactions **(Figure 3.17 (a) and (b))**. The pale red and blue triangles on the surface of the toluene ring indicate very weak π…π stacking interactions **(Figure 3.17 (a))**. Also, the curvedness in a range of -4 to 0.4 Å for compound **2.1E** displays a flat green region with a yellowish spot around the toluene ring surfaces, revealing the presence of π…π stacking interaction **(Figure 3.17 (d))**.

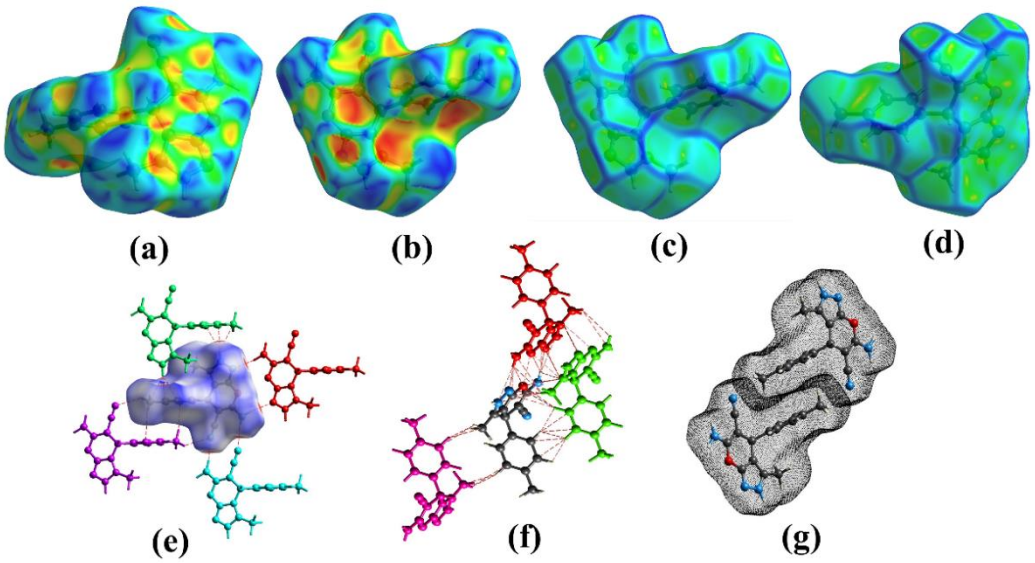

Figure 3.17: (a) and (b) Shape-index, (c) and (d) Curvedness, both side views of compound **2.1E**, (e) Non-covalent hydrogen bonding, (f) short interactions within 3.8 Å, (g) π…π interaction, in compound **2.1E**

The different types of interactions found within the supramolecular framework of compound **2.1E** are also supported by the Hirshfeld calculation of weak interactions within the cluster of 3.8 Å radius from a single crystals fragment, as shown in **Figure 3.17 (e) & (f)**. The π…π stacking interactions in the supramolecular association are also supported by **Figure 3.17 (g)**.

Table 3.7: Enrichment ratio (ER) of compound **2.1E**

Atoms	**H**	**C**	**N**	**O**
H	44.4	Actual contacts (%)		
C	16.9	2.2		
N	26.9	2.3	0.6	
O	5.3	0.7	0	0.7
Surface %	68.95	12.15	15.20	3.70
H	47.5	Random contacts (%)		
C	16.8	1.5		
N	21.0	3.7	2.3	
O	5.1	0.9	1.1	0.1
H	0.93	Enrichment ratio		
C	1.01	1.49		
N	1.28	0.62	0.26	
O	1.04	0.78	0.00	5.11

The enrichment ratio (ER) of the atomic contacts is derived from the Hirshfeld surface analysis data that enable the analysis of the tendency of the chemical species to interact in pairs for forming crystal packing of compound **2.1E** and are tabulated in **Table 3.7**. The hydrogen atom occupies 68.95% of the total surface, but its contacts are not favorable, with an ER value of 0.93. The favorable contacts with values greater than unity are C…H, N…H, O…H, C…C, and O…O interactions. Among these contacts, C…C enrichment ratio is 1.49, which supports the presence of π…π stacking interactions in the crystal packing to reinforce the supramolecular structure.

3.6. Synthesis of 2-oxospiro[indoline-3,4'-pyran]-5'-carbonitrile derivatives

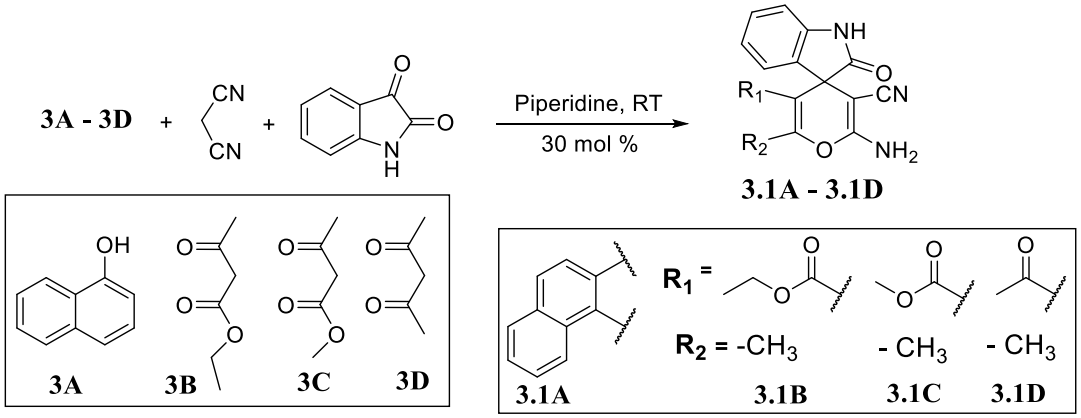

Scheme 3

The derivatives of 2-oxospiro[indoline-3,4'-pyran]-5'-carbonitrile were synthesized as in **scheme 3**. It was synthesized using piperidine as a catalyst from isatin, malononitrile, and 1,3-diketone or 4-hydroxy derivatives. The reaction was carried out at room temperature, and all the synthesized compounds **(3.1A-3.1D)** were recrystallized from acetone to get a crystal for SC-XRD analysis.

3.7. Experimental

^{1}H NMR (300 MHz) and ^{13}C NMR (75 MHz) spectra were collected using a JEOL AL300 FTNMR spectrometer using TMS as an internal reference, and chemical shift values are presented in δ, ppm units. The compounds' melting points were recorded using an electrically heated instrument and were uncorrected. Thin-layer

chromatography (TLC) on pre-coated aluminum sheets from Merck was used to monitor all reactions, and chromatograms were seen under UV radiation.

3.7.1. General procedure for the synthesis of 2-oxospiro[indoline-3,4'-pyran]-5'-carbonitrile derivatives (3.1A-3.1D)

Ethanol (30 mL) was taken in a 100 mL round bottom flask, and isatin (0.5 mmol) and malononitrile (0.5 mmol) were added and stirred. Diketone / 4-hydroxy derivatives (0.5 mmol) were added to this mixture, followed by piperidine (30 mole %). Stir the mixture at room temperature in an open space for 8 hours. The reaction was monitored by TLC (using ethyl acetate and hexane as eluent). After completion of the reaction, the precipitate was filtered and washed with iced cold ethanol to get a pure compound (**3.1A-3.1D**).

3.7.1.1. 2-amino-2'-oxospiro[benzo[h]chromene-4,3'-indoline]-3-carbonitrile (3.1A): Orange solid, yield: 80%, m.p. 284°C; **^{1}H NMR (300 MHz, $CDCl_3$):** δ ppm 6.52 (1H, d, Ar-H, *J* = 7.2 Hz); 6.97 (2H, t, Ar-H, *J* = 7.2 Hz); 7.04 (1H, d, Ar-H, *J* = 7.2 Hz); 7.26 (1H, t, Ar-H, *J* = 7.2 Hz); 7.42 (2H, s, NH2); 7.50-7.69 (3H, m, Ar-H); 7.85 (1H, d, Ar-H, *J* = 7.2 Hz); 8.24 (1H, d, Ar-H, *J* = 7.2 Hz); 10.65 (1H, s, NH); **^{13}C NMR (75 MHz, $CDCl_3$):** δ ppm 53.82, 59.21, 115.33, 117.25, 118.17, 120.13, 123.50, 124.82, 125.65, 125.78, 125.82, 126.46, 127.23, 127.91, 132.46, 135.16, 139.52, 143.82, 168.57, 177.20; **MS (m/z):** 340.10 (M+1).

3.7.1.2. 2'-amino-5'-butyryl-6'-methyl-2-oxospiro[indoline-3,4'-pyran]-3'-carbonitrile (3.1B): Orange solid, yield: 82%, m.p. 250°C; **^{1}H NMR (300 MHz, $CDCl_3$):** δ ppm 0.73 (3H, t, CH3, *J* = 6 Hz); 2.27 (3H, s, CH_3); 3.65-3.80 (2H, m, CH_2); 6.75 (1H, d, Ar-H, *J* = 6 Hz); 6.89 (1H, t, Ar-H, *J* = 6 Hz); 7.01 (1H, d, Ar-H, *J* = 6 Hz); 7.10 (2H, s, NH_2); 7.14 (1H, t, Ar-H, *J* = 6 Hz); 10.36 (1H, s, NH); **^{13}C NMR (75 MHz, $CDCl_3$):** δ ppm 13.73, 17.66, 19.12, 41.58, 48.86, 57.43, 109.44, 115.18, 117.34, 124.82, 127.79, 129.81, 141.13, 154.20, 159.19, 168.24, 199.82; **MS (m/z):** 324.13 (M+1).

3.7.1.3 methyl 2'-amino-3'-cyano-6'-methyl-2-oxospiro[indoline-3,4'-pyran]-5'-carboxylate (3.1C): Orange solid, yield: 87%, m.p. 242°C; **^{1}H NMR (300 MHz,**

$CDCl_3$): δ ppm 2.26 (3H, s, CH_3); 3.30 (3H, s, CH_3); 6.75 (1H, d, Ar-H, *J* = 6 Hz); 6.89 (1H, t, Ar-H, *J* = 6 Hz); 7.01 (1H, d, Ar-H, *J* = 6 Hz); 7.11 (2H, s, NH_2); 7.13 (1H, t, Ar-H, *J* = 6 Hz); 10.36 (1H, s, NH); **^{13}C NMR (75 MHz, $CDCl_3$):** δ ppm 17.32, 50.38, 52.26, 57.44, 102.21, 115.17, 117.32, 124.83, 127.76, 127.83, 129.82, 141.89, 155.03, 159.25, 167.18, 168.26; **MS (m/z):** 312.09 (M+1).

3.7.1.4 3'-acetyl-6'-amino-2'-methyl-2-oxospiro[indoline-3,4'-pyran]-5'-carbonitrile (3.1D): Pale Yellow solid, yield: 76%, m.p. 245°C; **^{1}H NMR (300 MHz, $CDCl_3$):** δ ppm 2.04 (3H, s, CH_3); 2.24 (3H, s, CH_3); 6.74 (1H, d, Ar-H, *J* = 6 Hz); 6.88 (1H, t, Ar-H, *J* = 6 Hz); 6.99 (1H, d, Ar-H, *J* = 6 Hz); 7.06 (2H, s, NH_2); 7.12 (1H, t, Ar-H, *J* = 6 Hz); 10.34 (1H, s, NH); **^{13}C NMR (75 MHz, $CDCl_3$):**δ ppm 17.38, 27.26, 48.62, 57.37, 109.42, 115.24, 117.27, 124.76, 127.78, 127.82, 129.83, 141.12, 154.16, 159.21, 168.18, 196.54; **MS (m/z):** 296.10 (M+1).

3.8. Results and discussions

A derivative of a series of 2-oxospiro[indoline-3,4'-pyran]-5'-carbonitrile **(3.1A-3.1D)** was synthesized by multi-component reaction using isatin, malononitrile, diketones/1-naphthol and piperidine as a catalyst at room temperature. These spiro compounds are crystallized using acetone to get a suitable crystal for analysis. The obtained crystal was studied by using single-crystal XRD and Hirshfeld surface analysis.

3.8.1. X-Ray Crystallographic studies and Hirshfeld surface analysis of compounds 3.1A, 3.1B, 3.1C and 3.1D

3.8.1.1. Crystal analysis of compound 3.1A

The spiro compound **3.1A** was recrystallized from acetone by slow solvent evaporation at room temperature. The chiral compound **3.1A** was analyzed using SC-XRD **(Figure 3.18).** The compound crystallized with cell lengths **a** = 8.8306(3) Å, **b** = 10.1697(3) Å, **c** = 20.6970(6) Å, i.e., **a** ≠ **b** ≠ **c**, and cell angles $\boldsymbol{\alpha}$ = 90°, $\boldsymbol{\beta}$ = 94.112(3)°, $\boldsymbol{\gamma}$ = 90°. The compound exhibits a monoclinic crystal system, with a space group of $P2_1/n$ containing four atoms in the unit cell **(Figure 3.19 (a))**.

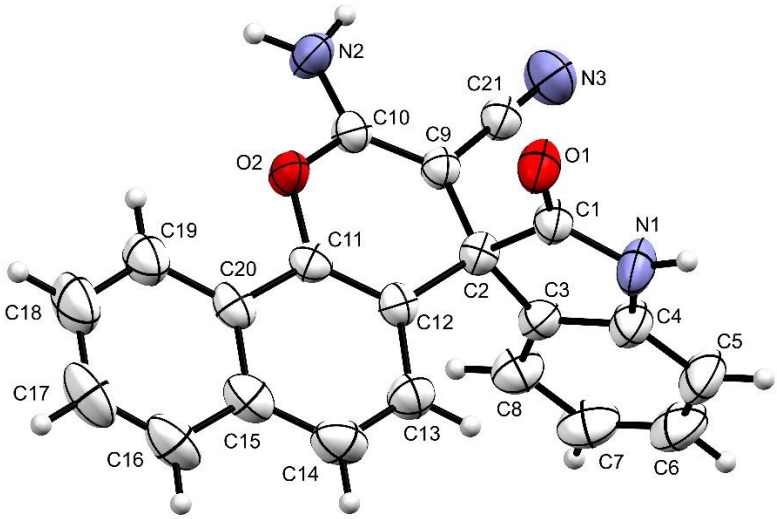

Figure 3.18: ORTEP of compound **3.1A**

The crystal structure of compound **3.1A** indicates that although the spiro carbon C2 is sp^3 hybridized, the pyran ring with other benzenoid rings is lying in a plane with the deviation of the carbon C9 and C10 by 0.256 Å and 0.284 Å respectively. The dihedral angle between the fused heterocyclic ring and the benzenoid ring is close to perpendicular with an angle of 85.51°. The crystallographic information of compound **3.1A** is summarized in **Table 3.8.**

Table 3.8: Crystal data of compounds **3.1A** and **3.1B**

Compound	**3.1A**	**3.1B**
Identification code	2224625	2222475
Formula weight	371.38	325.32
Temperature (K)	293(2)	293(2)
Crystal system	monoclinic	monoclinic
Space group	$P2_1/n$	$P2_1/c$
a/Å	8.8306(3)	7.8443(2)
b/Å	10.1697(3)	20.3294(6)
c/Å	20.6970(6)	10.0386(2)
α/°	90	90
β/°	94.112(3)	103.840(2)
γ/°	90	90
Volume ($Å^3$)	1853.90(10)	1554.38(7)
Z	4	4
ρ ($calcg/cm^3$)	1.331	1.390
μ (mm^{-1})	0.091	0.101

F(000)	776	680.0
Crystal size (mm^3)	0.3 × 0.28 × 0.24	0.26 × 0.24 × 0.22
Radiation	MoKα (λ = 0.71073)	MoKα (λ = 0.71073)
2Θ range for data collection (°)	6.532 to 54.88	6.684 to 54.554
Index ranges	-11 ≤ h ≤ 11, -10 ≤ k ≤ 13, -25 ≤ l ≤ 26	-9 ≤ h ≤ 9, -24 ≤ k ≤ 25, -12 ≤ l ≤ 11
Reflections collected	14972	12374
Independent reflections	3941 [Rint = 0.0385, Rsigma = 0.0387]	3287 [Rint = 0.0396, Rsigma = 0.0389]
Data/restraints/parameters	3941/0/263	3287/0/224
Goodness-of-fit on F^2	1.099	1.064
Final R indexes [I>=2σ (I)]	R1 = 0.0559, wR2 = 0.1526	R1 = 0.0493, wR2 = 0.1279
Final R indexes [all data]	R1 = 0.0792, wR2 = 0.1695	R1 = 0.0660, wR2 = 0.1396
Largest diff. peak/hole/e $Å^{-3}$	0.27/-0.40	0.23/-0.29

Supramolecular framework of compound 3.1A: The self-assembly of compound **3.1A** was formed by the strong intermolecular interactions of N-H…O and N-H…N. The carbonyl oxygen O1 acts as a bifurcated acceptor and forms non-covalent hydrogen bonds N1-H1…O1 and N2-H2A…O1 interactions with a distance of 2.167 Å and 2.082 Å, respectively. These interactions result in the formation of $R_2^2(8)$ and $R_2^2(14)$, respectively, which involves three molecules together and reinforces the supramolecular framework of the structure **(Figure 3.19 (b))**. Moreover, the N2-H2B…N3 interactions with a distance of 2.280 Å form the graph set $R_2^2(12)$ to associate the molecules in the crystal structure **(Figure 3.19 (c))**. The non-covalent interactions found in the crystal compound **3.1A** are shown in **Table 3.9.**

Table 3.9: Hydrogen bonds and other intermolecular interactions in compound **3.1A**

Donor-H...Acceptor	D – H, Å	H...A, Å	D...A, Å	D - H...A,°
N1-H1…O1	0.860	2.167	2.975	156.39
N2-H2A…O1	0.921	2.082	2.982	165.25
N2-H2B…N3	0.888	2.280	3.119	157.37
C8-H8...π (C3-C8)	0.930	3.691	4.581	161.05

C6-H6...π (C11-C15C20)	0.930	2.844	3.874	145.76
C7-H7...π (C11-C15C20)	0.930	3.493	3.817	114.65
C14-H14...π (C15-C20)	0.930	3.309	3.986	131.41
N2-H2B...π (C11-C15C20)	0.888	3.740	3.914	94.74
N2-H2A…π (C2C9-C12O2)	0.921	3.263	3.627	106.06
Other contacts				
O1…N2		2.982		
O1…N1		2.975		
O2…C10		3.196		
N3…π (C15-C20)		3.591		
Intramolecular				
N2-H2B…C21	0.888	2.619	2.842	95.28
C19-H19…O2	0.930	2.431	2.740	99.37
C13-H13…π (C1-C4N1)		2.703		

The molecular association of the crystal structure is supported by the C-H…π interactions. However, the interchain connections of the molecules result in infinite chains due to extensive C-H…π interactions. These C-H…π interactions involving the benzene and pyran rings was observed **(Figure 3.20 (a))**. The C6-H6…Cg, C7-H7…Cg, C8-H8…Cg and C14-H14…Cg (where Cg is centroid) with a distance of 2.844 Å, 3.493 Å, 3.691 Å, and 3.309 Å, respectively, which linked the different layers of the crystal compound **3.1A**. Then, N2-H2A…Cg and N2-H2B…Cg with a distance of 3.740 Å and 3.263 Å, respectively, reinforced the molecular association **(Figure 3.20 (b))**. Nitrogen atom N3 of the nitrile group forms lone pair…π interaction with the benzenoid ring.

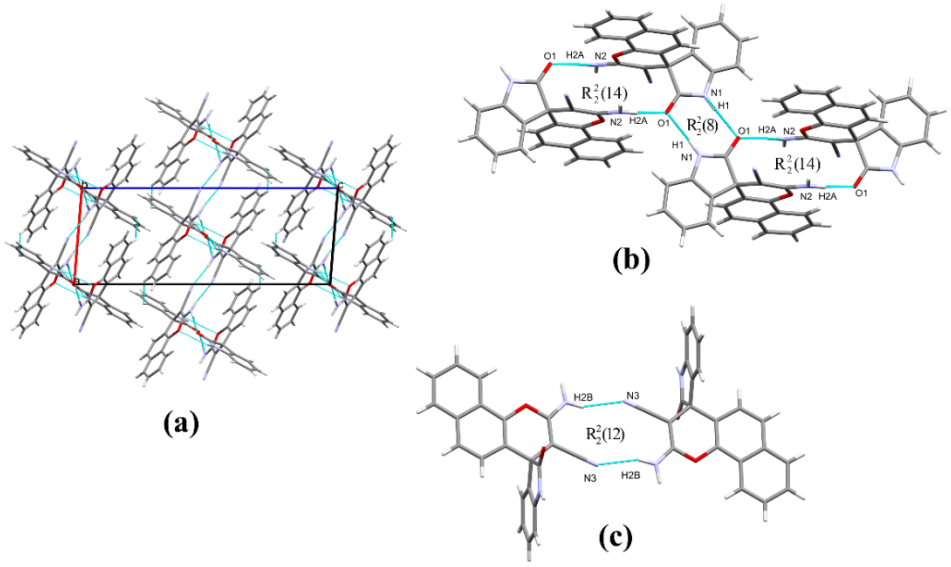

Figure 3.19: (a) Packing diagram, (b) N-H…O interactions, (c) N-H…N interactions, in compound **3.1A**

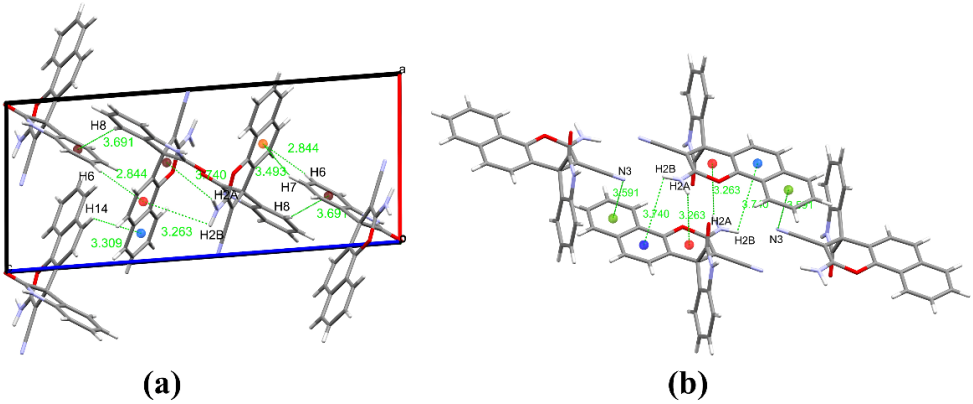

Figure 3.20: (a) C-H…π and N-H…π interactions, (b) N-H…π and lone pair…π interactions, in compound **3.1A**

Hirshfeld surface analysis of compound 3.1A: Hirshfeld surface was mapped over d_{norm} in the range of -0.4713 Å to 2.7185 Å for compound **3.1A** as shown in **Figure 3.21 (a) and (b).** The region of bright red spots in the d-norm plot corresponds to short contacts, which are more dominant intermolecular N-H…O and N-H…N interactions. A region of light red spots in the d-norm was due to the C-H…O interactions.

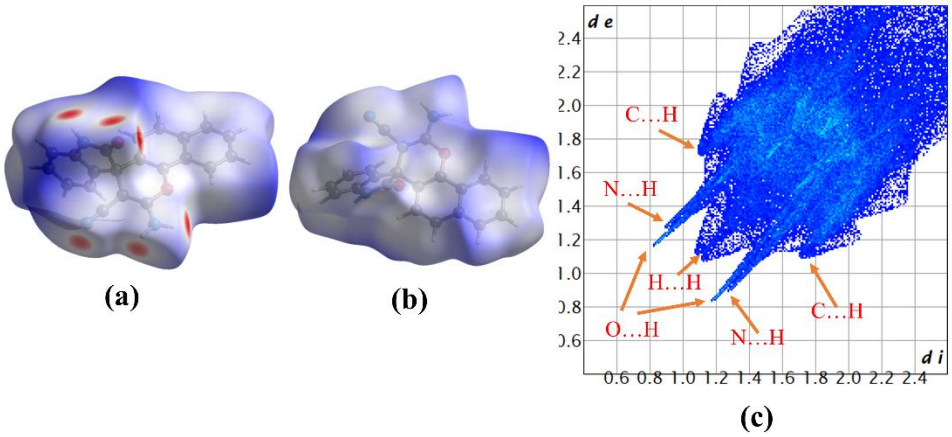

Figure 3.21: (a) and (b) Hirshfeld surface d_{norm} both side view, (c) 2D fingerprint plot showing H…H, O…H, N…H and C…H interactions, in compound **3.1A**

The relative percentage contributions of the non-covalent interactions in Hirshfeld surface analysis are represented by a 2D fingerprint plot of compound **3.1A (Figure 3.21 (c)).** These interactions are H…H(40.2%), C…H(25.0%), O…H(14.8%), N…H(12.4%), C…N(4.5%), C…C(1.4%), C…O(1.0%) and O…O(0.5%). The C…H/H…C interactions contributed 25% of the total contact. They appeared as a pair of distinct spikes in the region of $d_i + d_e \approx 2.8$ Å, showing a pair of wings indicating the presence of C-H…π interactions. Moreover, O…H/H…O and N…H/H…N interactions have a pair of distinct spikes in the region of $d_i + d_e \approx 2.05$ Å and 2.2 Å, respectively. The C…C interactions contribute 1.4% of the Hirshfeld surface, which indicates the presence of the π…π stacking interactions in the crystal compound **3.1A**.

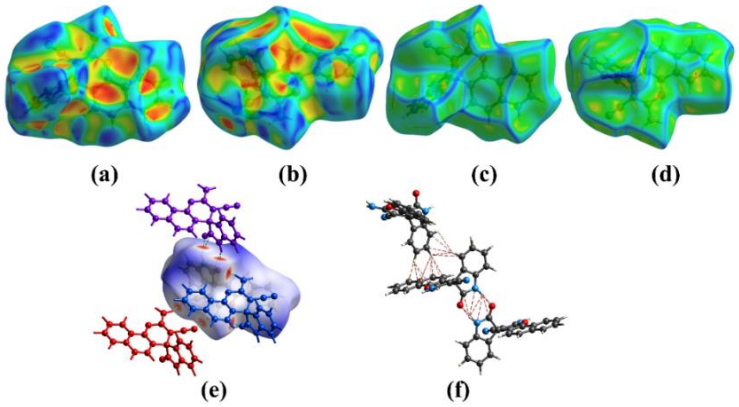

Figure 3.22: (a) and (b) Shape index both side view, (c) and (d) Curvedness both side view, (e) non-covalent hydrogen bond, (f) short non-covalent interactions, in compound **3.1A**

The shape index of the Hirshfeld surface was mapped for compound **3.1A**, where the complimentary red and blue triangles are found in the surface over the pyran ring, and confirmed the π…π stacking interactions in the crystal structure. The yellow-red color concave region around the aromatic ring represents the acceptor region, where the C-H…π and N-H…π interactions occur **(Figure 3.22 (a) & (b)).** The Curvedness plot of the Hirshfeld surface also indicates the flat green region around the pyran ring. The reddish-yellow spots of the curvedness show the strong non-covalent hydrogen bond interactions **(Figure 3.22 (c) & (d)).**

The enrichment ratio (ER) of compound **3.1A** is calculated from the interatomic contacts between pairs of atoms derived from the Hirshfeld surface analysis. This quantity allows the prediction of the propensity of two atoms to form intermolecular interactions. Generally, atomic contacts with a greater enrichment ratio value than unity indicate a high tendency to form intermolecular contacts. The enrichment ratio values of the compound **3.1A** are given in **Table 3.10,** which indicates that C…H/H…C, O…H/H…O, N…H/H…N and C…N/N…C contacts have ER values greater than unity (ER>1). It indicates that C…H, O…H, N…H, and C…N interactions are favorable and act as an important contributor to the stability of the crystallized molecule. Although the H…H is the most abundant interaction (40.2%), the ER of the H…H interactions (E_{HH} = 0.91) is slightly impoverished and disfavored. Moreover, the C…H interaction validates the molecules exhibiting C-H…π interactions. The enrichment ratio of C…C, N…N, O…O, C…O, and O…N interactions are lower than unity and disfavored.

Table 3.10: Enrichment ratio (ER) of compound **3.1A**

Atoms	**H**	**C**	**N**	**O**
H	40.2	Actual contacts (%)		
C	25	1.4		
N	12.4	4.5	0	
O	14.8	1	0.3	0.5
Surface %	66.30	16.65	8.60	8.55
H	44.0	Random contacts (%)		
C	22.1	2.8		
N	11.4	2.9	0.7	

O	11.3	2.8	1.5	0.7
H	0.91	Enrichment ratio		
C	1.13	0.51		
N	1.09	1.57	0.00	
O	1.31	0.35	0.20	0.68

3.8.1.2. Crystal analysis of compound 3.1B

The spiro compound **3.1B** was crystallized in acetone at room temperature by slowly evaporating the solvent. The chiral compound **3.1B** was analyzed using single-crystal XRD **(Figure 3.23).** The compound crystallized with cell lengths **a** = 7.8443(2) Å, **b** = 20.3294(6) Å, **c** = 10.0386(2) Å, i.e., **a** ≠ **b** ≠ **c** and cell angles $\boldsymbol{\alpha}$ = 90°, $\boldsymbol{\beta}$ = 103.840(2)°, $\boldsymbol{\gamma}$ = 90°. The compound exhibits a monoclinic crystal system, with a space group of $P2_1/c$ containing four molecules per unit cell **(Figure 3.24 (a))**.

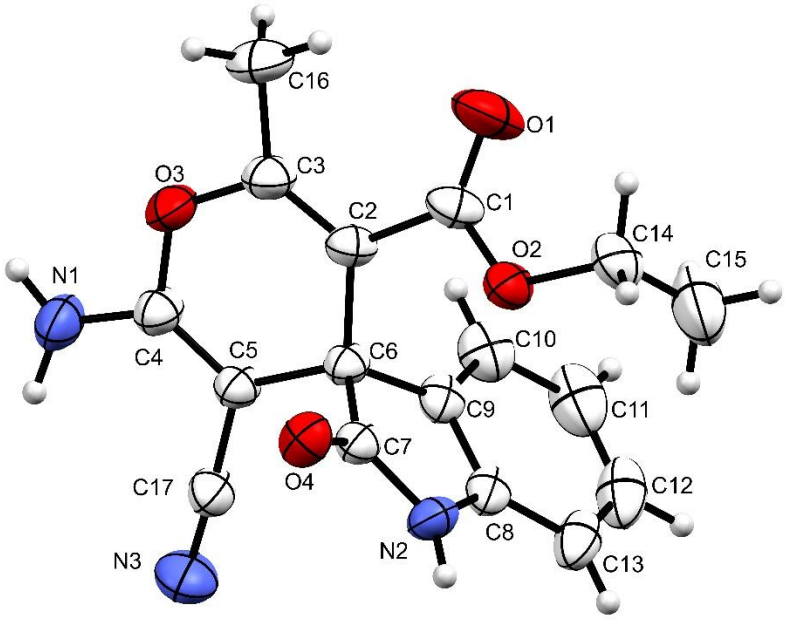

Figure 3.23: ORTEP of compound **3.1B**

The crystal structure of compound **3.1B** shows that although the spiro carbon C6 is sp^3 hybridized, the pyran ring lies on a plane including the C6 atom. Similarly, the fused heterocyclic ring also adopts a planar structure. The atoms C6, C8, C9, and N2 are coplanar, and atom C7 deviates from the plane by 0.124 Å. The dihedral angle

between the plane of the fused heterocyclic ring and the pyran ring is 83.31°. The crystallographic information of compound **3.1B** is summarized in **Table 3.8.**

Supramolecular framework of compound 3.1B: The crystal structure of compound **3.1B** shows that it involves in strong intermolecular interactions of N-H…N, N-H…O, and C-H…O to form self-assembly of the molecules. The nitrogen N3 of the cyanide group acts as a bifurcated acceptor and forms N1-H1B…N3 and N2-H2…N3 interactions with a distance of 2.638 Å and 2.581 Å, respectively, and form $R_2^2(12)$ and $R_2^2(14)$ graph set, respectively **(Figure 3.24 (b))**. However, N1-H1A…O4 intermolecular interaction with a distance of 2.013 Å shows a $R_2^2(14)$ graph set to reinforce the supramolecular association **(Figure 3.24 (d))**. The non-covalent interactions found in compound **3.1B** are tabulated in **Table 3.11.**

Table 3.11: Hydrogen bond and other intermolecular interactions in compound **3.1B**

Donor-H...Acceptor	D – H, Å	H...A, Å	D...A, Å	D - H...A,°
N2-H2…N3	0.860	2.581	3.335	146.91
N1-H1B…N3	0.934	2.638	3.253	123.89
N1-H1A…O4	0.866	2.013	2.868	169.04
N14-H14A…O4	0.970	2.683	3.243	117.24
C12-H12…O1	0.930	2.559	3.340	141.73
C15-H15A…O1	0.960	2.701	3.490	139.87
C14-H14A...π(C8-C13)	0.970	3.513	3.636	134.44
C14-H14B...π(C8-C13)	0.970	2.891	3.636	89.50
C10-H10…π(C8-C13)	0.930	3.764	4.586	149.03
Other contacts				
N2…O4		3.035		
N1…O4		2.868		
Intramolecular				
N1-H1B…C17	0.934	2.536	2.815	97.56
C16-H16B…O1	0.960	2.273	2.893	121.51

C14-H14B…O1	0.970	2.278	2.679	103.74
C15-H15B…π(C8-C13)		3.367		
C15-H15C…π(C8-C13)		3.254		
O2...π(C8-C13)		2.682		

Then, O4 and the ester group interaction form C14-H14A…O4 interaction with a distance of 2.683 Å generate a graph set $R_2^2(16)$ **(Figure 3.24 (d))**. Ester oxygen O1 also acts as a bifurcated acceptor and interacts with C15-H15A…O1 and C12-H12…O1 with a distance of 2.701 Å and 2.559 Å, respectively. C14-H14A…O4, C15-H15A…O1, and C12-H12…O1 in association with N2-H2…N3 also generates a graph set $R_4^3(17)$ **(Figure 3.25 (a))**. Further, compound **3.1B** show some C-H…π interactions at the pyran rings and benzenoid ring plane. The benzenoid ring involved the interactions of C14-H14A…Cg, C14-H14B…Cg and C10-H10…Cg with a distance of 3.513 Å, 2.891 Å, and 3.764 Å help the molecules' association **(Figure 3.25 (b))**. The crystal packing of **3.1B** is stabilized by the interactions involving four molecules, which form the graph sets $R_4^3(17)$ and $R_4^3(18)$ respectively **(Figure 3.25 (a))**.

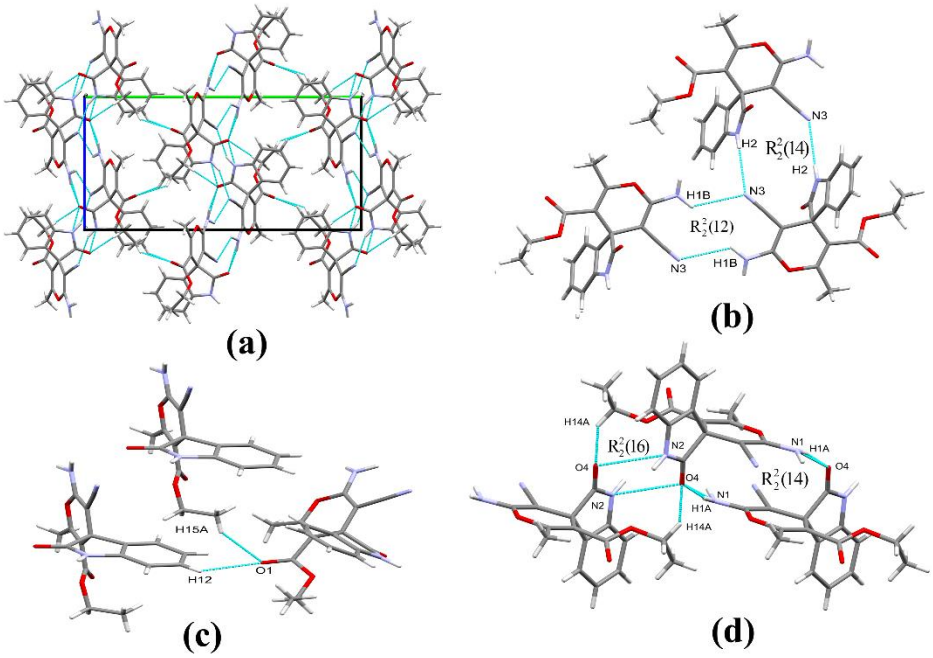

Figure 3.24: (a) Packing diagram, (b) C-H…N and N-H…N interactions, (c) C-H…O interactions, (d) C-H…O and N-H…O interactions, in compound **3.1B**

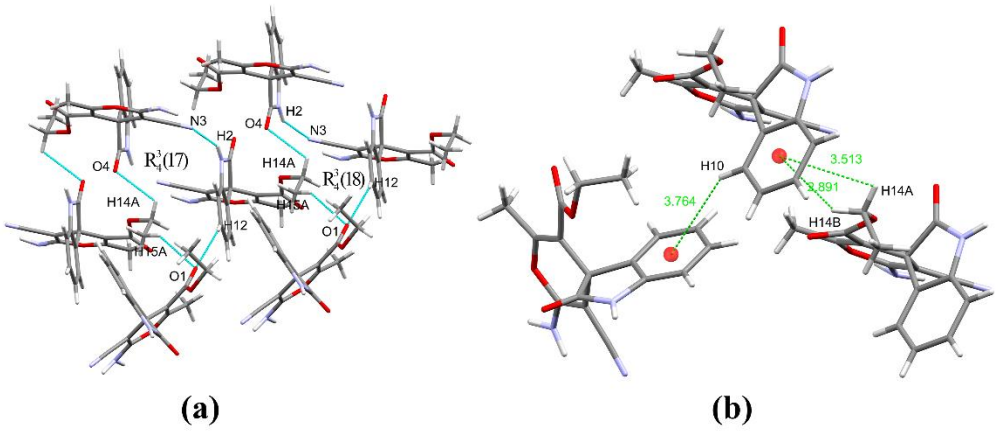

Figure 3.25: (a) C-H…O and N-H…N interactions showing graph sets, (b) C-H…π interactions, in compound **3.1B**

Hirshfeld surface analysis of compound 3.1B: The Hirshfeld surface was mapped over d_{norm} in the range of -0.5694 Å to 1.3868 Å for compound **3.1B** (**Figure 3.26 (a) and (b)).** The region of bright red spots corresponds to short contacts, which are more dominant intermolecular N-H…O interactions. A region of lighter dull red spots was due to N-H…N and C-H…O interactions.

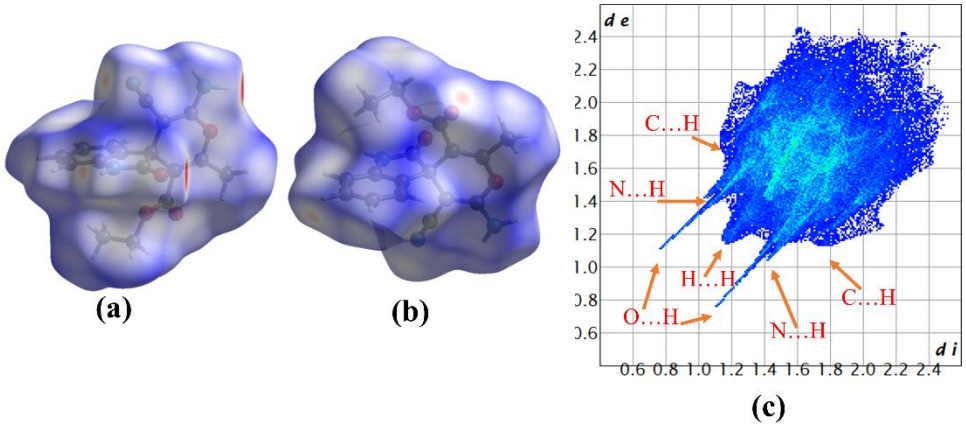

Figure 3.26: (a) and (b) Hirshfeld surface d_{norm} both side view, (c) 2D fingerprint plot showing H…H, O…H, N…H and C…H interactions, in compound **3.1B**

The relative percentage contributions of non-covalent interactions in the Hirshfeld surface are represented by a 2D fingerprint plot of compound **3.1B (Figure 3.26 (c)).** Those interactions are H…H(45.3%), O…H(21.5%), C…H(13.6%), N…H(13.6%), C…O(2.1%), N…O(1.7%), C…N(1.2%), O…O(0.9%) and

C…C(0.1%). H…H has the highest contribution and appears as a single spike in the middle of the 2D fingerprint plot. The O…H/H…O interactions contributed 21.5% and appeared as a pair of distinct spikes in the 2D fingerprint plot of compound **3.1B** in the region of $d_i + d_e \approx 1.85$ Å. However, the N…H/H…N and C…H/H…C interactions have equal contributions to the fingerprint plot, and they are having pair of distinct spikes with $d_i + d_e \approx 2.45$ Å and 2.85 Å, respectively. The C…H/H…C fingerprint plot showed a wing, which indicated the presence of C-H…π interactions.

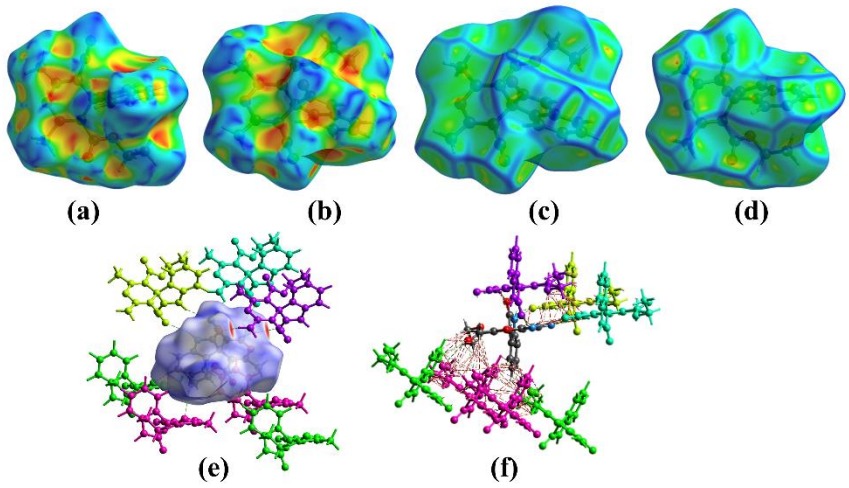

Figure 3.27: (a) and (b) Hirshfeld surface shape index both side view, (c) and (d) Curvedness both side view, (e) non-covalent hydrogen bonding interaction, (f) short interactions in compound **3.1B**

The Hirshfeld surface shape index was mapped for compound **3.1B**, which does not show complimentary red and blue triangles around the aromatic ring surface, indicating the absence of π…π stacking interactions in the compound. The yellowish-red color around the aromatic ring indicates the acceptor region where the C-H…π and N-H…π interactions occur **(Figure 3.27 (a) & (b)).** The Hirshfeld surface curvedness plot also confirms the absence of a flat green region, which was the characteristic of π…π stacking interactions. The yellowish-red spot of the curvedness shows the strong non-covalent hydrogen bond interactions **(Figure 3.27 (c) & (d)).** The presence of weak non-covalent interactions is also supported by the Hirshfeld analysis of the crystal packing around 3.8 Å from the single crystal **(Figure 3.27 (e) & (f))**.

The enrichment ratio (ER) of compound **3.1B** is calculated from the Hirshfeld surface analysis of the interatomic contacts between pairs of interacting atoms. ER is useful in predicting the favorable contacts that are the binding force of the molecular association in a crystal. The ER values less than unity indicates disfavored intermolecular interactions. However, a value more than unity indicates the propensity of the interacting atoms to form intermolecular interactions. The ER values of compound **3.1B** in **Table 3.12** shows that N…H/H…N, C…H/H…C, and O…H/H…O contacts are favored (ER > 1). Interestingly, the H…H contact is disfavored (E_{HH} = 0.93), but it constitutes 69.65% total surface of the crystal. The C…H/H…C favored contacts are attributed to the contribution of C-H…π interactions in the packing of the crystal. Moreover, the N…H/H…N contacts are also favored (E_{NH} = 1.18) and may be attributed to the contribution of N-H…π interactions. The other interactions are disfavored in the enrichment ratio calculation.

Table 3.12: Enrichment ratio (ER) of compound **3.1B**

Atoms	**H**	**C**	**N**	**O**
H	45.3	Actual contacts (%)		
C	13.6	0.1		
N	13.6	1.2	0	
O	21.5	2.1	1.7	0.9
Surface %	69.65	8.55	8.25	13.55
H	48.5	Random contacts (%)		
C	11.9	0.7		
N	11.5	1.4	0.7	
O	18.9	2.3	2.2	1.8
H	0.93	Enrichment ratio		
C	1.14	0.14		
N	1.18	0.85	0.00	
O	1.14	0.91	0.76	0.49

3.8.1.3. Crystal analysis of compound 3.1C

The spiro compound **3.1C** was recrystallized in acetone at room temperature by slow evaporation of the solvent. The chiral compound **3.1C** was analyzed using single-crystal X-ray diffraction **(Figure 3.28).** The compound crystallized with cell lengths **a** = 9.1073(3) Å, **b** = 11.7068(4) Å, **c** = 14.2796(4) Å, i.e., **a** ≠ **b** ≠ **c** and cell

angles $\boldsymbol{\alpha}$ = 90°, $\boldsymbol{\beta}$ = 91.422(3)°, $\boldsymbol{\gamma}$ = 90°, i.e., $\boldsymbol{\alpha = \gamma = 90°, \beta \neq 90°}$. It indicates that the compound exhibits a monoclinic crystal system, with space group $P2_1/n$ that contains four molecules per unit cell **(Figure 3.29 (a)).**

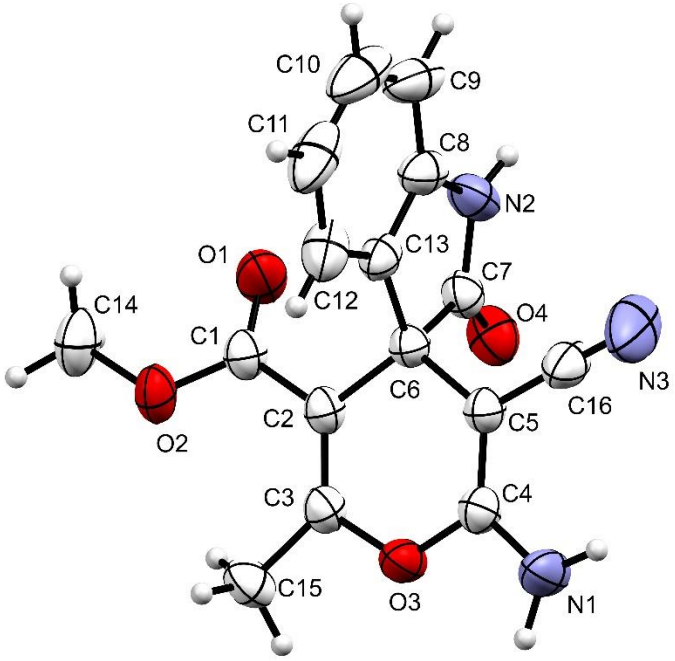

Figure 3.28: ORTEP diagram of **3.1C**

Although the spiro carbon C6 is sp^3 hybridized, the chiral asymmetric compound **3.1C** crystal structure shows that the atoms C2-C5 and O3 lie in one plane with the carbon C6 atom. Similarly, the fused heterocyclic ring also adopts a planar structure. The plane of the fused heterocyclic ring is almost perpendicular to the plane of the pyran ring. The dihedral angle between the two planes is 87.14°. The crystallographic information is summarized in **Table 3.13.**

Table 3.13: Crystal data of compounds **3.1C** and **3.1D**

Compound	**3.1C**	**3.1D**
Identification code	2222472	2222471
Formula weight	311.29	295.29
Temperature (K)	293(2)	293(2)
Crystal system	monoclinic	monoclinic
Space group	$P2_1/n$	$P2_1/n$
a/Å	9.1073(3)	7.5954(2)
b/Å	11.7068(4)	7.9549(2)

c/Å	14.2796(4)	23.5107(7)
α/°	90	90
β/°	91.422(3)	97.115(3)
γ/°	90	90
Volume (Å^3)	1521.98(8)	1409.59(7)
Z	4	4
ρ (calcg/cm^3)	1.359	1.391
μ (mm^{-1})	0.100	0.099
F(000)	648.0	616.0
Crystal size (mm^3)	0.32 × 0.25 × 0.24	0.2 × 0.2 × 0.19
Radiation	MoKα (λ = 0.71073)	MoKα (λ = 0.71073)
2Θ range for data collection (°)	6.296 to 54.57	6.79 to 54.862
Index ranges	-11 ≤ h ≤ 11, -14 ≤ k ≤ 14, -17 ≤ l ≤ 17	-9 ≤ h ≤ 8, -8 ≤ k ≤ 10, -24 ≤ l ≤ 29
Reflections collected	12618	11203
Independent reflections	3194 [Rint = 0.0312, Rsigma = 0.0313]	3008 [Rint = 0.0286, Rsigma = 0.0292]
Data/restraints/parameters	3194/0/218	3008/0/209
Goodness-of-fit on F^2	1.051	1.056
Final R indexes [I>=2σ (I)]	R1 = 0.0475, wR2 = 0.1198	R1 = 0.0435, wR2 = 0.1052
Final R indexes [all data]	R1 = 0.0648, wR2 = 0.1321	R1 = 0.0543, wR2 = 0.1130
Largest diff. peak/hole/e Å^{-3}	0.18/-0.23	0.19/-0.20

Supramolecular framework of compound 3.1C: The molecular interactions of compound **3.1C** involves a strong N-H…O intermolecular interaction between the hydrogen H2 of the amide group with the carbonyl oxygen O1 of the ester moiety at a bond distance of 2.004 Å, which results in the formation of $R_2^2(14)$ graph set **(Figure 3.29 (b))**. The oxygen O4 acts as a bifurcated acceptor and forms an N-H…O bond with the hydrogen H1B from the amine group at a distance of 1.906 Å. It also forms a C-H...O bond with the benzenoid hydrogen H10 at a distance of 2.613 Å. The hydrogen H1B of the amine group is bifurcated and forms N-H...C bond with the partially positive carbon C7 within the fused heterocyclic ring having a bond distance of 2.844 Å. This intermolecular N-H…O, C-H…O, and N-H…C interactions altogether involve four molecules of compound **2.1C** form $R_4^3(25)$ graph sets **(Figure 3.30 (a))**. The N-H…O and N-H…C interactions formed by the bifurcated hydrogen H1B together with

the C-H…N interactions between the alkyl hydrogen H15B and the nitrogen N3 from the cyano group at an interaction distance 2.480 Å also forms $R_4^4(24)$ and $R_4^4(26)$ graph sets which involved four molecules of compound **3.1C (Figure 3.29 (c) and (d))**.

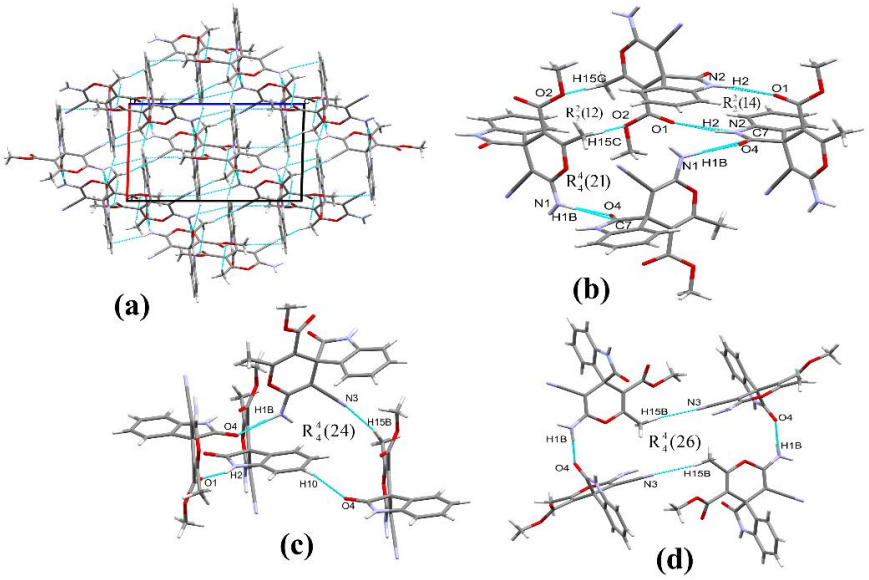

Figure 3.29: (a) Crystal packing along the b-axis, (b) C-H…O and N-H…O interactions, (c) and (d) C-H…O and C-H…N interactions, in compound **3.1C**

Furthermore, this C-H…N interaction, including the C-H…O interaction formed by the bifurcated acceptor O4 along with the N-H…C interaction formed between the hydrogen H1A of the amine group and the carbon C10 of the fused heterocyclic ring at a distance of 2.817 Å forming $R_3^2(15)$ graph set. C-H stabilizes the crystal packing within the unit cell C-H…N interaction mentioned above and the C-H…O interactions between the alkyl hydrogen H15C and the oxygen O2 of the ester moiety at an interaction distance of 2.620 Å. These C-H…O interactions stabilize the crystal packing, forming a graph set of $R_2^2(12)$ **(Figure 3.29 (b))**. Beyond these interactions, the molecular association of compound **3.1C** shows two C-H…π interactions at the two sides of the benzenoid ring plane with the amine hydrogen H1A and the alkyl hydrogen H14B of the ester moiety at a distance of 2.909 Å and 2.954 Å respectively **(Figure 3.30 (b))**. The hydrogen bonds and other non-covalent intermolecular interactions are illustrated in **Table 3.14.**

Table 3.14: Hydrogen bonds and other intermolecular interactions in **3.1C**

Donor-H...Acceptor	D – H, Å	H...A, Å	D...A, Å	D - H...A,°
C10-H10…O4	0.930	2.613	3.498	159.33
N1-H1B…O4	0.929	1.906	2.828	171.13
N1-H1B…C7	0.929	2.844	3.761	169.29
C15-H15C…O2	0.960	2.620	3.394	137.82
N2-H2…O1	0.860	2.044	2.886	165.93
N1-H1A…C10	0.853	2.817	3.495	137.65
C15-H15B…N3	0.960	2.480	3.421	166.54
N1-H1A…π(C8-C13)	0.853	2.909	3.533	131.5
C14-H14B…π(C8-C13)	0.96	2.954	3.537	120.29
C14-H14C…π(C8-C13)	0.960	3.793	3.537	67.39
C14-H14A...π(C8-C13)	0.960	3.368	3.537	92.19
Intramolecular				
C14-H14B…O1	0.960	2.609	2.628	80.57
C14-H14C…O1	0.960	2.579	2.628	82.30
C15-H15B…O2	0.960	2.415	2.853	107.35
N1-H1A…C16	0.853	2.550	2.822	99.70

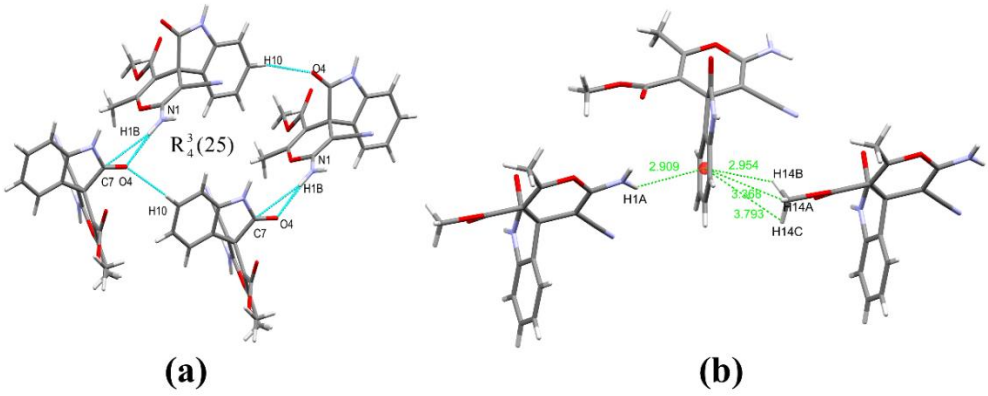

Figure 3.30: (a) N-H…O and C-H…O interactions showing graph set, (b) C-H…π and N-H…π interactions, in compound **3.1C**

Hirshfeld surface analysis of compound 3.1C: The Hirshfeld surface mapped over the d_{norm} in the range of -0.60 to 1.47 Å for compound **3.1C** is displayed in **Figure**

3.31 (a) and (b). The lighter white and blue regions of the Hirshfeld surface indicate weaker interactions due to more extended contacts, which are more significant or equal to the van der Waals interatomic distances. The region of bright red spots corresponds to short contacts, which arise due to N-H…O interactions that are more dominant than other contacts. The lighter red, dull color spots also correspond to weaker C-H…O, C-H…N, and N-H…C interactions. The intensity of the red color decreases as a decrease in bond strength.

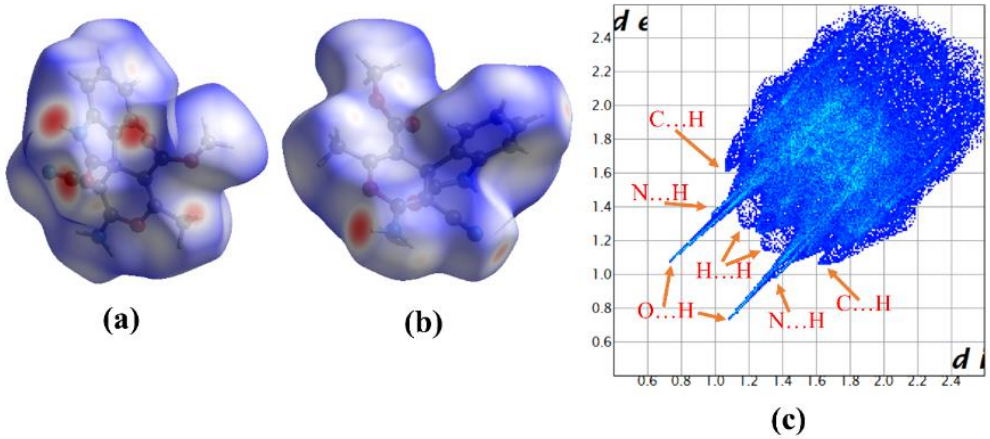

Figure 3.31: (a) and (b) Hirshfeld surface d_{norm} both side view, (c) 2D fingerprint plot showing H…H, O…H, N…H and C…H interactions, in compound **3.1C**

The 2D fingerprint plot of compound **3.1C** shows the relative percentage contributions of non-covalent interaction to the Hirshfeld surface **(Figure 3.31 (c))**. Those interactions are H…H(36.3%), O…H(25.1%), C…H(19.7%), N…H(16.5%), O…O(1.0%), O…N(0.6%), C…O(0.5%) and C…N(0.3%). The O…H/H...O interactions appear as a pair of distinct spikes in the 2D fingerprint plot of compound **3.1C** in the region of $d_i + d_e \approx 1.8$ Å. Similarly, N...H intermolecular interactions also appear as a pair of distinct shorter spikes that clubbed to the O…H spike in the region of $d_i + d_e \approx 2.4$ Å in the 2D fingerprint plot. The C-H...π and C...H contacts also appear in the same region on the 2D fingerprint plot in the region of $d_i + d_e \approx 2.7$ Å, which appears as a characteristic flipped wings-like pattern.

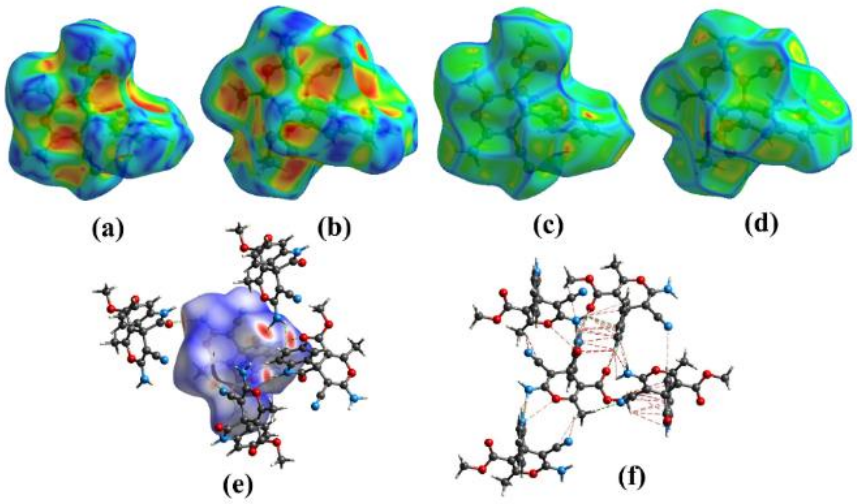

Figure 3.32: (a) and (b) shape index both side view, (c) and (d) curvedness both side view, (e) non-covalent hydrogen bond interactions, (f) non-covalent short contacts interactions, in compound **3.1C**

The red and blue regions indicate the acceptor and donor properties in the Hirshfeld shape index. The Hirshfeld surface mapped over the shape index in a range of -1 to 1 Å for compounds **3.1C** does not have any complementary pair of red and blue triangles having an edge-to-edge connection around the pyran ring surface which indicates the absence of stacking interactions **(Figure 3.32 (a) & (b))**. The concave regions with yellowish-red color in the shape index around the surface of the benzenoid ring indicate the acceptor region where weak C-H...π interactions occur. In the curvedness plot, the yellow and red-yellow colored spots indicate weak and robust hydrogen bond interactions in the crystal. Similarly, the Hirshfeld surface mapped over the curvedness in a range of -4 to 0.4 Å for compound **3.1C** also does not have a flat green region with a yellowish spot around the pyran ring surface, which indicate the absence of stacking interaction **(Figure 3.32 (c) and (d))**.

The non-covalent N-H…O, N-H…C, C-H…O, C-H…N, C-H…π and N-H…π interactions found within the supramolecules are also supported by the Hirshfeld analysis around the cluster of radius 3.8 Å of a single crystals fragments **(Figure 3.32 (e) & (f)).**

The enrichment ratio (ER) of compound **3.1C** is an important estimation of the interatomic contacts between the interacting atoms calculated from the Hirshfeld

surface analysis. Usually, the atoms with greater enrichment ratio values than unity indicate a high propensity to form intermolecular contacts. The enrichment ratio values of the compound **3.1C** are given in **Table 3.15,** which suggests that C…H/H…C, N…H/H…N and O…H/H…O contacts have enrichment ratio greater than unity (ER > 1). Thus, these interactions are favorable and act as an important contributor to the stability of the crystallized molecule. The H…H interactions occupy around 67% of the Hirshfeld surface, but the enrichment ratio value is only 0.81, and the interaction was disfavored. Therefore, the C…H interactions also validate the existence of C-H…π interactions in the crystal molecule. In some other interactions, C…C, N…N, C…N, O…O, O…C, and O…N interaction values are less than unity, and their interactions are disfavored.

Table 3.15: Enrichment ratio (ER) of compound **3.1C**

Atoms	**H**	**C**	**N**	**O**
H	36.3	Actual contacts (%)		
C	19.7	0		
N	16.5	0.3	0	
O	25.1	0.5	0.6	1
Surface %	66.95	10.25	8.70	14.10
H	44.8	Random contacts (%)		
C	13.7	1.1		
N	11.6	1.8	0.8	
O	18.9	2.9	2.5	2.0
H	0.81	Enrichment ratio		
C	1.44	0.00		
N	1.42	0.17	0.00	
O	1.33	0.17	0.24	0.50

3.8.1.4. Crystal analysis of compound 3.1D

The spiro compound **3.1D** was recrystallized in acetone at room temperature by slow evaporation of the solvent. The chiral compound **3.1D** was analyzed using single-crystal X-ray diffraction **(Figure: 3.33).** The compound crystallized with cell lengths **a** = 7.5954(2) Å, **b** = 7.9549(2) Å, **c** = 23.5107(7) Å, i.e., **a** ≠ **b** ≠ **c** and cell angles $\boldsymbol{\alpha}$ = 90°, $\boldsymbol{\beta}$ = 97.115(3)°, $\boldsymbol{\gamma}$ = 90°, i.e., $\boldsymbol{\alpha = \gamma = 90°, \beta \neq 90°}$. It indicates that

the compound exhibits a monoclinic crystal system, with space group $P2_1/c$ that contains four molecules per unit cell **(Figure 3.34 (a)).**

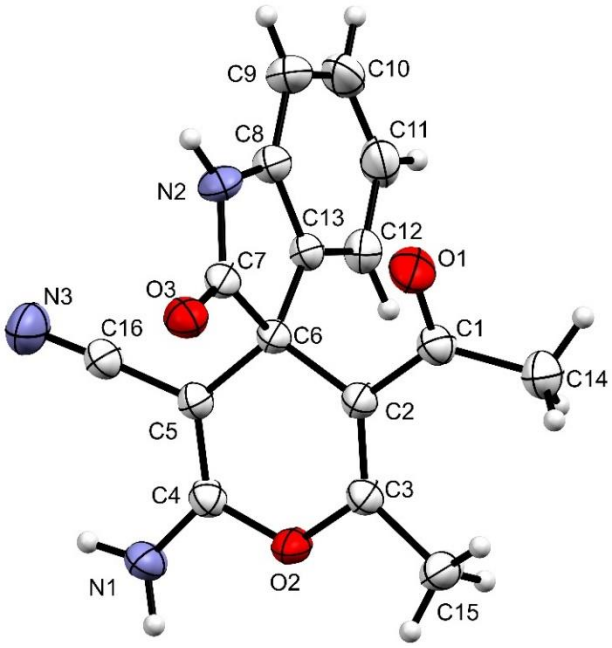

Figure 3.33: ORTEP diagram of **3.1D**

The chiral asymmetric compound **3.1D** crystal structure shows that although the spiro carbon C6 is sp^3 hybridized, the atoms C2, C3, C4, C5, and O2 lie in one plane with the carbon C6 atom. Similarly, the fused heterocyclic ring also adopts a planar structure. The plane of the fused heterocyclic ring almost lies perpendicular to the plane of the pyran ring. The dihedral angle between the two planes is 85.83°. The crystallographic information is summarized in **Table 3.13.**

Supramolecular framework of compound 3.1D: The crystal structure of compound **3.1D** involves a strong N-H…N intermolecular interaction at a bond distance of 2.341 Å between the hydrogen H1B of the amino group and the nitrogen N3 of the cyano group. Ith results in the formation of an asymmetric dimer containing the $R_2^2(12)$ graph set **(Figure 3.34 (b))**. The carbon C4 of the pyran ring is a partially positive charge. It forms C-H…C intermolecular interaction with the alky hydrogen H15C from the different layers at a distance of 2.869 Å which results in forming $R_2^2(10)$ graph sets. The carbon C7 and oxygen O3 from the fused heterocyclic ring act as a bifurcated acceptor and interact through C-H…C, C-H…O, N-H…C, and N-H…O

through intermolecular interactions with the hydrogen H9 from the benzenoid ring moiety and the other hydrogen H1A from the amine group at a distance of 2.818 Å, 2.387 Å, 2.871 Å and 1.957 Å respectively. These N-H…C and N-H…O between the two compounds results in the formation of another $R_2^2(12)$ graph sets as well as an $R_2^2(14)$ graph set **(Figure 3.34 (b))**.

Similarly, these C-H…C and C-H…O interactions, along with the N-H…O interactions at a distance of 2.285 Å between the hydrogen H2 and the oxygen O1 from the amide group and the carbonyl group, respectively, also form a graph sets of $R_2^2(10)$ and $R_2^2(11)$ **(Figure 3.34 (c))**. The crystal packing of compound **3.1D** is also stabilized by those C-H…C, C-H…O, N-H…C, and N-H…O interactions found for the bifurcated acceptor as the N-H…O interactions between the amide and the carbonyl group. Beyond these, the supramolecular interaction also displays C-H…π from both the two faces of the aromatic benzenoid ring plane where the hydrogen H10 comes from the benzenoid itself and the other hydrogen H14C and H14A comes from the other alkyl group **(Figure 3.34 (d))**.

Table 3.16: Hydrogen bonds and other intermolecular interactions in **3.1D**

Donor-H...Acceptor	D – H, Å	H...A, Å	D...A, Å	D - H...A,°
C14-H14A…C10	0.960	2.793	3.516	132.82
N2-H2…O1	0.860	2.285	3.054	149.07
C9-H9…O3	0.930	2.387	3.217	148.56
C9-H9…C7	0.930	2.818	3.645	148.63
C15-H15C…C4	0.960	2.869	3.741	151.62
N1-H1B…N3	0.863	2.341	3.160	158.58
N1-H1A…O3	0.909	1.957	2.863	175.24
N1-H1A…C7	0.909	2.871	3.721	156.32
C10-H10…π(C8-C13)	0.93	3.208	4.006	145.06
C14-H14C…π(C8-C13)	0.96	2.981	3.48	113.66
C14-H14A…π(C8-C13)	0.96	3.082	3.48	106.57
Intramolecular				
C15-H15B…C1	0.960	2.803	3.134	101.20
N1-H1B…C16	0.863	2.595	2.837	97.38

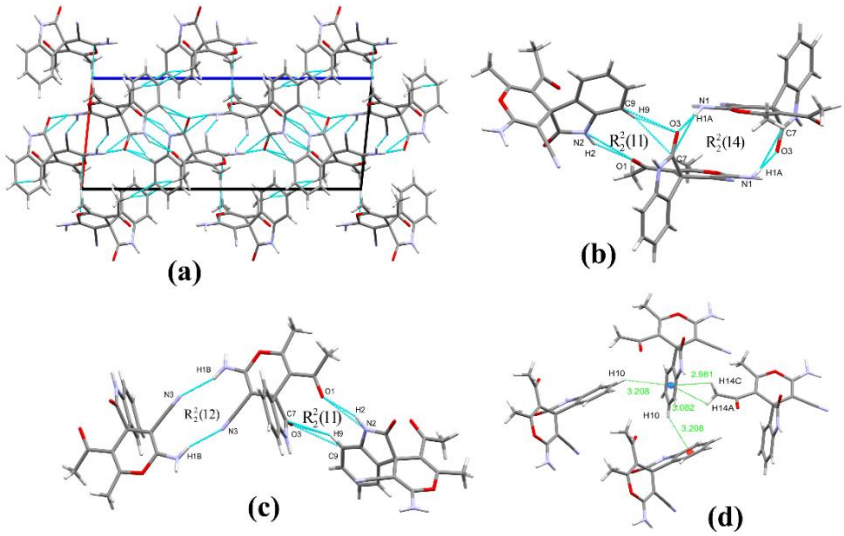

Figure 3.34: (a) Packing diagram, (b) N-H…O and C-H…O interactions, (c) N-H…N, C-H…O and N-H…O interactions, and (d) C-H...π interactions, in compound **3.1D**

Hirshfeld surface analysis of compound 3.1D: The Hirshfeld surface mapped over the d_{norm} in the range of -0.58 Å to 1.55 Å for compound **3.1D** is displayed in **Figure 3.35 (a) and (b).** The lighter white and blue regions of the Hirshfeld surface indicate weaker interactions due to more extended contacts, which are more significant or equal to the van der Waals interatomic distances. The region of the red spots corresponds to short contacts which arise from N-H…N, N-H…N, and C-H…O interactions. The intensity of the red color increases for interactions with shorter bond distances and vice versa.

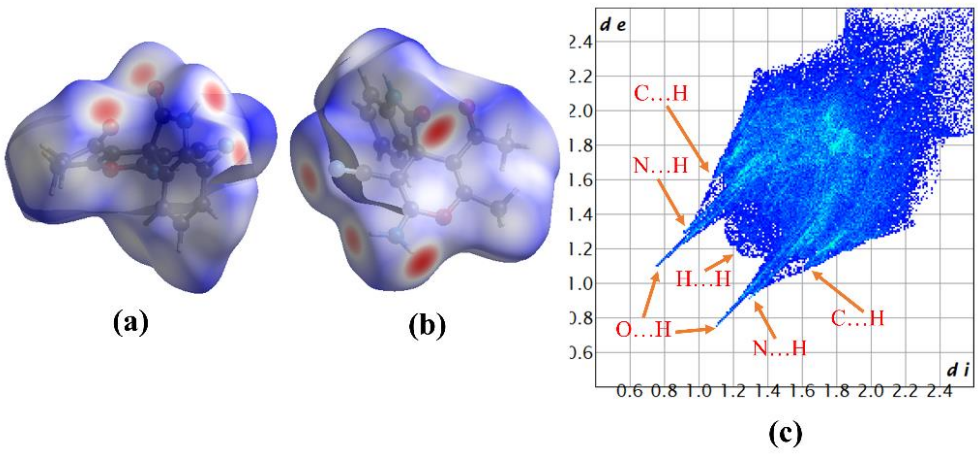

Figure 3.35: (a) and (b) Hirshfeld surface d_{norm} both side view, (c) 2D fingerprint plot showing O…H, N…H, C…H and H…H interactions, in compound **3.1D**

The 2D fingerprint plot of compound **3.1D** shows the relative percentage contributions of non-covalent interaction to the Hirshfeld surface **(Figure 3.35 (c))**. Those interactions are H…H(33.0%), O…H(25.0%), C…H(20.6%), N…H(17.4%), C…O(1.6%), O…N(0.8%), C…N(0.7%), O…O(0.5%), C…C(0.3%) and N…N(0.1%). O…H/H...O interactions appear as a pair of distinct longer spikes in the 2D fingerprint plot of compound **3.1D** in the region of $d_i + d_e \approx 1.8$ Å. Similarly, N...H/H...N intermolecular interactions also appear as a pair of distinct shorter spikes close to the O…H spike in the region of $d_i + d_e \approx 2.2$ Å in the 2D fingerprint plot. The C-H...π intermolecular interactions also appear within the C...H contacts in the same region on the 2D fingerprint plot in the region of $d_i + d_e \approx 2.7$ Å, which appears as a characteristic wings-like pattern. The relative contribution of C…C close contacts, which account for 0.3%, indicates the absence of stacking interaction.

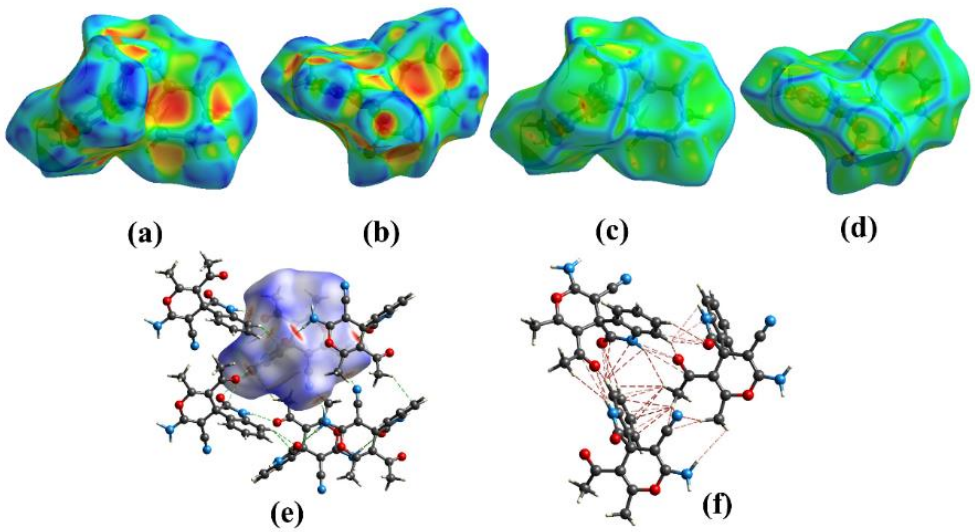

Figure 3.36: (a) and (b) Shape index both side view, (c) and (d) Curvedness both side view, (e) non-covalent hydrogen bonding interactions, (f) non-covalent short contacts within 3.8 Å radius, of compound **3.1D**

In the Hirshfeld shape index, the red region indicates acceptor property, and the blue region indicates donor property. The Hirshfeld surface mapped over the shape index in a range of -1 to 1Å for compounds **3.1D** does not have any complementary pair of red and blue triangles having an edge-to-edge connection around the pyran ring surface which indicates the absence of stacking interactions **(Figure 3.36 (a) & (b))**. The yellowish-red colored concave regions in the shape index around the surface of

the benzenoid ring indicate the acceptor region where weak C-H...π interaction occurs. In the curvedness plot, the yellow and yellow-red colored spots indicate weak interactions and strong hydrogen bond interactions in the crystal. Similarly, the Hirshfeld surface mapped over the curvedness in a range of -4 to 0.4 Å for compound **3.1D** also does not have a flat green region with a yellowish spot around the pyran ring surface, which indicate the absence of stacking interactions between the aromatic ring **(Figure 3.36 (c) & (d))**.

The presence of weak non-covalent N-H…O, N-H…N, N-H…C, C-H…C, C-H…O and C-H…π interactions is also supported by Hirshfeld weak intermolecular interactions analysis. The calculation is done around the cluster of radius 3.4 Å from single crystal fragments **(Figure 3.36 (e) & (f)).**

The enrichment ratio (ER) of compound **3.1D** was calculated from the interatomic contacts between pairs of atoms resulting from Hirshfeld surface analysis. The enrichment ratio values indicate the prediction of the tendency of two atoms to form intermolecular interactions. Generally, the interaction bearing a greater enrichment ratio value than unity has positive interactions between the interacting atoms. The enrichment ratio of compound **3.1D** is given in **Table 3.17**. The hydrogen contributes 64.5% of the total surface, but the enrichment ratio of H…H contacts is only 0.79, less than unity and disfavored interaction. The ER of C…H, N…H, and O…H are more than unity and favorable contacts; they are an important contributor to the stability of the crystal. Moreover, the C…H interactions indicate the presence of C-H…π interactions in the molecules. The other interactions C…C, N…N, O…O, C…N, C…O, and O…N, show an enrichment ratio lower than unity, and their interactions are disfavored.

Table 3.17: Enrichment ratio of compound **3.1D**

Atoms	**H**	**C**	**N**	**O**
H	33	Actual contacts (%)		
C	20.6	0.3		
N	17.4	0.7	0.1	
O	25	1.6	0.8	0.5
Surface %	64.50	11.75	9.55	14.20

H	41.6	Random contacts (%)		
C	15.2	1.4		
N	12.3	2.2	0.9	
O	18.3	3.3	2.7	2.0
H	0.79	Enrichment ratio		
C	1.36	0.22		
N	1.41	0.31	0.11	
O	1.36	0.48	0.29	0.25

3.9. *In silico* molecular docking studies of compounds 2.1A-2.1F and 3.1A-3.1D

There are several mechanisms that a cell can use to fix a problem, like damaged DNA or a block to replication. However, these mechanisms can take a long time, and it is essential in the cell to continue the cell cycle, and cell cycle checkpoints (Chk) help with this to fix (Clarke & Giménez-Abián, 2000; Foloppe et al., 2006; Rhind & Russell, 1998). Checkpoints are signal transduction pathways that identify a problem and halt the fundamental cell cycle machinery until the issue is resolved by delaying the progression of the cell cycle. The checkpoint kinase 1 (Chk1) is a main factor of the DNA damage response, a molecular network allotted to continue genome integrity (Maugeri-Saccà et al., 2013). Checkpoint-1 kinase plays an essential role in the G2M cell cycle control, so its inhibition by small molecules is of significant therapeutic interest in oncology (Sanchez et al., 1997).

Human aldo-keto reductase family one member C3 (AKR1C3) is called a hormone activity controller and prostaglandin F (PGF) synthase that controls the possession of hormone receptors and cell proliferation. Many studies have investigated AKR1C3 inhibitors because of their overexpression in metabolic diseases, various hormone-dependent and hormone-independent carcinomas, and the emergence of clinical drug resistance (Liu et al., 2020). A promising therapeutic target for prostate cancer that resists castration is AKR1C3 (Zhou & Limonta, 2014).

Lung cancer accounts for 11.7% of all cancers worldwide, and in terms of incidence and mortality, it is the most common type of cancer. A malignant tumor poses the greatest threat to human life and health (Sung et al., 2021). The transmembrane receptor tyrosine kinase, anaplastic lymphoma kinase (ALK), was first

discovered in the nucleophosmin (NPM) of anaplastic cells of lymphoma (Bossi et al., 2010). The ALK protein has been observed to stimulate mitogenic and anti-apoptotic signaling pathways linked with various human cancers (Tripathy et al., 2011). As a result, the ALK receptor has appeared as an attractive target for cancer treatment. Spirooxindole derivatives have been shown to have anti-cancer activity and to be a promising scaffold in this regard (Parthasarathy et al., 2013). Therefore, all the synthesized compounds in scheme 3 were subjected to docking studies against the human anaplastic lymphoma kinase protein to determine the potential binding and to predict their activity as an anti-cancer agent.

The compounds synthesized in scheme **2** and scheme **3** are studied for the binding interaction with Chk1, ARK1C3, and ALK enzyme retrieved from the RSCB protein data bank (PDB id: 6FC8, 1S2A and 2XP2, respectively) using AutoDockVina. The protein was prepared using chimera by removing co-factors, co-crystallized ligands, and embedded water. Polar hydrogen and Kollman charges are added using Autodock tool software and saved in pdbqt format. The ligands are converted from their CIF file to PDB using mercury software and then converted into pdbqt format using open babel. The Chk1 grid parameters are set as x = 2.41, y = -2.87, z = 41.89; 15 Å x 15 Å x 21.82 Å, that of ARK1C3 grid parameters are x = 24.91, y = -27.48, z = 61.07; 20 Å x 20 Å x 32 Å, while 2XP2 grid parameter is set at x = 29.61, y = 47.37, 9.75; 40 Å x 40 Å x 40 Å. Redocking validates the docking results. Therefore, the docking results were analyzed using discovery studio and pymol.

Compounds **2.1A, 2.1B, 2.1C, 2.1E,** and **2.1F** from scheme **2** are docked with the Chk1 enzyme for their binding affinities calculation. The results show that all the compounds formed a hydrogen bond with residue Cys87 with a pyran oxygen atom and amine hydrogen in **2.1B** and **2.1E**, pyrazole ring nitrogen and its hydrogen in **2.1C** at the highly conserved ATP binding pocket, except **2.1A** which show hydrogen bond with Glu85 and Ser147 **(Figure 3.37 (a))**. Compounds **2.1A, 2.1C**, and **2.1F** have hydrogen bonding with Glu85 residue with the amine hydrogen atom, where Glu85 and Cys87 are the suggested hydrogen bond interactions in the active site of Chk1. The binding scores are tabulated in **Table 3.18**, which shows that compounds **2.1A, 2.1B,**

and **2.1E**, respectively, exhibited docking scores -8.1, -7.6, and -7.5 kcal/mol, respectively **(Figure 3.37 (c))**.

Table 3.18: Binding score and residue involved in the interaction of **2.1A-2.1F** with Chk1 protein

Chk1			
Compounds	Docking score (kcal/mol)	Residues involved in H-bond	Residues involved in other interactions (π…anion, π…cation, π...σ, π...π, π…alkyl, and alkyl)
2.1A	-8.1	Glu85, Ser147	Leu15, Val23, Ala36, Val68, Leu84, Cys87, Leu137
2.1B	-7.6	Glu17, Cys87, Glu91	Val23, Ala36, Val68, Leu84, Leu137, Asp148
2.1C	-6.9	Glu85, Cys87	Leu15, Val23, Ala36, Tyr86, Leu137
2.1E	-7.5	Cys87	Val23, Ala36, Val68, Leu84, Glu91, Leu137, Asp148
2.1F	-6.3	Glu85, Cys87	Leu15, Val23, Ala36, Tyr86, Glu134, Leu137

Compound **2.1B** interacts with Glu17 and Glu91 through a carbon-hydrogen bond with the methoxy group to stabilize the interaction. The π-π stacked interaction was exhibited with amino acid residue Tyr86 in compounds **2.1C** and **2.1F**, π-σ interaction with Leu137 in **2.1A, 2.1C,** and **2.1F**, and π-sulfur interaction with Cys87 amino acid residue in **2.1C** and **2.1F** at the active site. The electrostatic π-anion interactions were exhibited with Glu91 and Asp148 in **2.1B** and **2.1E**. Hydrophobic alkyl interaction was also displayed with Val23, Leu84, Leu15, Leu137, and Val23 residues. All compounds exhibited hydrophobic π-alkyl interactions with Val23, Ala36, Val68, Leu84, and Leu137; beyond this, **2.1C** and **2.1F** show Leu15 and Cys87 whereas **2.1A** also exhibit π-alkyl interaction. The compounds' orientation in the

enzyme's active site is almost identical except for **2.1A**, which has an opposite orientation to the others.

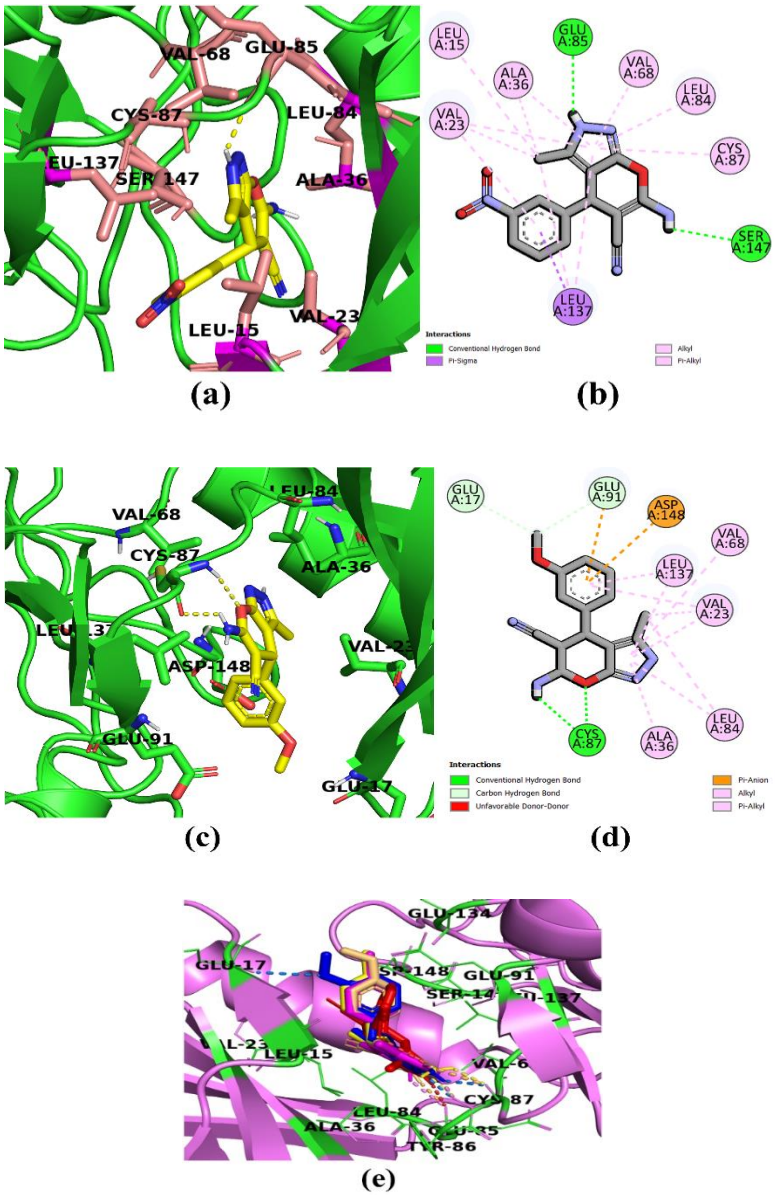

Figure 3.37: Binding of compounds in Chk1 enzyme (a) & (b) **2.1A,** (c) & (d) **2.1B**, (e) overlay diagram: **2.1A** (red), **2.1B** (blue), **2.1C** (magenta), **2.1F** (orange)

Table 3.19: Binding score and residue involved in the interaction of **2.1A-2.1F** with ARK1C3 protein

AKR1C3			
Compounds	Docking score (kcal/mol)	Residues involved in H-bond	Residues involved in other interactions (π…anion, π…cation, π...σ, π...π, π…alkyl, and alkyl)
2.1A	-9.4	Ser217	Tyr24, Tyr55
2.1B	-9.2	Gln190	Tyr24, Tyr55, His117, Tyr216, Gln222, Trp227, Phe306
2.1C	-8.6	Asp50, Gln190	Tyr24, Leu54, Trp227, Lys270
2.1E	-8.5	Gln190	Tyr24, Leu54, Tyr55, His117, Tyr216, Gln222, Trp227
2.1F	-8.9	Glu192, Tyr216, Ser221, Arg223	Tyr24, Tyr55, Trp227

The synthesized compounds from scheme **2** also did the computational screening with the AKR1C3 enzyme, and their binding affinities are displayed in **Table 3.19**. The compound **2.1A** illustrate the highest binding affinities with a core of -9.4 kcal/mol, having a hydrogen bonding with residue Ser217. Methyl group of the pyrazole ring in **2.1A** forms σ-π interaction with Tyr24 of the target receptor. Tyr55 residue exhibits C-H-π (T-shaped) stacking with pyrazole ring and π-alkyl interactions in the active site of the enzyme **(Figure 3.38 (a))**. The hydrogen bond interaction with Gln190 was found in **2.1B (Figure 3.38 (b))** with amine nitrogen, and the interaction was stabilized by hydrophobic π-σ interaction. C-H-π stacking interaction with the methyl group of pyrazole ring with Tyr216 and methoxy group with Trp227, C-H-π (T-shaped) interaction was also found between the benzene ring with Tyr24 and pyrazole ring with Tyr55. Their arrangement in the enzyme's active site is not the same; **2.1C** and **2.1E** are arranged in the same orientation, **2.1A** structure is arranged at the pyranopyrazole moiety inside the cavity, but in **2.1F**, the peranopyrazole ring

conformation changes. Thus, all the compounds enter the active site pocket of the ARK1C3 enzyme **(Figure 3.38 (c))**.

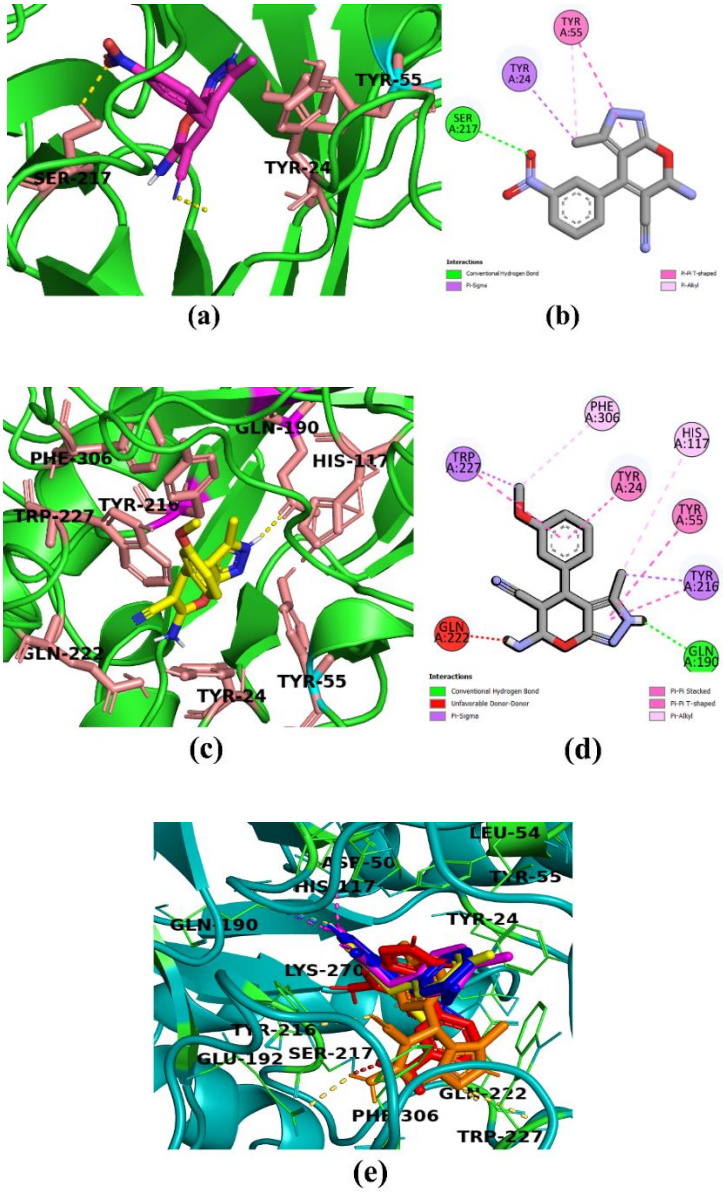

Figure 3.38: Compounds binding in ARK1C3 protein (a) & (b) **2.1A,** (c) & (d) **2.1B**, (e) overlay diagram: **2.1A** (red), **2.1B** (blue), **2.1C** (magenta), **2.1E** (yellow), **2.1F** (orange)

The binding study with ALK receptor of the scheme **3** compounds was studied by molecular docking. All four compounds **(3.1A-3.1D)** show hydrogen bonding with the receptor enzyme **(Table 3.20)**. Compound 3.1A shows higher estimated binding

energy with a binding score of -8.7 kcal/mol. In compound **3.1A**, the hydrogen bonding interaction favors the primary amino nitrogen present in the bulkier chromene ring with Asp1276 **(Figure 3.39 (a) & (b))**. Moreover, the chromene ring was found to have other electrostatic interactions, π-cation with Arg1275 and π-anion with Glu1167 residues, and hydrophobic interaction of residue Phe1127 exhibit π-σ and π-π T-shaped interaction. Thus, the indoline ring show π-alkyl interaction with Ala1126 residue. The other compounds, **3.1B, 3.1C**, and **3.1D**, also form hydrogen bonding with Arg1253, Lys1150, and Asn1254 residues of the ALK enzyme active site **(Figure 3.39 (c) & (d))**. The π-σ interaction is also found with Val1130 in **3.1C** and **3.1D**, but **3.1B** exhibited π-anion interaction with Asp1270 residue. The π-alkyl and alkyl interactions stabilized the non-covalent interactions between the compounds and enzyme in its active site. All the compounds are entered in the ATP binding site except **3.1A**, which is entered outside this binding site shown in **Figure 3.39 (e)**.

Table 3.20: Docking scores and residues involved in the interactions of **Scheme 3** compounds with ALK protein

	ALK		
Compounds	Docking score (kcal/mol)	Residues involved in H-bond	Residues involved in other interactions (π…anion, π…cation, π...σ, π...π, π…alkyl, and alkyl)
3.1A	-8.7	Asp1276	Ala1126, Phe1127, Glu1167, Arg1275
3.1B	-6.1	Arg1253	Val1130, Ala1148, Leu1256, Asp1270
3.1C	-6.4	Lys1150, Arg1253	Leu1123, Val1130, Ala1148, Leu1196, Leu1256
3.1D	-7.1	Lys1150, Asn1254	Leu1122, Val1130, Ala1148, Leu1196, Leu1256

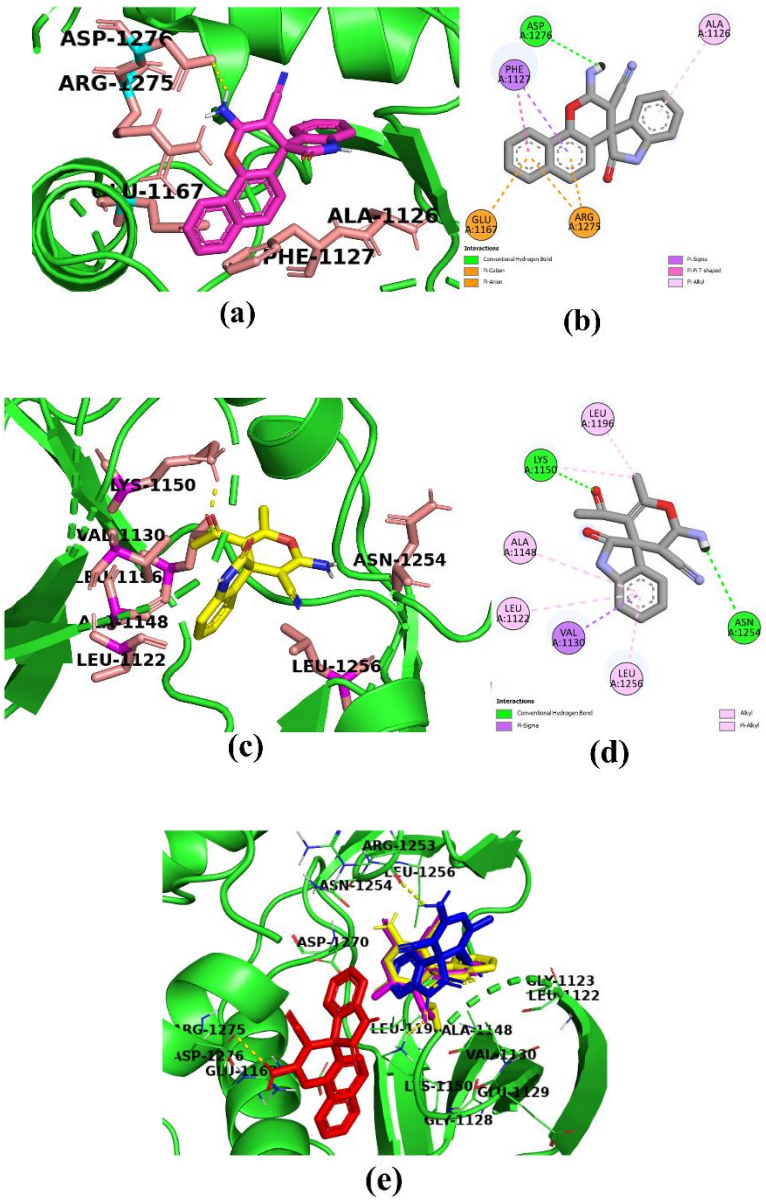

Figure 3.39: Binding in ALK protein (a) & (b) **3.1A,** (c) & (d) **3.1D**, (e) overlay diagram: **3.1A** (red), **3.1B** (blue), **3.1C** (yellow), **3.1D** (magenta)

3.10 Conclusion:

This chapter described the synthesis of a new series of pyranopyrazoles and spiro oxindole compounds studied and analyzed. Those compounds forming suitable crystals are subjected to single-crystal X-ray diffraction. These crystal data are analyzed for the supramolecular framework, Hirshfeld surface analysis, and enrichment ratio from the atomic contacts of Hirshfeld surface analysis. The

supramolecular framework structure of the crystal compound was studied, and the interatomic interactions of the atoms play an important role in forming the crystal architecture of all compounds. The intermolecular interactions C-H…O, C-H…N, C-H…π, N-H…H, and π…π are some of the important interactions in all the crystals. These interactions are also important for the design of the drug, stabilization of the structure, material science, etc. The non-covalent interactions in the crystal compounds are important for the association of the molecules.

The Hirshfeld surface analysis also confirms the intermolecular interactions in the supramolecular framework. The interatomic interaction of molecular surfaces is analyzed and shows the molecular association's importance. The hydrogen atom occupies almost 50% of the molecular surface in all compounds. Still, the enrichment ratio of the H…H atomic interaction in most compounds is less than unity with disfavored interaction.

The compounds of scheme 2 are synthesized via multicomponent reaction, where the electron-donating substituents on the benzaldehyde give a better yield than the electron-withdrawing group containing phenyl ring. The substituent present at the para position to the aldehyde group containing electron-donating property yields more product than the electron-attracting group, but the electron-donating group at the meta-position gives more yield. The crystal studies show that compounds containing electron-donating groups form π-π stacking interaction at the phenyl ring, but the chloro-substituted benzene has lone pair-π interaction in the crystal. Moreover, the electron-donating group containing compounds formed an unsymmetrical dimer with N-H…N interaction, but the dimer interaction is not formed in rest of the compounds. The enrichment ratio studies show that C…C contact in electron-donating rich compounds is enriched. In contrast, the C…O interaction in the electron-withdrawing containing compound is enriched with a value more than unity.

The compounds of scheme 3 show that the carbonyl group-containing ethyl in the ester group gives less yield than that of the methyl-containing group, whereas the ketone group containing gives the least yield in the synthesis. Compound **3.1A** shows the lone pair-π interaction with the naphthol aromatic ring with the cyano nitrogen

atom, which is confirmed by the enrichment ratio value of more than unity in C…N interaction, and none of the other compounds formed this interaction in their crystal structure.

The docking results show that compound **2.1A** has the highest score in enzyme Chk1 and AKR1C3 with binding scores of -8.1 and -9.4 kcal/mol, respectively. The compound has hydrogen bonding with Glu85, Ser147 with Chk1, and Ser217 with AKR1C3 enzyme in their active site. The docking score indicates that the meta-substituent gives better results than the para-substituent. The electron-withdrawing group is also more favored for binding with the active site of the Chk1 and AKR1C3 proteins.

The Compound **3.1A** displays a hydrogen bond with Asp1276 with ALK enzyme in the active site and a binding score of -8.7 kcal/mol. The compound **2.1A** acts as a dual inhibitor of Chk1 and AKR1C3 enzymes. The molecular docking studies showed that compound **3.1A** shows the highest binding affinity, but the binding pocket is slightly different from the other compounds. It is because of the presence of the bulky group naphthol in compound **3.1A** all other compounds are posing in the same orientation.

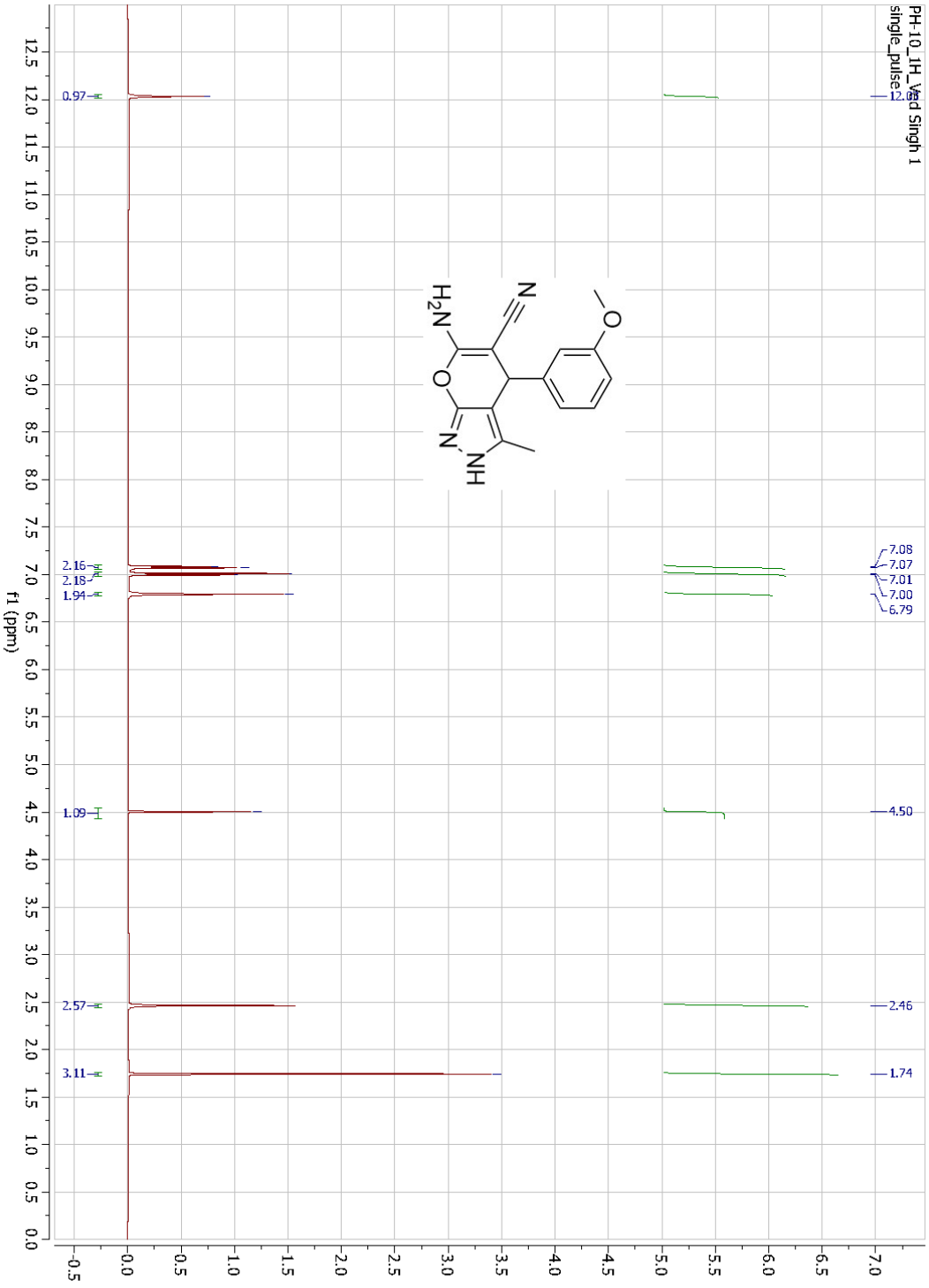

Figure 3.40: ^{1}H NMR Spectra of compound **2.1B**

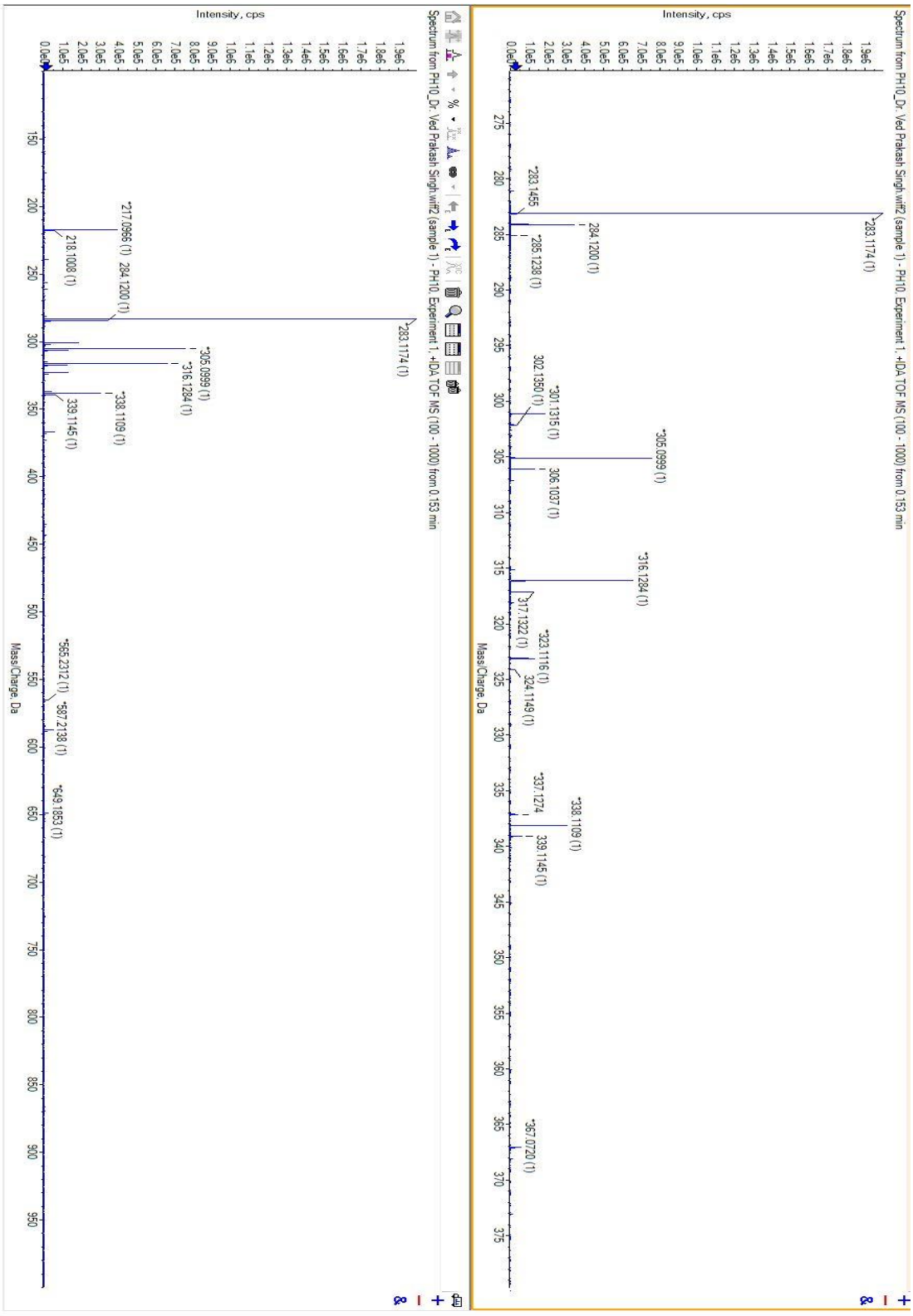

Figure 3.41: HRMS Spectra of compound **2.1B**

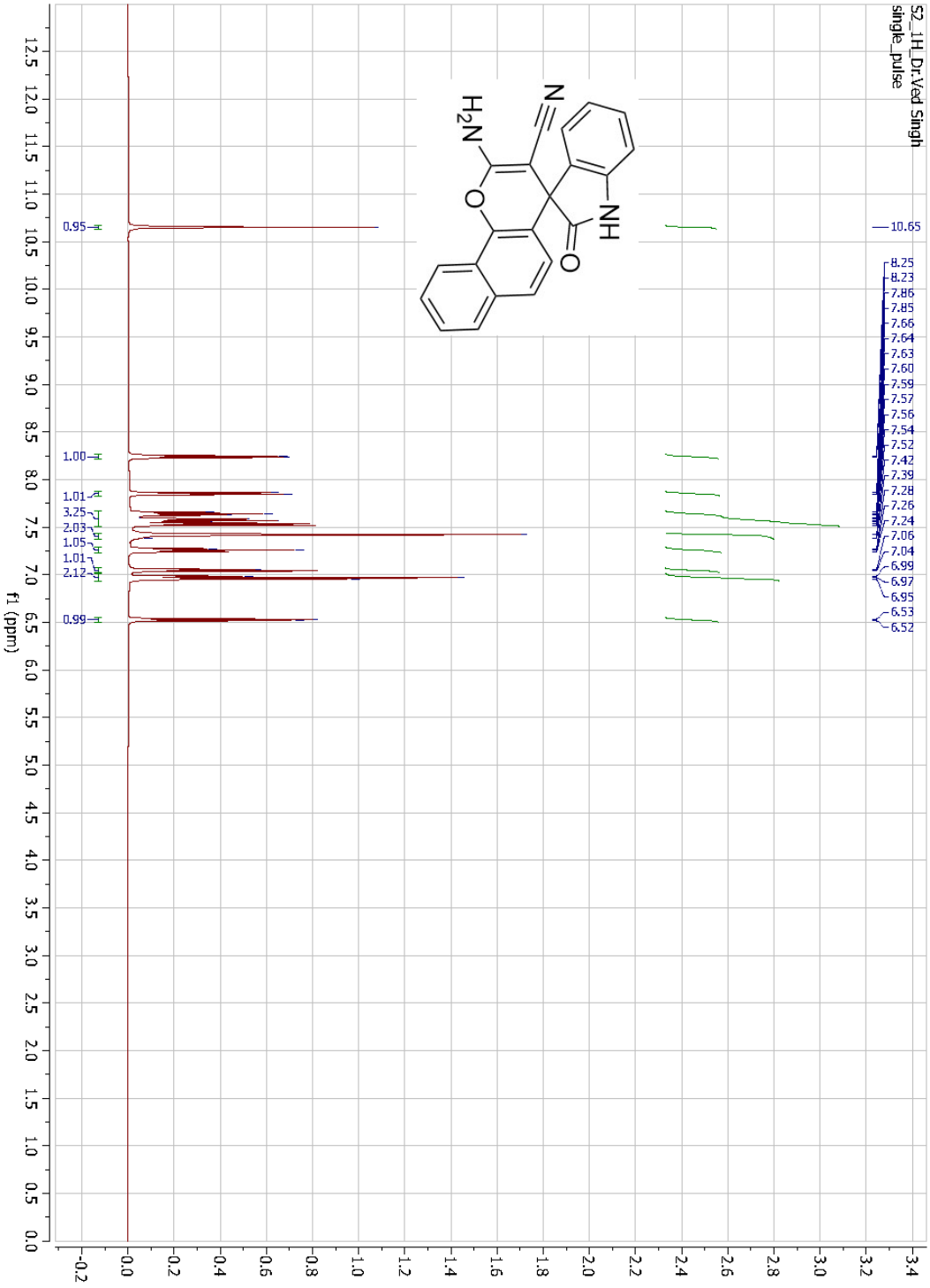

Figure 3.42: ^{1}H NMR Spectra of compound **3.1A**

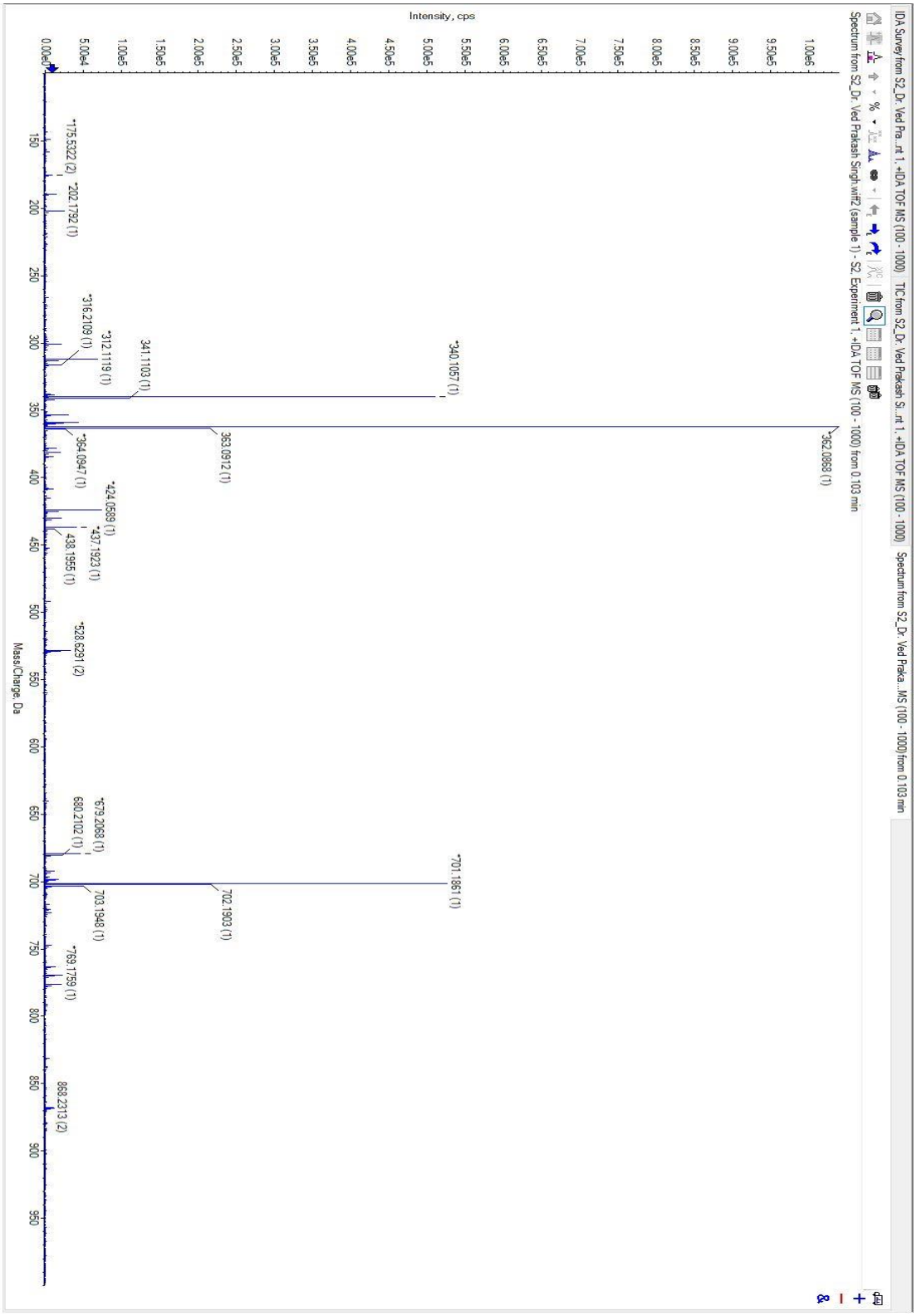

Figure 3.43: HRMS Spectra of compound **3.1A**

CHAPTER 4

4. SYNTHESIS AND STUDY OF FLEXIBLE PYRIDINE–BASED HYBRID MOLECULES

4.1 Introduction

The hybridization of natural and unnatural bioactive compounds is one of the most promising and fundamentally new approaches for designing new lead structures and discovering new and powerful drugs in medicinal chemistry (Tietze et al., 2003). A natural product hybrid (sometimes called a conjugate or chimera) is a synthetic compound having two or more natural product-derived fragments bonded by at least one carbon-carbon bond. This idea is inspired by nature itself, as many known natural products are made of fragments from different biosynthetic pathways. An example is the vincristine hybrid molecule of vindoline and catharanthine. It is an indole-dimeric alkaloid drug of choice for lymphatic leukemia (Camps et al., 2000). Neither of the monomeric compounds exhibits any useful activity. In many cases, artificial hybrid molecules with partial structures of natural compounds have been shown to exhibit more potent activity than the original compounds themselves (Arndt et al., 2001; Tietze et al., 2003). The concept based on the combination of fragments of bioactive compounds seems to have advantages since an almost inexhaustible variety of such hybrid structures can be designed and is potentially accessible in light of recent advances in molecular biology and contemporary synthetic organic chemistry (Burke & Schreiber, 2004).

Pyridones are an interesting class of hexagonal heterocyclic scaffolds with nitrogen, oxygen, and five carbon atoms, which have also been used as bioisosteres for amides, pyrimidines, pyranones, pyrazines, pyridines, and phenol rings. Pyridone exists in two isomeric forms according to the relative position between the nitrogen heteroatom and the carbonyl group (Katritzky et al., 2010). It includes the 2- and 4-(1H)-pyridone as a backbone component of many drugs. Furthermore, a study of the isomerization between pyridinone and the corresponding hydroxy pyridine indicates that the former is preferable, especially under physiological conditions. Milrinone is a potent cardiac stimulant, pirfenidone is an agent for idiopathic pulmonary fibrosis

(IPF), gimeracil and tazemetostat are considered antineoplastic drugs, ciclopirox is an antifungal agent, and doravirine is a valuable anti-HIV-medicine as in Figure 4 (Cho & Kopp, 2010; Harada et al., 2017; Niewerth et al., 2003; Sanchez et al., 2019; Shipley et al., 1996).

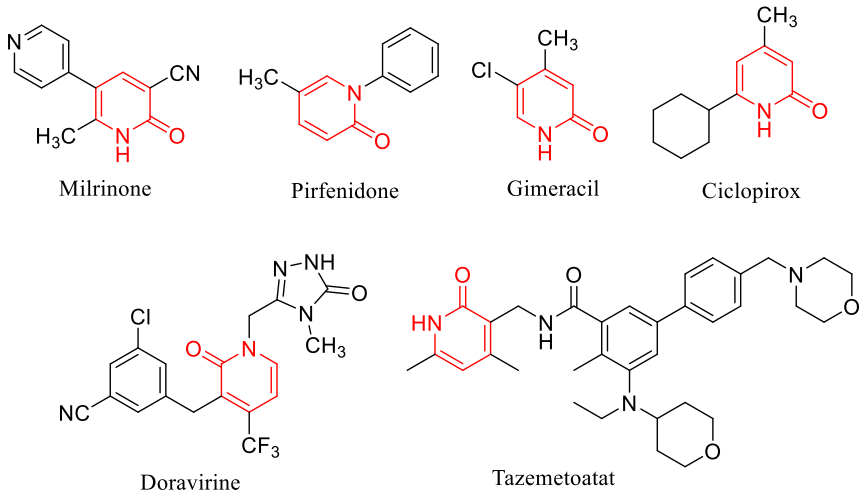

Figure 4.1: Marketed drugs containing pyridone

Natural compounds such as coumarin (1,2-benzopyrone or 2H-1-benzopyran-2-one) and coumarin derivatives are abundant in plants as heterosides or free forms. Due to their various biological functions, these compounds have gained prominence in recent years (Küpeli Akkol et al., 2020). In previous studies on coumarin derivatives, Antitumor (Vianna et al., 2012), anti-inflammatory (Fylaktakidou et al., 2004), anti-HIV (Harvey et al., 1988), triglyceride lowering (Madhavan et al., 2003), antibacterial and antifungal (Al-Haiza et al., 2003), anticoagulant (Jung et al., 2001), and central nervous system stimulant effects (Moffett, 1964) activity were observed. However, hydroxy coumarins have also been shown to have a potent antioxidant and protective effect against oxidative stress by scavenging reactive oxygen species. Clinical studies (Stanchev et al., 2008) have also documented these compounds' cytostatic activity against prostate cancer, malignant melanoma, and metastatic kidney cell carcinoma. In the gastric carcinoma cell line, it was determined that 3 and 4-hydroxy coumarins inhibit cell proliferation (Budzisz, 2003). An oral anticoagulant known as warfarin is a synthetic compound frequently used to treat and prevent blood clots **(Figure 4.2)**.

Dicumarol, an anticoagulant, and vitamin K-depleting hydroxycoumarin were isolated from molding sweet-clover hay.

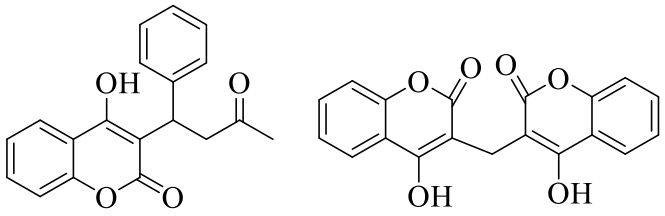

Warfarin Dicumarin

Figure 4.2: Marketed drug of 4-hydroxycoumarin

A phenol derivative, sesamol (3,4-methylenedioxyphenol) **(Figure 4.3)** is a well-known antioxidant that comes from the sesame oil from seeds of the Sesamum species lignans plant (Bankole et al., 2008). Sesamol has been shown to have several beneficial effects, including antioxidants, cardiovascular effects, chemoprevention, antimutagenic, and antihepatotoxic effects. It induces the apoptotic pathway in cancer cells (Alencar et al., 2009). Several studies have indicated that sesamol may be widely used to manage and treat numerous carcinomas (Prakash et al., 2020). It has exclusively been reported to cause apoptosis in various cancer cells, including liver, breast, skin, and human colon cancer cells (Liu et al., 2017).

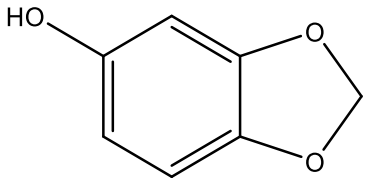

Figure 4.3: Sesamol

4.2 Present work

The design of hybrid molecules has been widely used to improve the bioactivities of the compounds, make the small molecules visible and defeat the acquired drug resistance. This chapter deals with the synthesis and studies of the 2-pyridone derivatives hybrid molecules with the introduction of aromatic rings to the active functional group of the 2-pyridone ring. The aromatic ring was introduced using the spacer (methylene group) through the nitrogen atom or oxygen atom in the presence of a base **(Figure 4.4)**. The synthesized compounds are also studied by *in silico* analysis to the binding affinities with the 5-LOX and COX-2 receptors.

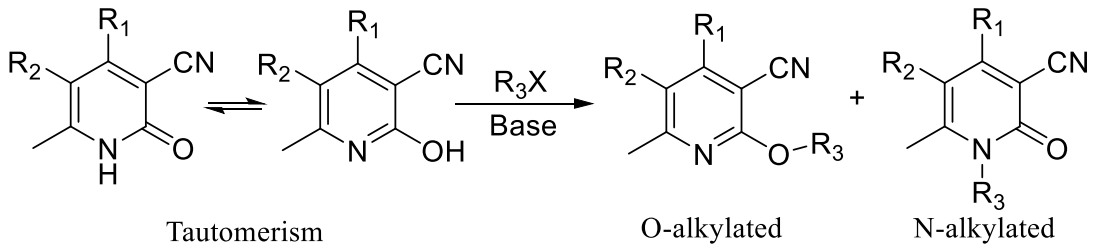

R_1 = 3-$NO_2C_6H_4$, 4-$OCH_3C_6H_4$, 4-$CH_3C_6H_4$
R_2 = COOEt
R_3 = methylene linked aromatic ring

Figure 4.4: Structural representation of designed hybrid molecules

4.3 Synthesis of aromatic ring linked with methylene bromide

The methylene bromide linked with the aromatic ring is synthesized as in **Scheme 4**, using 1,2-dibromoethane or 1,3-dibromo-propane and the aromatic ring containing hydroxy group. These compounds can be further utilized to hybridize 2-pyridone in the following scheme. The synthesized methylene bromide-linked aromatic rings are given in **Figure 4.5.**

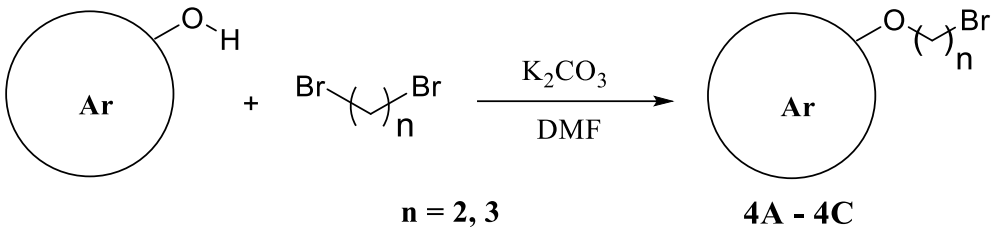

Scheme 4

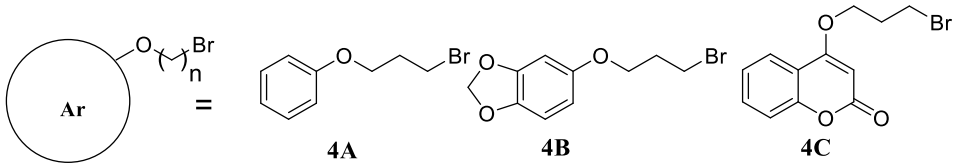

Figure 4.5: Structures of methylene bromide linked aromatic ring

4.4 Experimental

Using TMS as an internal reference, ^{1}H NMR (600 MHz) and ^{13}C NMR (150 MHz) spectra were recorded on a Bruker AVANCE NEO 600 MHz FTNMR

spectrometer. Chemical shift values are expressed in δ, ppm units. Thin-layer chromatography (TLC) was used to monitor all the reactions on Merck's pre-coated aluminum sheets. UV light was used to view the chromatograms. Both column chromatography and flash chromatography used silica gel with meshes of 60-120 and 230-400, and eluents were mixtures of ethyl acetate and hexane.

4.4.1 General procedure for the synthesis of methylene bromide linked aromatic ring (4A – 4C)

Either phenol, 4-hydroxycoumarin, or sesamol (14.50 mmol) was dissolved in 15 mL of dimethylformamide using a 100 mL round bottom flask, and potassium carbonate (28.96 mmol) was added and stirred for 30 minutes at room temperature. After 30 minutes of stirring, either 1,3-dibromopropane or 1,2-dibromoethane (43.44 mmol) was added to the reaction mixture and continued stirring for 12 hours. The completion of the reaction was monitored using TLC. A rotary evaporator removed the solvent, and the residue was extracted with chloroform (3 x 100 mL) and washed with water (3 x 50 mL). The organic layer was collected, combined, and dried over anhydrous sodium sulfate. The crude product was then subjected to flash chromatography using ethyl acetate and hexane as eluent. The pure compounds (**4A-4C**) were collected at 10% of the EtOAc/Hexane.

4.4.1.1 (3-bromopropoxy)benzene (4A): Liquid in nature, Yield: 0.42g (79%); **^{1}H NMR (600 MHz, $CDCl_3$):** δ ppm 2.13 (2H, m, CH_2); 3.77 (2H, t, CH_2, *J* = 7.1 Hz); 4.08 (2H, t, CH_2, *J* = 7.1 Hz); 6.92 (2H, d, Ar-H, *J* = 7.5 Hz); 7.13 (1H, dd, Ar-H, *J* = 7.5 Hz, *J* = 1.5 Hz); 7.42 (2H, dd, Ar-H, *J* = 7.5 Hz, *J* = 1.5 Hz); **^{13}C NMR (150 MHz, $CDCl_3$):** δ ppm 29.9, 32.9, 67.1, 114.4, 120.3, 129.3, 159.4; **MS (m/z):** 216.00 (M+1).

4.4.1.2 5-(3-bromopropoxy)benzo[d][1,3]dioxole (4B): white solid, Yield: 76.3%; **^{1}H NMR (600 MHz, $CDCl_3$):** δ ppm 2.25-2.30 (2H, m, CH_2); 3.58 (2H, t, CH_2, *J* = 6.5 Hz); 4.02 (2H, t, CH_2, *J* = 5.8 Hz); 5.90 (2H, s, CH_2); 6.33 (1H, s, Ar-H); 6.50 (1H, d, Ar-H, *J* = 7.5 Hz), 6.70 (1H, d, Ar-H, *J* = 8.4 Hz); **^{13}C NMR (150 MHz, $CDCl_3$):** δ ppm 29.9, 32.9, 67.1, 101.2, 101.5, 107.7, 108.9, 144.4, 149.4, 152.7; **MS (m/z):** 260.99 (M+1).

4.4.1.3 4-(3-bromopropoxy)-2H-chromen-2-one (4C): white solid, Yield: 72.1%; **^{1}H NMR (600 MHz, $CDCl_3$):** δ ppm 2.44-2.48 (2H, m, CH_2); 3.63 (2H, t, CH_2, *J* = 6.3 Hz); 4.31 (2H, t, CH_2, *J* = 5.8 Hz); 5.73 (1H, s, CH); 7.24-7.38 (2H, m, Ar-H); 7.56 (1H, td, Ar-H, *J* = 7.5 Hz, J = 1.5 Hz), 7.80 (1H, d, Ar-H, *J* = 7.9 Hz); **^{13}C NMR (150 MHz, $CDCl_3$):** δ ppm 30.7, 33.0, 64.2, 86.0, 116.2, 116.4, 123.3, 125.4, 128.3, 152.5, 162.4, 168.6; **MS (m/z):** 282.99 (M+1).

4.5 Synthesis of 2-pyridine-based hybrid derivatives

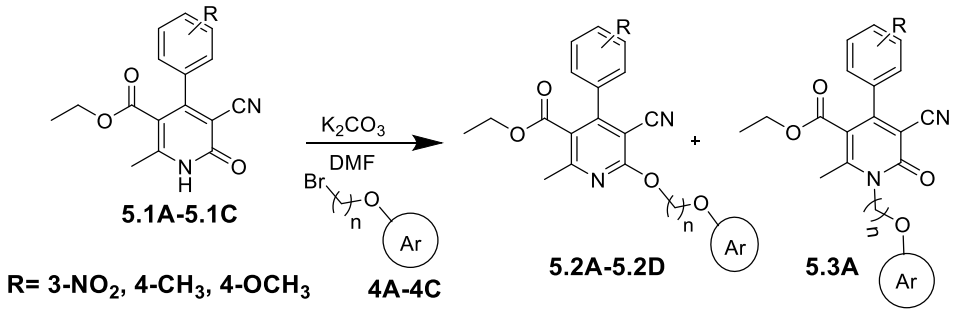

Scheme 5

Scheme 5 is designed to synthesize the pyridine-aromatic ring hybrid molecules from the 2-pyridone derivatives (**5.1A-5.1C**) and methylene bromide-linked aromatic rings (**4A-4C**) derived from scheme 4. The chemical reaction was done using DMF as a solvent in the presence of potassium carbonate as a base to give the target compounds **(Figure 4.6)** for studying nature's interactions.

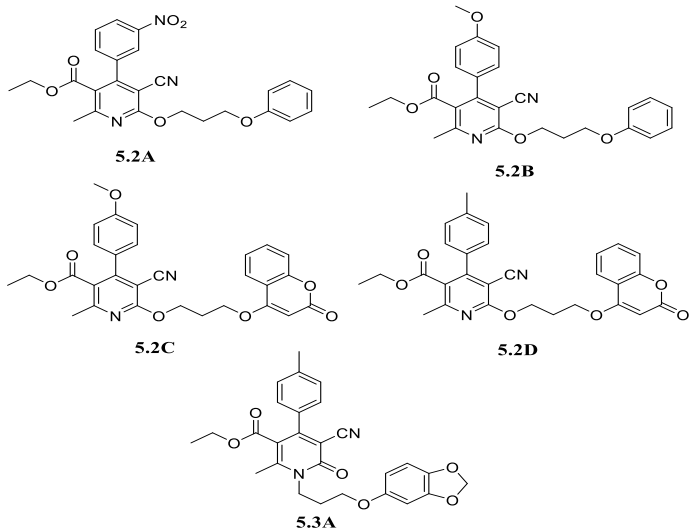

Figure 4.6: Structure of pyridine-aromatic ring hybrid molecules

4.6 Experimental

^{1}H NMR (600 MHz) and ^{13}C NMR (150 MHz) spectra were recorded on a Bruker AVANCE NEO 600 MHz FTNMR spectrometer, using TMS as an internal reference, and the chemical shift values are expressed in δ, ppm units. Thin-layer chromatography (TLC) was used to monitor all the reactions on Merck's pre-coated aluminum sheets using an appropriate solvent system. UV light was used to view the chromatograms. Ethyl acetate and hexane were used as eluents in flash column chromatography, and silica gel (230-400 mesh) was used to purify the product from scheme 5.

4.6.1 General procedure for the synthesis of pyridine hybrid molecules (5.2A-5.2D, 5.3A)

In a 100 ml round bottom flask, the compounds **5.1A-5.1C** (3.4 mmol) and potassium carbonate (6.7 mmol) were taken in DMF (20 mL) and stirred for 20 minutes. Compound **4A-4C** (6.7 mmol) was added and stirred for 12 hours at room temperature. TLC (30% EtOAc / Hexane) was used to monitor the completion of the reaction. When the reaction was completed, DMF was removed under reduced pressure using a rotary evaporator, and the reaction mixture was extracted with ethyl acetate/water (100 mL/100 mL X 3). The ethyl acetate layer was combined and dried with anhydrous Na_2SO_4 and filtered. The solvent was removed, and the product was purified using flash chromatography. The pure compounds **(5.2A-5.2D & 5.3A)** were collected at 30-40% EtOAc/Hexane. The products were recrystallized from EtOAc/Hexane.

4.6.1.1 Ethyl-5-cyano-2-methyl-4-(3-nitrophenyl)-6-(3-phenoxypropoxy)nicotinate (5.2A): White solid, Yield: 67.4%, m.p. 124°C; **^{1}H NMR (600 MHz, $CDCl_3$):** δ ppm 0.97 (3H, t, CH_3, *J* = 7.2 Hz); 2.25 – 2.38 (2H, m, CH_2); 2.59 (3H, s, CH_3); 4.03 (2H, q, CH_2, *J* = 6.9 Hz); 4.18 (2H, t, CH_2, *J* = 6.0 Hz); 4.72 (2H, t, CH_2, *J* = 6.0 Hz); 6.89 – 7.02 (3H, m, Ar-H); 7.24 – 7.32 (2H, dd, Ar-H, *J* = 7.5 Hz, *J* = 1.2 Hz); 7.63 – 7.72 (2H, m, Ar-H); 8.22 (1H, s, Ar-H); 8.33 (1H, m, Ar-H); **^{13}C NMR (150 MHz, $CDCl_3$):** δ ppm14.1, 22.0, 29.0, 60.9, 64.5, 65.0, 91.6, 108.5,

114.4, 114.6, 120.3, 122.7, 124.4, 129.3, 130.1, 133.5, 138.9, 148.4, 154.5, 159.4, 164.7, 164.9, 166.0; **MS (m/z):** 462.17(M+1).

4.6.1.2 Ethyl 5-cyano-4-(4-methoxyphenyl)-2-methyl-6-(3-phenoxypropoxy)nicotinate (5.2B): White solid, Yield: 73%, m.p. 109°C; **^{1}H NMR (600 MHz, $CDCl_3$):** δ ppm 0.96 (3H, t, CH_3, *J* = 7.2 Hz); 2.27 – 2.36 (2H, m, CH_2); 2.53 (3H, s, CH_3); 3.84 (3H, s, CH_3); 4.02 (2H, q, CH_2, *J* = 7.2 Hz); 4.18 (2H, t, CH_2, *J* = 6.0 Hz); 4.67 (2H, t, CH_2, *J* = 6.0 Hz); 6.89 – 6.99 (5H, m, Ar-H); 7.24 – 7.32 (4H, m, Ar-H); **^{13}C NMR (150 MHz, $CDCl_3$):** δ ppm 13.9, 20.8, 22.4, 29.3, 55.8, 59.7, 64.5, 66.1, 91.3, 109.1, 114.1, 114.7, 116.2, 121.3, 129.1, 129.7, 132.1, 154.5, 159.4, 161.1, 163.9, 164.9, 167.5; **MS (m/z):** 447.18(M+1).

4.6.1.3 Ethyl 5-cyano-4-(4-methoxyphenyl)-2-methyl-6-(3-((2-oxo-2H-chromen-4-yl)oxy)propoxy)nicotinate (5.2C): White solid, Yield: 76%, m.p. 140°C; **^{1}H NMR (600 MHz, $CDCl_3$):** δ ppm 0.97 (3H, t, CH_3, *J* = 7.1 Hz); 2.45 – 2.49 (2H, m, CH_2); 2.53 (3H, s, CH_3); 3.85 (3H, s, CH_3); 4.04 (2H, q, CH_2, *J* = 7.1 Hz); 4.36 (2H, t, CH_2, *J* = 5.9 Hz); 4.74 (2H, t, CH_2, *J* = 6.1 Hz); 5.72 (1H, s, CH); 6.94 – 7.00 (2H, m, Ar-H); 7.24 – 7.34 (4H, m, Ar-H); 7.54 – 7.56 (1H, m, Ar-H); 7.82 – 7.85 (1H, m, Ar-H); **^{13}C NMR (150 MHz, $CDCl_3$):** δ ppm 14.1, 22.0, 29.8, 55.8, 60.9, 62.2, 64.5, 86.0, 91.8, 109.5, 114.8, 116.2, 116.4, 123.4, 125.4, 128.4, 129.6, 130.4, 152.5, 154.5, 161.1, 162.4, 164.7, 164.9, 166.0, 168.6; **MS (m/z):** 515.19(M+1).

4.6.1.4 Ethyl 5-cyano-2-methyl-6-(3-((2-oxo-2H-chromen-4-yl)oxy)propoxy)-4-(p-tolyl)nicotinate (5.2D): White solid, Yield: 69%, m.p. 160°C; **^{1}H NMR (600 MHz, $CDCl_3$):** δ ppm 0.93 (3H, t, CH_3, *J* = 7.2 Hz); 2.40 (3H, s, CH_3); 2.47 (2H, m, CH_2, *J* = 6.02 Hz); 2.54 (3H, s, CH_3); 4.01 (2H, q, CH_2, *J* = 7.2 Hz); 4.36 (2H, t, CH_2, *J* = 6.0 Hz); 4.74 (2H, t, CH_2, *J* = 6.0 Hz); 5.71 (1H, s, CH);7.21 – 7.33 (6H, m, Ar-H); 7.53 – 7.56 (1H, m, Ar-H); 7.82 – 7.85 (1H, m, Ar-H); **^{13}C NMR (150 MHz, $CDCl_3$):** δ ppm 14.1, 21.3, 22.0, 29.8, 60.9, 62.2, 64.6, 86.1, 91.8, 109.5, 114.6, 116.2, 116.4, 123.4, 125.4, 127.3, 128.3, 129.6, 132.2, 135.0, 152.5, 154.5, 162.4, 164.7, 164.9, 166.0, 168.6; **MS (m/z):** 499.18(M+1).

4.6.1.5 Ethyl 6-(3-(benzo[d][1,3]dioxol-5-yloxy)propoxy)-5-cyano-2-methyl-4-(p-tolyl)nicotinate (5.3A): White solid, Yield: 78%, m.p. 176°C; **^{1}H NMR (600 MHz,**

$CDCl_3$): δ ppm 0.85 (3H, t, CH_3, *J* = 7.2 Hz); 2.23 (2H, m, CH_2); 2.39 (3H, s, CH_3); 2.56 (3H, s, CH_3); 3.91 (2H, q, CH_2, *J* = 7.2 Hz); 3.98 - 4.03 (2H, m, CH_2); 4.34 (2H, t, CH_2, *J* = 7.4 Hz); 5.92 (2H, s, CH_2);6.31 (1H, dd, Ar-H, *J* = 8.5 Hz, 2.5 Hz); 6.47 (1H, d, Ar-H, *J* = 2.5 Hz); 6.71 (1H, d, Ar-H, *J* = 8.5 Hz) 7.22 – 7.28 (4H, m, Ar-H); **^{13}C NMR (150 MHz, $CDCl_3$):** δ ppm 14.1, 21.3, 22.0, 29.0, 60.9, 64.5, 65.0, 91.6, 101.2, 101.5, 107.7, 108.9, 109.5, 114.6, 127.3, 129.5, 132.2, 135.0, 144.4, 149.4, 152.7, 154.5, 164.7, 164.9, 166.0; **MS (m/z):** 475.18(M+1).

4.7 Results and discussions

A series of pyridine-linked hybrid molecules **(5.2A – 5.2D, 5.3A)** are synthesized in **Scheme 5**, and these synthesized compounds with suitable crystals are studied for their supramolecular framework and Hirshfeld surface. The 2-pyridone compounds are linked with the methylene bromide aromatic ring through the carbonyl oxygen and nitrogen atom. All the compounds obtained were subjected to molecular docking to study their interaction with COX-2 and 5-LOX proteins in their active sites.

4.7.1 X-Ray crystallographic studies and Hirshfeld surface analysis of compounds 5.2A – 5.2D, 5.3A

4.7.1.1 Crystal analysis of compound 5.2A

The compound **5.2A** was recrystallized in ethyl acetate at room temperature by slow evaporation of the solvent. The chiral asymmetric compound **5.2A** was analyzed using single-crystal X-ray diffraction **(Figure 4.7)**. The compound crystallized with cell lengths **a** = 7.6935(2) Å, **b** = 8.1164(2) Å, **c** = 18.8202(5) Å, i.e., **a ≠ b ≠ c** and cell angles $\boldsymbol{\alpha}$ =96.749(2)°, $\boldsymbol{\beta}$= 97.363(2)°, $\boldsymbol{\gamma}$ = 94.646(2)°, i.e., $\boldsymbol{\alpha \neq \beta \neq \gamma \neq 90°}$. It indicates that the compound is exhibiting a triclinic crystal system, with space group *P*-1 that contains two molecules per unit cell (Z:2, Z':1) **(Figure 4.8 (a))**.

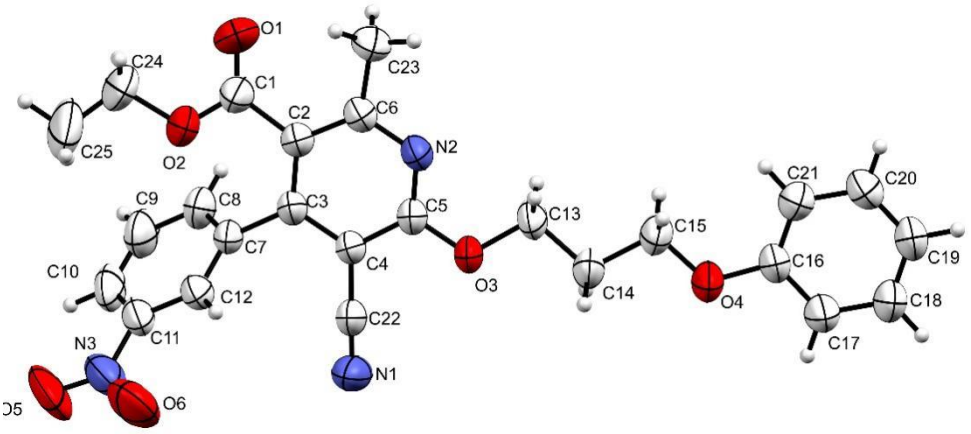

Figure 4.7: ORTEP diagram of **5.2A**

The chiral asymmetric compound **5.2A** crystal structure shows that the nitrobenzene ring twisted away from the plane of the parent pyridine ring with a dihedral angle of 62.26°. The phenyl ring deviates from the parent pyridine ring plane at a dihedral angle of 7.33°. All three rings are sp^2 hybridized and facilitate the delocalization of π-orbitals. The nitrobenzene ring plane is turned away from the plane of the phenyl ring plane at a 67.59° dihedral angle. The conformation of the linker methylene moiety is arranged in the antiperiplanar conformation. The crystallographic information is summarized in **Table 4.1**.

Supramolecular framework of compound 5.2A: The molecular association of compound **5.2A** involves C-H…O and C-H…N intermolecular interactions between two ring planes. The C-H…O interactions between the phenyl hydrogen H17 and the oxygen O4 at 2.656 Å and between the phenyl hydrogen H21 and the carbonyl oxygen O1 from the ester moiety at 2.638 Å form $R_2^2(8)$ and $R_2^2(28)$ graph sets respectively **(Figure 4.8 (b))**. The hydrogen (H10) from the nitrobenzene ring also interacts with the nitrogen N1 of the nitrile group and forms C-H…N interaction at 2.738 Å, resulting in a graph set notation of $R_2^2(18)$. The extensive C-H…O and C-H…N contacts between the molecules result in the formation of a polymeric layer of sheets. The different layers of sheets are connected by H…H interactions between the linker hydrogen at 2.366 Å, 2.338 Å, and 2.383 Å as well as between the nitrobenzene ring hydrogen at 2.351 Å. The crystal packing with the unit cell is stabilized by the H…H

interactions between the methylene hydrogen as well as π…π interaction between the pyridine ring and the phenyl ring at 4.108 Å **(Figure 4.8 (d))**.

Table 4.1: Crystal data of compounds **5.2A** and **5.2B**

Compound	**5.2A**	**5.2B**
Identification code	2222479	2222478
Molecular formula	$C_{25}H_{23}N_3O_6$	$C_{26}H_{26}N_2O_5$
Formula weight	461.46	446.49
Temperature(K)	293(2)	293.9(3)
Crystal system	Triclinic	Monoclinic
Space group	*P*-1	$P2_1/c$
a(Å)	7.6935(2)	8.0740(2)
b(Å)	8.1164(2)	21.8083(6)
c(Å)	18.8202(5)	13.6485(4)
α(°)	96.749(2)	90
β(°)	97.363(2)	106.245(3)
γ(°)	94.646(2)	90
Volume($Å^3$)	1151.91(5)	2307.28(11)
Z	2	4
ρ (g/cm^3)	1.330	1.285
μ(mm^{-1})	0.096	0.090
F(000)	484.0	944.0
Crystal size(mm^3)	0.26 × 0.24 × 0.22	0.25 × 0.22 × 0.2
Radiation	MoKα (λ = 0.71073)	MoKα (λ = 0.71073)
2Θ range for data collection(°)	6.45 to 54.686	6.41 to 54.844
Index ranges	-9 ≤ h ≤ 9, -8 ≤ k ≤ 10, -21 ≤ l ≤ 24	-10 ≤ h ≤ 10, -27 ≤ k ≤ 28, -16 ≤ l ≤ 17
Reflections collected	15017	19841
Independent reflections	4876	4916
Data/restraints/parameters	4876/0/309	4916/0/301
Goodness-of-fit on F^2	1.106	1.065
Final R indexes [I>=2σ (I)]	R_1 = 0.0628, wR_2 = 0.1814	R_1 = 0.0475, wR_2 = 0.1177
Final R indexes [all data]	R_1 = 0.0968, wR_2 = 0.2068	R_1 = 0.0699, wR_2 = 0.1312
Largest diff.peak/hole/e $Å^{-3}$	0.33/-0.27	0.17/-0.22

The C-H…N interaction also facilitates π…π interaction between the nitrobenzene rings at 4.53 Å. The supramolecular structure of compound **5.2A** also displays π…π interactions between the pyridine ring and the phenyl ring at the other

side of the plane at 4.023 Å **(Figure 4.8 (d))** and between the phenyl ring to phenyl ring at 4.593 Å **(Figure 4.8 (c))**. The non-covalent interactions are given in **Table 4.2**.

Table 4.2: Hydrogen bonds and other intermolecular interactions in **5.2A**

Donor-H...Acceptor	D – H, Å	H...A, Å	D...A, Å	D - H...A,°
C17-H17…O4	0.930	2.656	3.535	157.980
C10-H10…N1	0.930	2.738	3.658	170.260
C21-H21…O1	0.930	2.638	3.528	160.360
C13-H13A…H15B	0.970	2.366	3.179	140.900
C13-H13A…H13A	0.970	2.338	3.145	140.170
C14-H14A…H15A	0.970	2.383	3.095	129.870
C9-H9…H9	0.930	2.351	3.091	136.200
Other contacts				
π(C16-C21)… π(C2-C6,N2)		4.108		
π(C16-C21)… π(C2-C6,N2)		4.023		
π(C7-C12)… π(C7-C12)		4.593		
Intramolecular				
C25-H25A…π(C7-C12)	0.960	3.166	3.932	138.02
C23-H23B…O1	0.960	2.637	2.910	96.70
C23-H23C…O1	0.960	2.743	2.910	90.24
C14-H14A…O3	0.97	2.561	2.377	68.17
C14-H14B…O3	0.970	2.568	2.377	67.79
C14-H14A…O4	0.970	2.497	2.360	70.63
C14-H14B…O4	0.970	2.612	2.360	64.37
C24-H24A…O1	0.97	2.868	2.65	67.29
C24-H24B…O1	0.970	2.372	2.650	95.66

Hirshfeld surface analysis of compound 5.2A: The Hirshfeld surface mapped over the $_{norm}$ in the range of -0.0764 Å to 1.4413 Å for compound **5.2A** is displayed in **Figure 4.9 (a) & (b)**. The region of red spots corresponds to shorter dominant contacts due to C-H…O and C-H…N interactions. The other lighter white and blue regions of the Hirshfeld surface indicate weaker interactions due to more extended contacts, which are more significant or equal to the van der Waals interatomic distances.

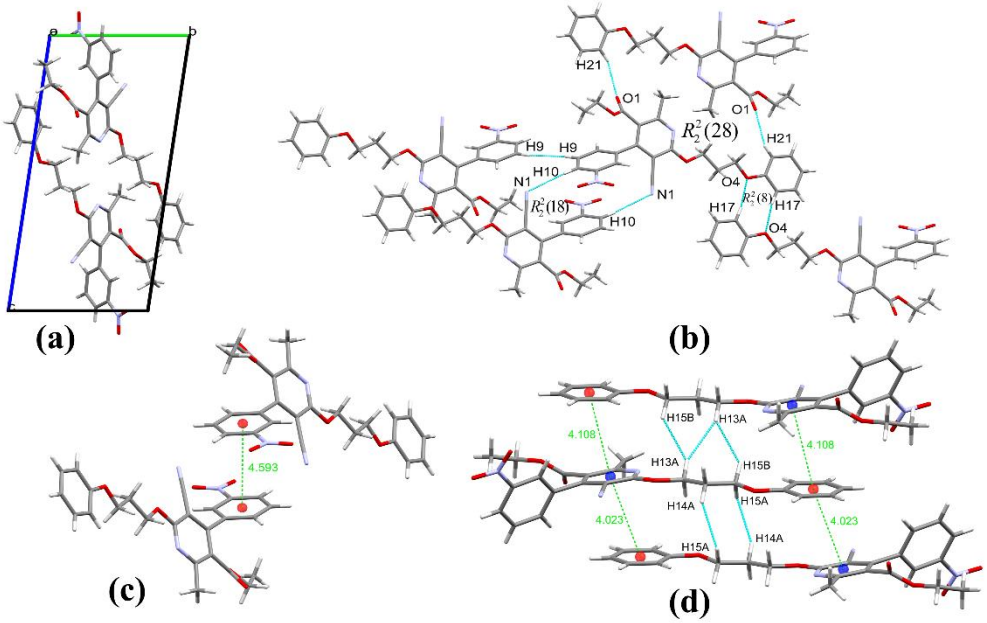

Figure 4.8: (a) crystal packing of **5.2A** along the a-axis (b) interactions showing graph sets (c) and (d) π…π stacking interactions in compound **5.2A**

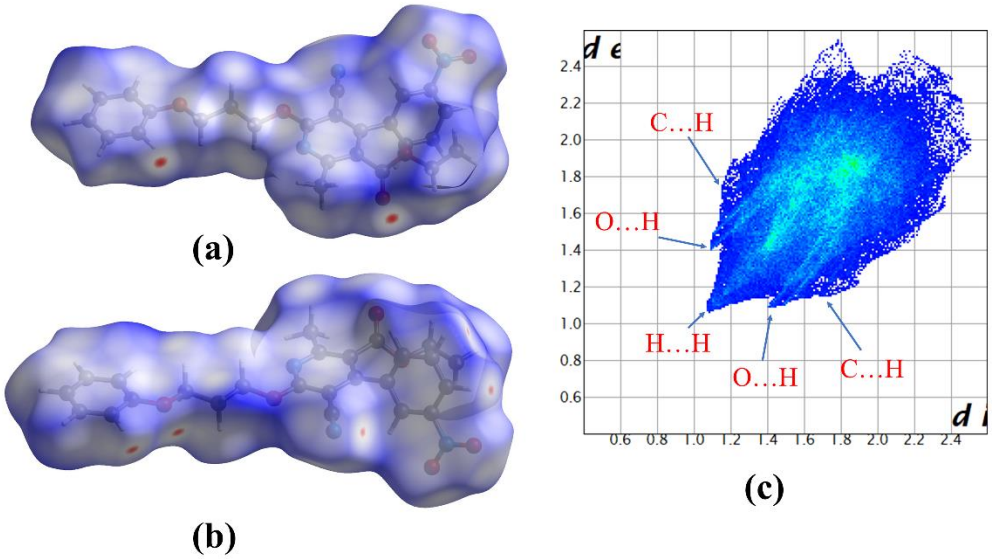

Figure 4.9: (a) & (b) Hirshfeld surface d_{norm} both side view (c) 2D fingerprint plot of compound **5.2A**

The relative percentage contributions of non-covalent interaction to the Hirshfeld surface are summarized by the 2-D fingerprint plot of compound **5.2A (Figure 4.9 (c))**. Those are H…H(46.3%), O...H(19.6%), N…H(11.4%), C…H(9.0%), C…C(4.8%), C…O(4.6%), O…O(1.7%), N…O(1.5%) and C…N(1.2%). The pair of spike-like patterns in the 2D fingerprint plot in the region of $d_i + d_e \approx 2.5$ Å represents O…H interactions. N…H interaction is also reflected around the spoke in the region

of $d_i + d_e \approx 2.6$ Å. C-H...π decompose within the C…H contacts, and it appears in the same region in the 2D fingerprint, which appears as a characteristic wing-like pattern in the region of $d_i + d_e \approx 2.9$ Å. The C…C contacts contributing 4.8% indicate the presence of π-π stacking interactions within the ring.

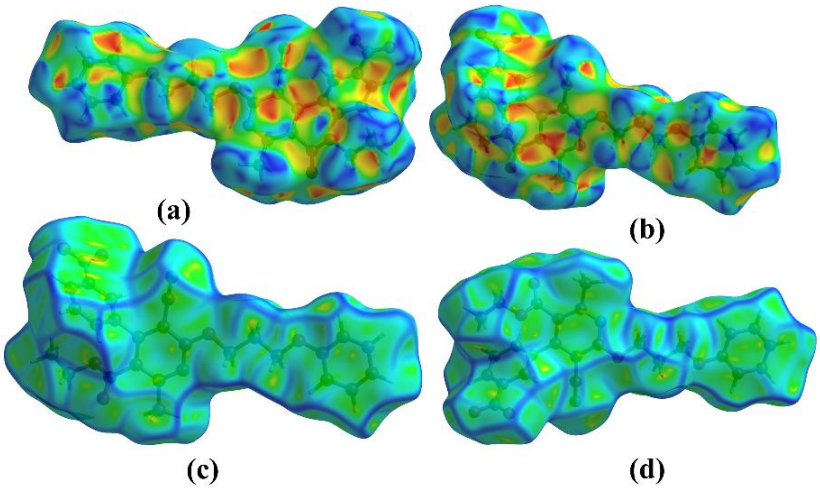

Figure 4.10: (a) and (b) Hirshfeld surface shape Index, (c) and (d) Curvedness, both side view, of compound **5.2A**

The shape-index red region indicates the acceptor property, and the blue region shows the donor property. The Hirshfeld surface mapped over the shape index in a range of -1 to 1 Å for compounds **5.2A (Figure 4.10 (a) & (b))**. It shows the presence of complementary pair of red and blue triangles having an edge-to-edge connection at both surfaces of the pyridine and the phenyl rings and at one side of the nitrobenzene ring, which indicate the presence of $\pi \ldots \pi$ stacking interactions between the aromatic rings. Similarly, the Hirshfeld surface mapped over the curvedness in a range of -4 to 0.4 Å for compound **5.2A** also display a flat green region with a yellowish spot around the aromatic ring surface, which indicate the presence of $\pi \ldots \pi$ stacking interaction between the aromatic rings **(Figure 4.10 (c) and (d)**.

The C-H…O, C-H…N, C-H…H, and π-π stacking interactions found within the supramolecular framework are also supported by the Hirshfeld analysis. Weak non-covalent intermolecular interactions in the crystal packing within the cluster of radius 3.8 Å from a single crystal fragment are shown in **Figure 4.11**.

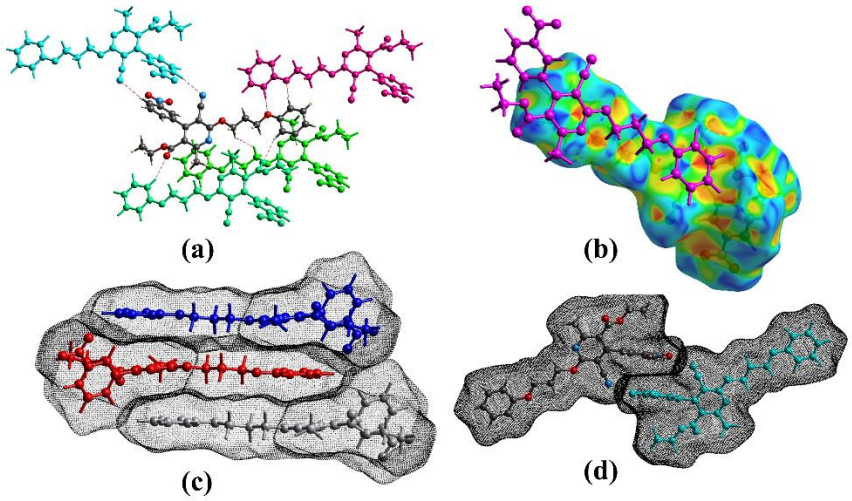

Figure 4.11: (a) C-H…O and C-H…N interactions, (b), (c) and (d) π…π interaction, in compound **5.2A**

Table 4.3: Enrichment ratio (ER) of compound **5.2A**

Atoms	H	C	N	O
H	46.3		Actual contacts (%)	
C	9	4.8		
N	11.4	1.2	0	
O	19.6	4.6	1.5	1.7
Surface %	66.30	12.20	7.05	14.55
H	44.0		Random contacts (%)	
C	16.2	1.5		
N	9.3	1.7	0.5	
O	19.3	3.6	2.1	2.1
H	1.05		Enrichment ratio	
C	0.56	3.22		
N	1.22	0.70	0.00	
O	1.02	1.30	0.73	0.80

The atomic interaction in the molecule of compound **5.2A** was evaluated using the enrichment ratio (ET), calculated with the Hirshfeld surface analysis. The enrichment ratio calculation table is shown in **Table 4.3,** which provides the propensity of the atomic interaction in the crystal structure. The H…H interaction contributes 66.03% of the total surface, and the E_{HH} = 1.05 indicates these interactions play an important role in the crystal structure of the compound. The C…H contact value E_{CH} = 0.56 is lower than unity, implying the interaction is unfavorable. On the other hand,

C…O, N…H, and O…H interactions with E_{CO} = 1.30, E_{NH} = 1.22, and E_{OH} = 1.02, respectively, are enhanced, showing the propensity to form these interactions. The most enriched interaction C…C with E_{CC} = 3.22 in the crystal compound illustrates the presence of the stacking π…π interactions in the crystal structure, and it enhanced the stability of the supramolecular system of compound **5.2A**. The O…O and C…N interactions value are lower than unity, and they have not favored interactions.

4.7.1.2 Crystal analysis of compound 5.2B

The compound **5.2B** was recrystallized in ethyl acetate at room temperature by slow evaporation of the solvent. The chiral asymmetric compound **5.2B** was analyzed using single-crystal X-ray diffraction **(Figure 4.12)**. The compound crystallized with cell lengths **a** = 8.0740(2) Å, **b** = 21.8083(6) Å, **c** = 13.6485(4) Å, i.e., **a** ≠ **b** ≠ **c** and cell angles $\boldsymbol{\alpha}$ = 90°, $\boldsymbol{\beta}$ = 106.245(3)°, $\boldsymbol{\gamma}$ = 90°, i.e.,$\boldsymbol{\alpha = \gamma = 90°, \beta \neq 90°}$. It indicates that the compound is exhibiting a monoclinic crystal system, with space group $P2_1/c$ that contains four molecules per unit cell (Z:4, Z':2) **(Figure 4.13 (a))**.

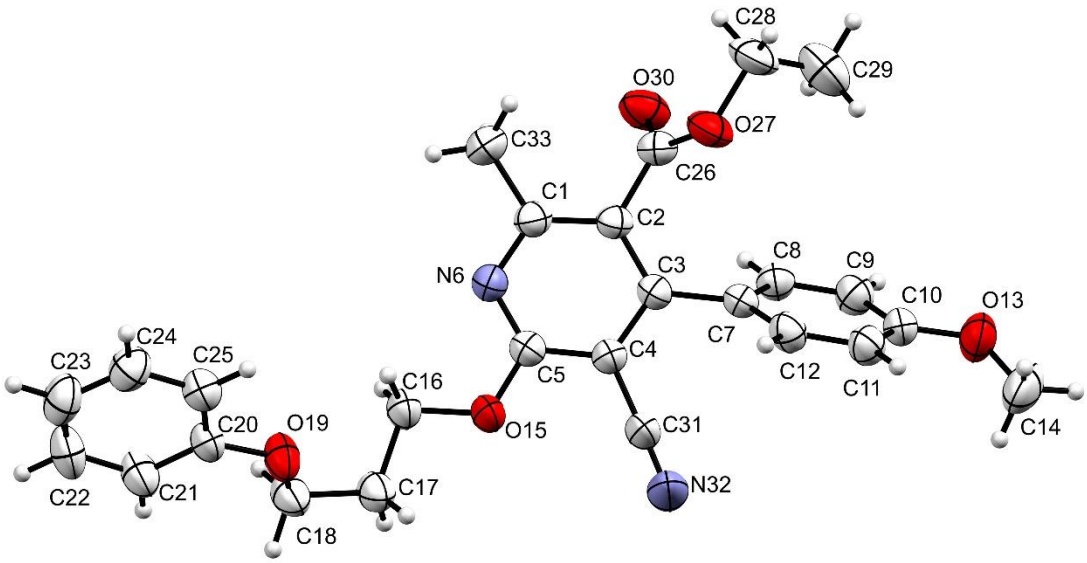

Figure 4.12: ORTEP diagram of compound **5.2B**

The chiral asymmetric compound **5.2B** crystal structure shows that the anisole ring twisted away from the plane of the parent pyridine ring and with a dihedral angle of 54.20°. The atoms O15, C16, C17, and C18 lie in the same plane as the pyridine plane. The phenyl ring also flips away from the parent pyridine ring plane at a dihedral angle of 64.68°. The phenyl ring plane also turns away from the anisole ring plane with

a 62.10° dihedral angle. All three rings are sp^2 hybridized and facilitate the delocalization of π-orbitals. The methylene linker shows anti-staggered conformation along the compound's C16-C17 and gauche conformation along C17-C18. The crystallographic information is summarized in **Table 4.1**.

Supramolecular framework of compound 5.2B: The molecular association of compound **5.2B** involves C-H…O, C-H…N, C-H…π, π…π stacking and dipole-dipole interactions. The most significant interactions within the supramolecular system are the C-H…O interactions between the anisole ring hydrogen H9 and the methoxy oxygen O13 at 2.651 Å. This C-H…O intermolecular interactions between the two molecules also form $R_2^2(8)$ graph set notation **(Figure 4.13 (c))**. The C-H…N interaction between the phenyl hydrogen H25 and nitrogen N32 of the nitrile group serves as the interconnectivity of the polymeric chain. The crystal packing within the unit cell is stabilized by dipole-dipole interaction between the carbonyl oxygen O30 of the ester moiety and the partially positive carbon C5 within the pyridine ring atom at 3.149 Å with the graph set notation of $R_2^2(12)$ **(Figure 4.13 (b))**. The non-covalent interactions in compound **5.2B** are shown in **Table 4.4.**

Table 4.4: Hydrogen bonds and other intermolecular interactions in **5.2B**

Donor-H...Acceptor	D – H, Å	H...A, Å	D...A, Å	D - H...A, °
C9-H9…O13	0.930	2.651	3.451	144.47
C25-H25…N32	0.930	2.668	3.316	127.41
C11-H11…π(C20-C25)	0.930	3.478	4.088	125.43
C14-H14A…π(C20-C25)	0.960	3.203	3.997	141.32
C21-H21…π(C7-C12)	0.930	3.334	4.224	158.74
C28-H28A…π(C7-C12)	0.970	3.108	3.724	122.83
Other contacts				
π(C1-C5,N6)…π(C1-C5,N6)		4.173		
π(C1-C5,N6)…π(C20-C25)		3.867		
O30…C5		3.149		
Intramolecular				
C28-H28B…O30	0.970	2.378	2.672	96.77
C33-H33B…C26	0.960	2.749	2.924	90.75
C16-H16A…N6	0.970	2.572	2.690	86.29
C16-H16B…N6	0.970	2.735	2.690	77.06

C12-H12…C31	0.930	2.721	2.990	97.61
C16-H16B…O19	0.970	2.544	2.903	101.88

Beyond this, the π…π stacking interaction between the pyridine ring in a parallel displaced fashion at 4.173 Å stabilizes the crystal packing **(Figure 4.14 (c))**. The extensive interaction of the weak interaction also displays another π…π stacking interaction at the other side of the pyridine ring plane with the phenyl ring at 3.867 Å **(Figure 4.14 (d))**. Furthermore, the anisole ring hydrogen H11 and its methoxy hydrogen H14A also interact with the p-orbital of the phenyl ring at the same side of the plane, having an interaction distance of 3.478 Å and 3.203 Å, respectively **(Figure 4.14 (b))**.

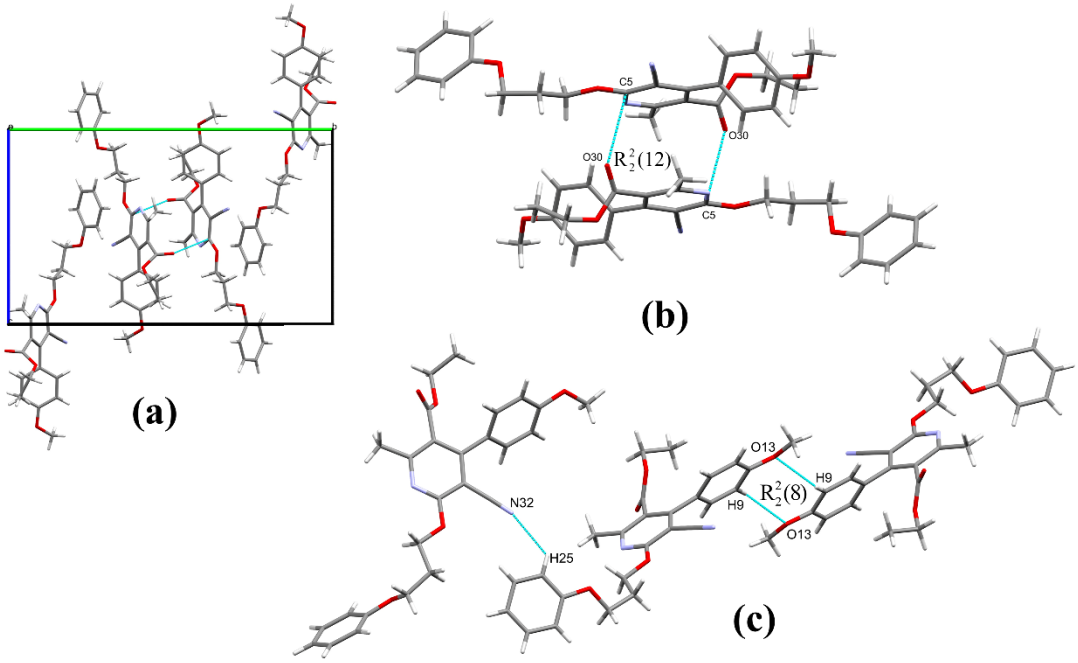

Figure 4.13: (a) crystal packing in **5.2B** along the a-axis, (b) and (c) interaction showing graph set, of compounds **5.2B**

Similarly, the anisole ring also exhibits C-H…π interactions at the two faces of the ring plane where the donor hydrogen comes from the phenyl hydrogen H21 and the hydrogen H28A of the ester moiety, which have an interaction distance of 3.334 Å and 3.724 Å, respectively **(Figure 4.14 (a))**. Thus, apart from the C-H…O and C-H…N interactions C-H…π, dipole-dipole and π…π stacking interactions play a crucial role in adopting the supramolecular association of compound **5.2B**.

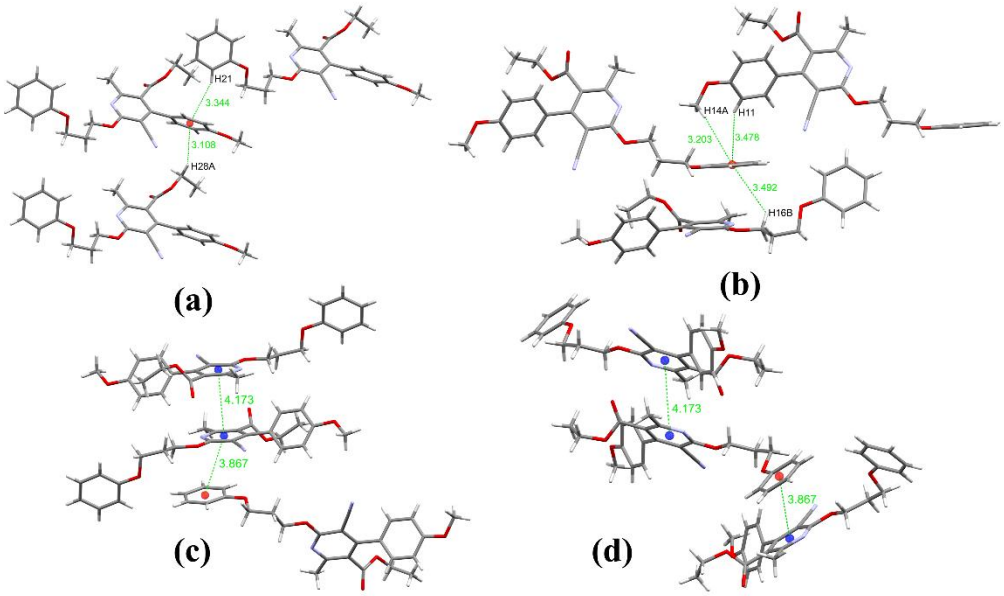

Figure 4.14: (a) & (b) C-H…π interactions, (c) & (d) π…π interactions, of compound **5.2B**

Hirshfeld surface analysis of compound 5.2B: The Hirshfeld surface mapped over the $_{norm}$ in the range of -0.0513 Å to 1.4390 Å for compound **5.2B** is displayed in **Figure 4.15 (a) and (b)**. The region of bright red spots corresponds to shorter dominant contacts due to C-H…O and dipole-dipole O30…C5. The lighter red, dull spots also arise due to C-H…N and C-H…C contacts which are weaker and have longer bond lengths. The other lighter white and blue regions of the Hirshfeld surface indicate weaker interactions due to more extended contacts, which are more significant or equal to the van der Waals interatomic distances.

The relative percentage contributions of non-covalent interaction to the Hirshfeld surface are summarized by the 2D fingerprint plot of compound **5.2B (Figure 4.15 (c))**. Those interactions are H…H(54.0%), C…H(17.0%), O...H(12.6%), N…H(9.4%), C…C(2.4%), C…O(1.7%), C…N(1.3%), N…O(0.9%) and O…O(0.7%). The pair of spike-like patterns in the 2D fingerprint plot in the region of $d_i + d_e \approx 2.5$ Å represents O…H interactions. N…H interaction is also reflected around the spoke in the region of $d_i + d_e \approx 2.6$ Å. Since C-H...π decompose within the C…H contacts and appears in the same region as that of the C…H interaction in the 2D fingerprint, which appears as a characteristic flip wing-like pattern in the region of

$d_i + d_e \approx 2.8$ Å. The C…C contacts contributing 2.4% indicate the presence of π…π stacking interactions within the ring.

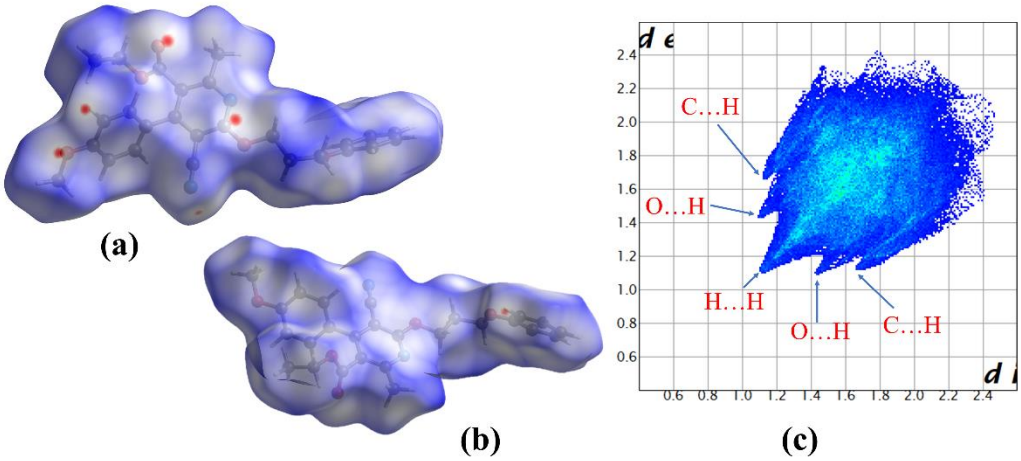

Figure 4.15: (a) and (b) Hirshfeld surface d_{norm} both side view, (c) 2D fingerprint plot, of compound **5.2B**

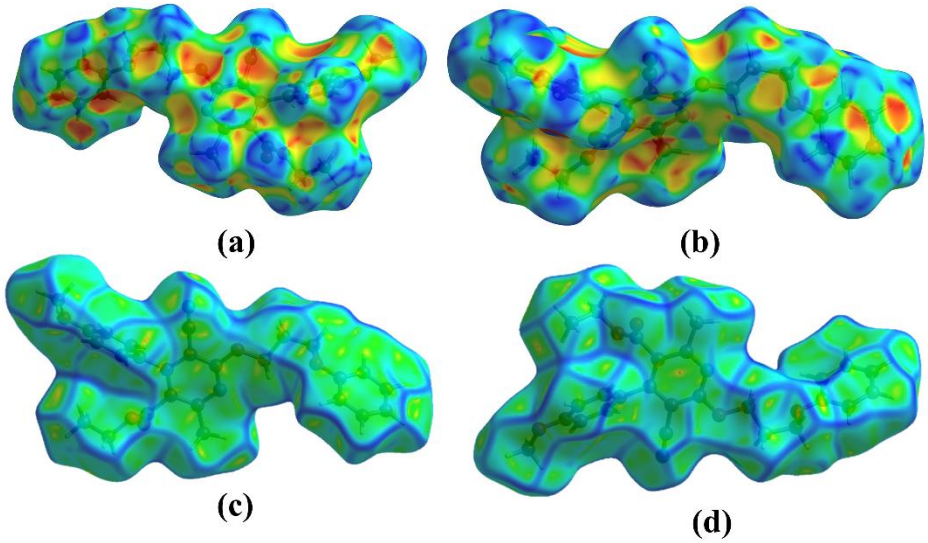

Figure 4.16: (a) and (b) Shape index, (c) and (d) Curvedness of compound **5.2B**

In the shape index, the red region indicates acceptor property, and the blue region indicates donor property. The Hirshfeld surface mapped over the shape index in a range of -1 to 1 Å for compounds **5.2B** shows the presence of complementary pair of red and blue triangles having an edge-to-edge connection at both surfaces of the pyridine ring and one side of the phenyl ring. It indicates the presence of π ... π stacking interactions between the aromatic rings **(Figure 4.16 (a) & (b))**. However, yellowish-

red colored concave regions in the shape index around the surface of the anisole and phenyl rings represent the acceptor region where C-H...π interactions occur. In the curvedness plot, the yellow and red-yellow coloured spots indicate weak interactions and strong hydrogen bond interactions in the crystal. Similarly, the Hirshfeld surface mapped over the curvedness in a range of -4 to 0.4 Å for compound **5.2B** also displays a flat green region with a yellowish spot around the aromatic ring surface, which indicates the presence of π ... π stacking interaction between the aromatic rings **(Figure 4.16 (c) and (d)).**

The C-H…O, C-H…N, C-H…π and π-π stacking interactions were found within the radius of 3.8 Å from the single crystal molecule of the Hirshfeld surface calculation. It also supported the supramolecular framework for weak non-covalent intermolecular interactions in the crystal packing, shown in **Figure 4.17**.

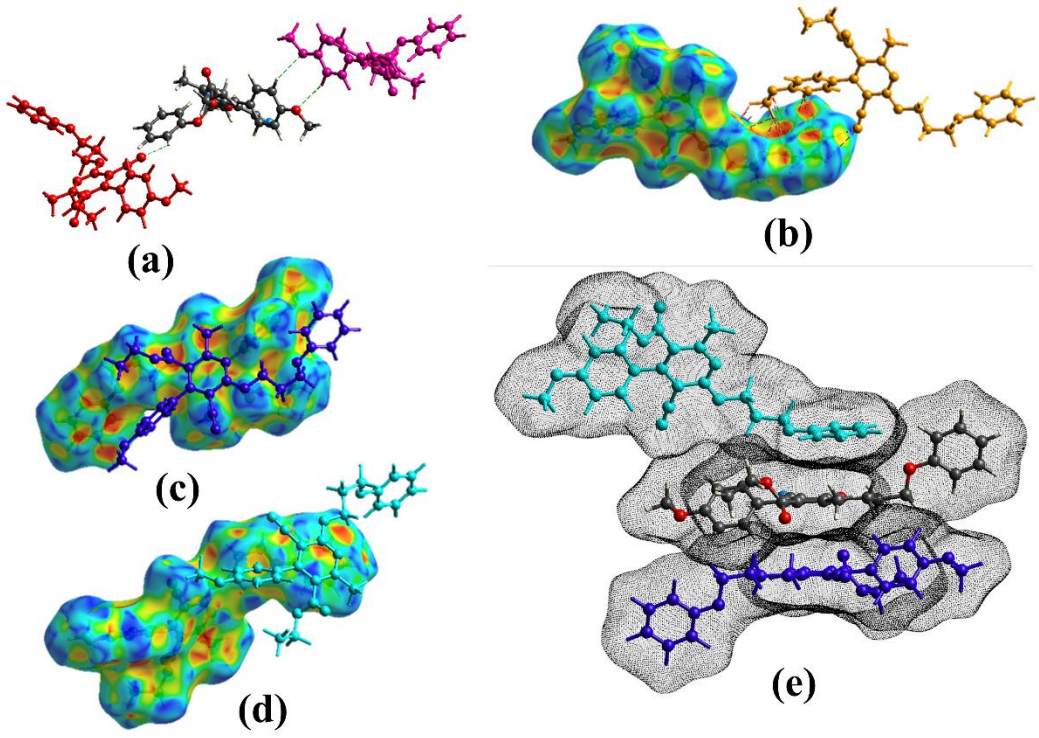

Figure 4.17: (a) & (b) C-H…O, C-H…N and C-H…π interaction, (c), (d) & (e) π…π interaction, of compound **5.2B**

The enrichment ratio (ET) of compound **5.2B** is obtained by comparing the actual contacts in the crystal with the computed contacts as if all types of contacts had a similar probability of forming and are tabulated in **Table 4.5**. The enrichment values

for H…H, N…H, O…H, C…C, and O…O are greater than unity, indicating that these pairs have a larger propensity to form interconnects in the crystal structure. Still, the random contact of O…O is only 0.7% which is significantly less to initiate interaction. The H…H contacts with E_{HH} = 1.0 and the random contacts account for 54.0% play a significant role in the stability of the crystal structure. The enrichment ratio of C…H is E_{CH} = 0.93 is less than unity with less propensity to form interactions.

Nonetheless, C…C contact accounts for E_{CC} = 1.56, which is the most enriched interaction and confirms the presence of π…π interactions as indicated in the supramolecular structure. The N…H and O…H interaction (E_{NH} = 1.10, E_{OH} = 1.03) are the main contributors to the crystal structure formation and support the interactions explained in the supramolecular framework. The C…N, C…O, and N…O inter-contacts have E_{CN} = 0.90, E_{CO} = 0.83, and E_{NO} = 0.93, respectively, and are less likely to form contacts in the crystal.

Table 4.5: Enrichment ratio (ER) of compound **5.2B**

Atoms	**H**	**C**	**N**	**O**
H	54	Actual contacts (%)		
C	17	2.4		
N	9.4	1.3	0	
O	12.6	1.7	0.9	0.7
Surface %	73.50	12.40	5.80	8.30
H	54.0	Random contacts (%)		
C	18.2	1.5		
N	8.5	1.4	0.3	
O	12.2	2.1	1.0	0.7
H	1.00	Enrichment ratio		
C	0.93	1.56		
N	1.10	0.90	0.00	
O	1.03	0.83	0.93	1.02

4.7.1.3 Crystal analysis of compound 5.2C

At room temperature, the compound **5.2C** was recrystallized from slow evaporation of ethyl acetate and hexane (30% ethyl acetate). The crystal was analyzed using single crystal X-Ray diffraction **(Figure 4.18)** and studied its structural

framework. The compound was crystallized with cell lengths **a** = 14.201(2) Å, **b** = 7.0175(6) Å, **c** = 27.397(4) Å, i.e., **a** ≠ **b** ≠ **c** and cell angles $\boldsymbol{\alpha}$ = 90°, $\boldsymbol{\beta}$ = 103.850(11)°, $\boldsymbol{\gamma}$ = 90°, i.e., $\boldsymbol{\alpha} = \boldsymbol{\beta}$ = 90°, $\boldsymbol{\beta} \neq$ 90°. The compound exhibits a monoclinic system of crystal, with space group $P2_1/n$, which contains four molecules in a unit cell (Z:4, Z':1) **(Figure 4.19 (a))**.

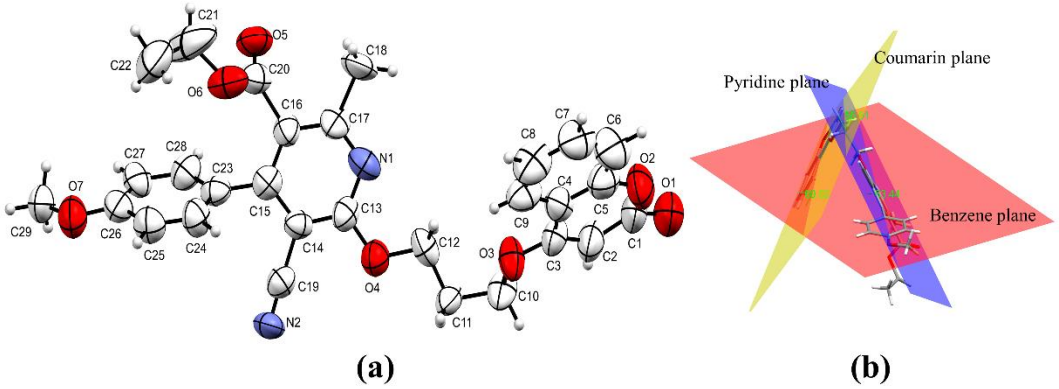

Figure 4.18: (a) ORTEP, (b) planes in compound **5.2C**

The compound **5.2C** is formed by three rings containing sp^2 hybridized atoms, forming a planar ring with delocalization of π-orbitals. A methylene linker linked the parent pyridine ring and the coumarin ring through the carbonyl oxygen atom of pyridine with 4-hydroxy coumarin. The conformation of methylene linker is gauche conformation through the C10-C11 bond and anti-staggered conformation along the C11-C12 bond. The parent pyridine ring plane is 63.44° away from the benzene ring plane. Then, the coumarin ring plane is flipped away from the pyridine ring plane through a dihedral angle of 56.91°, and the benzene ring plane formed a 60.82° dihedral angle with the pyridine ring plane **(Figure 4.18 (b))**. The compound **5.2C** crystal information is summarized in **Table 4.6.**

Table 4.6: Crystal data of compounds **5.2C, 5.2D** and **5.3A**

Compound	**5.2C**	**5.2D**	**5.3A**
Identification code	2219752	2219833	2219750
Empirical formula	C_{29} H_{25} N_2 O_7	C_{29} H_{26} N_2 O_6	C_{27} H_{26} N_2 O_6
Formula weight	513.51	498.52	474.5
Temperature (K)	293(2)	293(2)	293(2)
Crystal system	monoclinic	monoclinic	triclinic
Space group	$P2_1/n$	$P2_1/n$	P-1

a/Å	14.210(2)	16.410(9)	6.9470(8)
b/Å	7.0175(6)	6.905(2)	8.3248(10)
c/Å	27.397(4)	23.262(11)	21.169(3)
α/°	90	90	92.201(9)
β/°	103.850(11)	92.19(4)	93.957(9)
γ/°	90	90	90.445(9)
Volume ($Å^3$)	2652.6(6)	2634(2)	1220.3(2)
Z	4	4	2
ρ ($calcg/cm^3$)	1.286	1.257	1.291
μ (mm^{-1})	0.093	0.089	0.092
F(000)	1076	1048	500
Radiation	MoKα (λ = 0.71073)	MoKα (λ = 0.71073)	MoKα (λ = 0.71073)
2Θ range for data collection (°)	2.982 to 49.274	2.984 to 51.976	3.86 to 51.998
Index ranges	-16 ≤ h ≤ 16, -7 ≤ k ≤ 8, -31 ≤ l ≤ 31	-20 ≤ h ≤ 20, -8 ≤ k ≤ 8, -28 ≤ l ≤ 27	-7 ≤ h ≤ 8, -10 ≤ k ≤ 10, -26 ≤ l ≤ 26
Reflections collected	14776	18174	13954
Independent reflections	4427 [Rint = 0.0986, Rsigma = 0.1153]	5185 [Rint = 0.0568, Rsigma = 0.0439]	4813 [Rint = 0.0639, Rsigma = 0.0524]
Data/restraints/parameters	4427/0/346	5185/0/338	4813/20/319
Goodness-of-fit on F^2	1.096	1.009	0.98
Final R indexes [I>=2σ (I)]	R1 = 0.1596, wR2 = 0.3654	R1 = 0.0441, wR2 = 0.1146	R1 = 0.0878, wR2 = 0.2033
Final R indexes [all data]	R1 = 0.2722, wR2 = 0.4182	R1 = 0.0732, wR2 = 0.1269	R1 = 0.1392, wR2 = 0.2435
Largest diff. peak/hole/e $Å^{-3}$	1.04/-0.29	0.25/-0.17	0.50/-0.35

Supramolecular framework of compound 5.2C: The compound **5.2C** was assembled due to the interactions of C-H…O and lone pair…π. The coumarin hydrogen H8 interacts with the methoxy oxygen O7 of the anisole moiety through a distance of 2.711 Å **(Figure 4.19 (d))**. Anisole hydrogen H25 formed intermolecular interaction with oxygen O1 of the coumarin moiety through C-H...O interactions of bond-length 2.376 Å. The oxygen O5 from the ester moiety interacts with the carbon C19 of the nitrile group, with 3.138 Å through lone pair…cation interactions. All these interactions formed a graph set $R_5^5(58)$ involving five molecules **(Figure 4.19 (b))**. Thus, the hydrogen H29A of anisole methyl interacts with the carbon C25 of the

anisole phenyl ring at 2.858 Å, resulting in the $R_3^3(22)$ graph set notation **(Figure 4.19 (c))**.

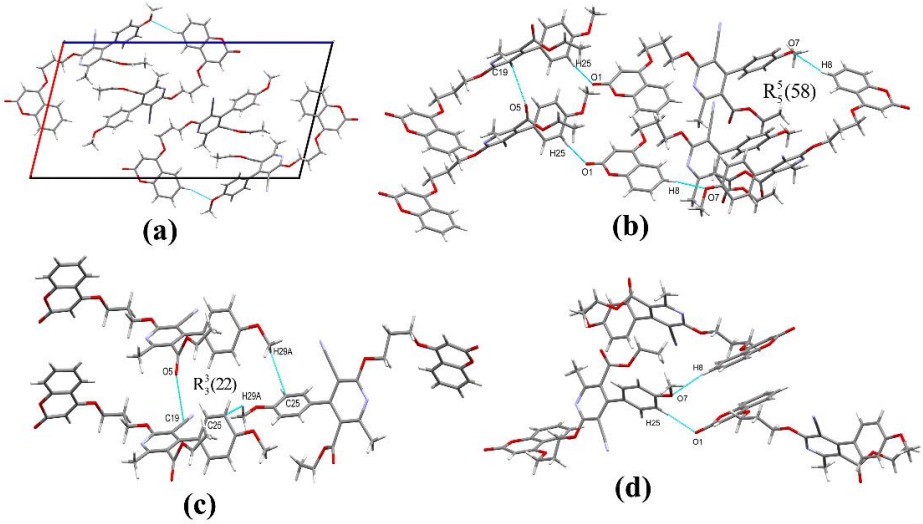

Figure 4.19: (a) Crystal packing in **5.2C** along the b-axis (b) & (c) interactions showing graph sets (d) C-H…O interaction, of compound **5.2C**

Therefore, the molecule's stability can also be stabilized by the C-H…π interactions, which formed the interlayer linking of the supramolecular structure. The pyridine π-orbital acts as a bifurcated acceptor from hydrogen H21 of the ester moiety and H11A of the methylene linker, with the interaction distance of 3.754 Å and 2.970 Å, respectively **(Figure 4.20 (a))**. Hydrogen H29A of the anisole moiety is involved in the C-H…π interaction with the benzene ring π-orbital to strengthen the molecules' self-assembly in forming a supramolecular network. In addition, π…π parallel stacking interactions at 3.619 Å and 3.957 Å between the coumarin ring on both sides also stabilized the crystal packing of compound **5.2C (Figure 4.20 (b))**. The non-covalent interactions found in compound **5.2C** are tabulated in **Table 4.7.**

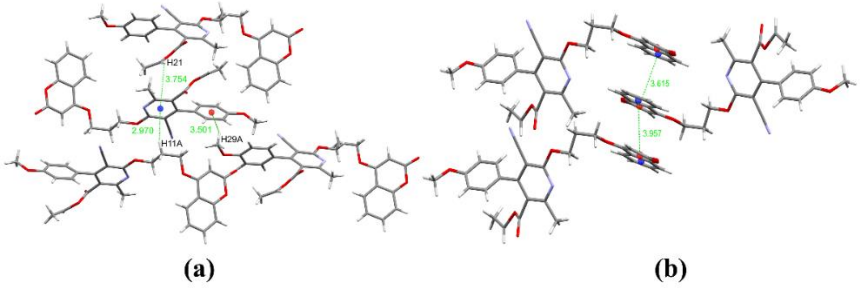

Figure 4.20: (a) C-H…π interaction, (b) π…π interaction, of compound **5.2C**

Table 4.7: Hydrogen bonds and other interactions in compound **5.2C**

Donor-H...Acceptor	D – H, Å	H...A, Å	D...A, Å	D - H...A,°
C25-H25…O1	0.930	2.376	3.281	164.67
C8-H8…O7	0.930	2.711	3.611	163.02
C26-H29A…C25	0.960	2.858	3.506	125.69
C29-H29A...π(C23-C28)	0.960	3.501	3.851	104.23
C21-H21...π(N1C13-C17)	0.933	3.754	3.942	94.70
C11-H11A…π(N1C13-C17)	0.970	2.970	3.851	151.58
Other contacts				
O5…C19		3.138		
π(O2C1-C5)...π(C4-C9)		3.615		
π(O2C1-C5)...π(C4-C9)		3.957		
Intramolecular contact				
C21-H21…O5	0.933	2.540	2.700	89.56
C18-H18B…O5	0.960	2.659	3.128	110.60
C12-H12A…N1	0.970	2.591	2.690	73.68
C12-H12B…N1	0.970	2.677	2.690	80.34
C12-H12A…O3	0.970	2.424	2.785	101.54
C9-H9…O3	0.931	2.499	2.781	97.68
C22-H22A...π(C23-C28)	0.961	3.242	3.923	129.50

Hirshfeld surface analysis of compound 5.2C: The d_{norm} of the Hirshfeld surface was mapped in the range of -0.2879 Å to 1.4603 Å for compound **5.2C**, as shown in **Figure 4.21 (a) and (b).** The region of bright red spots on the $_{norm}$ surface corresponds to the shorter interactions due to C-H…O contacts. The more intense red colour with a larger size indicates the more dominant interaction and vice versa. The bright-red spots near the hydrogen and oxygen atoms are donors and acceptors of a potential C-H…O interaction.

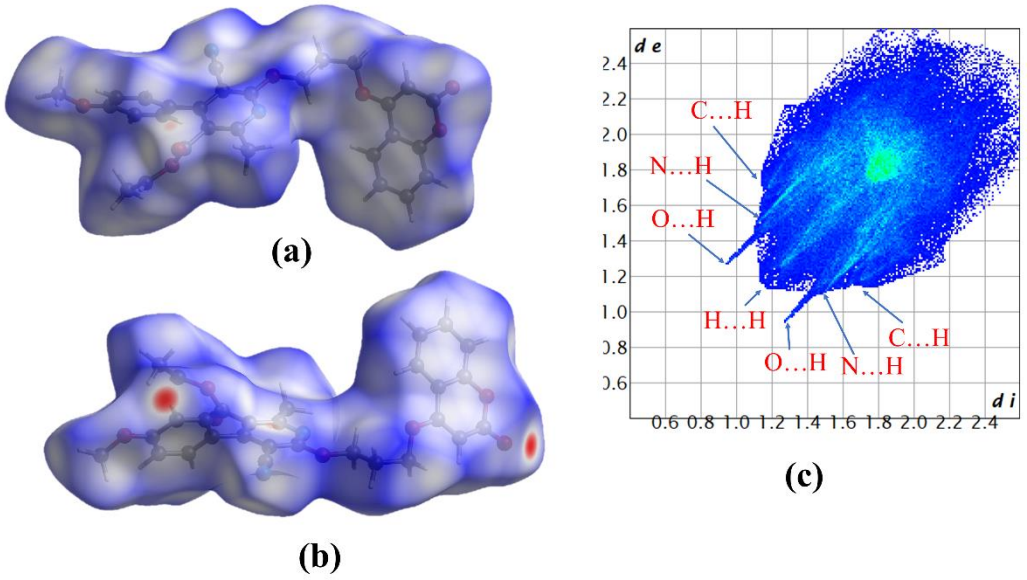

Figure 4.21: (a) and (b) Hirshfeld surface d_{norm} both side view (c) 2D fingerprint plot of compound **5.2C**

The 2D fingerprint plot of compound **5.2C (Figure 4.21 (c))** derived from a Hirshfeld surface offers a suitable visual summary of the frequency of each combination of d_i and d_e across the surface of the molecule. Non-covalent interactions with percentage contribution are shown as H…H(43.1%), O…H(23.8%), C…H(13.5%), N…H(10.7%), C…C(5.2%), C…O(2.7%), N…O(0.5%) and O…O(0.4%). The H…H interaction is the dominant interaction with 43.1% contribution and is found in the region of $d_i + d_e \approx 2.25$ Å. The O…H interactions are found as a pair of spikes in the 2D fingerprint plot in the region of $d_i + d_e \approx 2.2$ Å. The C…H interactions are shown as a wing-like pattern in the region of $d_i + d_e \approx 2.8$ Å, and C-H…π interactions are also included in the C…H interactions. The C…C interaction accounts for 5.2% of the 2D fingerprint plot, which indicates the presence of π…π stacking interactions.

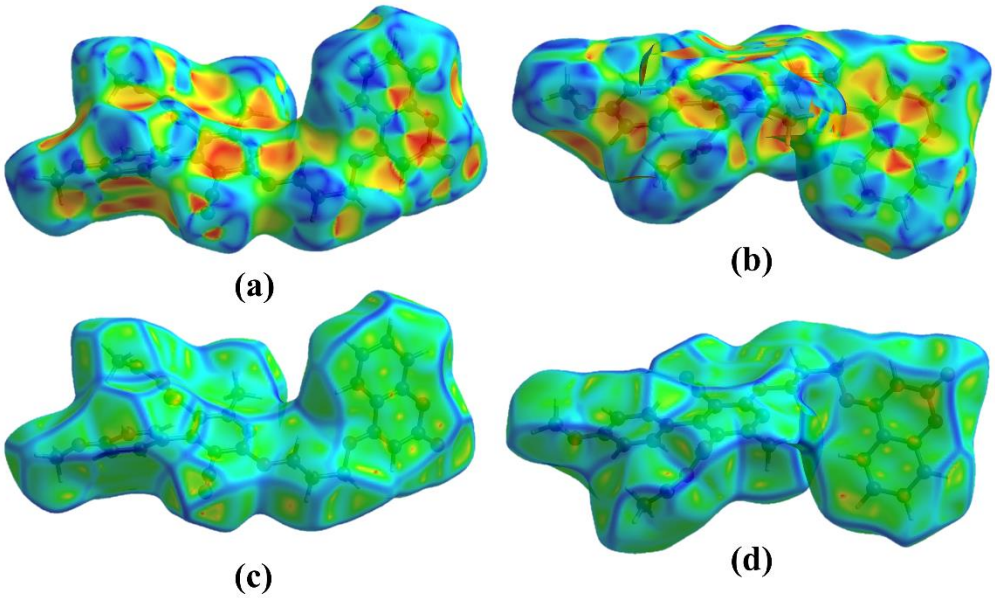

Figure 4.22: (a) and (b) Shape index, (c) and (d) Curvedness, both side view of compound **5.2C**

The shape index of the Hirshfeld surface of compound **5.2C** was mapped over in the range of -1.0 Å to 1.0 Å **(Figure 4.22 (a) & (b))**. The reddish-yellow curvature above and below the pyridine ring confirmed the C-H…π interactions. The complementary pair of blue and red triangles around the surface of coumarin indicates the presence of π…π stacking interactions between the rings, reinforcing the molecule's supramolecular structure. The curvedness was a plot in the range of -4.0 – 4.0 Å also displays a flat green region with red and yellow spots around the coumarin ring, which support the presence of π…π parallel stacking interactions between the coumarin rings **(Figure 4.22 (c) & (d))**. Yellow spots around it also indicate a short non-covalent interaction around the pyridine ring.

The Hirshfeld surface calculation of weak interactions within the radius 3.8 Å from a single crystal fragment supports the different interactions found in the supramolecular framework of compound **5.2C**, shown in **Figure 4.23.**

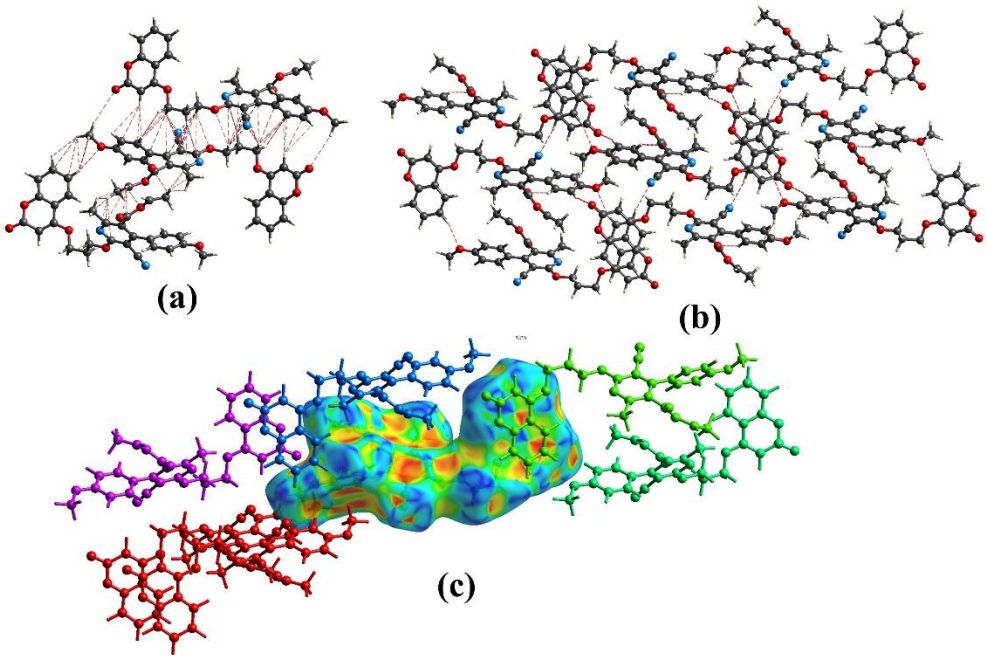

Figure 4.23: (a) weak non-covalent interaction, (b) C-H…O interaction, (c) C-H…π interaction, of compound **5.2C**

The interactions were evaluated using the enrichment ratio (ER) calculated from the Hirshfeld surface analysis. The value of the enrichment ratio is likely to be normally larger than unity for pairs of elements with a high propensity to make contacts in crystals. In contrast, the pairs that tend to evade contacts are related with a lower enrichment ratio than unity. The enrichment ratio of compound **5.2C** is illustrated in **Table 4.8**. The H…H contacts account for 43.1% of the actual contacts, and E_{HH} = 0.96 is close to unity to be considered favored interactions. The enrichment ratio of N…H(E_{NH} = 1.42) and O…H(E_{OH} = 1.28) indicates they are highly enriched, displaying the propensity to form these interactions in the crystal structure. In addition, the higher value of E_{CC} = 2.94 indicates the tendency to form interactions in the crystal. The presence of π…π interactions in the crystal structure is also supported by the enrichment ratio of C…C contacts. The contribution of C…H, C…O, N…O, and O…O is smaller than unity and is not favored. The molecule has no direct contact between C…N and N…N.

Table 4.8: Enrichment ratio (ER) of compound **5.2C**

Atoms	H	C	N	O
H	43.1	Actual contacts (%)		
C	13.5	5.2		
N	10.7	0	0	
O	23.8	2.7	0.5	0.4
Surface %	67.10	13.30	5.60	13.90
H	45.0	Random contacts (%)		
C	17.8	1.8		
N	7.5	1.5	0.3	
O	18.7	3.7	1.6	1.9
H	0.96	Enrichment ratio		
C	0.76	2.94		
N	1.42	0.00	0.00	
O	1.28	0.73	0.32	0.21

4.7.1.4 Crystal analysis of compound 5.2D

The chiral asymmetric compound **5.2D** was recrystallized from slow evaporation of ethyl acetate at room temperature. The crystal was analyzed using single crystal XRD **(Figure 4.24 (a))**. The compound crystallized with cell lengths **a** = 16.410(9) Å, **b** = 6.905(2) Å, **c** = 23.262(11) Å, i.e., **a ≠ b ≠ c** and cell angles α= 90°, β = 92.19°, γ = 90°, i.e., **α = γ = 90°, β ≠ 90°**. The compound exhibits a monoclinic crystal system, with space group $P2_1/n$ that contains four molecules per unit cell (Z:4, Z':1) **(Figure 4.25 (a))**.

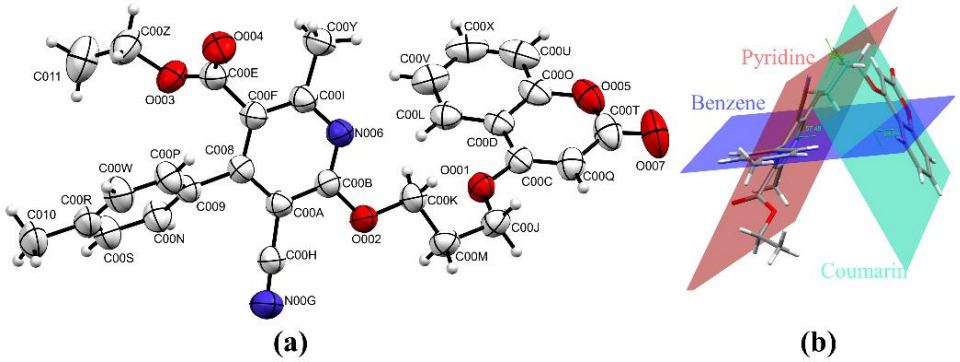

Figure 4.24: (a) ORTEP diagram, (b) planes, in compound **5.2D**

The molecule **5.2D** is formed by three-ring systems with sp^2 hybridized atoms, facilitating the delocalization of π-orbitals. The benzene ring plane is twisted away from the plane of the pyridine ring plane and forms a dihedral angle of 57.48°. The coumarin ring plane also flipped away from the parent pyridine ring plane with a dihedral angle of 54.99°; the benzene ring plane formed a dihedral angle with the coumarin ring plane at 67.68° **(Figure 4.24 (b))**. A methylene linker links the coumarin ring and parent pyridine ring with gauche conformation concerning the carbon C00M-C00J bond and anti-staggered conformation with the C00K-C00M bond. The crystal information of compound **5.2D** is summarized in **Table 4.6.**

Supramolecular framework of compound 5.2D: The molecular association of compound **5.2D** involves C-H…O and C-H…N interactions. The oxygen of the ester moiety O004 acts as a bifurcated acceptor of hydrogen H01D from ethyl ester moiety at 2.654 Å, and electron pair donor towards the nitrile carbon C00H forming cation - lone pair bond with 3.209 Å. These interactions result in the formation of $R_3^3(16)$ $R_4^4(22)$ and graph set notation **(Figure 4.25 (b))**; these interactions interlink different molecule layers. The nitrogen N00G of the nitrile group interacted with the methyl linker hydrogen H00B through 2.504 Å, along the plane of the pyridine, and formed a graph set $R_2^2(18)$ notation **(Figure 4.25 (c))**.

The oxygen O007 of the coumarin moiety formed a hydrogen bond with benzene hydrogen H00S at 2.449 Å. This bond interconnects the different layers of the molecular association to strengthen the supramolecular structure **(Figure 4.25 (c))**. The molecular self-assembly of compound **5.2D** displayed C-H…π interaction and π…π stacking interactions. The C-H…π interaction was formed from both sides of the pyridine ring through the distance of 3.509 Å and 2.963 Å, towards hydrogen H01D of ester ethyl and hydrogen H00F of methyl linker, respectively **(Figure 4.26 (a))**. The toluene methyl hydrogen H01B also formed C-H…π with the benzene ring of the toluene moiety to assist the stability of the compound **5.2D** at 3.422 Å. In addition, the molecular packing within the unit cell is stabilized by parallel π…π stacking interaction of the coumarin ring, and this alternate π…π stacking of both the rings at 3.731 Å and 3.705 Å highly stabilized the supramolecular framework of the crystal molecule

(Figure 4.26 (b)). The non-covalent interactions of compound **5.2D** are listed in **Table 4.9.**

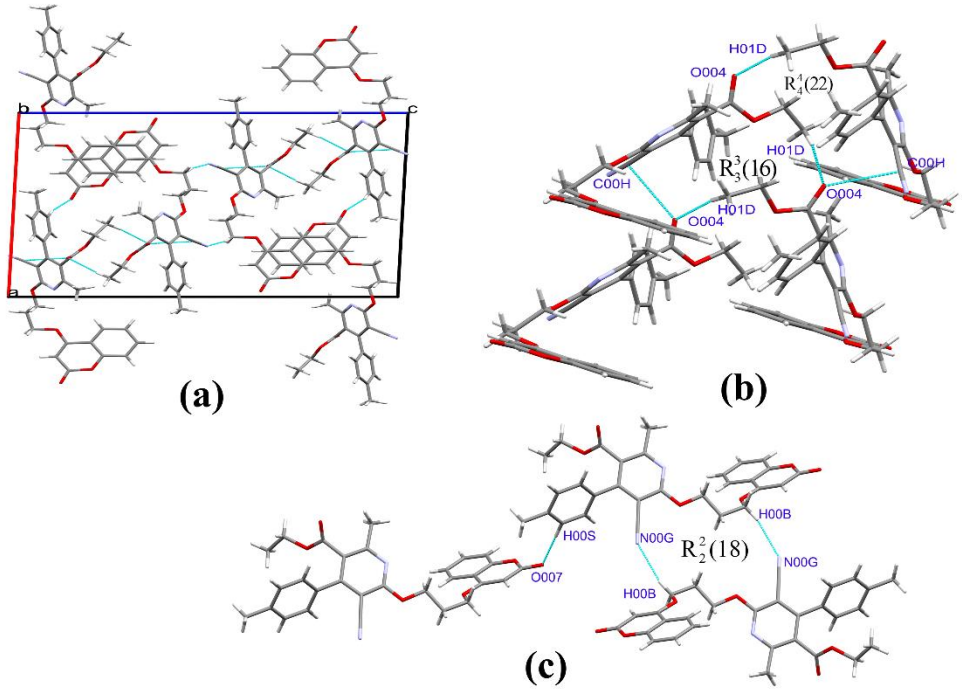

Figure 4.25: (a) Crystal packing in **5.2D** along the b-axis, (b) C-H…O and other interactions, (c) C-H…N and C-H…O interaction, of compound **5.2D**

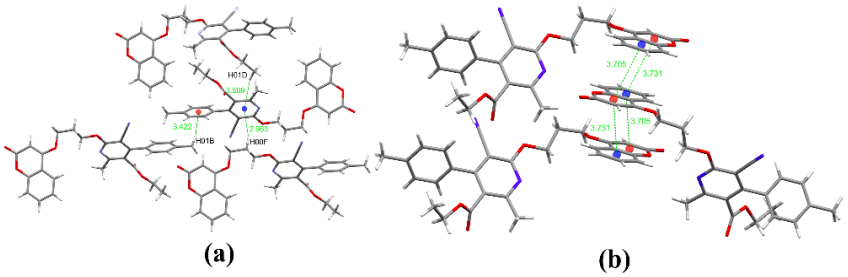

Figure 4.26: (a) C-H…π interaction, (b) π…π interaction, in compound **5.2D**

Table 4.9: Hydrogen bond and other interactions in compound **5.2D**

Donor-H...Acceptor	D – H, Å	H...A, Å	D...A, Å	D - H...A,°
C011-H01D…O004	0.961	2.654	3.606	170.63
C00J-H00B…N00G	0.970	2.504	3.455	166.86
C00S-H00S…O007	0.930	2.449	3.361	166.88
C011-H01D...π(C00A,B,F,I,8,N006)	0.961	3.509	3.929	109.05
C00M-H00F...π(C00A,B,F,I,8,N006)	0.971	2.963	3.841	151.04
C010-H01B...π(C00N,R,9,P,W,S)	0.595	3.422	3.958	117.54

Other contacts				
O004…C00H		3.209		
π(C00D,X,V,O,U,L)... π(C00O,Q,D,T,C,O005)		3.731		
π(O005,C00C,D,T,Q,O)... π(C00O,U,V,X,L,D)		3.705		
Intramolecular				
C00L-H00L…O001	0.930	2.477	2.771	98.41
C00K-H00C…N006	0.970	2.667	2.667	79.57
C00K-H00D…N006	0.970	2.555	2.667	85.88
C00Y-H00H…O004	0.960	2.640	3.165	114.76
C00N-H00N…C00H	0.930	2.898	3.127	95.46
C00P-H00P…C00E	0.930	2.853	3.078	95.08
C00K-H00D…O001	0.970	2.475	2.835	58.76

Hirshfeld surface analysis of compound 5.2D: The Hirshfeld surface of compound **5.2D** is mapped over d_{norm} in the range of -0.2299 – 1.4861 Å and is displayed in **Figure 4.27 (a) and (b).** The region of bright red spots in the d_{orm} corresponds to the short contacts of C-H…O and C-H…N interactions. The size and intensity of the spots depend on the distance of interaction. The more intense the red color of the interaction and the larger the spots, and vice versa in Hirshfeld surface intended to the more dominant interactions.

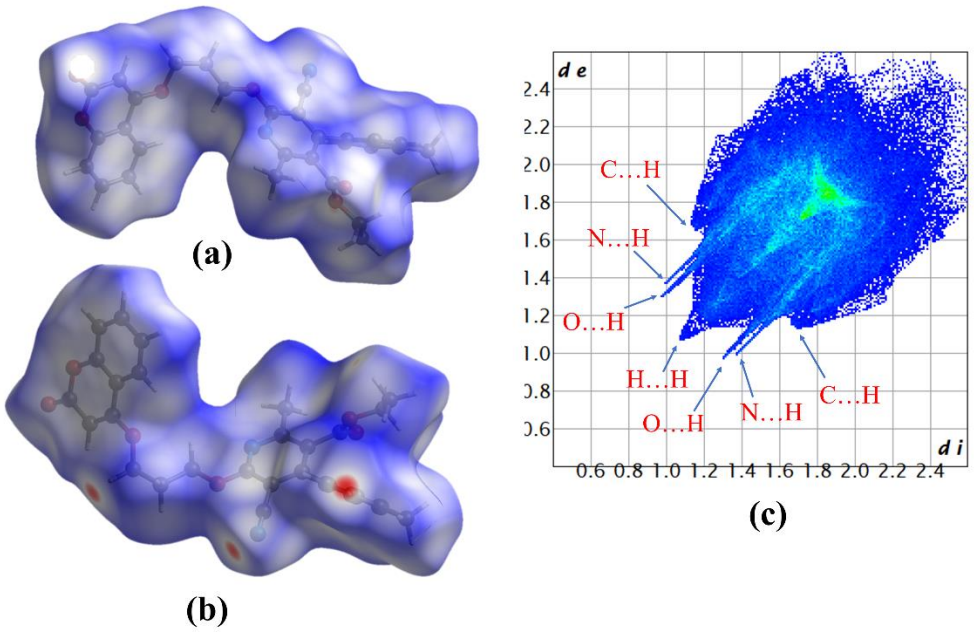

Figure 4.27: (a) and (b) Hirshfeld surface d_{norm} both side view, (c) 2D fingerprint plot, of compound **5.2D**

The 2D fingerprint plot of compound **5.2D** represents the relative contribution of the non-covalent interactions to the Hirshfeld surface **(Figure 4.27 (c))**. The interactions with their percentage contributions are H…H(46.7%), O…H(20.9%), C…H(13.4%), N…H(11.0%), C…C(5.1%), C…O(2.6%), O…O(0.2%) and O…N(0.1%). A pair of spike-like patterns in the region of $d_i + d_e \approx 2.3$ Å represents the O…H/H…O interactions, contributing 20.9% of the Hirshfeld surface of the molecule. The N…H interactions contribute 11.0% of the surface with a spike in the region $d_i + d_e \approx 2.4$ Å in the fingerprint plot. This interaction associates the molecules through the C-H…N interactions. The C-H…π and C-H contacts appeared in the same region of the 2D fingerprint plot, which appeared as a wing-like pattern in the region $d_i + d_e \approx 3.0$ Å, and this contact accounts for 13.4% of the Hirshfeld surface. The C…C interactions account for 5.1%, which signifies the presence of π…π stacking interactions in the compound, and C…O interactions with 2.6% imply the lone pair…π interactions.

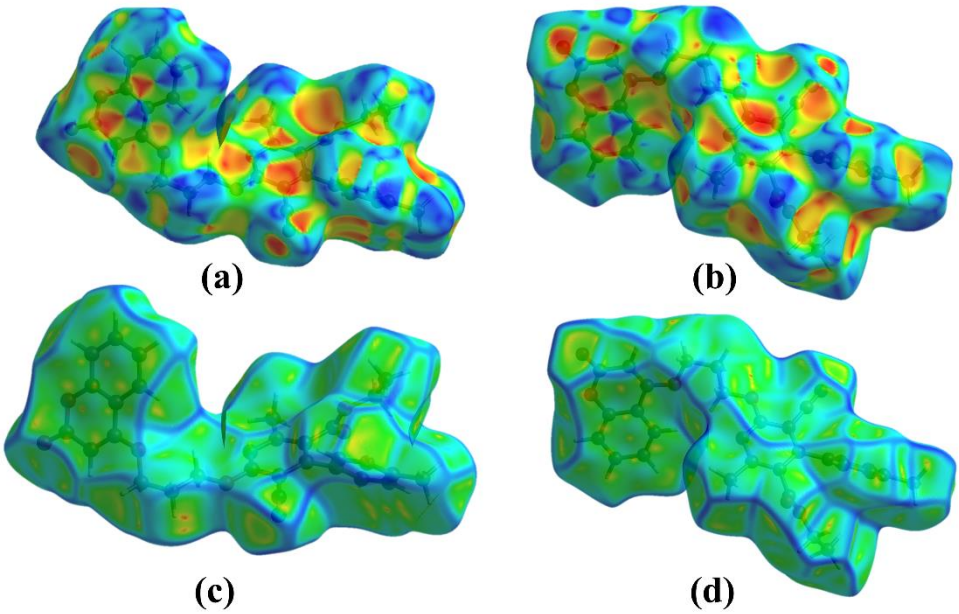

Figure 4.28: (a) and (b) Hirshfeld surface shape index, (c) and (d) curvedness, both side view of compound **5.2D**

The shape index in the range of -1 Å to 1 Å for compound **5.2D** shows complimentary pair of blue and red triangles, having an edge-to-edge connection at the surface of the coumarin rings, which indicates the presence of π…π stacking interactions between the two rings **(Figure 4.28 (a) & (b))**. The yellowish-red color

concave regions around the aromatic rings represent the acceptor region of C-H…π interactions, and the blue region represents the donor region of the surface. The curvedness plot in the region of -4 – 0.4 Å for compound **5.2D** displayed a flat green region with a yellowish-red spot around the surface of the coumarin rings. This flat green region represents the presence of π…π stacking interactions between the rings **(Figure 4.28 (c) & (d))**.

The C-H…O, C-H…N, C-H…π and π…π interactions found within the 3.8 Å region of the Hirshfeld calculation for weak non-covalent intermolecular interactions also supported the supramolecular association of the crystal compound **5.2D (Figure 4.29)**.

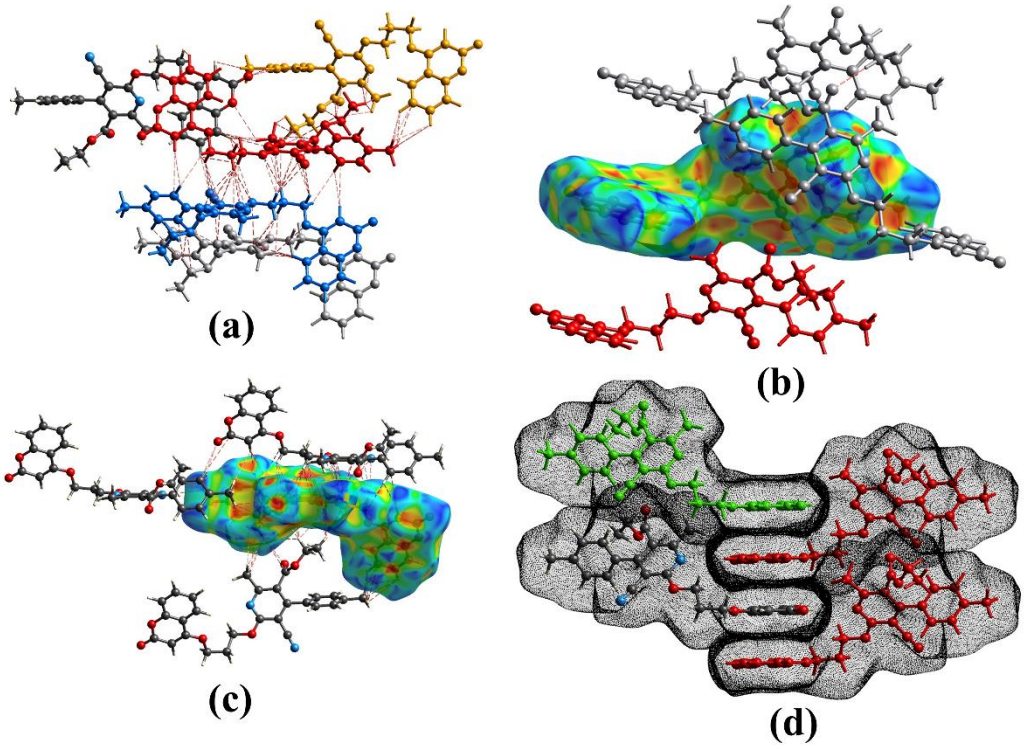

Figure 4.29: (a) and (c) weak interactions, (b) C-H…π interaction, (d) π…π interaction, of compound **5.2D**

The enrichment ratio (ER) is a useful tool for evaluating the favorable contacts that are important for the association of the molecules to form the supramolecular structure. The ER value is calculated from the interatomic contacts between pairs of interacting atoms in Hirshfeld surface analysis. The enrichment ratio values given in **Table 4.10** indicated that N…H/H…N, O…H/H…O, and C…C contacts show ER

values more than unity, and their contacts are favorable. The enrichment ratio values also confirm the C-H…O and C-H…N interactions in the supramolecular association. The C…C contacts (E_{CC} = 2.97) confirmed the presence of π…π stacking interactions in the molecule, which play an important role in the molecular association of the crystal compound **5.2D.** The hydrogen atom generates more than 69% of the total surface, but the nitrogen atom occupies only around 5% of the surface. Although the H…H contacts are the most abundant interactions, the enrichment ratio of the H…H (E_{HH} = 0.97) indicates that this interaction also plays an important role in the association of the molecule.

Table 4.10: Enrichment ratio of compound **5.2D.**

Atoms	**H**	**C**	**N**	**O**
H	46.7	Actual contacts (%)		
C	13.4	5.1		
N	11	0	0	
O	20.9	2.6	0.1	0.2
Surface %	69.35	13.10	5.55	12.00
H	48.1	Random contacts (%)		
C	18.2	1.7		
N	7.7	1.5	0.3	
O	16.6	3.1	1.3	1.4
H	0.97	Enrichment ratio		
C	0.74	2.97		
N	1.43	0.00	0.00	
O	1.26	0.83	0.08	0.14

4.7.1.5 Crystal analysis of compound 5.3A

The compound **5.3A** was crystallized from the slow evaporation of ethyl acetate at room temperature. The crystal was analyzed using SC-XRD **(Figure 4.30)**, and studied its structural framework. The compound crystallized with cell lengths **a** = 6.9470(8) Å, **b** = 8.3248(10) Å, **c** = 21.169(3) Å, i.e., **a** ≠ **b** ≠ **c** and cell angles $\boldsymbol{\alpha}$ = 92.201(9)°, $\boldsymbol{\beta}$ = 93.957(9)°, $\boldsymbol{\gamma}$ = 90.445(9)°, i.e., $\boldsymbol{\alpha \neq \beta \neq \gamma}$. The compound exhibits a triclinic crystal system, with space group $P\bar{1}$, which contains two molecules in a unit cell (Z:2, Z':1) **(Figure 4.31 (a))**.

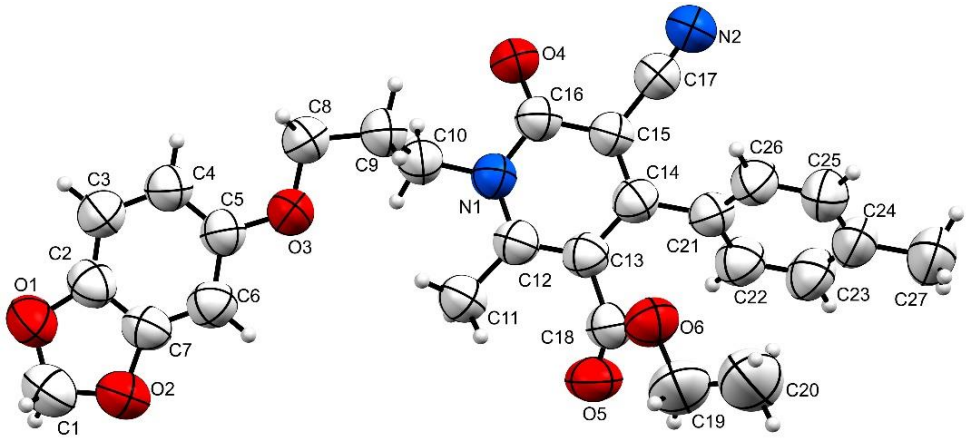

Figure 4.30: ORTEP of compound **5.3A**

Compound **5.3A** is composed of three rings with sp^2 hybridized atoms, resulting in the planar ring with delocalized π-orbitals. The benzene ring planes make a dihedral angle of 57.27° away from the parent pyridone ring. The sesamol ring flip at 6.55° away from the parent pyridone ring, and the benzene ring plane is 52.94° from the sesamol ring plane. A propane linker linked the parent pyridone ring and the sesamol ring through the nitrogen atom of pyridone. The conformation of the methylene linker is antiperiplanar through the C9 - C10 bond and gauche conformation through the C8-C9 bond. The crystal information of compound **5.3A** is summarized in **Table 4.6.**

Supramolecular framework of compound 5.3A: The molecular assembly of compound **5.3A** involves C-H…O, C-H…N, and lone pair…π interactions. Carbonyl oxygen atom O4 of the pyridone acts as a bifurcated acceptor in the molecular layer with H4 and H8B, with the distance of 2.396 Å and 2.653 Å, respectively, and results in the formation of a graph set of $R_2^1(7)$ **(Figure 4.31 (b)),** which make the association of the molecule in the layer. Then, the hydrogen (H3) from the sesamol ring formed a C3-H3…N2 interaction at the distance of 2.688 Å, and this interaction resulted in the formation of $R_2^2(9)$ graph set notation **(Figure 4.31 (b))**. In addition, the interaction C8-H8B…O4 formed a molecule in a layer to make the structure as a plane and is stabilized by $R_2^2(14)$ graph set notation **(Figure 4.31 (b))**. These interactions help in making the supramolecular framework. Ester oxygen O5 acts as an acceptor to form non-covalent hydrogen bonding with H1B and H26, as well as a donor of electrons to

the carbon C17 of the nitrile group. The interaction of carbon C1 from the sesamol ring C1-H1B…O5 strengthens the molecule's association through 2.620 Å, with graph set $R_2^2(30)$ **(Figure 4.31 (c))**.

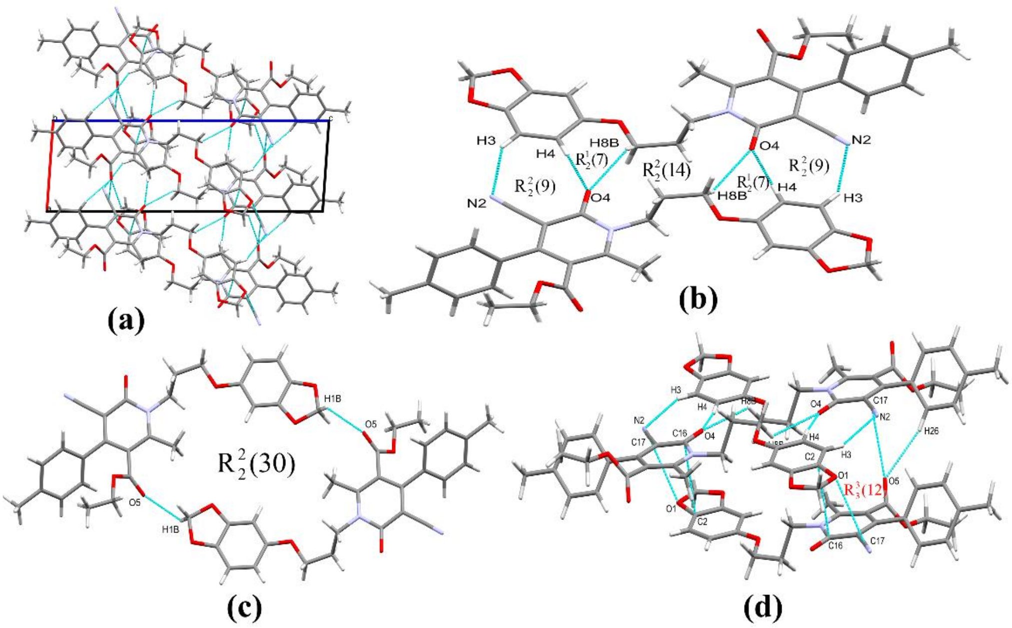

Figure 4.31: (a) crystal packing in **5.3A** along the b-axis, (b) and (c) C-H…O interactions showing graph sets, (d) C-H…O and other interactions of compound **5.3A**

The non-covalent interaction of C26-H26 with O5 of the neighboring molecule has a bond length of 2.660 Å. Results from the interlayer interaction of the supramolecular framework of compound **5.3A**. The carbon C17 of the nitrile acts as a bifurcated acceptor, resulting in interlayer interaction with the oxygen atom O1 and O5, forming a lone pair…cation interaction with 3.212 Å and 3.167 Å, respectively. These interlayer interactions are important in the formation of the association of the molecules and formed $R_3^3(12)$ graph set **(Figure 4.31 (d))**. The crystal packing within the unit cell displays also displays C-H…π and lone pair…π interactions with the pyridone ring and sesamol aromatic ring.

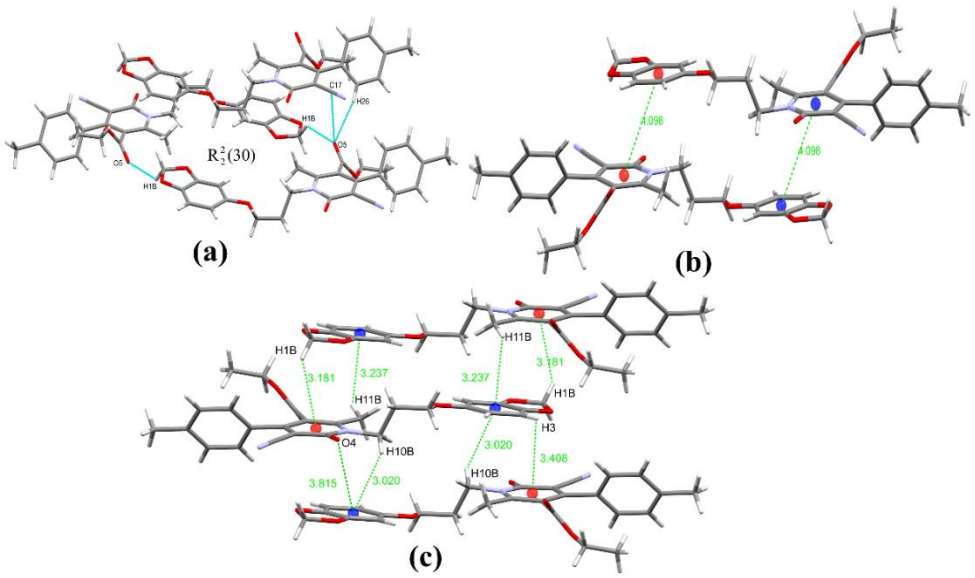

Figure 4.32: (a) C-H…O interactions showing graph set, (b) π…π interaction, (c) C-H…π interaction, of compound **5.3A**

The C-H…π interactions are formed by linker hydrogen H10B and methyl H11B with sesamol aromatic rings at 3.020 Å and 3.234 Å, respectively. Pyridone ring and hydrogen atoms H1B and H3 display C-H…π interactions through 3.181 Å and 3.408 Å, respectively. The lone pair…π interactions are also displayed between pyridone O4 and the sesamol ring with 3.815 Å **(Figure 4.32 (c))**. The extensive network of the crystal also displays a weak π…π stacking interaction between the sesamol benzenoid ring and the pyridone ring moiety at an interaction distance of 4.098 Å **(Figure 4.32 (b))**. The non-covalent interactions of the crystal compound **5.3A** are tabulated in **Table 4.11.**

Table 4.11: Hydrogen bond and other interactions in compound **5.3A**

Donor-H...Acceptor	D – H, Å	H...A, Å	D...A, Å	D - H...A,°
C1-H1B…O5	0.970	2.620	3.287	126.17
C26-H26…O5	0.930	2.660	3.563	163.87
C4-H4…O4	0.930	2.396	3.319	171.29
C8-H8B…O4	0.970	2.653	3.284	123.02
C3-H3…N2	0.930	2.688	3.508	147.46
Other contacts				
C17…O5		3.167		
C17…O1		3.212		
C2…C16		3.391		

Intramolecular				
C10-H10A…O3	0.970	2.520	2.933	105.59
C10-H10B…O4	0.970	2.379	2.649	95.17
C9-H9A…O4	0.970	2.710	3.138	107.25
C11-H11B…O5	0.959	2.414	2.977	117.140
C19-H19B…O5	0.970	2.206	2.629	105.000

Hirshfeld surface analysis of compound 5.3A: The Hirshfeld surface of compound **5.3A** was mapped over d_{norm} in the range of -0.2719 – 1.5298 Å in **Figure 4.33 (a) and (b).** The red spot region of the d_{norm} corresponds to the shorter contacts due to the C-H…O and C-H…N interactions. The intensity and size of the spots depend on the interactions' distance. The dominant interactions are indicated with more intense colour and larger size of the spots, and vice versa.

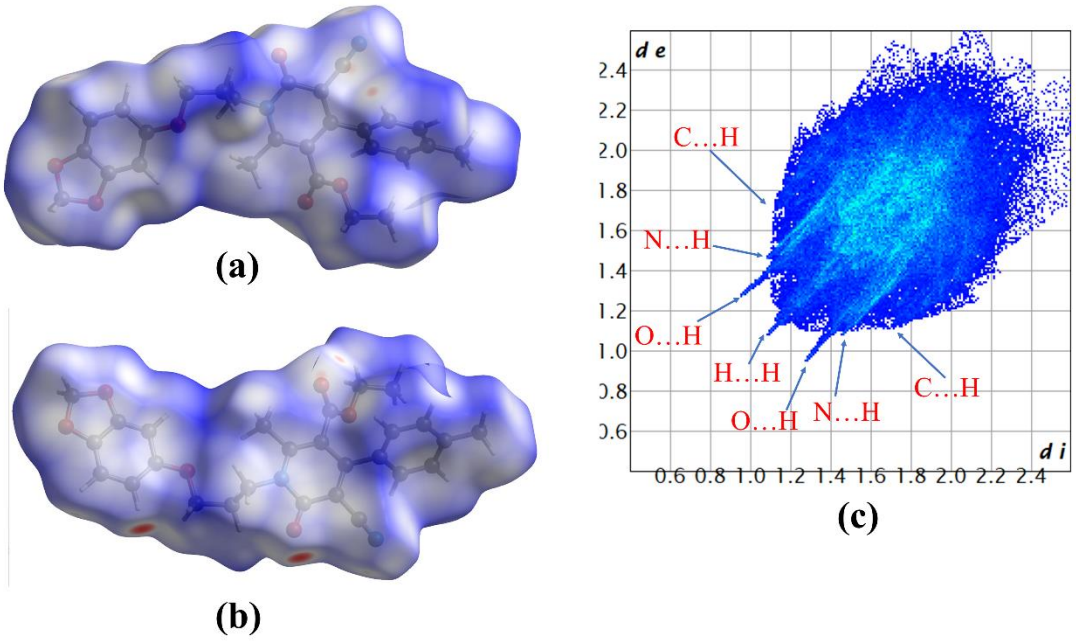

Figure 4.33: (a) and (b) Hirshfeld surface d_{norm} both side view, (c) 2D fingerprint plot, of compound **5.3A**

The 2D fingerprint plot of compound **5.3A** represents the relative percentage contribution of non-covalent interaction to the Hirshfeld surface **(Figure 4.33 (c))**. The non-covalent interactions are H…H(48.9%), O…H(17.4%), C…H(16.1%), N…H(8.9%), C…O(4.1), O…O(1.6%), C…C(1.4%), C…N(0.8%) and O…N(0.7%). The H…H interaction is found in the region of $d_i + d_e \approx 2.2$ Å. A pair of spikes in the region of $d_i + d_e \approx 2.25$ Å indicates O…H interactions. The wing-like pattern in the

$d_i + d_e \approx 2.8$ Å represents the C…H contacts, including the C-H…π interactions. The C…C contacts account for 1.4%, implying weak π…π stacking interactions.

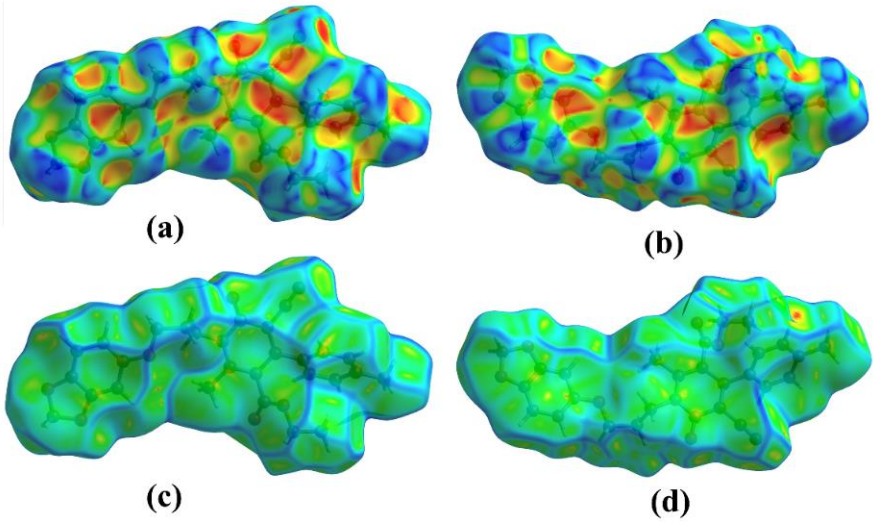

Figure 4.34: (a) and (b) Hirshfeld surface shape index, (c) and (d) Curvedness of compound **5.3A**

The shape index surface was mapped over a range of -1 Å to 1 Å for compound **5.3A**, showing the presence of yellowish red color concave region and indicating the C-H…π and lone pair…π interactions **(Figure 4.34 (a) & (b))**. The complementary pair of red and blue triangles are found on the sesamol ring on the surface, which indicates the presence of π…π stacking interactions. The pyridone ring also formed the small complementary pair of red and blue triangles, indicating weak π…π stacking interactions. The sesamol ring and the parent pyridone ring interact with a weak stacking interaction, resulting in the molecule's interlayer interactions. The curvedness in the range of -4.0 – 4.0 Å for compound **5.3A** also displayed a flat green region with a yellow spot around the sesamol ring and pyridone ring, which indicates the presence of π…π stacking interactions between the rings **(Figure 4.34 (c) & (d))**. The benzene hydrogen shows a reddish-yellow spot, which indicates the short interaction with the other benzene hydrogen.

The non-covalent interactions in the supramolecular framework, supported by the Hirshfeld surface calculation within the radius of 3.4 Å from a single crystal fragment, are shown in **Figure 4.35.**

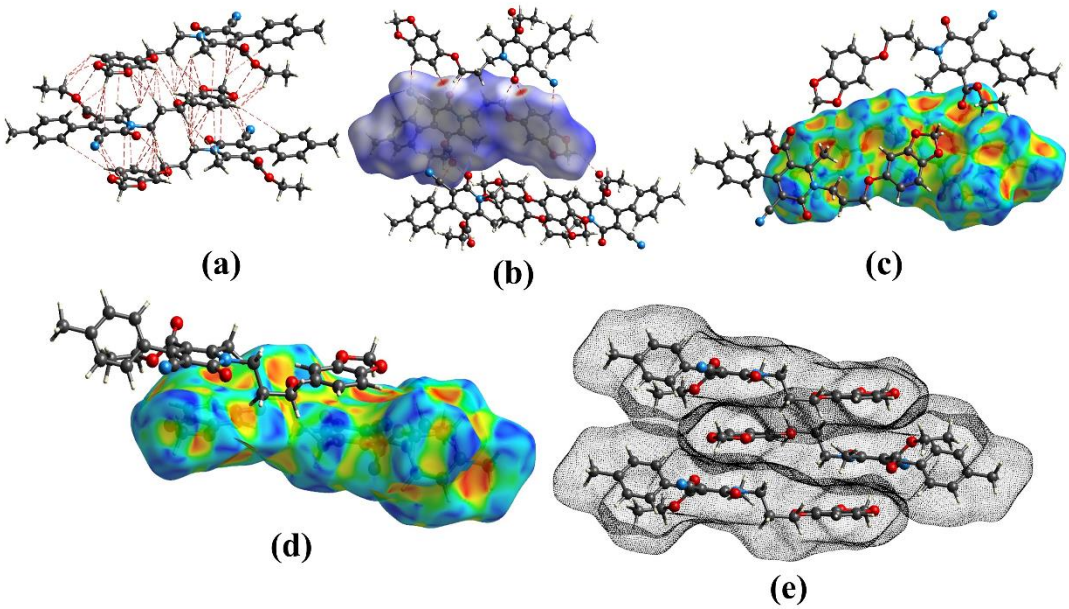

Figure 4.35: (a) weak interactions, (b) C-H…O interaction, (c) and (d) C-H…π interaction, (e) π…π interaction, of compound **5.3A**

The enrichment ratio (ER) of the intermolecular contacts for compound **5.3A** was studied to analyze the propensity of two contact atoms. The enrichment ratio is a descriptor derived from the Hirshfeld surface analysis. It is the ratio between the proportion of actual contacts in a crystal and the theoretical proportion of random contacts. **Table 4.12** shows the enrichment ratio of compound **5.3A**. The hydrogen atom occupies around 70% of the surface; H…H contacts can be considered favored with E_{HH} = 1.00 and constitutes most of the contacts. The N…H and O…H contacts are also favored (E_{NH} =1.31, E_{OH} = 1.00) and play an important short interaction in the crystal compound. The C…H contact having E_{CH} = 0.97 is also fruitful and is an important interaction in this compound. The C…C contact show E_{CC} = 0.99, indicating the presence of weak π…π stacking interaction in the crystal structure. The contacts C…O, and O…O are also favored (E_{CO} = 1.39, E_{OO} = 1.05), indicating these interactions are important and help in the molecular association of the compound. The C…N and O…N contacts are impoverished with E_{CN} = 0.69 and E_{ON} = 0.58, respectively.

Table 4.12: Enrichment ratio (ER) of compound **5.3A**

Atoms	H	C	N	O
H	48.9	Actual contacts (%)		
C	16.1	1.4		
N	8.9	0.8	0	
O	17.4	4.1	0.7	1.6
Surface %	70.10	11.90	4.85	12.35
H	49.1	Random contacts (%)		
C	16.7	1.4		
N	6.8	1.2	0.2	
O	17.3	2.9	1.2	1.5
H	1.00	Enrichment ratio		
C	0.97	0.99		
N	1.31	0.69	0.00	
O	1.00	1.39	0.58	1.05

4.8 *In silico* docking studies of synthesized compounds in Scheme 5

The body's natural protective response to various intrinsic and extrinsic stimuli is inflammation. Chronic inflammation for an extended period is frequently linked to the onset and progression of autoimmune, cardiovascular, neurological, cancer, arthritis, and other diseases (Coussens & Werb, 2002; Lucas et al., 2006). Many human inflammatory diseases are primarily caused by the excessive production of mediators of the arachidonic acid (AA) cascade. Mainly through cyclooxygenase (COX) and lipoxygenase (LOX) pathways (P et al., 2018; Vane, 2000). 5-lipoxygenase (5-LOX) and Cyclooxygenase-2 (COX-2) are upregulated and co-expressed, endorsing cancer cell proliferation and angiogenesis. It causes several human cancers. Studies show that blocking COX-2 and 5-LOX simultaneously may have additional advantages for controlling cancer cell proliferation.

In silico or molecular docking analysis is an important tool for studying the host-guest chemistry of compounds. The ability of compounds to interact with the COX-2 enzyme (PDB ID: 5KIR) and 5-LOX enzyme (PDB ID: 6NCF) was retrieved from the RCSB protein data bank. The enzyme was prepared by removing cofactors, embedded water molecules, and co-crystallized ligands. Afterward, using the Autodock tools software, hydrogens and Kohlmann charges were added to enzymes

and saved in pdbqt format. The ligand's CIF files are converted to PDB format in Mercury software. The grid parameter for the target enzyme binding cavity was determined based on native ligands. The grid parameters employed for COX-2 docking are centered at x = 23.287, y = 0.587, z = 34.435; 20 Å x 20 Å x 20 Å, while docking for 5-LOX are centered at x = 11.277, y = -21.891, z = -18.408; 20 Å x 20 Å x 20 Å. The docking results are validated by re-docking. Docking poses were visualized and analyzed using discovery studio and pymol software. The docking scores and interactions are given in **Table 4.13.**

Table 4.13: Docking scores and residues involved in the interactions of synthesized compounds

5-LOX			
Compounds	Docking score (kcal/mol)	Residues involved in H-bond	Residues involved in other interactions (π…anion, π…cation, π...σ, π...π, π…alkyl, and alkyl)
5.2A	-7.6	Arg101, His130	Val107, Val110, Lys133, Arg138
5.2B	-7.6	Arg101, His130, Thr137	Arg101, Val107, Val110, His130, Lys133, Arg138
5.2C	-8.3	Arg101, His130	Val107, Val110, His130, Arg138, Tyr142, Asp166, Arg165, Pro168
5.2D	-8.6	Arg101, His130, Thr137, Gln141	Leu66, Val107, Val110, His130, Lys133, Arg138
5.3A	-8.4	Arg101, His130, Arg165	Val107, Val110, His130, Lys133, Pro164, Arg165, Asp166
COX-2			
Compounds	Docking score (kcal/mol)	Residues involved in H-bond	Residues involved in other interactions (π…anion, π…cation, π...σ, π...π, π…alkyl, and alkyl)
5.2A	-9.1	Arg120, Tyr355, Ser530	Val89, Val116, Val349, Leu352, Tyr355, Phe518, Val523, Ala527

5.2B	-8.7	Arg120, Tyr355	Val89, Val116, Val349, Leu352, Tyr355, Phe381, Leu384, Tyr385, Trp387, Phe518, Val523, Ala527
5.2C	-9.1	Ser353	Val89, His90, Leu93, Val116, Arg120, Val349, Leu352, Tyr355, Phe381, Leu384, Tyr385, Trp387, Phe518, Val523, Ala527
5.2D	-8.7		Val89, His90, Leu93, Val116, Arg120, Val349, Leu352, Tyr355, Tyr385, Tyr387, Phe518, Val523, Ala527, Val527
5.3A	-5.7	Arg120, Ser530	Val89, Leu93, Val116, Val349, Leu352, Tyr355, Tyr385, Tyr387, Phe518, Val523, Ala527

The docking studies of the synthesized compounds with 5-LOX show that **5.2D, 5.3A**, and **5.2C** have high binding affinities towards 5-LOX with binding energies -8.6, -8.4, and -8.3 kcal/mol, respectively. The least energy conformation orientation in the active site of the enzyme is almost similar **(Figure 4.36 (e))**. All the compounds formed a hydrogen bond with residue Arg101 and His130 **(Figure 4.36 (a) to (d))**. In compound **5.2D**, Arg101 acts as a bifurcated acceptor with the ether oxygen O001 and O002 of the linker and Gln141 with coumarin carbonyl oxygen O007. In addition, the residue His130 and Thr137 also formed hydrogen bonds through cyano nitrogen N00G and the carbonyl oxygen of coumarin O007 to help the stability of the ligand in the active site. The T-shaped π-π interaction of the phenyl ring with His130 in the active site was found in **5.2D** and **5.3A**. The electrostatic interaction of π-cation of compound **5.2D** was formed with His130 residue.

Then, the phenyl ring of all compound form π-alkyl interactions with Val110 and His130 residue. Further, the π-alkyl hydrophobic interaction was formed with Lys133 in **5.2D** and **5.3A**, Val107 in **5.2D** and **5.2C**, and Arg165 in **5.3A** and **5.2C**. The compound **5.3A** also formed hydrogen bonds with Agr101 and Arg165 residue through pyridone carbonyl oxygen O4 and sesamol O and a weak carbon-hydrogen bond with residue His130. The electronic π-cation and π-anion interaction in **5.3A** are also found in His130 and Asp166, respectively. Moreover, hydrophobic alkyl interactions with residues Arg138 and Leu166 are found in compound **5.2D (Figure 4.36 (a) & (b))**, Val107 in compound **5.3A (Figure 4.36 (c) & (d))** and, Arg138 and

Val107 in compound **5.2C**. Thus, π-σ hydrophobic interaction is found only in **5.2D** with Val107 residue.

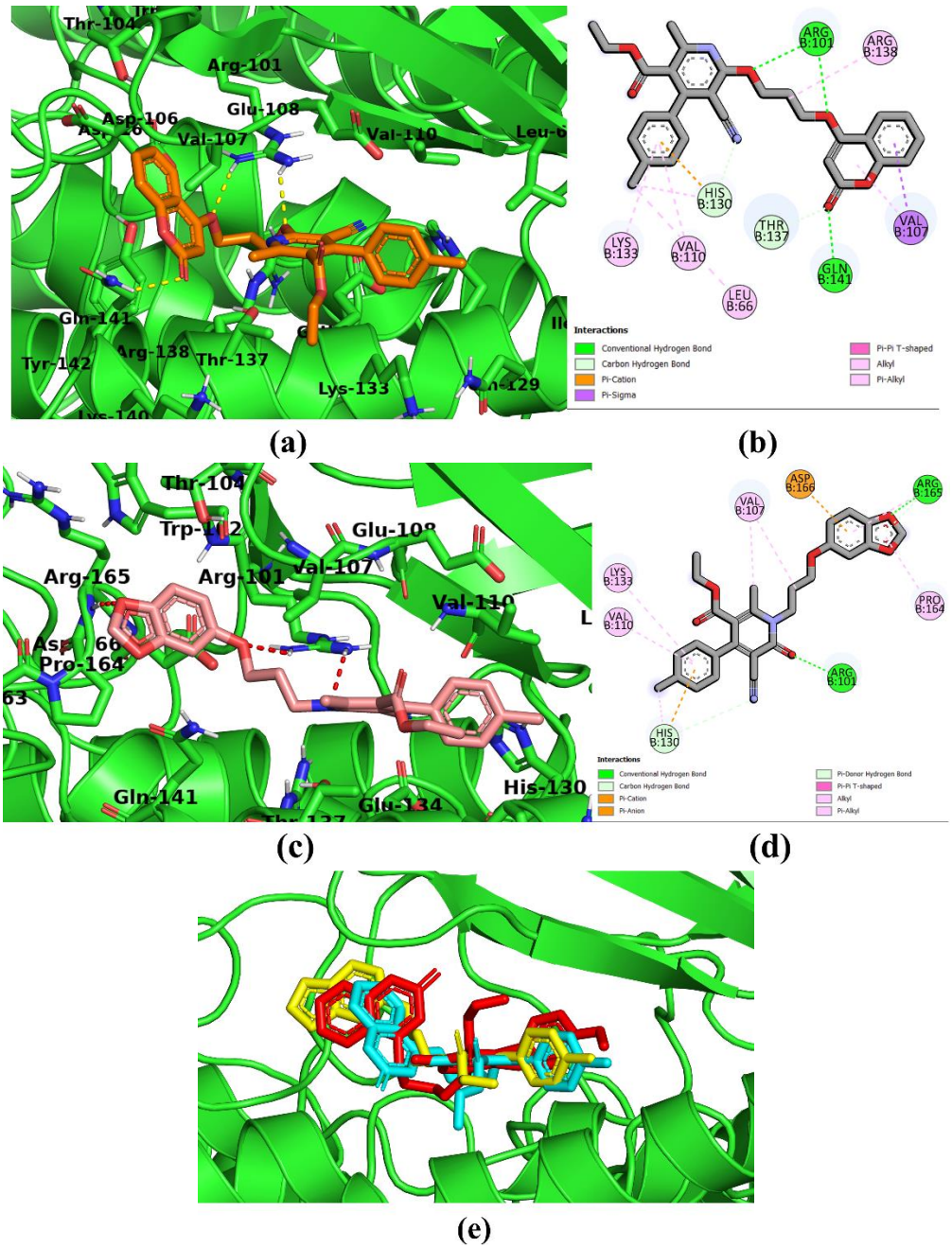

Figure 4.36: Binding modes of compounds in the active sites of 5-LOX (a) and (b) **5.2D**, (c) and (d) **5.3A**, (e) overlay diagram: **5.2D** (cyan), **5.3A** (yellow) and **5.2C** (red)

The docking of these compounds in the active sites of COX-2 indicates that compounds **5.2A, 5.2C**, and **5.2B** illustrated high binding affinities, and their binding affinities are -9.1, -9.1, and -8.7, respectively. All these compounds show similar

orientation in the active site shown in **Figure 4.37 (e)**, and they had hydrogen bond interaction with the residue Arg120 and Tyr355 except **5.2C**, which formed a hydrogen bond with Ser353. The ether linker O4 compound **5.2A** acts as a bifurcated hydrogen bond acceptor with Arg120 and hydrogen bond with Ser530 and Tyr355 with the cyano nitrogen N1 and propyl linker carbon by a weak hydrogen bond **(Figure 4.37 (a) & (b))**. Tyr355 in compound **5.2A** acts as a trifurcated acceptor and facilitates hydrogen bonds with ether linker and π-alkyl interactions with propyl moiety and a methyl group.

The π-alkyl interactions are also found with the residues of Phe518, Val349, Val523, and Val89. Moreover, π-σ interactions are found with residues Val116, Leu352, and Ala527. In compound **5.2C**, the π-σ interactions are shown at Val89, Val116, and Tyr385 residues. Thus, the residues His90, Tyr355, Phe381, Trp387, Phe518, Val349, Val523, Ala527, Leu352, Val116, Val 89 and Leu93 interact through π-alkyl interactions. However, the π-alkyl interactions with **5.2B** were formed by the residues Tyr355, Phe381, Trp387, Phe518, Val349, Val523, Ala527, Leu352, and Val89. The stability of these compounds is also reinforced by the alkyl interactions in the enzyme's active sites.

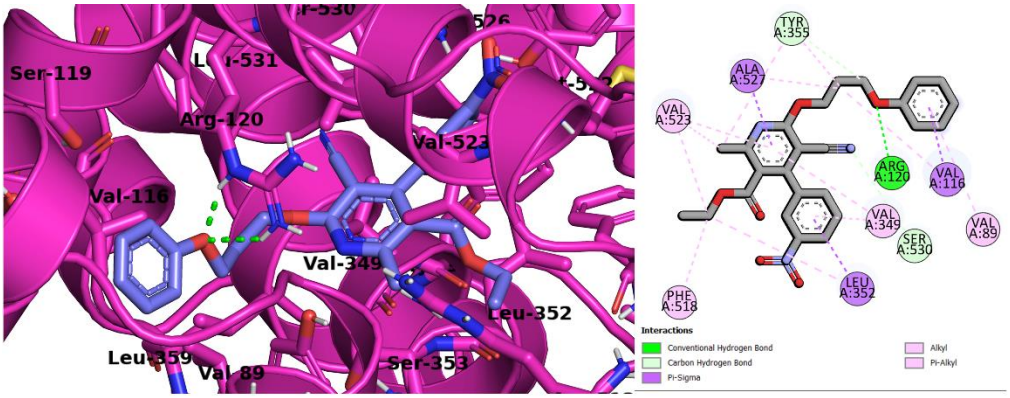

(a) **(b)**

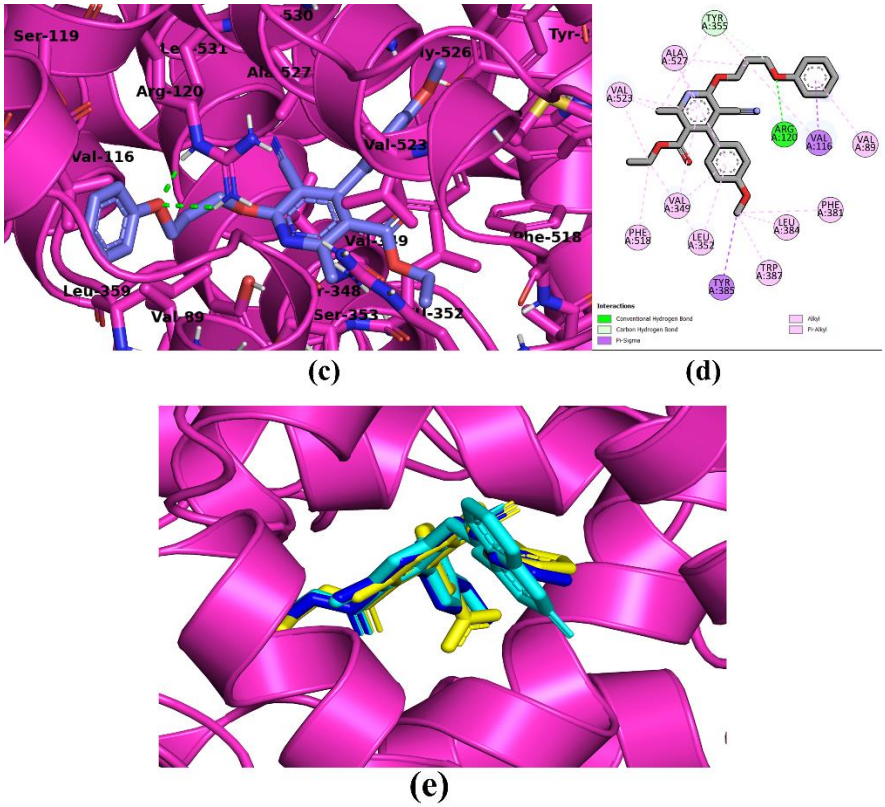

Figure 4.37: (a) and (b) compound **5.2A**, (c) and (d) compound **5.2B** binding mode in the active site of COX-2 (e) overlay diagram of **5.2A** (yellow), **5.2C** (cyan), and **5.2B** (blue)

4.9 Conclusion

A new hybrid molecule of pyridine–aromatic ring derivatives is synthesized in this chapter, where all the synthesis compounds are studied and analyzed. The compounds which form suitable crystals are analyzed using single-crystal X-ray diffraction. The crystal data were studied for supramolecular framework using mercury software and Hirshfeld surface analysis using crystal explorer software. The interatomic interactions among the atoms of the self-assembly form the supramolecular framework of the crystals. The important interactions which play an essential role in the crystal structure are C-H…O, C-H…π, and π…π interactions. All these interactions are also important for drug design, structural stabilization, crystal engineering, etc. The non-covalent interactions of the molecules also stabilize the crystal structure. The Hirshfeld surface analysis results also support the supramolecular interactions in the supramolecular framework. The enrichment ratio of the compounds is also calculated

and analyzed, which supports the molecular interactions found in the supramolecular framework.

Flexible pyridine-based hybrid molecules are synthesized using the aromatic ring linked with methylene bromide and the pyridone core using Potassium carbonate as the base catalyst in DMF solvent. The aromatic ring linked with methylene bromide is synthesized as the no of the aromatic ring increases, and the product yield slightly decreases. When these react with the 2-pyridone core of the compounds, it is found that the carbonyl group of the pyridone was more reactive to linked with the methylene bromide to give O-linked product, but **5.3A** formed only the product which is linked with NH of the pyridone making N-linked product. Moreover, on the other end of the methylene, sesamol gives only an N-linked product, whereas benzene and coumarin do not provide the N-linked product in the same reaction condition.

The crystal structure study shows that all the compounds exhibit π-π interactions through the phenyl ring in **5.2A**, phenyl and pyridone in **5.2B**, between the coumarin ring in **5.2C** and **5.2D**, but in **5.3A**, it is found between the pyridone ring and sesamol ring. Compounds **5.2A** and **5.3A** form a sheet-like structure, but all the other compounds are not crystallized in a sheet structure. A flat green surface also confirmed Hirshfeld surface analysis in the shape index of all the compounds. Molecular docking studies of all the compounds done with COX-2 and 5-LOX receptors, and the result shows that the binding energy of **5.2D** is -8.6 kcal/mol for 5-LOX protein and **5.2A** and **5.2C** is -9.1 kcal/mol for COX-2 protein. The molecular docking score indicates the electron-donating methyl group in **5.2D** give the highest score in 5-LOX protein, but in COX-2 protein, the electron-withdrawing group **5.2A** exhibit the best score.

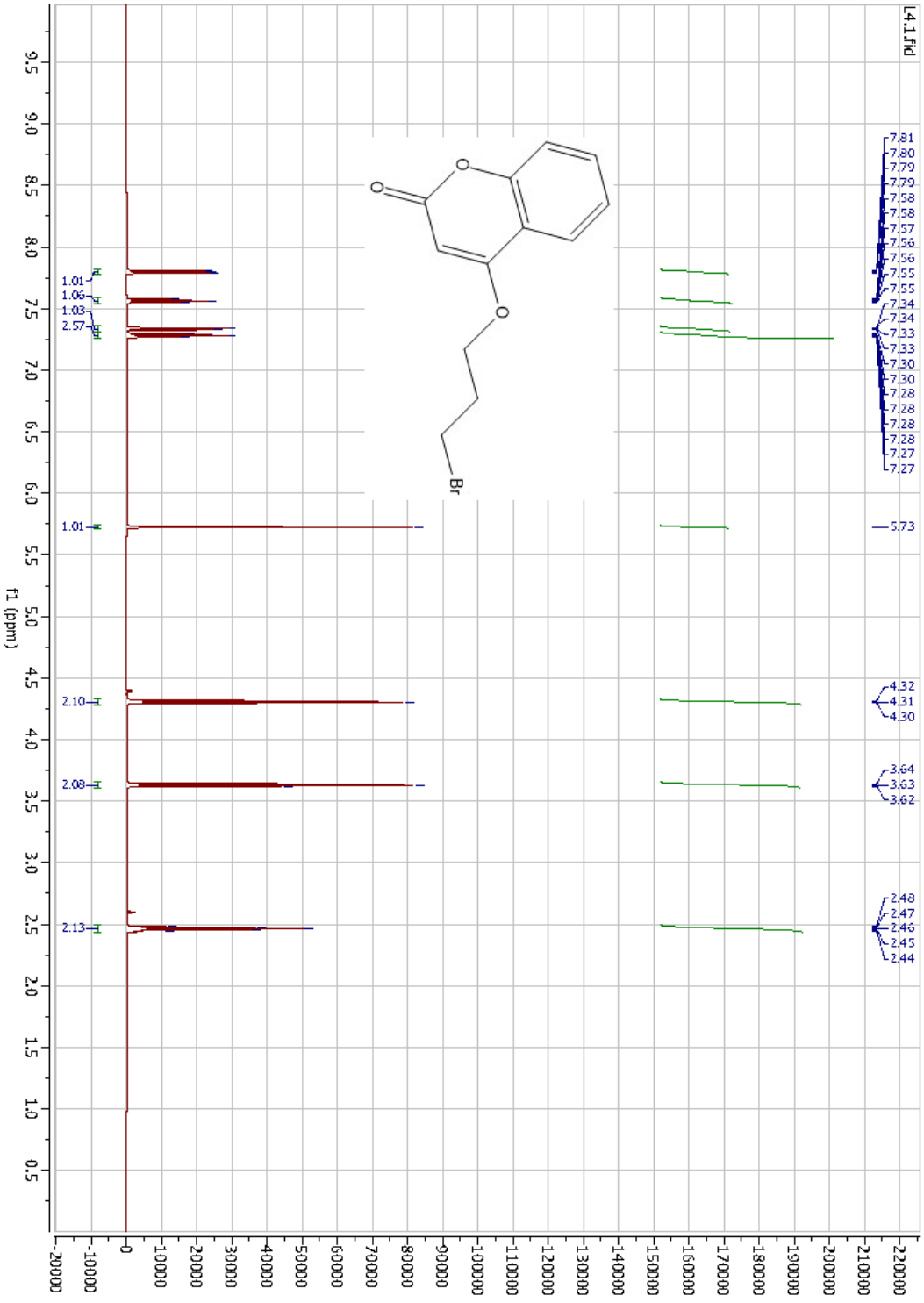

Figure 4.38: ^{1}H NMR spectra of compound **4C**

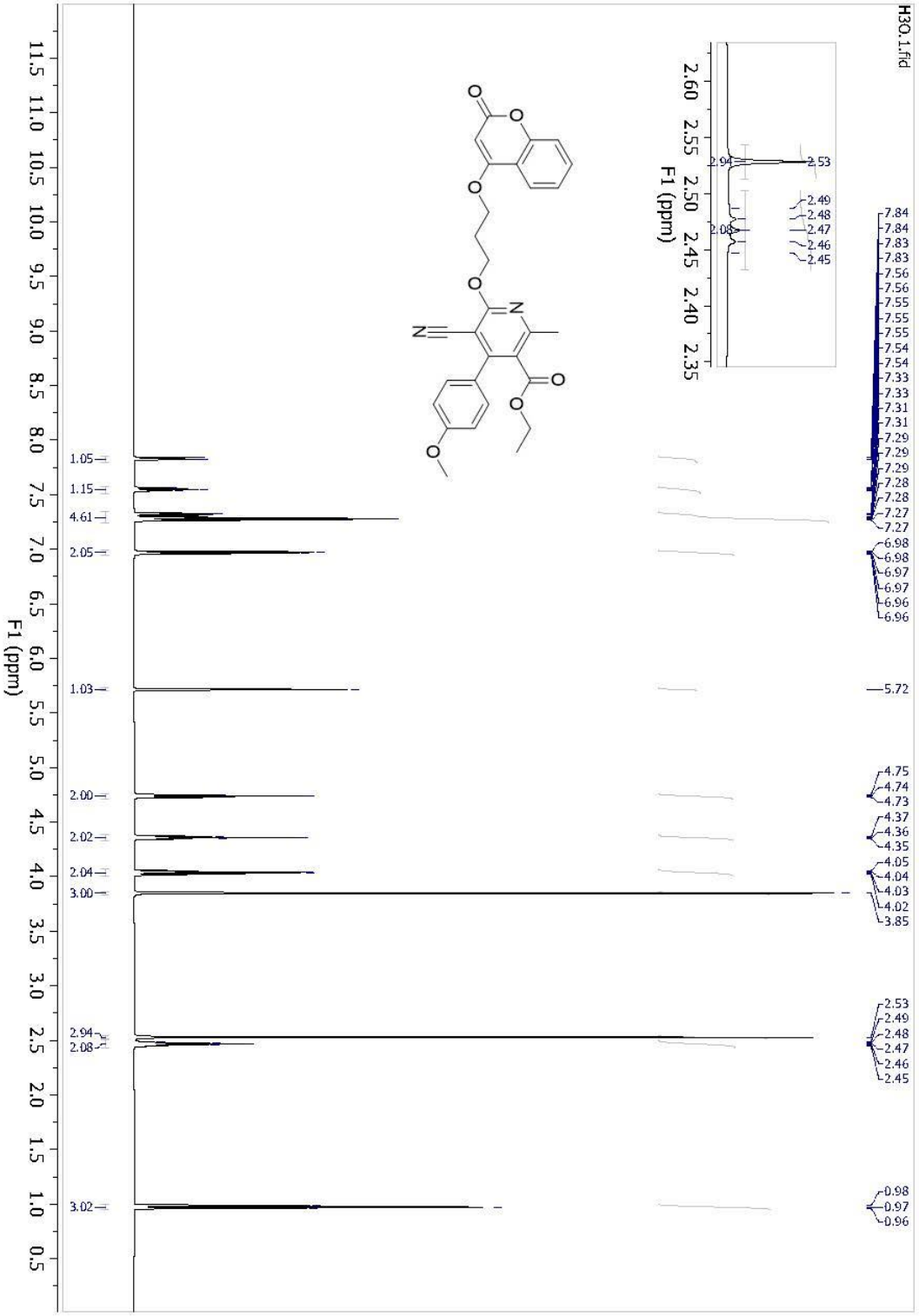

Figure 4.39: ^{1}H NMR spectra of compound **5.2C**

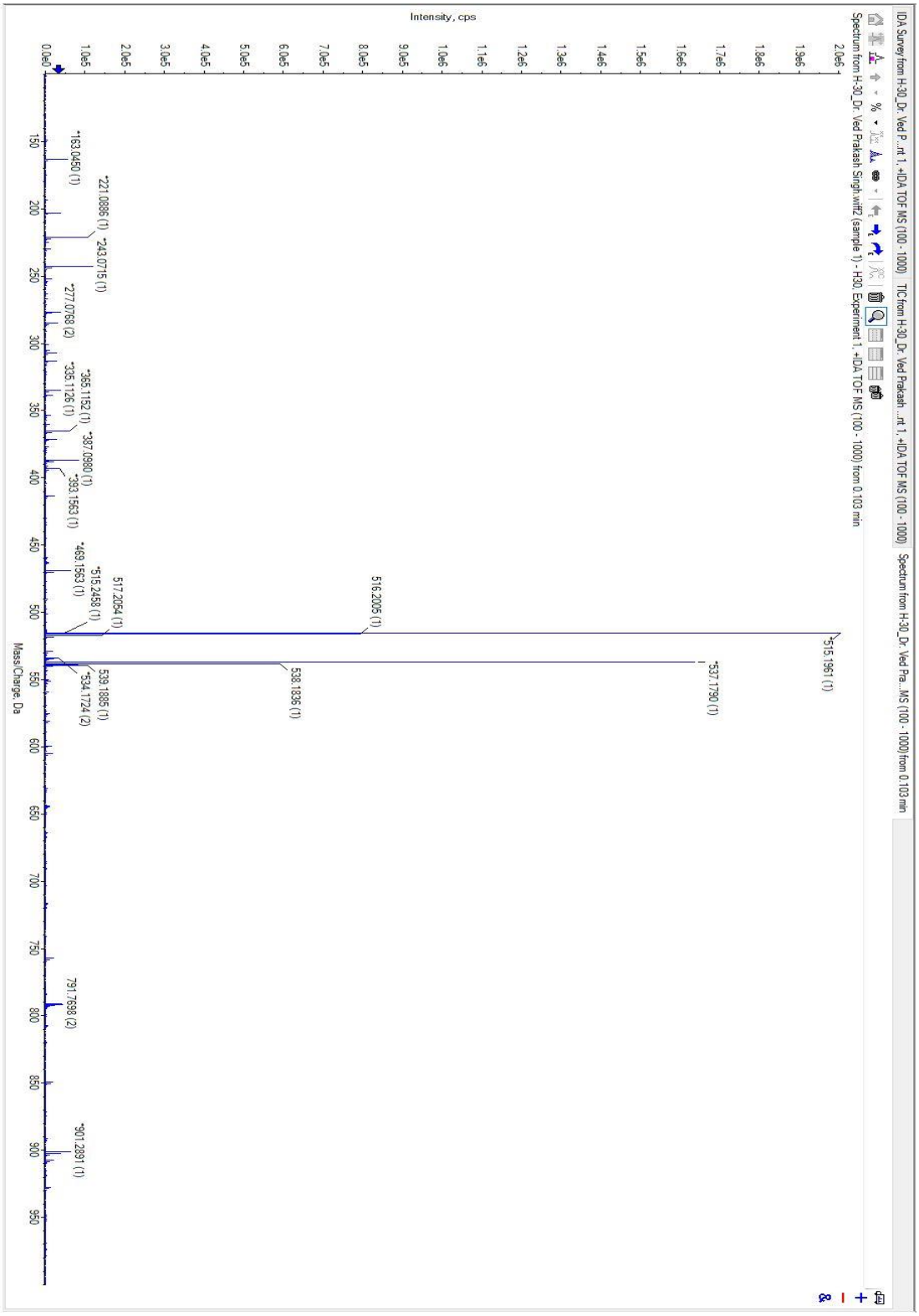

Figure 4.40: HRMS spectra of compound **5.2C**

CHAPTER 5

SUMMARY AND CONCLUSION

Molecular interactions are the forces that attract or repel non-bonded atoms and molecules. It plays a significant role in all aspects of chemistry, biochemistry, and biophysics, including drug design, protein folding, nanotechnology, material science, sensors, and the origin of life. Molecular interactions are the interactions between molecules or atoms that are not linked by chemical bonds. Molecular recognition and ligand binding with proteins are the most important life processes within the cell, for example, catalysis, receptor trafficking, substrate transport, gene regulation, signal transmission, and switching off and on biological pathways.

The general introduction to the hybridization of molecules in drug design, the linking of pharmacophores, and multi-targeted drugs are included in **Chapter 1**. The advantage of hybrid molecules is that for treating complex diseases, a single molecule can act on multiple types of targets simultaneously. The importance of bioisosteres in medicinal chemistry and its role in structural changes to improve the activities of the drug and ADME are also highlighted in chapter 1. Hence, new molecules have been synthesized to investigate the roles of weak and aromatic interactions in biological systems and orientation preferences.

Chapter 2 is the design, synthesis, and study of the 2-pyridone-based hybrid molecules, with their supramolecular properties and Hirshfeld surface analysis, including enrichment ratio. The synthesized compounds are undergone for molecular docking to study their biological activities. **Scheme 1** includes the multicomponent reaction for synthesizing 4H-pyrans **(1.1A–1.1I)**, which are converted to 3,4-dihypyridones **(1.2A-1.2I)** using iodine catalysis or using excess formic acid under reflux condition. These 3,4-dihydropyridines are then further oxidized to 2-pyridone **(1.3A-1.3I)** derivatives with DDQ under microwave and thermal-assisted reactions. All these reactions are efficient and give good yields. The ring rearrangement of 4H-pyrans into 3,4-dihydropyridones was done by either iodine catalysis or formic acid catalysis; these catalysts provide almost the same yield. The oxidation of 3,4-dihydropyridones was done using DDQ as an oxidizing agent under thermal and

microwave conditions; the yields of both reactions are the same. Though, the microwave reaction is faster and saves time. The compound 3,4-dihydropyridones also undergoes auto-oxidation in small quantities at room temperature.

The compounds which form suitable crystals in **scheme 1** were studied using single-crystal X-ray diffraction and Hirshfeld surface analysis. All the 2-pyridones-based hybrid molecules give suitable single crystals. Among them, compounds **1.3A, 1.3B,** and **1.3I** exhibited an orthorhombic crystal system, **1.3C – 1.3F; 1.3H** presented the monoclinic crystal system; and **1.3G** showed a triclinic crystal system. The molecules of all the crystals formed unsymmetrical dimer with N-H…O non-covalent intermolecular interactions of the nitrogen atom and carbonyl oxygen atom of the 2-pyridone ring. The compounds **1.3A, 1.3G, 1.3H**, and **1.3I** crystallized with symmetry-independent molecules containing two molecules in a single crystal, and their molecules are oriented slightly differently in space with different contacts. None of the compounds formed π…π stacking interactions in their aromatic rings. The C-H…π interactions are seen in all the compounds in their supramolecular framework. The lone pair…π interactions are also found in compounds **1.3A** - **1.3E, 1.3H**, and **1.3I**. It is found between the aromatic ring and the lone electron pair of the oxygen atom, a chlorine atom, and a nitrogen atom. The halogen bond between chlorine or bromine atom with oxygen or nitrogen atom also existed in **1.3A-1.3C** compounds.

The crystal structure study shows that para chloro substitution on **1.3A** does not form lone pair-π interaction with a chlorine atom, which is formed in ortho and meta chloro substitution **1.3B** and **1.3D** with pyridone ring and phenyl ring, respectively. In addition, **1.3A**, linked through lone pair-π interaction with O2A and **1.3B**, exhibit similar interactions with cyano nitrogen N1 to the pyridone ring. **1.3G** does not show the lone pair-π interactions among the ortho-substituted compounds. The para substitution also shows that **1.3A** and **1.3I** exhibit the lone pair-π interaction, but **1.3F** does not demonstrate this interaction.

Hirshfeld's surface analysis of the compounds confirmed the interactions in the supramolecular framework. The enrichment ratio calculation of all the compounds illustrates that hydrogen atoms generate more than 50% of the total molecular surface. Still, their enrichment ratio of H…H contact is less than unity which shows that it does

not help much in the molecular association. The contact O…H in the enrichment ratio is more than unity (>1), indicating that it plays a very important role in the molecular interaction to assemble the molecules in their crystal. The C…H interactions in most compounds except **1.3A** and **1.3B** are more than unity to impart the association of the molecule. N…H contact is also enriched in all compounds except **1.3B**, which is less than unity and plays an essential role in the non-covalent molecular interaction. The hetero atoms chlorine and bromine in compounds **1.3A-1.3D** also play an indispensable role; their interaction with hydrogen atoms is mainly enriched. Their interaction with carbon atoms is also more than unity, which indicates the presence of lone pair…π interactions among the compounds. Most of the compounds' C…C enrichment ratio is enriched with more than one ER value, but there were no π…π stacking interactions in the compounds. The wing-like structure in the 2D fingerprint plot indicates C-H…π interaction in all the compounds. The absence of a flat green region in the curvedness and shape index revealed the lack of π…π stacking interaction.

The synthesized compounds of Scheme 1 are subjected to molecular docking with Eg5 and survivin protein for their activity towards tumor suppressor in human cancer cells. The binding score of compounds **1.3A – 1.3I** with the Eg5 receptor is studied. It found that **1.3I** showed the highest binding affinity with a binding score of -7.2 kcal/mol and hydrogen bonding interaction with Glu118 and Pro137 at the active binding pocket. The docking score of the survivin protein with the synthesized compounds indicates that **1.3C** has the highest binding affinity with a -6.8 kcal/mol binding score. It forms a hydrogen bonding with Lys90 at the allosteric cavity near the dimerization interface of the Eg5 receptor. In addition to the hydrogen bonding, electrostatic π-anion interaction and hydrophobic π-alkyl and alkyl interactions are exhibited. The molecular docking results show that the Eg5 protein binding score with **1.3I** is the highest, with the para substitution of methyl group followed by the meta chloro substitution **1.3B**. Moreover, the docking score of survivin protein is most heightened in di-substitution, i.e., 2-bromo-4-chloro, followed by the ortho substitution.

A new series of pyranopyrazoles and spirooxindole derivatives are synthesized in **chapter 3** and studies their non-covalent interactions using Mercury and

CrystalExplorer software. The pyranopyrazole derivatives **(2.1A-2.1F)** were synthesized from the multicomponent reaction of malononitrile, derivatives of benzaldehyde, 1,3-diketones, and hydrazine hydrate using a piperidine catalyst under reflux condition in **Scheme 2**. Compounds of scheme 2 are synthesized via a multicomponent reaction, where the electron-donating substituents on the benzaldehyde produce a better yield than those with an electron-withdrawing group. The substituent present at the para position to the aldehyde group containing electron-donating property yields more product than the electron-attracting group, but the electron-donating group at the meta-position gives more yield.

The synthesized compounds **2.1B, 2.1C**, and **2.1E** form a suitable crystal for SC-XRD. The compounds **2.1B** and **2.1E** are crystallized in a triclinic crystal system and orthorhombic crystal systems in compound **2.1C**. The supramolecular framework shows N-H…N interactions play the leading role in compound **2.1B - 2.1E**. The interaction of C-H…N interactions in **2.1B** and **2.1E** also contribute to the supramolecular structure. C-H…O and N-H…O interactions were found only in compound **2.1B** among **2.1B** to **2.1E**. The C-H…π interactions are found in all the synthesized compounds. The aromatic interaction of π…π stacking was observed in **2.1B** and **2.1E** and is also important in molecular recognition. Lone pair…π interactions are found in the compounds which do not show π…π stacking interactions; the compound **2.1C** exemplify lone pair…π interaction between oxygen and chlorine atom. The crystal studies show that compounds containing electron-donating groups form π-π stacking interaction at the phenyl ring, but the chloro-substituted benzene interacted with lone pair-π interaction in the crystal. Moreover, the electron-donating compounds formed an unsymmetrical dimer with N-H…N interaction, but the dimer interaction is not present in other compounds.

Hirshfeld's surface analysis of the compounds also confirmed the intermolecular interactions in the supramolecular framework. The enrichment ratio calculation indicates that hydrogen atom represents more than 60% of the total surfaces, and the enrichment ratio value of all the compounds are less than unity. Yet, their contribution to the interaction plays an important role in participating in C…H, N…H, and O…H interactions. The interaction of hydrogen atoms with other atoms is

enriched in most interactions. The π…π interactions are also reflected in the enrichment ratio, in which C…C interaction is more than unity. The O…O interactions in **2.1B** and **2.1E** are also enriched, which contributes to the molecular association in the crystal, but for **2.1C** is zero as there is no actual contact with it.

The molecular docking studies were done on the compounds of **Scheme 2** for Chk1 and AKR1C3 enzymes for anti-tumor activity. The docking score indicates that the meta-substituent gives better results than the para-substituent. The electron-withdrawing group is also more favored in the active site of the Chk1 and AKR1C3 receptors. All the compounds enter the active sites of the Chk1 and AKR1C3 enzymes. **2.1A** score highest in both the enzymes with -8.1 and -9.4 kcal/mol, respectively. Compound **2.1A** displayed the hydrogen bonding interaction with Glu85 and Ser147 in Chk1, but in ARK1C3, it exhibits Ser217 residue. Then, **2.1B** illustrates the next higher score in both enzymes involving Cys87, Glu17, and Glu91 with Chk1; therefore, Gln190 residue is involved in ARK1C3 enzymes. The compound **2.1A** exhibit dual activity with enzyme Chk1 and AKR1C3 towards tumor suppression.

In **Scheme 3**, 2-oxospiro[indoline-3,4'-pyran]-5'-carbonitrile derivatives were synthesized and studied. The multicomponent reaction of isatin, malononitrile, and diketones/ hydroxybenzene derivatives using piperidine base at room temperature used to synthesize 2-oxospiro[indoline-3,4'-pyran]-5'-carbonitrile derivatives **(3.1A-3.1D)**. Piperidine has been used for the first time to synthesize spirooxindole derivatives from the reaction of isatin and malononitrile. The synthesized compounds are crystalized in acetone to get suitable crystals for analysis using SC-XRD. All the compounds are crystallized in a monoclinic crystal system with $P2_1/n$ in **3.1A, 3.1C, 3.1D**, and $P2_1/c$ space group in compound **3.1B**.

The supramolecular framework of **scheme 3** compounds illustrates N-H…O and C-H…O interactions are the most dominant non-covalent interactions in all compounds. To form a molecular association, the N-H…N interaction is the primary intermolecular interaction in **3.1A, 3.1B**, and **3.1D**, but this interaction is not found in **3.1C**. C-H…π interactions are found in all the compounds, but the π…π interaction is absent in all the compounds. Lone pair…π interaction was found in **3.1A** between the cyano nitrogen atom and the indole moiety of the molecule.

Hirshfeld surface analysis of the synthesized compounds supports the supramolecular framework structure of the compound. The enrichment ratio calculation indicates the involvement of atoms in the molecular interaction. Hydrogen atoms contribute more than 64% of the total surface of all the molecules, and their ER values are less than unity between 0.79 – 0.93. The interaction of hydrogen atoms with carbon, oxygen, and nitrogen atoms is enriched with their ER values being more than unity in all compounds. The ER value of C…C contact also confirmed the absence of π…π interactions, where its values are less than 0.5. The E_{CN} value of **3.1A** is 1.57, indicating the presence of nitrogen lone pair interaction with the p-orbital of the indole moiety of the compound; no other compounds have ER values higher than unity.

The scheme 3 compounds are studied with their molecular binding affinities in the active cavity of the ALK receptor enzyme. The compound **3.1A** exhibited the highest binding score with -8.7 kcal/mol, forming hydrogen bonds with Asp1276 and other electrostatic and hydrophobic interactions. All other compounds **(3.1B - 3.1D)** are entered inside the ATP binding cavity of the enzyme with almost the same orientation.

The compounds of scheme 3 show that the carbonyl group-containing ethyl in the ester group gives less yield than that of the methyl-containing group, where the ketone group is the least in the yield. Compound **3.1A** shows the lone pair-π interaction with the naphthol aromatic ring with the cyano nitrogen atom, which is confirmed by the enrichment ratio value of more than unity in C…N interaction, and none of the other compounds formed this interaction in their crystal structure. The molecular docking studies showed that compound **3.1A** shows the highest binding affinity, but the binding pocket is slightly different from the other compounds. It is because of the presence of the bulky group naphthol in compound **3.1A** all other compounds are posing in the same orientation.

The synthesis and study of flexible pyridine-based hybrid molecules are contained in **chapter 4**. The series of aromatic rings linked with the methylene bromide was the first synthesis in **Scheme 4** using the aromatic ring containing hydroxy group

and dibromo alkanes, using potassium carbonate as a catalyst. It gives an aromatic ring linked to methylene bromide **(4A-4C)**, which was used for further reaction.

The compounds from **scheme 4** and the 2-pyridone derivatives were reacted using K_2CO_3 as a base catalyst and DMF as a solvent under room temperature to give flexible pyridine-based hybrid derivatives **(5.2A-5.2D, 5.3A)**. However, the O-alkylation was the preferred product in compound **5.2A-5.2D** without any N-link product, and N-alkylation was formed in compound **5.3A** with no O-linked product was formed. All these compounds formed suitable crystals for the single-crystal X-ray diffraction analysis. The aromatic ring linked with methylene bromide was synthesized as the aromatic ring increased, and the product yield slightly decreased. When these react with the 2-pyridone core of the compounds, it was found that the carbonyl group of the pyridone was more reactive to linked with the methylene bromide to give O-linked product, but **5.3A** formed only the product which is connected with NH of the pyridone making N-linked product. Moreover, on the other end of the methylene, sesamol gives only an N-linked product, whereas benzene and coumarin do not provide the N-linked product in the same reaction condition.

The supramolecular framework of the synthesis compounds shows that C-H…O and C-H…N interactions are the significant non-covalent intermolecular interactions in all crystals, except in compound **5.2C**. In **5.2C**, C-H…N interaction is absent. All the structures displayed the aromatic π…π stacking interactions. The compound **5.2A** and **5.2B** show the π…π stacking interaction through the phenyl ring and pyridine ring, and **5.2A** displays the stacking interaction between the nitrobenzene rings, and thus, **5.2B** displays the interaction with pyridine ring on the opposite side of the other interaction. The π…π parallel stacking interaction is found in the coumarin ring moiety of the compound **5.2C** and **5.2D** with two ring systems, while **5.3A** also experiences this stacking interaction through the sesamol ring and pyridone ring. All the compounds are stabilized by C-H…π interactions involving the pyridine ring and the aromatic ring systems. The lone pair…π interaction is found only in compound **5.3A** between the pyridone carbonyl oxygen and sesamol benzene ring.

Hirshfeld surface analysis of the synthesized compounds displayed that; all the interactions found in the supramolecular framework are confirmed with this analysis.

The enrichment ratio calculation indicated that the hydrogen atom plays an essential role in the molecular association of the compound. A hydrogen atom occupies more than 65% of the total surface in all compounds, and the ER values are also close to unity (0.96-1.05), reveals these interactions are enriched in all the compounds. The ER values of C…C are high except **5.3A** (0.99), which proved the presence of aromatic π…π stacking interactions in all compounds. The interactions C…H, N…H, and O…H are enriched with their enrichment ratios greater than 1, and they all are important interactions in the crystal compounds.

The computational studies of the synthesized compounds in scheme 5 were done with 5-LOX and COX-2 enzymes. Compounds **5.2D, 5.3A**, and **5.2C** show high binding affinities towards 5-LOX enzymes with a docking score of -8.6, -8.4, and -8.3 kcal/mole, respectively. They all display a similar orientation in the active site of the enzyme. The residues Arg101, Gln141, Thr137, His130, and Arg165 are involved in the formation of hydrogen bonding. The docking analysis of these compounds with COX-2 enzyme also displays a similar orientation in the region of the enzyme's active site. The high binding scores are -9.1, -9.1, and -8.7 in compounds **5.2A, 5.2C,** and **5.2B**, respectively. The residue involved in the hydrogen bonding is Arg120, Tyr355, Ser530, and Ser353, in which compound **5.2D** does not show any hydrogen bond with the amino acid residues.

The larger aromatic ring of the molecule with stronger aromatic π…π stacking interaction shows a better and higher binding score in the 5-LOX enzyme. Still, the reverse is found in the COX-2 enzymes with a smaller aromatic molecule, revealing a higher score. The compounds with greater C-H…π interactions in the supramolecular framework also experience a better score in the COX-2 enzyme.

The crystal structure study shows that all the compounds exhibit π-π interactions through the phenyl ring in **5.2A**, phenyl and pyridone in **5.2B**, between the coumarin ring in **5.2C** and **5.2D**, but in **5.3A**, it is found between the pyridone ring and sesamol ring. Compounds **5.2A** and **5.3A** form a sheet-like structure, but all the other compounds are not crystallized in a sheet structure. A flat green surface also confirmed Hirshfeld surface analysis in the shape index of all the compounds. The molecular docking score indicates the electron-donating methyl group in **5.2D** gives the highest

score in the 5-LOX receptor, but in the COX-2 receptor, the electron-withdrawing group **5.2A** exhibit the best score.

The present study covers the synthesis of new hybrid molecules and studies its supramolecular framework structure, Hirshfeld surface analysis covering the 2D fingerprint plot, d_{norm}, shape index, curvedness, and enrichment ratio. The computational studies of the synthesized compounds with the cancer-causing enzymes found that compounds **1.3I** and **1.3B** showed the best binding affinities towards the Eg5 enzyme, and **1.3C** showed the docking score -6.8 kcal/mol in the survivin enzyme. Compound **2.2A** shows the docking score of -8.1 and -9.4 kcal/mol for Chk1 and AKR1C3 enzymes to act as dual inhibitors for the above two enzymes. **3.1A** is the best score compound for the ALK enzyme, but the binding pocket differs from other compounds of the same series. The compound **5.2D** scored best in 5-LOX enzyme with a score of -8.6 kcal/mol forming hydrogen bonding residue Arg101, Gln141, Thr137, and His130 residues. Thus, compound **5.2A** scores -9.1 kcal/mol for the COX-2 enzyme, showing hydrogen bonding with Arg120, Tyr355, and Ser530 residues. The compound **5.2A** also scores -8.4 kcal/mol binding affinities in the 5-LOX enzyme and is potent for COX-2 and 5-LOX enzymes.

These results can be further utilized in the drug design based on different donor-receptor groups and the design of hybridized analogues of different drugs based on their donor-receptor groups. These non-covalent interactions can be utilized as a key in drug design and the design of new materials applied in various areas of industry. The synthesized compounds with higher scores in the molecular docking can be further studied through in *vivo/vitro* experiments to develop a new drug for respective target receptors therapeutics.

REFERENCES

Alencar, J. S., Pietri, S., Culcasi, M., Orneto, C., Piccerelle, P., Reynier, J. P., Portugal, H., Nicolay, A., & Kaloustian, J. (2009). Interactions and antioxidant stability of sesamol in dry-emulsions. *Journal of Thermal Analysis and Calorimetry*, *98*(1), 133–143. https://doi.org/10.1007/s10973-009-0102-8

Al-Haiza, M., Mostafa, M., & El-Kady, M. (2003). Synthesis and Biological Evaluation of Some New Coumarin Derivatives. *Molecules*, *8*(2), 275–286.

Arndt, S., Emde, U., Bäurle, S., Friedrich, T., Grubert, L., & Koert, U. (2001). Quinone-Annonaceous Acetogenins: Synthesis and Complex I Inhibition Studies of a New Class of Natural Product Hybrids. *Chemistry*, *7*(5), 993–1005. https://doi.org/10.1002/1521-3765(20010302)7:5<993::AID-CHEM993>3.0.CO;2-S

Auffinger, P., Hays, F. A., Westhof, E., & Ho, P. S. (2004). Halogen bonds in biological molecules. *Proceedings of the National Academy of Sciences*, *101*(48), 16789–16794. https://doi.org/10.1073/pnas.0407607101

Bankole, M., Shittu, L., Ahmed, T., Bankole, M., Shittu, R., Terkula, K., & Ashiru, O. (2008). Synergistic Antimicrobial Activities Of Phytoestrogens In Crude Extracts Of Two Sesame Species Against Some Common Pathogenic Microorganisms. *African Journal of Traditional, Complementary and Alternative Medicines*, *4*(4), 427. https://doi.org/10.4314/ajtcam.v4i4.31237

Baron, R., & McCammon, J. A. (2013). Molecular Recognition and Ligand Association. *Annual Review of Physical Chemistry*, *64*(1), 151–175. https://doi.org/10.1146/annurev-physchem-040412-110047

Berman, H. M., Battistuz, T., Bhat, T. N., Bluhm, W. F., Bourne, P. E., Burkhardt, K., Feng, Z., Gilliland, G. L., Iype, L., Jain, S., Fagan, P., Marvin, J., Padilla, D., Ravichandran, V., Schneider, B., Thanki, N., Weissig, H., Westbrook, J. D., & Zardecki, C. (2002). The Protein Data Bank. *Acta Crystallographica Section D Biological Crystallography*, *58*(6), 899–907. https://doi.org/10.1107/S0907444902003451

Bissantz, C., Kuhn, B., & Stahl, M. (2010). A Medicinal Chemist's Guide to Molecular Interactions. *Journal of Medicinal Chemistry*, *53*(14), 5061–5084. https://doi.org/10.1021/jm100112j

Borisy, A. A., Elliott, P. J., Hurst, N. W., Lee, M. S., Lehár, J., Price, E. R., Serbedzija, G., Zimmermann, G. R., Foley, M. A., Stockwell, B. R., & Keith, C. T. (2003). Systematic discovery of multicomponent therapeutics. *Proceedings of the National Academy of Sciences*, *100*(13), 7977–7982. https://doi.org/10.1073/pnas.1337088100

Bossi, R. T., Saccardo, M. B., Ardini, E., Menichincheri, M., Rusconi, L., Magnaghi, P., Orsini, P., Avanzi, N., Borgia, A. L., Nesi, M., Bandiera, T., Fogliatto, G., & Bertrand, J. A. (2010). Crystal Structures of Anaplastic Lymphoma Kinase in Complex with ATP Competitive Inhibitors. *Biochemistry*, *49*(32), 6813–6825. https://doi.org/10.1021/bi1005514

Brammer, L., Bruton, E. A., & Sherwood, P. (2001). Understanding the Behavior of Halogens as Hydrogen Bond Acceptors. *Crystal Growth & Design*, *1*(4), 277–290. https://doi.org/10.1021/cg015522k

Budzisz, E. (2003). Cytotoxic effects, alkylating properties and molecular modelling of coumarin derivatives and their phosphonic analogues. *European Journal of Medicinal Chemistry*, *38*(6), 597–603. https://doi.org/10.1016/S0223-5234(03)00086-2

Burke, M. D., & Schreiber, S. L. (2004). A Planning Strategy for Diversity-Oriented Synthesis. *Angewandte Chemie International Edition*, *43*(1), 46–58. https://doi.org/10.1002/anie.200300626

Camps, P., El Achab, R., Morral, J., Muñoz-Torrero, D., Badia, A., Baños, J. E., Vivas, N. M., Barril, X., Orozco, M., & Luque, F. J. (2000). New Tacrine−Huperzine A Hybrids (Huprines): Highly Potent Tight-Binding Acetylcholinesterase Inhibitors of Interest for the Treatment of Alzheimer's Disease. *Journal of Medicinal Chemistry*, *43*(24), 4657–4666. https://doi.org/10.1021/jm000980y

Chan, A. W. E., Laskowski, R. A., & Selwood, D. L. (2010). Chemical Fragments that Hydrogen Bond to Asp, Glu, Arg, and His Side Chains in Protein Binding Sites. *Journal of Medicinal Chemistry*, *53*(8), 3086–3094. https://doi.org/10.1021/jm901696w

Chen, T., Li, M., & Liu, J. (2018). π–π Stacking Interaction: A Nondestructive and Facile Means in Material Engineering for Bioapplications. *Crystal Growth & Design*, *18*(5), 2765–2783. https://doi.org/10.1021/acs.cgd.7b01503

Cho, M. E., & Kopp, J. B. (2010). Pirfenidone: An anti-fibrotic therapy for progressive kidney disease. *Expert Opinion on Investigational Drugs*, *19*(2), 275–283. https://doi.org/10.1517/13543780903501539

Chothia, C., & Janin, J. (1975). Principles of protein–protein recognition. *Nature*, *256*(5520), 705–708. https://doi.org/10.1038/256705a0

Clark, T., Hennemann, M., Murray, J. S., & Politzer, P. (2007). Halogen bonding: The σ-hole: Proceedings of "Modeling interactions in biomolecules II", Prague, September 5th–9th, 2005. *Journal of Molecular Modeling*, *13*(2), 291–296. https://doi.org/10.1007/s00894-006-0130-2

Clarke, D. J., & Giménez-Abián, J. F. (2000). Checkpoints controlling mitosis. *BioEssays*, *22*(4), 351–363. https://doi.org/10.1002/(SICI)1521-1878(200004)22:4<351::AID-BIES5>3.0.CO;2-W

Claudio Viegas-Junior, Eliezer J. Barreiro, & Carlos Alberto Manssour Fraga. (2007). Molecular Hybridization: A Useful Tool in the Design of New Drug Prototypes. *Current Medicinal Chemistry*, *14*(17), 1829–1852. https://doi.org/10.2174/092986707781058805

Connolly, M. L. (1986). Shape complementarity at the hemoglobin ?1?1 subunit interface. *Biopolymers*, *25*(7), 1229–1247. https://doi.org/10.1002/bip.360250705

Corradi, E., Meille, S. V., Messina, M. T., Metrangolo, P., & Resnati, G. (2000). Halogen Bonding versus Hydrogen Bonding in Driving Self-Assembly Processes. *Angewandte Chemie International Edition*, *39*(10), 1782–1786. https://doi.org/10.1002/(SICI)1521-3773(20000515)39:10<1782::AID-ANIE1782>3.0.CO;2-5

Costa, P. J. (2017). The halogen bond: Nature and applications. *Physical Sciences Reviews*, *2*(11). https://doi.org/10.1515/psr-2017-0136

Cotesta, S., & Stahl, M. (2006). The environment of amide groups in protein–ligand complexes: H-bonds and beyond. *Journal of Molecular Modeling*, *12*(4), 436–444. https://doi.org/10.1007/s00894-005-0067-x

Coussens, L. M., & Werb, Z. (2002). Inflammation and cancer. *Nature*, *420*(6917), 860–867. https://doi.org/10.1038/nature01322

Dancey, J. E., & Chen, H. X. (2006). Strategies for optimizing combinations of molecularly targeted anticancer agents. *Nature Reviews Drug Discovery*, *5*(8), 649–659. https://doi.org/10.1038/nrd2089

de Silva, A. P., Gunaratne, H. Q. N., Gunnlaugsson, T., & Nieuwenhuizen, M. (1996). Fluorescent switches with high selectivity towards sodium ions: Correlation of ion-induced conformation switching with fluorescence function. *Chemical Communications*, *16*, 1967. https://doi.org/10.1039/cc9960001967

de Silva, A. P., & Sandanayake, K. R. A. S. (1989). Fluorescent PET (photo-induced electron transfer) sensors for alkali metal ions with improved selectivity against protons and with predictable binding constants. *Journal of the Chemical Society, Chemical Communications*, *16*, 1183. https://doi.org/10.1039/c39890001183

Desiraju, G. R. (2011). A Bond by Any Other Name. *Angewandte Chemie International Edition*, *50*(1), 52–59. https://doi.org/10.1002/anie.201002960

Desiraju, G. R., & Gavezzotti, A. (1989). Crystal structures of polynuclear aromatic hydrocarbons. Classification, rationalization and prediction from molecular structure. *Acta Crystallographica Section B Structural Science*, *45*(5), 473–482. https://doi.org/10.1107/S0108768189003794

Desiraju, G. R., Ho, P. S., Kloo, L., Legon, A. C., Marquardt, R., Metrangolo, P., Politzer, P., Resnati, G., & Rissanen, K. (2013). Definition of the halogen bond (IUPAC Recommendations 2013). *Pure and Applied Chemistry*, *85*(8), 1711–1713. https://doi.org/10.1351/PAC-REC-12-05-10

Dick, A., & Cocklin, S. (2020). Bioisosteric Replacement as a Tool in Anti-HIV Drug Design. *Pharmaceuticals*, *13*(3), 36. https://doi.org/10.3390/ph13030036

Ding, F., Leow, M. L., Ma, J., William, R., Liao, H., & Liu, X.-W. (2014). Collective Synthesis of 4-Hydroxy-2-pyridone Alkaloids and Their Antiproliferation Activities. *Chemistry - An Asian Journal*, *9*(9), 2548–2554. https://doi.org/10.1002/asia.201402466

Duan, L., Wang, T.-Q., Bian, W., Liu, W., Sun, Y., & Yang, B.-S. (2015). Centrin: Another target of monastrol, an inhibitor of mitotic spindle. *Spectrochimica*

Acta Part A: Molecular and Biomolecular Spectroscopy, *137*, 1086–1091. https://doi.org/10.1016/j.saa.2014.08.050

Foloppe, N., Fisher, L. M., Howes, R., Potter, A., Robertson, A. G. S., & Surgenor, A. E. (2006). Identification of chemically diverse Chk1 inhibitors by receptor-based virtual screening. *Bioorganic & Medicinal Chemistry*, *14*(14), 4792–4802. https://doi.org/10.1016/j.bmc.2006.03.021

Forlani, L., Cristoni, G., Boga, C., Todesco, P. E., Vecchio, E. D., Selva, S., & Monari, M. (2002). Reinvestigation of the tautomerism of some substituted 2-hydroxypyridines. *Arkivoc*, *2002*(11), 198–215. https://doi.org/10.3998/ark.5550190.0003.b18

Fu, R., Sun, Y., Sheng, W., & Liao, D. (2017). Designing multi-targeted agents: An emerging anticancer drug discovery paradigm. *European Journal of Medicinal Chemistry*, *136*, 195–211. https://doi.org/10.1016/j.ejmech.2017.05.016

Fylaktakidou, K., Hadjipavlou-Litina, D., Litinas, K., & Nicolaides, D. (2004). Natural and Synthetic Coumarin Derivatives with Anti-Inflammatory / Antioxidant Activities. *Current Pharmaceutical Design*, *10*(30), 3813–3833. https://doi.org/10.2174/1381612043382710

Hamada, Y., & Kiso, Y. (2012). The application of bioisosteres in drug design for novel drug discovery: Focusing on acid protease inhibitors. *Expert Opinion on Drug Discovery*, *7*(10), 903–922. https://doi.org/10.1517/17460441.2012.712513

Han, Z., Czap, G., Chiang, C., Xu, C., Wagner, P. J., Wei, X., Zhang, Y., Wu, R., & Ho, W. (2017). Imaging the halogen bond in self-assembled halogenbenzenes on silver. *Science*, *358*(6360), 206–210. https://doi.org/10.1126/science.aai8625

Harada, K., Ferdous, T., Harada, T., Takenawa, T., & Ueyama, Y. (2017). Gimeracil enhances the antitumor effect of cisplatin in oral squamous cell carcinoma cells in vitro and in vivo. *Oncology Letters*, *14*(3), 3349–3356. https://doi.org/10.3892/ol.2017.6602

Harvey, R. G., Cortez, C., Ananthanarayan, T. P., & Schmolka, S. (1988). A new coumarin synthesis and its utilization for the synthesis of polycyclic coumarin

compounds with anticarcinogenic properties. *The Journal of Organic Chemistry*, *53*(17), 3936–3943. https://doi.org/10.1021/jo00252a011

Hawkins, P. C. D., Skillman, A. G., & Nicholls, A. (2007). Comparison of Shape-Matching and Docking as Virtual Screening Tools. *Journal of Medicinal Chemistry*, *50*(1), 74–82. https://doi.org/10.1021/jm0603365

Hendlich, M. (1998). Databases for Protein–Ligand Complexes. *Acta Crystallographica Section D Biological Crystallography*, *54*(6), 1178–1182. https://doi.org/10.1107/S0907444998007124

Hille, B. (1992). Ionic channels of excitable membranes (second edition): By Bertil Hille; Sinauer Associates (distributed by W.H. Freeman); Sunderland, MA, 1992; xiv + 607 pages. £37.95. ISBN 0878933239. *FEBS Letters*, *306*(2–3), 277–278. https://doi.org/10.1016/0014-5793(92)81020-M

Hu, L., Benson, M. L., Smith, R. D., Lerner, M. G., & Carlson, H. A. (2005). Binding MOAD (Mother Of All Databases). *Proteins: Structure, Function, and Bioinformatics*, *60*(3), 333–340. https://doi.org/10.1002/prot.20512

Huang, F., & Anslyn, E. V. (2015). Introduction: Supramolecular Chemistry. *Chemical Reviews*, *115*(15), 6999–7000. https://doi.org/10.1021/acs.chemrev.5b00352

Huang, S. (2002). Rational drug discovery: What can we learn from regulatory networks? *Drug Discovery Today*, *7*(20), s163–s169. https://doi.org/10.1016/S1359-6446(02)02463-7

Hulsman, N., Medema, J. P., Bos, C., Jongejan, A., Leurs, R., Smit, M. J., de Esch, I. J. P., Richel, D., & Wijtmans, M. (2007). Chemical Insights in the Concept of Hybrid Drugs: The Antitumor Effect of Nitric Oxide-Donating Aspirin Involves A Quinone Methide but Not Nitric Oxide nor Aspirin. *Journal of Medicinal Chemistry*, *50*(10), 2424–2431. https://doi.org/10.1021/jm061371e

Imai, Y. N., Inoue, Y., & Yamamoto, Y. (2007). Propensities of Polar and Aromatic Amino Acids in Noncanonical Interactions: Nonbonded Contacts Analysis of Protein−Ligand Complexes in Crystal Structures. *Journal of Medicinal Chemistry*, *50*(6), 1189–1196. https://doi.org/10.1021/jm061038a

Infield, D. T., Rasouli, A., Galles, G. D., Chipot, C., Tajkhorshid, E., & Ahern, C. A. (2021). Cation-π Interactions and their Functional Roles in Membrane

Proteins. *Journal of Molecular Biology*, *433*(17), 167035. https://doi.org/10.1016/j.jmb.2021.167035

Irwin, J. J., & Shoichet, B. K. (2005). ZINC − A Free Database of Commercially Available Compounds for Virtual Screening. *Journal of Chemical Information and Modeling*, *45*(1), 177–182. https://doi.org/10.1021/ci049714+

Jelsch, C., Ejsmont, K., & Huder, L. (2014). The enrichment ratio of atomic contacts in crystals, an indicator derived from the Hirshfeld surface analysis. *IUCrJ*, *1*(2), 119–128. https://doi.org/10.1107/S2052252514003327

Jessen, H. J., & Gademann, K. (2010). 4-Hydroxy-2-pyridone alkaloids: Structures and synthetic approaches. *Natural Product Reports*, *27*(8), 1168. https://doi.org/10.1039/b911516c

Jones, S., & Thornton, J. M. (1996). Principles of protein-protein interactions. *Proceedings of the National Academy of Sciences*, *93*(1), 13–20. https://doi.org/10.1073/pnas.93.1.13

Jung, J.-C., Jung, Y.-J., & Park, O.-S. (2001). A convenient one-pot synthesis of 4-hydroxycoumarin, 4-hydroxythiocoumarin, and 4-hydroxyquinolin-2(1 *H*)-one. *Synthetic Communications*, *31*(8), 1195–1200. https://doi.org/10.1081/SCC-100104003

Kapoor, T. M., Mayer, T. U., Coughlin, M. L., & Mitchison, T. J. (2000). Probing Spindle Assembly Mechanisms with Monastrol, a Small Molecule Inhibitor of the Mitotic Kinesin, Eg5. *Journal of Cell Biology*, *150*(5), 975–988. https://doi.org/10.1083/jcb.150.5.975

Katritzky, A. R., Ramsden, C. A., Joule, J. A., & Zhdankin, V. V. (2010). Structure of Six-membered Rings. In *Handbook of Heterocyclic Chemistry* (pp. 37–86). Elsevier. https://doi.org/10.1016/B978-0-08-095843-9.00003-3

Kerru, N., Gummidi, L., Maddila, S., Gangu, K. K., & Jonnalagadda, S. B. (2020). A Review on Recent Advances in Nitrogen-Containing Molecules and Their Biological Applications. *Molecules*, *25*(8), 1909. https://doi.org/10.3390/molecules25081909

Kim, C.-Y., Chang, J. S., Doyon, J. B., Baird, T. T., Fierke, C. A., Jain, A., & Christianson, D. W. (2000). Contribution of Fluorine to Protein−Ligand Affinity in the Binding of Fluoroaromatic Inhibitors to Carbonic Anhydrase II.

Journal of the American Chemical Society, *122*(49), 12125–12134. https://doi.org/10.1021/ja002627n

Kolesnichenko, I. V., & Anslyn, E. V. (2017). Practical applications of supramolecular chemistry. *Chemical Society Reviews*, *46*(9), 2385–2390. https://doi.org/10.1039/C7CS00078B

Korcsmáros, T., Szalay, M. S., Böde, C., Kovács, I. A., & Csermely, P. (2007). How to design multi-target drugs: Target search options in cellular networks. *Expert Opinion on Drug Discovery*, *2*(6), 799–808. https://doi.org/10.1517/17460441.2.6.799

Kuang, W.-B., Huang, R.-Z., Qin, J.-L., Lu, X., Qin, Q.-P., Zou, B.-Q., Chen, Z.-F., Liang, H., & Zhang, Y. (2018). Design, synthesis and pharmacological evaluation of new 3-(1H-benzimidazol-2-yl)quinolin-2(1H)-one derivatives as potential antitumor agents. *European Journal of Medicinal Chemistry*, *157*, 139–150. https://doi.org/10.1016/j.ejmech.2018.07.066

Kubinyi, H. (2001). Hydrogen Bonding: The Last Mystery in Drug Design? In B. Testa, H. van de Waterbeemd, G. Folkers, & R. Guy (Eds.), *Pharmacokinetic Optimization in Drug Research* (pp. 513–524). Verlag Helvetica Chimica Acta. https://doi.org/10.1002/9783906390437.ch28

Küpeli Akkol, E., Genç, Y., Karpuz, B., Sobarzo-Sánchez, E., & Capasso, R. (2020). Coumarins and Coumarin-Related Compounds in Pharmacotherapy of Cancer. *Cancers*, *12*(7), 1959. https://doi.org/10.3390/cancers12071959

Le Guellec, R., Paris, J., Couturier, A., Roghi, C., & Philippe, M. (1991). Cloning by differential screening of a Xenopus cDNA that encodes a kinesin-related protein. *Molecular and Cellular Biology*, *11*(6), 3395–3398. https://doi.org/10.1128/MCB.11.6.3395

Leckband, D., & Israelachvili, J. (2001). Intermolecular forces in biology. *Quarterly Reviews of Biophysics*, *34*(2), 105–267. https://doi.org/10.1017/S0033583501003687

Lee, C.-W., Cao, H., Ichiyama, K., & Rana, T. M. (2005). Design and synthesis of a novel peptidomimetic inhibitor of HIV-1 Tat–TAR interactions: Squaryldiamide as a new potential bioisostere of unsubstituted guanidine.

Bioorganic & Medicinal Chemistry Letters, *15*(19), 4243–4246. https://doi.org/10.1016/j.bmcl.2005.06.077

Legon, A. C. (2010). The halogen bond: An interim perspective. *Physical Chemistry Chemical Physics*, *12*(28), 7736. https://doi.org/10.1039/c002129f

Lehn, J.-M. (1985). Supramolecular Chemistry: Receptors, Catalysts, and Carriers. *Science*, *227*(4689), 849–856. https://doi.org/10.1126/science.227.4689.849

Lehn, J.-M. (1988). Supramolecular Chemistry—Scope and Perspectives Molecules, Supermolecules, and Molecular Devices(Nobel Lecture). *Angewandte Chemie International Edition in English*, *27*(1), 89–112. https://doi.org/10.1002/anie.198800891

Lemmerer, A., Bernstein, J., & Spackman, M. A. (2012). Supramolecular polymorphism of the 1: 1 molecular salt (adamantane-1-carboxylate-3,5,7-tricarboxylic acid)·(hexamethylenetetraminium). A "failed" crystal engineering attempt. *Chem. Commun.*, *48*(13), 1883–1885. https://doi.org/10.1039/C1CC15849J

Li, L.-N., Wang, L., Cheng, Y.-N., Cao, Z.-Q., Zhang, X.-K., & Guo, X.-L. (2018). Discovery and Characterization of 4-Hydroxy-2-pyridone Derivative Sambutoxin as a Potent and Promising Anticancer Drug Candidate: Activity and Molecular Mechanism. *Molecular Pharmaceutics*, *15*(11), 4898–4911. https://doi.org/10.1021/acs.molpharmaceut.8b00525

Liao, S.-M., Du, Q.-S., Meng, J.-Z., Pang, Z.-W., & Huang, R.-B. (2013). The multiple roles of histidine in protein interactions. *Chemistry Central Journal*, *7*(1), 44. https://doi.org/10.1186/1752-153X-7-44

Lin, J. H., & Lu, A. Y. H. (1997). Role of Pharmacokinetics and Metabolism in Drug Discovery and Development. *Pharmacological Reviews*, *49*(4), 403–449.

Liu, Y., He, S., Chen, Y., Liu, Y., Feng, F., Liu, W., Guo, Q., Zhao, L., & Sun, H. (2020). Overview of AKR1C3: Inhibitor Achievements and Disease Insights. *Journal of Medicinal Chemistry*, *63*(20), 11305–11329. https://doi.org/10.1021/acs.jmedchem.9b02138

Liu, Z., Ren, B., Wang, Y., Zou, C., Qiao, Q., Diao, Z., Mi, Y., Zhu, D., & Liu, X. (2017). Sesamol Induces Human Hepatocellular Carcinoma Cells Apoptosis

by Impairing Mitochondrial Function and Suppressing Autophagy. *Scientific Reports*, *7*(1), 45728. https://doi.org/10.1038/srep45728

Lu, D., Huang, Q., Wang, S., Wang, J., Huang, P., & Du, P. (2019). The Supramolecular Chemistry of Cycloparaphenylenes and Their Analogs. *Frontiers in Chemistry*, *7*, 668. https://doi.org/10.3389/fchem.2019.00668

Lu, M., Zhu, H., Wang, X., Zhang, D., Xiong, L., Xu, L., & You, Y. (2016). The prognostic role of Eg5 expression in laryngeal squamous cell carcinoma. *Pathology*, *48*(3), 214–218. https://doi.org/10.1016/j.pathol.2016.02.008

Lucas, S.-M., Rothwell, N. J., & Gibson, R. M. (2006). The role of inflammation in CNS injury and disease: The role of inflammation in CNS. *British Journal of Pharmacology*, *147*(S1), S232–S240. https://doi.org/10.1038/sj.bjp.0706400

Lundstrom, K. (2006). Structural genomics for membrane proteins. *Cellular and Molecular Life Sciences*, *63*(22), 2597–2607. https://doi.org/10.1007/s00018-006-6252-y

Madhavan, G. R., Balraju, V., Mallesham, B., Chakrabarti, R., & Lohray, V. B. (2003). Novel coumarin derivatives of heterocyclic compounds as lipid-Lowering agents. *Bioorganic & Medicinal Chemistry Letters*, *13*(15), 2547–2551. https://doi.org/10.1016/S0960-894X(03)00490-6

Martinez, C. R., & Iverson, B. L. (2012). Rethinking the term "pi-stacking." *Chemical Science*, *3*(7), 2191. https://doi.org/10.1039/c2sc20045g

Mas-Torrent, M., & Rovira, C. (2011). Role of Molecular Order and Solid-State Structure in Organic Field-Effect Transistors. *Chemical Reviews*, *111*(8), 4833–4856. https://doi.org/10.1021/cr100142w

Maugeri-Saccà, M., Bartucci, M., & De Maria, R. (2013). Checkpoint kinase 1 inhibitors for potentiating systemic anticancer therapy. *Cancer Treatment Reviews*, *39*(5), 525–533. https://doi.org/10.1016/j.ctrv.2012.10.007

Mayur, Y., Peters, G., Rajendra Prasad, V., Lemos, C., & Sathish, N. (2009). Design of New Drug Molecules to be Used in Reversing Multidrug Resistance in Cancer Cells. *Current Cancer Drug Targets*, *9*(3), 298–306. https://doi.org/10.2174/156800909788166619

McGaughey, G. B., Gagné, M., & Rappé, A. K. (1998). π-Stacking Interactions. *Journal of Biological Chemistry*, *273*(25), 15458–15463. https://doi.org/10.1074/jbc.273.25.15458

McKinnon, J. J., Spackman, M. A., & Mitchell, A. S. (2004). Novel tools for visualizing and exploring intermolecular interactions in molecular crystals. *Acta Crystallographica Section B Structural Science*, *60*(6), 627–668. https://doi.org/10.1107/S0108768104020300

Meng, X.-Y., Zhang, H.-X., Mezei, M., & Cui, M. (2011). Molecular Docking: A Powerful Approach for Structure-Based Drug Discovery. *Current Computer Aided-Drug Design*, *7*(2), 146–157. https://doi.org/10.2174/157340911795677602

Metrangolo, P., Neukirch, H., Pilati, T., & Resnati, G. (2005). Halogen Bonding Based Recognition Processes: A World Parallel to Hydrogen Bonding. *Accounts of Chemical Research*, *38*(5), 386–395. https://doi.org/10.1021/ar0400995

Meyer, E. A., Castellano, R. K., & Diederich, F. (2003). Interactions with Aromatic Rings in Chemical and Biological Recognition. *Angewandte Chemie International Edition*, *42*(11), 1210–1250. https://doi.org/10.1002/anie.200390319

Millan, M. J. (2006). Multi-target strategies for the improved treatment of depressive states: Conceptual foundations and neuronal substrates, drug discovery and therapeutic application. *Pharmacology & Therapeutics*, *110*(2), 135–370. https://doi.org/10.1016/j.pharmthera.2005.11.006

Mita, A. C., Mita, M. M., Nawrocki, S. T., & Giles, F. J. (2008). Survivin: Key Regulator of Mitosis and Apoptosis and Novel Target for Cancer Therapeutics. *Clinical Cancer Research*, *14*(16), 5000–5005. https://doi.org/10.1158/1078-0432.CCR-08-0746

Moffett, R. B. (1964). Central Nervous System Depressants. VII. [1] Pyridyl Coumarins. *Journal of Medicinal Chemistry*, *7*(4), 446–449. https://doi.org/10.1021/jm00334a010

Mohsin, N. ul A., & Ahmad, M. (2018). Hybrid organic molecules as antiinflammatory agents; a review of structural features and biological activity. *Turkish Journal of Chemistry*, *42*. https://doi.org/10.3906/kim-1706-58

Mondal, S., Giri, D., & Mugesh, G. (2020). Halogen Bonding in the Molecular Recognition of Thyroid Hormones and Their Metabolites by Transport Proteins and Thyroid Hormone Receptors. *Journal of the Indian Institute of Science*, *100*(1), 231–247. https://doi.org/10.1007/s41745-019-00153-5

Morphy, R., Kay, C., & Rankovic, Z. (2004). From magic bullets to designed multiple ligands. *Drug Discovery Today*, *9*(15), 641–651. https://doi.org/10.1016/S1359-6446(04)03163-0

Morris, G. M., & Lim-Wilby, M. (2008). Molecular Docking. In A. Kukol (Ed.), *Molecular Modeling of Proteins* (Vol. 443, pp. 365–382). Humana Press. https://doi.org/10.1007/978-1-59745-177-2_19

Munshi, P., Skelton, B. W., McKinnon, J. J., & Spackman, M. A. (2008). Polymorphism in 3-methyl-4-methoxy-4′-nitrostilbene (MMONS), a highly active NLO material. *CrystEngComm*, *10*(2), 197–206. https://doi.org/10.1039/B712869J

Nepali, K., Sharma, S., Sharma, M., Bedi, P. M. S., & Dhar, K. L. (2014). Rational approaches, design strategies, structure activity relationship and mechanistic insights for anticancer hybrids. *European Journal of Medicinal Chemistry*, *77*, 422–487. https://doi.org/10.1016/j.ejmech.2014.03.018

Niewerth, M., Kunze, D., Seibold, M., Schaller, M., Korting, H. C., & Hube, B. (2003). Ciclopirox Olamine Treatment Affects the Expression Pattern of *Candida albicans* Genes Encoding Virulence Factors, Iron Metabolism Proteins, and Drug Resistance Factors. *Antimicrobial Agents and Chemotherapy*, *47*(6), 1805–1817. https://doi.org/10.1128/AAC.47.6.1805-1817.2003

O'Connor, D. S., Schechner, J. S., Adida, C., Mesri, M., Rothermel, A. L., Li, F., Nath, A. K., Pober, J. S., & Altieri, D. C. (2000). Control of Apoptosis during Angiogenesis by Survivin Expression in Endothelial Cells. *The American Journal of Pathology*, *156*(2), 393–398. https://doi.org/10.1016/S0002-9440(10)64742-6

P, J. J., Manju, S. L., Ethiraj, K. R., & Elias, G. (2018). Safer anti-inflammatory therapy through dual COX-2/5-LOX inhibitors: A structure-based approach. *European Journal of Pharmaceutical Sciences*, *121*, 356–381. https://doi.org/10.1016/j.ejps.2018.06.003

Parthasarathy, K., Praveen, C., Balachandran, C., Senthil kumar, P., Ignacimuthu, S., & Perumal, P. T. (2013). Cu(OTf)2 catalyzed three component reaction: Efficient synthesis of spiro[indoline-3,4′-pyrano[3,2-b]pyran derivatives and their anticancer potency towards A549 human lung cancer cell lines. *Bioorganic & Medicinal Chemistry Letters*, *23*(9), 2708–2713. https://doi.org/10.1016/j.bmcl.2013.02.086

Patani, G. A., & LaVoie, E. J. (1996). Bioisosterism: A Rational Approach in Drug Design. *Chemical Reviews*, *96*(8), 3147–3176. https://doi.org/10.1021/cr950066q

Petti, M. A., Shepodd, T. J., Barrans, R. E., & Dougherty, D. A. (1988). "Hydrophobic" binding of water-soluble guests by high-symmetry, chiral hosts. An electron-rich receptor site with a general affinity for quaternary ammonium compounds and electron-deficient .pi. Systems. *Journal of the American Chemical Society*, *110*(20), 6825–6840. https://doi.org/10.1021/ja00228a036

Planas-Silva, M. D., & Filatova, I. S. (2007). Estrogen-dependent regulation of Eg5 in breast cancer cells. *Anti-Cancer Drugs*, *18*(7), 773–779. https://doi.org/10.1097/CAD.0b013e3280a02f2b

Politzer, P., Murray, J. S., & Clark, T. (2010). Halogen bonding: An electrostatically-driven highly directional noncovalent interaction. *Physical Chemistry Chemical Physics*, *12*(28), 7748. https://doi.org/10.1039/c004189k

Pozzan, A. (2006). Molecular Descriptors and Methods for Ligand Based Virtual High Throughput Screening in Drug Discovery. *Current Pharmaceutical Design*, *12*(17), 2099–2110. https://doi.org/10.2174/138161206777585247

Prakash, O., Usmani, S., Gupta, A., Singh, R., Singh, N., & Ved, A. (2020). Bioactive Polyphenols as Promising Natural Medicinal Agents Against Cancer: The Emerging Trends and Prospective Goals. *Current Bioactive Compounds*, *16*(3), 243–264. https://doi.org/10.2174/1573407214666181030122046

Reilly, S. W., Puentes, L. N., Wilson, K., Hsieh, C.-J., Weng, C.-C., Makvandi, M., & Mach, R. H. (2018). Examination of Diazaspiro Cores as Piperazine Bioisosteres in the Olaparib Framework Shows Reduced DNA Damage and

Cytotoxicity. *Journal of Medicinal Chemistry*, *61*(12), 5367–5379. https://doi.org/10.1021/acs.jmedchem.8b00576

Rhind, N., & Russell, P. (1998). Mitotic DNA damage and replication checkpoints in yeast. *Current Opinion in Cell Biology*, *10*(6), 749–758. https://doi.org/10.1016/S0955-0674(98)80118-X

Rovnyak, G. C., Atwal, K. S., Hedberg, A., Kimball, S. D., Moreland, S., Gougoutas, J. Z., O'Reilly, B. C., Schwartz, J., & Malley, M. F. (1992). Dihydropyrimidine calcium channel blockers. 4. Basic 3-substituted-4-aryl-1,4-dihydropyrimidine-5-carboxylic acid esters. Potent antihypertensive agents. *Journal of Medicinal Chemistry*, *35*(17), 3254–3263. https://doi.org/10.1021/jm00095a023

Ryan, B. M., O'Donovan, N., & Duffy, M. J. (2009). Survivin: A new target for anti-cancer therapy. *Cancer Treatment Reviews*, *35*(7), 553–562. https://doi.org/10.1016/j.ctrv.2009.05.003

Saijo, T., Ishii, G., Ochiai, A., Yoh, K., Goto, K., Nagai, K., Kato, H., Nishiwaki, Y., & Saijo, N. (2006). Eg5 expression is closely correlated with the response of advanced non-small cell lung cancer to antimitotic agents combined with platinum chemotherapy. *Lung Cancer*, *54*(2), 217–225. https://doi.org/10.1016/j.lungcan.2006.06.018

Salonen, L. M., Ellermann, M., & Diederich, F. (2011). Aromatic Rings in Chemical and Biological Recognition: Energetics and Structures. *Angewandte Chemie International Edition*, *50*(21), 4808–4842. https://doi.org/10.1002/anie.201007560

Sanchez, R. I., Fillgrove, K. L., Yee, K. L., Liang, Y., Lu, B., Tatavarti, A., Liu, R., Anderson, M. S., Behm, M. O., Fan, L., Li, Y., Butterton, J. R., Iwamoto, M., & Khalilieh, S. G. (2019). Characterisation of the absorption, distribution, metabolism, excretion and mass balance of doravirine, a non-nucleoside reverse transcriptase inhibitor in humans. *Xenobiotica*, *49*(4), 422–432. https://doi.org/10.1080/00498254.2018.1451667

Sanchez, Y., Wong, C., Thoma, R. S., Richman, R., Wu, Z., Piwnica-Worms, H., & Elledge, S. J. (1997). Conservation of the Chk1 Checkpoint Pathway in Mammals: Linkage of DNA Damage to Cdk Regulation Through Cdc25.

Science, *277*(5331), 1497–1501. https://doi.org/10.1126/science.277.5331.1497

Sashidhara, K. V., Kumar, A., Kumar, M., Sarkar, J., & Sinha, S. (2010). Synthesis and in vitro evaluation of novel coumarin–chalcone hybrids as potential anticancer agents. *Bioorganic & Medicinal Chemistry Letters*, *20*(24), 7205–7211. https://doi.org/10.1016/j.bmcl.2010.10.116

Scapin, G. (2006). Structural Biology and Drug Discovery. *Current Pharmaceutical Design*, *12*(17), 2087–2097. https://doi.org/10.2174/138161206777585201

Scott Lokey, R., & Iverson, B. L. (1995). Synthetic molecules that fold into a pleated secondary structure in solution. *Nature*, *375*(6529), 303–305. https://doi.org/10.1038/375303a0

Shen, T., & Huang, S. (2016). Repositioning the Old Fungicide Ciclopirox for New Medical Uses. *Current Pharmaceutical Design*, *22*(28), 4443–4450. https://doi.org/10.2174/1381612822666160530151209

Shepodd, T. J., Petti, M. A., & Dougherty, D. A. (1986). Tight, oriented binding of an aliphatic guest by a new class of water-soluble molecules with hydrophobic binding sites. *Journal of the American Chemical Society*, *108*(19), 6085–6087. https://doi.org/10.1021/ja00279a093

Sherrill, C. D. (2013). Energy Component Analysis of π Interactions. *Accounts of Chemical Research*, *46*(4), 1020–1028. https://doi.org/10.1021/ar3001124

Shi, Y., & Zhou, C.-H. (2011). Synthesis and evaluation of a class of new coumarin triazole derivatives as potential antimicrobial agents. *Bioorganic & Medicinal Chemistry Letters*, *21*(3), 956–960. https://doi.org/10.1016/j.bmcl.2010.12.059

Shipley, J. B., Tolman, D., Hastillo, A., & Hess, M. L. (1996). Milrinone: Basic and Clinical Pharmacology and Acute and Chronic Management: *The American Journal of the Medical Sciences*, *311*(6), 286–291. https://doi.org/10.1097/00000441-199606000-00011

Simal, C., Lebl, T., Slawin, A. M. Z., & Smith, A. D. (2012). Dihydropyridones: Catalytic Asymmetric Synthesis, N- to C-Sulfonyl Transfer, and Derivatizations. *Angewandte Chemie International Edition*, *51*(15), 3653–3657. https://doi.org/10.1002/anie.201109061

Spackman, M. A., & Byrom, P. G. (1997). A novel definition of a molecule in a crystal. *Chemical Physics Letters*, *267*(3–4), 215–220. https://doi.org/10.1016/S0009-2614(97)00100-0

Spackman, M. A., & Jayatilaka, D. (2009). Hirshfeld surface analysis. *CrystEngComm*, *11*(1), 19–32. https://doi.org/10.1039/B818330A

Stanchev, S., Momekov, G., Jensen, F., & Manolov, I. (2008). Synthesis, computational study and cytotoxic activity of new 4-hydroxycoumarin derivatives. *European Journal of Medicinal Chemistry*, *43*(4), 694–706. https://doi.org/10.1016/j.ejmech.2007.05.005

Sun, D., Lu, J., Ding, K., Bi, D., Niu, Z., Cao, Q., Zhang, J., & Ding, S. (2013). The expression of Eg5 predicts a poor outcome for patients with renal cell carcinoma. *Medical Oncology*, *30*(1), 476. https://doi.org/10.1007/s12032-013-0476-0

Sun, X., Shi, X., Sun, X., Luo, Y., Wu, X., Yao, C., Yu, H., Li, D., Liu, M., & Zhou, J. (2011). Dimethylenastron suppresses human pancreatic cancer cell migration and invasion in vitro via allosteric inhibition of mitotic kinesin Eg5. *Acta Pharmacologica Sinica*, *32*(12), 1543–1548. https://doi.org/10.1038/aps.2011.130

Sung, H., Ferlay, J., Siegel, R. L., Laversanne, M., Soerjomataram, I., Jemal, A., & Bray, F. (2021). Global Cancer Statistics 2020: GLOBOCAN Estimates of Incidence and Mortality Worldwide for 36 Cancers in 185 Countries. *CA: A Cancer Journal for Clinicians*, *71*(3), 209–249. https://doi.org/10.3322/caac.21660

Szumilak, M., Wiktorowska-Owczarek, A., & Stanczak, A. (2021). Hybrid Drugs—A Strategy for Overcoming Anticancer Drug Resistance? *Molecules*, *26*(9), 2601. https://doi.org/10.3390/molecules26092601

Taniguchi, H., Ebina, M., Kondoh, Y., Ogura, T., Azuma, A., Suga, M., Taguchi, Y., Takahashi, H., Nakata, K., Sato, A., Takeuchi, M., Raghu, G., Kudoh, S., Nukiwa, T., & the Pirfenidone Clinical Study Group in Japan. (2010). Pirfenidone in idiopathic pulmonary fibrosis. *European Respiratory Journal*, *35*(4), 821–829. https://doi.org/10.1183/09031936.00005209

Thakuria, R., Nath, N. K., & Saha, B. K. (2019). The Nature and Applications of π–π Interactions: A Perspective. *Crystal Growth & Design*, *19*(2), 523–528. https://doi.org/10.1021/acs.cgd.8b01630

Tietze, L. F., Bell, H. P., & Chandrasekhar, S. (2003). Natural Product Hybrids as New Leads for Drug Discovery. *Angewandte Chemie International Edition*, *42*(34), 3996–4028. https://doi.org/10.1002/anie.200200553

Tojiboev, A., Zhurakulov, S., Englert, U., Wang, R., Kalf, I., Vinogradova, V., Turgunov, K., & Tashkhodjaev, B. (2020). Hirshfeld Surface Analysis and Energy Framework for Crystals of Quinazoline Methylidene Bridged Compounds. *The 2nd International Online Conference on Crystals*, 1. https://doi.org/10.3390/proceedings2020062001

Tripathy, R., McHugh, R. J., Ghose, A. K., Ott, G. R., Angeles, T. S., Albom, M. S., Huang, Z., Aimone, L. D., Cheng, M., & Dorsey, B. D. (2011). Pyrazolone-based anaplastic lymphoma kinase (ALK) inhibitors: Control of selectivity by a benzyloxy group. *Bioorganic & Medicinal Chemistry Letters*, *21*(24), 7261–7264. https://doi.org/10.1016/j.bmcl.2011.10.055

Uchiyama, S., Fukatsu, E., McClean, G. D., & de Silva, A. P. (2016). Measurement of Local Sodium Ion Levels near Micelle Surfaces with Fluorescent Photoinduced-Electron-Transfer Sensors. *Angewandte Chemie International Edition*, *55*(2), 768–771. https://doi.org/10.1002/anie.201509096

Vane, J. R. (2000). The Mechanism of Action of Anti-Inflammatory Drugs. In C. N. Serhan & H. D. Perez (Eds.), *Advances in Eicosanoid Research* (pp. 1–23). Springer Berlin Heidelberg. https://doi.org/10.1007/978-3-662-04047-8_1

Vianna, D. R., Hamerski, L., Figueiró, F., Bernardi, A., Visentin, L. C., Pires, E. N. S., Teixeira, H. F., Salbego, C. G., Eifler-Lima, V. L., Battastini, A. M. O., von Poser, G. L., & Pinto, A. C. (2012). Selective cytotoxicity and apoptosis induction in glioma cell lines by 5-oxygenated-6,7-methylenedioxycoumarins from Pterocaulon species. *European Journal of Medicinal Chemistry*, *57*, 268–274. https://doi.org/10.1016/j.ejmech.2012.09.007

Vitaku, E., Smith, D. T., & Njardarson, J. T. (2014). Analysis of the Structural Diversity, Substitution Patterns, and Frequency of Nitrogen Heterocycles among U.S. FDA Approved Pharmaceuticals: Miniperspective. *Journal of*

Medicinal Chemistry, *57*(24), 10257–10274. https://doi.org/10.1021/jm501100b

Weiss, M. S., Brandl, M., Sühnel, J., Pal, D., & Hilgenfeld, R. (2001). More hydrogen bonds for the (structural) biologist. *Trends in Biochemical Sciences*, *26*(9), 521–523. https://doi.org/10.1016/S0968-0004(01)01935-1

Wheeler, S. E. (2011). Local Nature of Substituent Effects in Stacking Interactions. *Journal of the American Chemical Society*, *133*(26), 10262–10274. https://doi.org/10.1021/ja202932e

Williams, D. H., Stephens, E., O'Brien, D. P., & Zhou, M. (2004). Understanding Noncovalent Interactions: Ligand Binding Energy and Catalytic Efficiency from Ligand-Induced Reductions in Motion within Receptors and Enzymes. *Angewandte Chemie International Edition*, *43*(48), 6596–6616. https://doi.org/10.1002/anie.200300644

Wissing, M. D., De Morrée, E. S., Dezentjé, V. O., Buijs, J. T., De Krijger, R. R., Smit, V. T. H. B. M., Van Weerden, W. M., Gelderblom, H., & van der Pluijm, G. (2014). Nuclear Eg5 (kinesin spindle protein) expression predicts docetaxel response and prostate cancer aggressiveness. *Oncotarget*, *5*(17), 7357–7367. https://doi.org/10.18632/oncotarget.1985

Wolff, S. K., Grimwood, D. J., McKinnon, J. J., Turner, M. J., Jayatilaka, D., & Spackman, M. A. (2012). *CrystalExplorer* (3.1) [Computer software].

Xiao, M., & Li, W. (2015). Recent Advances on Small-Molecule Survivin Inhibitors. *Current Medicinal Chemistry*, *22*(9), 1136–1146. https://doi.org/10.2174/0929867322666150114102146

Xu, J., Lacoske, M. H., & Theodorakis, E. A. (2014). Neurotrophic Natural Products: Chemistry and Biology. *Angewandte Chemie International Edition*, *53*(4), 956–987. https://doi.org/10.1002/anie.201302268

Zacharias, N. (2002). Cation–π interactions in ligand recognition and catalysis. *Trends in Pharmacological Sciences*, *23*(6), 281–287. https://doi.org/10.1016/S0165-6147(02)02027-8

Zhang, B., & Studer, A. (2015). Recent advances in the synthesis of nitrogen heterocycles via radical cascade reactions using isonitriles as radical acceptors.

Chemical Society Reviews, *44*(11), 3505–3521. https://doi.org/10.1039/C5CS00083A

Zhang, W., Koehler, K. F., Harris, B., Skolnick, P., & Cook, J. M. (1994). Synthesis of benzo-fused benzodiazepines employed as probes of the agonist pharmacophore of benzodiazepine receptors. *Journal of Medicinal Chemistry*, *37*(6), 745–757. https://doi.org/10.1021/jm00032a007

Zhou, P., Huang, J., & Tian, F. (2012). Specific Noncovalent Interactions at Protein-Ligand Interface: Implications for Rational Drug Design. *Current Medicinal Chemistry*, *19*(2), 226–238. https://doi.org/10.2174/092986712803414150

Zhou, W., & Limonta, P. (2014). AKR1C3 Inhibition Therapy in Castration-Resistant Prostate Cancer and Breast Cancer: Lessons from Responses to SN33638. *Frontiers in Oncology*, *4*. https://doi.org/10.3389/fonc.2014.00162

Zhu, L., Cheng, P., Lei, N., Yao, J., Sheng, C., Zhuang, C., Guo, W., Liu, W., Zhang, Y., Dong, G., Wang, S., Miao, Z., & Zhang, W. (2011). Synthesis and Biological Evaluation of Novel Homocamptothecins Conjugating with Dihydropyrimidine Derivatives as Potent Topoisomerase I Inhibitors. *Archiv Der Pharmazie*, *344*(11), 726–734. https://doi.org/10.1002/ardp.201000402

BIO-DATA OF THE CANDIDATE

1. NAME : Laldingluaia Khiangte

2. DATE OF BIRTH : 19th July, 1977

3. FATHER'S NAME : K. Vanlalṭana

4. PERMANENT ADDRESS : Luangmual, Aizawl, Mizoram.

PIN-796009

5. EMAIL ADDRESS : dinga012@gmail.com

6. EDUCATIONAL QUALIFICATIONS :

Examination passed	Year of Passing	Board/University	Division	% of marks	Subjects
HSLC	1993	Mizoram Board of School Education	I	65.66	English, Mizo, Mathematics, Science, Social sciences
HSSLC/ PU(Sc)	1995	North Eastern Hill University	II	50.11	English, Biology, Physics, Chemistry, Mathematics
B. SC (Chemistry)	1998	North Eastern Hill University	II	59.00	Chemistry, Botany, Zoology, GFC
M. Sc (Chemistry)	2000	North Eastern Hill University	I	68.17	Chemistry
CSIR-UGC NET	2005	CSIR-UGC	LS		Chemical Sciences

LIST OF PUBLICATIONS

1. **Laldingluaia Khiangte**, Biki Hazarika, Swarnadeep Biswas, Lalhruaizela, Ramesh Kataria, Pradeep Kumar Shukla, Ved Prakash Singh. "Design, Synthesis and structural study of two symmetry-independent pyridone analogue in the asymmetric unit*". Journal of Molecular Structure*. **(Accepted).**

2. Lalhruaizela, Brilliant N. Marak, Biki Hazarika, **Laldingluaia Khiangte**, Ved Prakash Singh. 2023. "Synthesis of Spirooxindoles and Study of their self-Assembly features; Hirshfeld Surface, Energy Framework and In Silico analysis". *ChemistrySelect* 2023, e202300169. doi.org/10.1002/slct.202300169 **(Accepted).**

3. Jayanta Dowarah, Biki Hazarika, Balkaran Singh Sran, **Dingtea Khiangte**, Ved Prakash Singh. "Design, synthesis, structural investigation and binding study of 2-pyridone-based pharmaceutical precursor with DNA". *Journal of Molecular Structure* 1282 (2023) 135182. https://doi.org/10.1016/j.molstruc.2023.135182 (IF: 3.841)

4. Brilliant N. Marak, Jayanta Dowarah, **Laldingluaia Khiangte**, Ved Prakash Singh. 2020. "A comprehensive insight on the recent development of Cyclic Dependent Kinase inhibitors as anticancer agents." *European Journal of Medicinal Chemistry 203 (2020) 112571* doi: 10.1016/j.ejmech.2020.112571 (IF: 7.088)

5. Brilliant N. Marak, Jayanta Dowarah, **Laldingluaia Khiangte**, Ved Prakash Singh. 2020. "Step toward repurposing drug discovery for COVID-19 therapeutics through in silico approach." *Drug Development Research 2021:82:347-392.* doi:10.1002/ddr.21757 (IF: 5.004)

CONFERENCES AND SEMINAR

1. Presented paper entitled, **"Synthesis, structural studies of dihydropyridones based analogs and in silico analysis"** at Second International Conference on Advances in Management, Engineering & Technology (ICAMET-2022)-(Online), organised by RSP Conference Hub, Coimbatore, Tamil Nadu, India on 25th & 26th June 2022.

2. Presented poster entitled, **"Pyridone based analog synthesis, study and molecular docking studies"** at 2nd Virtual international Conference on Biotechnology and Bioinformatics (ICBB-2022) during 30-31 July, 2022, organized by Inside Biosolutions, France & OMIC-A-Research and Innovation, Turkey in technical collaboration with Indian Science and Technology Foundation and Annotation Analytics, India.

PARTICULARS OF THE CANDIDATE

NAME OF CANDIDATE	**:**	Laldingluaia Khiangte
DEGREE	**:**	Doctor of Philosophy (Ph. D)
DEPARTMENT	**:**	Industrial Chemistry
TITLE OF THESIS	**:**	Synthesis and study of novel hybrid molecules
DATE OF ADMISSION	**:**	16th August, 2018

APPROVAL OF RESEARCH PROPOSAL:

1. DRC	**:**	16th April, 2019
2. BOS	**:**	23rd April, 2019
3. SCHOOL BOARD	**:**	8th May, 2019
4. MZU REGN. NO.	**:**	1807294
5. Ph.D REGN. NO. & DATE:		MZU/Ph.D./1252 of 18.06.2018
6. EXTENSION	**:**	NA

Head

Department of Industrial Chemistry

ABSTRACT

SYNTHESIS AND STUDY OF NOVEL HYBRID MOLECULES

AN ABSTRACT SUBMITTED IN PARTIAL FULFILLMENT OF THE REQUIREMENTS FOR THE DEGREE OF DOCTOR OF PHILOSOPHY

LALDINGLUAIA KHIANGTE

MZU REGISTRATION NO.: 1807294

PH.D REGISTRATION NO. : MZU/Ph.D./1252 of 16.08.2018

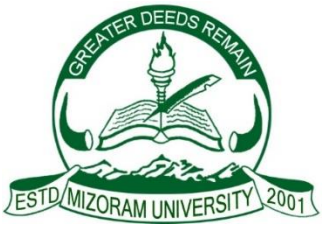

DEPARTMENT OF INDUSTRIAL CHEMISTRY

SCHOOL OF PHYSICAL SCIENCES

DECEMBER, 2022

SYNTHESIS AND STUDY OF NOVEL HYBRID MOLECULES

BY

LALDINGLUAIA KHIANGTE

Department of Industrial Chemistry

Under the supervision of

Dr. VED PRAKASH SINGH

Submitted

In partial fulfillment of the requirement of the Degree of Doctor of Philosophy in Industrial Chemistry of Mizoram University, Aizawl.

ABSTRACT

Heterocyclic compounds are found naturally in the components of the biological systems, occupying more than half of the naturally occurring compounds. Nitrogen-containing heterocycles are the main structural component of small-molecule drugs, which accounts for 75% of the total small structural medicines. Nitrogen atoms can quickly form hydrogen bonds with the target biological system; thus, they have a wide range of pharmacophores.

Today's drug development strategies aim to parallel modes of action to multiple targets. To focus on the design strategies for developing new drugs, hybridizing molecules is one of the most popular methods to develop multi-target drug development. The advantages of hybrid molecules are treating a complex disease using a single molecule with two or more pharmacophores, increasing activity, reducing toxicity, and therapeutic effectiveness.

Molecular recognition is the key feature in the biological processes which involve various intermolecular non-covalent interactions, including hydrogen bonding, π-π stacking interactions, and van der Waals forces. The study of non-covalent interactions is essential for medicinal chemists, which is the special glue to hold the receptor and drug together.

Chapter **1** is the introduction containing the literature surveyed related to the present work. The heterocyclic compounds are the compounds of chemist interest due to their wide applications. Hybridizing molecules is important to develop better activity and multi-target drugs to facilitate fewer toxic effects. Molecular hybridization proposes the rational drug design of the ligands or prototypes through the fusion of two or more known bioactive structures. It leads to the new hybrid molecule containing two or more active sites. The multi-targeted pharmacophore model of the hybrid molecule can be divided into four distinct types based on the degree of pharmacophore overlapping: conjugated pharmacophore with the cleavable or non-cleavable linker, fused and merged pharmacophore.

The principles of bioisostere are improved oral absorption, membrane permeability, and ADME of the medicines. The bioisostere can also rationalize a lead compound into a better potency, increase selectivity, lesser side effects, etc. Non-covalent interactions are the center of supramolecular chemistry and molecular recognition, which are crucial for understanding many energetic and structural properties. Intermolecular interactions such as hydrogen bonding, π-stacking, anion-π, cation-π, and π-π stacking interactions play an essential role in the stability of supramolecular materials with different orientations by varying chemical environments. Molecular recognition refers to the contact between two molecules through various forms of bonding. It is also important in applied biochemistry since it decides whether a molecule has clinically beneficial qualities.

Chapter 2 contains the synthesis and studies of the 2-pyridone-based hybrid derivatives. Scheme 1 starts with the multicomponent reaction of 1,3-diketone, aldehyde, and malononitrile in ethanol using piperidine as the catalyst to form 4-pyrans. 4-pyrans treated with iodine or excess formic acid converted into pyridone ring. This dihydropyridone, on oxidation with DDQ, formed a 2-pyridone core and benzene moiety. The 2-pyridone-based hybrid molecules synthesized compounds forming suitable crystals are studied with their supramolecular framework, Hirshfeld surface analysis, and in silico molecular docking.

The crystals obtained from this chapter formed a crystal system of orthorhombic, monoclinic, and triclinic systems. Four compounds, 1**.3A, 1.3G, 1.3H**, and **1.3I**, are two symmetry-independent molecules among the synthesized compounds. The molecular self-assembly was mainly assisted by the hydrogen bonding involving N-H…O, C-H…O, and C-H…N interactions. The Hirshfeld surface analysis is done with all the crystal compounds to compare the supramolecular structure of the compounds. Enrichment ratio calculation from Hirshfeld's surface analysis is also done, and it shows that C…H, N…H, and O…H interactions are enriched in most of the compounds. Still, H…H contacts are not favored interactions with an enrichment ratio of less than unity.

In silico molecular docking analysis of the compounds with Eg5 and Survivin protein illustrate those compounds **1.3I** and **1.3C** show the highest binding scores of -7.2 kcal/mol and -6.8 kcal/mol, respectively. Thus, the detailed binding affinities would simplify the future rationalization of inhibitor design and optimization of structural features.

Chapter 3 deals with the synthesis and study of pyranopyrazoles and spirooxindole derivatives. The pyranopyrazole derivatives are successfully synthesized from a novel synthetic route reacting 1,3-diketones, malononitrile, aromatic aldehyde, and hydrazine hydrate using piperazine as a base catalyst in ethanol at reflux conditions. Substituted pyrano[2,3-c]pyrazole structures are important heterocyclic compounds with various biological activities. The pyranopyrazole compounds forming suitable crystals are analyzed for their supramolecular framework, which involves N-H…N, N-H…O, and C-H…N interactions. These are the primary interactions to assist their molecular association. The supramolecular framework displays that N-H…N and N-H…O are the major interactions among all in the dimerization of the molecules in the crystal lattice.

The Hirshfeld surface analysis of the crystal compounds is carried out to support the non-covalent interactions observed in the supramolecular structure. The enrichment ratio of the interatomic contacts is calculated using the relative percentage contribution of the 2D fingerprint plot. It found that C…H, N…H, and O…H interactions are enriched in all the compounds. The molecular docking studies of the synthesized compounds were done with checkpoints kinase 1 (Chk1) and human Aldo-keto reductase family 1 member 3 (AKR1C3) protein. The compound **2.1A** showed the highest docking score of -8.1 kcal/mol and -9.4 kcal/mol, respectively, with the enzymes Chk1 and AKR1C3 in their active sites.

The spirooxindole derivatives of indole-pyran hybrid molecules are synthesized in the novel synthetic route involving multicomponent reaction of 1,3-diketone/4-hydroxy derivative, malononitrile, and isatin using piperidine as a base catalyst in ethanol at room temperature in scheme 3. The supramolecular framework structure of these molecules displays the interaction N-H…O, C-H…O, and N-H…N,

which plays a significant role in the molecular association. Hirshfeld surface analysis studies support the intermolecular non-covalent interactions observed in the supramolecular structure. The enrichment ratio calculation results in the interaction C…H, N…H, and O…H are enriched, and other interactions in the compounds are not enriched except C…N in **3.1A**. The molecular docking studies of the synthesized molecule with anaplastic lymphoma kinase (ALK) protein illustrate compound **3.1A** scored the highest binding affinities -8.7 kcal/mol in the binding pocket, forming a hydrogen bond with Asp1276 amino acid residue.

In chapter 4, flexible Pyridine-based hybrid molecules are successfully synthesized in Scheme 5, which contains a flexible methylene linker using anhydrous K_2CO_3 as a catalyst in DMF solvent at room temperature. The 2-pyridone derivatives are used as a starting scaffold in the design of the hybrid molecules, and these are linked with an aromatic ring by a methylene group. The synthetic method involves the alkylation of the 2-pyridone core at the functional groups, i.e., O-alkylation and N-alkylation; the O-alkylation was the preferred site compared with the N-alkylation.

The suitable crystals are studied using SC-XRD and analyzed their supramolecular framework and Hirshfeld surface analysis, including enrichment ratio. The C-H…O and C-H…N interactions are the significant interactions found in all the compounds, and the presence of π…π stacking interactions are also present between the aromatic system of the molecule. The synthesized flexible hybrid molecules are docked with COX-2 and 5-LOX proteins for their biological activities. The docking results showed that compound **5.2D** has the highest binding score in 5-LOX protein, and **5.2A**, with a binding score of -9.1 kcal/mol, are the most promising compounds.

Chapter 5 summarizes the thesis and conclusion of the studies on the supramolecular framework, including the non-covalent interactions, Hirshfeld surface analysis, and molecular docking studies. Depending upon the size of the substituents, the non-covalent interactions and the biological activity of the molecules also change. The present studies deliver the importance of non-covalent interactions in crystal engineering and drug design.